

**A Measurement of the Diffractive Proton
Structure Function $F_2^{D(3)}$ at Low Q^2 at the
H1 Experiment at HERA**

Carrie-anne Louise Johnson

A thesis submitted to
The University of Birmingham
for the degree of
DOCTOR OF PHILOSOPHY

School of Physics and Astronomy
University of Birmingham
April 2002

Abstract

A measurement is presented of the diffractive proton structure function describing the process $ep \rightarrow eXY$, where X and Y represent the hadronic final states into which the exchanged virtual photon and the proton dissociate respectively. The data, with an integrated luminosity of 3.74 pb^{-1} , were collected with unbiased triggers using the H1 detector at the HERA positron proton collider in 1999. The measurement is presented in the form of a 3-dimensional structure function $F_2^{D(3)}(\beta, Q^2, x_p)$, integrated over the region $M_Y < 1.6 \text{ GeV}$ and $|t| < 1 \text{ GeV}^2$. The kinematic range covered is $1.5 \text{ GeV}^2 < Q^2 < 45 \text{ GeV}^2$, $0.001 < \beta < 0.9$ and $10^{-4} \lesssim x_p < 0.05$. Previous published H1 results for $F_2^{D(3)}(\beta, Q^2, x_p)$ only exist for $Q^2 \geq 4.5 \text{ GeV}^2$ and $\beta \geq 0.01$ hence not only does this analysis provide a new high precision measurement of $F_2^{D(3)}(\beta, Q^2, x_p)$ but it also provides kinematic coverage at lower Q^2 and β values than has previously been possible. The results were extracted with full statistical and systematic errors and a good agreement is generally observed in the region of overlap with previous H1 measurements. The Q^2 dependence at fixed values of x_p exhibits rising scaling violations for most of the β range, which start to fall only at the highest values of β . This behaviour is expected for the exchange of a gluon-dominated pomeron which evolves according to the DGLAP equations. Comparisons with different models of diffraction were made and a value for the effective pomeron intercept $\alpha_{\mathbb{P}}(0) = 1.107 \pm 0.026$ (stat.) was obtained from a Regge-motivated fit.

Acknowledgements

I have received a lot of help and support throughout the course of my Ph.D. from people in Birmingham and at DESY, and from my family and friends. I would like to acknowledge here specific people who contributed to my learning and achieving in one way or another.

Whilst this thesis is written entirely by myself, and the work herein my own, I have received invaluable help from several people and would like to acknowledge the help that I have received. Firstly I would like to thank Paul Newman for introducing me to the methods and techniques required to measure the diffractive structure function, which I did not develop myself [69] [76] [78]. Working with him on H1 1997 data previously, which is now an H1 preliminary result [78], allowed me to develop the required skills to perform an analysis. The work I performed on the diffractive event selection was very useful although the treatment of the forward detectors used in the analysis is based on work carried out by Paul Thompson [105]. Thanks to Frank-Peter Schilling who performed the fits to the final data points, and for producing the relevant plots which are presented in chapter 5. For the trigger efficiency plot I would like to thank Yves Coppens. Thanks also go to Tomas Lastovicka and Doris Eckstein for their help with selecting the inclusive deep-inelastic scattering events from the 1999 minimum bias data sample. All other work represents my own efforts.

I would like to thank my supervisor Ian Kenyon for his continued support and advice. I would especially like to thank Paul Newman for his continuous help and encouragement throughout my Ph.D, and for introducing me to a fascinating area of particle physics and for not getting fed up with my persistent questions. Thanks to Paul Thompson and Frank-Peter Schilling for always being willing and able to assist with various technical aspects of the analysis. Thanks also to Yves Coppens for helping out with the analysis towards the end, and good luck for continuing to look at the 1999 data. I am grateful to Paul Newman, Paul Thompson and Ian Kenyon for proof-reading all or part of this thesis, and for making many helpful suggestions.

Physics aside, I've had the good fortune to have been supported by my family and friends throughout the last three and a half years. Thank you for keeping me sane. Thanks to my parents and sister for always being there. Maybe you'll believe that I'll finally leave university now! Finally, thanks to my husband Lionel. Not only for financially supporting me when my funding came to an end but also for sticking by me through both the good and bad times, and when I had to spend time away from home. For never giving up on me, and for his amazing love and friendship throughout - thank you.

A Note on Units

In this work, a system of natural units will be used, whereby $\hbar = c = 1$.

Between October 1998 and September 2001, this work was supported financially by the UK Particle Physics and Astronomy Research Council (P.P.A.R.C.).

Dedicated

to

Lionel

Contents

1	The H1 Detector	3
1.1	Introduction	3
1.2	Overview of H1	5
1.3	Tracking in the H1 Detector	7
1.3.1	The Central Tracking Detector (CTD)	8
1.3.2	The Forward Tracking Detector (FTD)	9
1.3.3	The Backward Drift Chamber (BDC)	10
1.4	Calorimetry in the H1 Detector	10
1.4.1	The Liquid Argon (LAr) Calorimeter	11
1.4.2	The Spacal Calorimeter	12
1.4.3	PLUG Calorimeter	13
1.4.4	The Tail Catcher (TC)	13
1.4.5	The Very Low Q^2 Spectrometer (VLQ)	14
1.5	Muon Detection	14
1.5.1	The Forward Muon Detector (FMD)	14
1.5.2	Central Muon Detection	15
1.6	Beam-line Instrumentation	15

1.6.1	The Forward Tagger System (FTS)	16
1.6.2	The Forward Proton Spectrometer (FPS)	16
1.6.3	The Forward Neutron Calorimeter (FNC)	16
1.7	The H1 Luminosity System	17
1.8	Triggering	18
1.9	HERA and H1 Upgrades	18
2	Deep-Inelastic Scattering (DIS)	20
2.1	Introduction	20
2.2	DIS at HERA	20
2.2.1	Kinematics	20
2.2.2	Inclusive Proton Measurements	23
2.2.3	The Quark Parton Model (QPM) and Bjorken Scaling	24
2.2.4	QCD and Gluons	25
2.2.5	QCD Evolution	26
2.2.6	Photoproduction	33
2.2.7	Saturation in Deep-Inelastic Scattering	34
3	Diffractive Physics	38
3.1	Diffraction at HERA	38
3.2	Kinematics of Deep-Inelastic Diffraction	39
3.3	The Diffractive Structure Function	42
3.4	Models of Diffraction	42
3.4.1	Regge Models	42

3.4.2	Hard Scattering Factorisation	46
3.4.3	Two Gluon Exchange Models	52
3.4.4	Soft Colour Models	57
4	Event Selection	61
4.1	Introduction	61
4.2	Monte Carlo Models	61
4.3	Event Selection	63
4.3.1	Level 1 Trigger Conditions	63
4.3.2	Sub-triggers for the 1999 Minimum Bias Run	64
4.3.3	Trigger Phases and Prescale Factors	66
4.4	Preliminary Data Selection	66
4.5	Reconstruction methods	67
4.5.1	Electron Method	67
4.5.2	Hadron Method	67
4.5.3	Double Angle Method	68
4.5.4	Electron-Double Angle Method	68
4.5.5	Resolutions in x and Q^2	69
4.6	DIS Event Selection	69
4.6.1	Vertex Efficiency	73
4.6.2	Spacal Calibration	73
4.6.3	Hadronic Calibration	78
4.6.4	Inclusive Control Distributions	78

4.7	Diffractive DIS Event Selection	80
4.7.1	Forward Detector Selection	81
4.7.2	Reconstruction and Resolution of Diffractive Variables	89
4.7.3	RAPGAP Reweight	90
4.7.4	Diffractive Control Distributions	92
4.7.5	M_Y Migration Correction	93
4.8	Summary of Diffractive Selection	101
5	Measurement of the Diffractive Proton Structure Function	102
5.1	Inclusive DIS Studies	102
5.1.1	Extraction of $F_2(x, Q^2)$	102
5.1.2	Background Contributions	103
5.1.3	Binning Scheme	103
5.1.4	Bin Centre Corrections	103
5.1.5	Acceptance and Purity Correction	105
5.1.6	Systematic Errors	107
5.1.7	Results for $F_2(x, Q^2)$	107
5.2	Diffractive Measurements	109
5.2.1	Measurement of $F_2^{D(3)}(\beta, Q^2, x_P)$	110
5.2.2	Background Contributions	110
5.2.3	Binning scheme	110
5.2.4	Radiative Corrections	111
5.2.5	Bin Centre Corrections	111

5.2.6	Acceptance and Purity Calculations	113
5.2.7	Systematic Errors	113
5.2.8	Results for $F_2^{D(3)}(\beta, Q^2, x_P)$	119
5.3	Interpretation of Results	124
5.3.1	Regge Parameterisation	124
5.3.2	Comparison with QCD Fits	129
5.3.3	$F_2^{D(3)}$ Model Comparisons	129
5.3.4	β and Q^2 dependence of $F_2^{D(3)}$	132
5.4	Summary	133
5.5	Future Prospects	134

List of Figures

1.1	The left figure shows the HERA accelerator with the PETRA pre-accelerator in the dotted box, an enlarged view of which is given on the right.	4
1.2	Sectional view of the H1 Detector illustrating the individual detector components.	6
1.3	Side view of the H1 Tracking Detectors.	7
1.4	Side view of the H1 calorimetry system.	11
1.5	$x-y$ view of the electromagnetic section of the Spacal showing the positions of individual cells and their grouping into modules.	12
1.6	The Forward Muon Detector illustrating the pre- and post-toroid layers on the left and the double layer structure on the right.	14
1.7	The integrated luminosity produced by HERA for the period 1992-2000. . .	17
2.1	(a) NC and CC deep-inelastic scattering processes. The kinematics of NC DIS are illustrated in (b).	21
2.2	Charge screening processes in QED(a) and QCD(b).	27
2.3	$F_2(x, Q^2)$ as measured by H1 (red circles), together with NMC [51] (green triangles) and BCDMS [52] (blue squares) fixed target data, as a function of Q^2 for different values of x for low x (a) and high x (b). The parameterisation shown is the result of a QCD fit.	28
2.4	The kinematic plane in x and Q^2 showing where the DGLAP and BFKL approximations are theoretically valid.	29

2.5	Depictions of the leading order DGLAP splitting functions. Figure (a) shows $g \rightarrow q\bar{q}$ for the splitting function P_{qg} , (b) shows $q \rightarrow q'g$ for P_{gq} and (c) shows $g \rightarrow gg$ for P_{gg}	30
2.6	The gluon distribution from next-to-leading order (NLO) DGLAP fits with starting scale $Q_0^2 = 4.0 \text{ GeV}^2$	31
2.7	Ladder diagram illustrating the ordering in transverse and longitudinal momenta (k_T and x respectively).	32
2.8	Examples of (a) direct and (b) resolved photoproduction processes.	34
2.9	H1 measurement of the structure function derivative $\lambda(x, Q^2)$. The solid lines indicate NLO QCD fits to the data and the dotted lines represent predictions evolved from 3.5 GeV^2 to lower Q^2	35
2.10	ZEUS measurement of $F_2(x, Q^2)$ as a function of Q^2 for fixed values of y	36
2.11	Dipole picture of γ^*p scattering.	37
3.1	Comparison between the colour flow properties of (a) standard and (b) diffractive DIS.	39
3.2	Kinematics of diffractive DIS.	40
3.3	$x_{\mathbb{P}}F_2^D(\beta, Q^2, x_{\mathbb{P}})$, where $F_2^D(\beta, Q^2, x_{\mathbb{P}})$ is the diffractive structure function, shown as a function of $x_{\mathbb{P}}$ in Q^2 and β bins.	43
3.4	$x_{\mathbb{P}}F_2^{D(3)}(\beta, Q^2, x_{\mathbb{P}})$ shown as a function of $x_{\mathbb{P}}$ at fixed $Q^2 = 18 \text{ GeV}^2$ in bins of low and high β respectively. The red curves represent combined pomeron (\mathbb{P}) and meson (\mathbb{R}) contributions and the blue curves correspond to the meson contribution only.	44
3.5	Corresponding (a) t -channel ($AB \rightarrow CD$) and (b) s -channel ($A\bar{C} \rightarrow \bar{B}D$) processes.	44
3.6	Chew-Frautschi plot for the highest intercept mesons.	45
3.7	Representation of the Regge vertex factorisation hypothesis.	47

3.8	Q^2 dependence of the effective pomeron trajectory $\alpha_{\mathbb{P}}(0)$ for inclusive and diffractive ep processes. The squares correspond to $\alpha_{\mathbb{P}}(0) = 1 + \lambda$ extracted from a fit to inclusive data [63] of the form $F_2 = cx^{-\lambda(Q^2)}$ for $x < 0.01$	50
3.9	The ratio of the diffractive to the inclusive cross section, $\rho^{D(3)}$, shown as a function of W for fixed values of β and Q^2	51
3.10	H1 measurement of $x_{\mathbb{P}}F_2^{D(3)}(\beta, Q^2, x_{\mathbb{P}})$ as a function of Q^2 illustrating the presence of scaling violations for (a) H1 1994 and 1995 data and (b) H1 1997 data. The 1995 data on figure (a) were measured in a similar kinematic region to the analysis presented in this thesis. The results presented in (b) represent a measurement of superior precision in comparison.	52
3.11	Measurement of $x_{\mathbb{P}}F_2^{D(3)}(\beta, Q^2, x_{\mathbb{P}})$ at fixed $x_{\mathbb{P}} = 0.003$ in bins of Q^2 as a function of β for H1 1997 data.	53
3.12	Pomeron parton distributions as a function of z in bins of Q^2	54
3.13	The dominant mechanism in diffractive DIS, Boson-Gluon Fusion.	54
3.14	(a)The virtual photon fluctuates into a $q\bar{q}$ pair or (b) a $q\bar{q}g$ state. The left hand diagrams illustrate the processes in the proton rest frame, whilst the infinite momentum frame interpretation is shown on the right.	55
3.15	The diffractive structure function $F_2^{D(3)}$, parameterised by H1 using the BEKW model [81], as a function of β at fixed $x_{\mathbb{P}}=0.001$. The dotted line gives the $q\bar{q}g$ contribution, the dashed and dotted-dashed lines show the $q\bar{q}$ transverse and longitudinal components respectively, and the sum total is represented by the solid line.	56
3.16	Q^2 dependence of $F_2^{D(3)}$ showing the transition at low Q^2 . The triangles are from a ZEUS analysis [83], the stars are Leading Proton Spectrometer data from the same publication and the circles are from a higher Q^2 analysis [84]. The dashed and solid curves show the saturation model predictions with $q\bar{q}$ and combined $q\bar{q}$ and $q\bar{q}g$ terms respectively.	57
3.17	Measurement of $x_{\mathbb{P}}F_2^{D(3)}(\beta, Q^2, x_{\mathbb{P}})$ as a function of (a) β and (b) Q^2 for H1 1997 data (red points) [78]. The curves represent two versions of the colour dipole model of [68] [82] (dashed) and an alternative model with QCD evolution taken from [85] (solid).	58

3.18	Soft colour interactions in diffractive scattering. (a) shows the colour strings (dashed lines) which exist between the final state particles, (b) and (c) illustrate how the rapidity gaps characteristic of diffractive interactions can be formed in the final state.	59
3.19	Measurement of $x_{\mathbb{P}} F_2^{D(3)}(\beta, Q^2, x_{\mathbb{P}})$ as a function of (a) β and (b) Q^2 for H1 1997 data (red points) [78]. The data are compared with semi-classical model predictions [87] (solid curves). An extension to the model for $M_X^2 < 4 \text{ GeV}^2$, where the model is not expected to be valid, is represented by the dotted curves.	60
4.1	Efficiencies for the three sub-triggers used in the 1999 minimum bias analysis: s0 (red triangles), s3(blue squares) and s9(purple circles), shown as a function of scattered positron energy E'_e	65
4.2	The quality of the kinematic reconstruction illustrated by the function δ defined in equation 4.14, for x (a) and Q^2 (b), using the Electron-Double Angle reconstruction method.	70
4.3	Vertex efficiency shown as a function of y_{eDA} for data (red points) and combined DJANGO and PHOJET Monte Carlo (blue points).	74
4.4	Distribution of generated divided by reconstructed positron energy for DJANGO in the cell $-16 \text{ cm} \lesssim x_{SPACAL} \lesssim -12 \text{ cm}$ and $-16 \text{ cm} \lesssim y_{SPACAL} \lesssim -12 \text{ cm}$. The mean of the distribution is 1.016 ± 0.005 and the width 0.023 ± 0.010	76
4.5	Reconstructed positron energy distribution for data (blue points) and DJANGO (red points) in the Spacal section $-48 \text{ cm} \lesssim x_{SPACAL} \lesssim -32 \text{ cm}$ and $0 \text{ cm} \lesssim y_{SPACAL} \lesssim 16 \text{ cm}$	77
4.6	Control distributions before the application of Spacal and LAr calorimeter calibrations for the positron energy (a), and ratio of double angle method to measured energy (b). The data points are shown, with statistical errors, by the black points, the DJANGO and PHOJET Monte Carlo contributions are denoted by the green and purple histograms respectively and the total Monte Carlo is shown in red.	79

4.7	Control distributions before the application of Spacal and LAr calorimeter calibrations for the total $E - p_z$ (a), transverse momentum balance (b) and y balance (c). The data points are shown, with statistical errors, by the black points, the DJANGO and PHOJET Monte Carlo contributions are denoted by the green and purple histograms respectively and the total Monte Carlo is shown in red.	80
4.8	Control distributions after the application of Spacal and LAr calorimeter calibrations for the positron energy (a), and the ratio of double angle method to measured energy (b). The data points are shown, with statistical errors, by the black points, the DJANGO and PHOJET Monte Carlo contributions are denoted by the green and purple histograms respectively and the total Monte Carlo is shown in red.	81
4.9	Control distributions after the application of Spacal and LAr calorimeter calibrations for total $E - p_z$ (a), transverse momentum balance (b) and y balance (c). The data points are shown, with statistical errors, by the black points, the DJANGO and PHOJET Monte Carlo contributions are denoted by the green and purple histograms respectively and the total Monte Carlo is shown in red.	82
4.10	Control distributions for the positron polar angle (a), positron azimuthal angle (b), hadronic polar angle (c), z -vertex distribution (d), and R_{SPACAL} (e). The kinematic distributions of Q^2 , x and y are shown in figures (f)-(i). The data points are shown, with statistical errors, by the black points, the DJANGO and PHOJET Monte Carlo contributions are denoted by the green and purple histograms respectively and the total Monte Carlo is shown in red.	84
4.11	Percentage of randomly triggered events with noise in the forward detectors shown for each HERA luminosity fill. The solid line represents the average noise level of $\sim 2\%$ over all fills.	86
4.12	The quality of the reconstruction illustrated by the function δ defined in equation 4.28, for the diffractive variable M_X	90

4.13	Diffractive control distributions before the application of the reweighting functions to RAPGAP for the inelasticity (a), x_p (b) and β (c). The data points are shown, with statistical errors, by the black points, the DJANGO and PHOJET Monte Carlo contributions are denoted by the green and purple histograms respectively, as before, and the RAPGAP, DIFFVM and COMPTON distributions are represented by the blue, dotted red and dotted blue histograms respectively. The total Monte Carlo is indicated by the solid red line.	91
4.14	Diffractive control distributions after the application of the reweighting functions to RAPGAP for the inelasticity (a), x_p (b) and β (c). The data points are shown, with statistical errors, by the black points, the DJANGO and PHOJET Monte Carlo contributions are denoted by the green and purple histograms respectively, as before, and the RAPGAP, DIFFVM and COMPTON distributions are represented by the blue, dotted red and dotted blue histograms respectively. The total Monte Carlo is indicated by the solid red line.	93
4.15	Control distributions after the application of the diffractive selection. The positron energy and angles are shown in figures (a)-(c), and the total $E - p_z$ of the positron and hadronic final state is shown in (d). The hadronic polar angle is given in (e) with p_t and y balance plots in (f) and (g). Figures (h)-(l) show the z -vertex, R_{SPACAL} and kinematic distributions, whilst the diffractive variables η_{MAX} and M_X , are shown in plots (m)-(n). The data points are shown, with statistical errors, by the black points, the DJANGO and PHOJET Monte Carlo contributions are denoted by the green and purple histograms respectively, as before, and the RAPGAP, DIFFVM and COMPTON distributions are represented by the blue, dotted red and dotted blue histograms respectively. The total Monte Carlo is indicated by the solid red line.	96
4.16	The η_{MAX} distribution for data (black points) and RAPGAP (blue histogram) and DJANGO (green histogram) Monte Carlos before diffractive cuts are applied. The total Monte Carlo is indicated by the red histogram.	97
4.17	Uncorrected ratio of elastic to proton dissociation data events as a function of pseudorapidity η_{MAX}	99

4.18	Uncorrected ratio of elastic to proton dissociation data events as a function of pseudorapidity η_{MAX} . Figure(a) represents the ratio in bins of low and high Q^2 represented by the black and red points respectively. The black and red points in figure (b) represent the ratio for low and high regions of x respectively.	100
5.1	Bin centre corrections for the inclusive proton structure function $F_2(x, Q^2)$ as a function of x in bins of Q^2	106
5.2	The inclusive proton structure function $F_2(x, Q^2)$ extracted from this measurement (red points) compared with a previous H1 publication [63] (blue points). The measurements are shown as a function of Q^2 in bins of x . . .	108
5.3	The inclusive proton structure function $F_2(x, Q^2)$ extracted from this measurement (red points) compared with a previous H1 publication [63] (blue points). The measurements are shown as a function of x in bins of Q^2 . . .	109
5.4	Radiative corrections for the diffractive structure function, $F_2^{D(3)}(\beta, Q^2, x_P)$ shown as a function of x_P for fixed values of β and Q^2 , with β increasing from left to right and Q^2 increasing from top to bottom.	112
5.5	Bin centre corrections for the diffractive structure function, $F_2^{D(3)}(\beta, Q^2, x_P)$ shown as a function of x_P for fixed values of β and Q^2 , with β increasing from left to right and Q^2 increasing from top to bottom.	114
5.6	Diffractive acceptance for the extraction of the diffractive structure function, $F_2^{D(3)}(\beta, Q^2, x_P)$ shown as a function of x_P for fixed values of β and Q^2 , with β increasing from left to right and Q^2 increasing from top to bottom.	115
5.7	Purity for the extraction of the diffractive structure function, $F_2^{D(3)}(\beta, Q^2, x_P)$ shown as a function of x_P for fixed values of β and Q^2 , with β increasing from left to right and Q^2 increasing from top to bottom.	116
5.8	The diffractive proton structure function extracted from the 1999 minimum bias data. $x_P F_2^{D(3)}(\beta, Q^2, x_P)$ is shown as a function of x_P for fixed values of β and Q^2 , with β increasing from left to right and Q^2 increasing from top to bottom. The data points are shown with inner statistical and outer total (statistical and systematic in quadrature) errors. A normalisation error of $\pm 8.5\%$ is not shown.	121

5.9	The diffractive proton structure function from this measurement (red points) compared with a previous unpublished H1 measurement [80] (blue points). $x_{\mathcal{P}} F_2^{D(3)}(\beta, Q^2, x_{\mathcal{P}})$ is shown as a function of $x_{\mathcal{P}}$ for fixed values of β and Q^2 . Both measurements are shown with total (statistical and systematic) errors. The statistical errors for the 1999 measurement are represented by the inner error bars.	122
5.10	The diffractive structure function from this measurement (red points) compared with a recent H1 measurement [78] (blue points). $x_{\mathcal{P}} F_2^{D(3)}(\beta, Q^2, x_{\mathcal{P}})$ is shown as a function of $x_{\mathcal{P}}$ for fixed values of β and Q^2 , with β increasing from left to right and Q^2 increasing from top to bottom. Both measurements are shown with inner statistical and outer total (statistical and systematic added in quadrature) errors. The vertical scale in the first three Q^2 bins has been altered with respect to the others.	123
5.11	The diffractive structure function from this measurement (red points) compared with a recent H1 measurement [78] (blue points). $x_{\mathcal{P}} F_2^{D(3)}(\beta, Q^2, x_{\mathcal{P}})$ is shown as a function of $x_{\mathcal{P}}$ at $Q^2 = 6.5 \text{ GeV}^2$ for fixed values of β . Both measurements are shown with inner statistical and outer total (statistical and systematic) errors. The 1997 data points are offset slightly from the central $x_{\mathcal{P}}$ values for clarity.	124
5.12	Comparison of the 1999 and 1997 $F_2^{D(3)}(\beta, Q^2, x_{\mathcal{P}})$ measurements evaluated as $(F_2^{D(3)}(1999) - F_2^{D(3)}(1997))/F_2^{D(3)}(1999)$ and presented as a function of $x_{\mathcal{P}}$ in bins of β increasing across the page and Q^2 increasing down the page. The error takes into account total errors on both measurements.	125
5.13	$x_{\mathcal{P}} F_2^{D(3)}(\beta, Q^2, x_{\mathcal{P}})$ from 1999 minimum bias data is shown as a function of $x_{\mathcal{P}}$ for fixed values of β and Q^2 , with β increasing from left to right and Q^2 increasing from top to bottom. The result of a phenomenological Regge fit to the data for $Q^2 > 6.5 \text{ GeV}^2$ is also shown for combined pomeron and meson exchange contributions (solid curve) and pomeron exchange only (dotted curve). The open circles indicate data points which were excluded from the fit.	127

- 5.14 $x_P F_2^{D(3)}(\beta, Q^2, x_P)$ from 1999 minimum bias data is shown as a function of x_P for fixed values of β and Q^2 , with β increasing from left to right and Q^2 increasing from top to bottom. The result of a phenomenological Regge fit to the data for all Q^2 is also shown for combined pomeron and meson exchange contributions (solid curve) and pomeron exchange only (dotted curve). The open circles indicate data points which were excluded from the fit. 128
- 5.15 $x_P F_2^{D(3)}(\beta, Q^2, x_P)$ from 1999 minimum bias data is shown as a function of x_P for fixed values of β and Q^2 , with β increasing from left to right and Q^2 increasing from top to bottom. The result of the QCD fit to the 1994 H1 data for both pomeron and meson exchange contributions is indicated by the solid curve and for pomeron exchange only by the dotted curve. The vertical scale in the first three Q^2 bins has been altered with respect to the others. 130
- 5.16 $x_P F_2^{D(3)}(\beta, Q^2, x_P)$ from 1999 minimum bias data (blue points) is shown as a function of x_P for fixed values of β and Q^2 , with β increasing from left to right and Q^2 increasing from top to bottom. The data are compared with predictions of the Soft Colour Interactions model [86] (dotted curves) and a refined version based on a generalised area law [106] (solid curves). The vertical scale in the first three Q^2 bins has been altered with respect to the others. 135
- 5.17 $x_P F_2^{D(3)}(\beta, Q^2, x_P)$ from 1999 minimum bias data (blue points) is shown as a function of x_P for fixed values of β and Q^2 , with β increasing from left to right and Q^2 increasing from top to bottom. The data are compared with the prediction of the semi-classical model [87] (solid curves). The dotted curves represent an extension of the model to $M_X^2 < 4 \text{ GeV}^2$, where the model is not expected to be valid. The vertical scale in the first three Q^2 bins has been altered with respect to the others. 136
- 5.18 $x_P F_2^{D(3)}(\beta, Q^2, x_P)$ at fixed x_P shown as a function of Q^2 (a) and β (b). The blue points represent the new 1999 data, the black points are H1 1997 data [78] and the curves are the result of a QCD fit to H1 1994 data [69] including both pomeron and meson contributions (solid curve) and pomeron only (dotted curves). 137

- 5.19 $x_P F_2^{D(3)}(\beta, Q^2, x_P)$ at fixed x_P shown as a function of Q^2 (a) and β (b). The data (blue points) are compared with the prediction of the semi-classical model [87] (solid curves). The dotted curves represent an extension of the model to $M_X^2 < 4 \text{ GeV}^2$, where the model is not expected to be valid. . . . 138
- 5.20 $x_P F_2^{D(3)}(\beta, Q^2, x_P)$ at fixed x_P shown as a function of Q^2 (a) and β (b). The data (blue points) are compared with the prediction of the saturation model [68] (solid curves). The $q\bar{q}$ transverse component is represented by the dashed curve, the longitudinal contribution by the dotted curve and the $q\bar{q}g$ term by the dotted-dashed curve. 139

List of Tables

4.1	Spacal IET trigger element definitions for the 1999 minimum bias running period.	64
4.2	L1, L2 and L4 conditions for the s0, s3 and s9 sub-triggers during the minimum bias 1999 running period.	65
4.3	Efficiency of detecting activity with various combinations of the forward detectors for data and inclusive DIS Monte Carlo (MC). The “MC FTS” column represents the Monte Carlo efficiency after the application of the FTS recalibrations and conditions which are unaffected are indicated by “_”.	88
4.4	Recalibration corrections signifying the probability with which activity is ignored in the Monte Carlo simulation for the PRT and FTS stations. . . .	88
5.1	Q^2 binning as used in the 1999 minimum bias data measurement of the inclusive structure function $F_2(x, Q^2)$	104
5.2	x binning as used in the 1999 minimum bias data measurement of the inclusive structure function $F_2(x, Q^2)$	104
5.3	β binning used in the 1999 minimum bias data measurement of the diffractive structure function $F_2^{D(3)}(\beta, Q^2, x_{\mathbb{P}})$	111
5.4	Values for the effective pomeron intercept $\alpha_{\mathbb{P}}(0)$ extracted for $Q^2 > 6.5$ GeV ² (fit A) and for all values of Q^2 (fit B). The latter is taken to be the actual value.	126

Introduction

The *Standard Model* [1] of high energy physics describes the fundamental particles, quarks and leptons, and the way in which they interact with each other through the exchange of gauge bosons. The unified electroweak theory precisely describes the interactions between these point-like quarks and leptons as mediated by photons (in electromagnetic interactions via *Quantum Electrodynamics* (QED)) and W^\pm , Z^0 bosons (in weak interactions). These point-like particles can therefore be used to probe the structure of complex hadrons such as protons, in order to gain knowledge of their internal structure and the dynamics that govern them.

The first evidence for proton sub-structure came from inelastic scattering experiments at SLAC [2] where high energy electrons were directed towards fixed nuclear targets. This process is referred to as *deep-inelastic scattering* (DIS). The reaction can be summarised as $ep \rightarrow e'X$ where X denotes a final state system of hadrons and a photon is exchanged. The measured inelastic cross section exhibited very little dependence on the four momentum transfer squared (Q^2). This behaviour, known as *scaling*, indicated the electron was scattering off point-like particles in the proton. These target particles, *partons*, were later identified as being the same quarks as those of the Standard Model with fractional charges and spin values of $\frac{1}{2}$. This is the *Quark Parton Model* (QPM) [3]. Experiments soon showed deviations from perfect scaling. The theory of *Quantum Chromodynamics* (QCD) [4] [5] is used to extend the QPM by taking into account strong interactions which are occurring between the quarks inside the proton. The strong force is mediated by gluons, which couple not only to the quarks but also to themselves (unlike QED photons).

The world's first lepton-proton collider, HERA, is situated at the DESY laboratory in Hamburg, Germany and has been operational since 1992. This thesis describes a measurement performed on a sample of DIS events collected in 1999 by H1, a multi-purpose detector located at one of the beam interaction points on the HERA ring. The first chapter provides an overview of the individual H1 detector components and the triggering system. A brief description of the recent upgrade procedure undertaken by HERA is also

presented. Results from HERA have proved invaluable in the understanding of DIS and QCD by accessing kinematic regions unavailable to other experiments and the upgraded detectors will continue to extend this further. A description of DIS at HERA is presented in chapter 2 and the measurement of the proton structure function F_2 is also discussed. The structure functions of the proton can be used to extract *parton densities* so the results from HERA provide detailed information on the quark and gluon content of the proton. Structure function measurements at HERA [6] [7] [8] have also exhibited a sustained rapid rise as $x \rightarrow 0$ (where x is the Bjorken scaling variable). Theoretical predictions had been ambiguous about the behaviour at small x so this was to a degree surprising. Ultimately at low enough x values the parton densities are expected to *saturate* but to date no firm evidence for this has been observed at HERA.

A subset of DIS events exhibit a very distinctive structure: the final state is well separated into proton remnant (Y) and photon dissociation (X) hadronic systems ($ep \rightarrow e'XY$). In these events a *large rapidity gap* is observed in the H1 detector in which no hadrons are present. Events of this kind, where the proton remains intact, or dissociates into a low mass object in spite of the violent nature of the interaction, are described as being *diffractive* in nature. The exchanged particle is known as the *pomeron*. In analogy to standard DIS, a diffractive structure function $F_2^{D(3)}$ can be defined where the partonic structure of the pomeron can be investigated rather than that of the whole proton. Chapter 3 reviews diffractive DIS at HERA and the extraction of the diffractive structure function and parton densities. An overview of models describing diffraction and the pomeron is also presented, with an emphasis on diffraction at low x and Q^2 - a kinematic region where few measurements of $F_2^{D(3)}$ have previously been performed. Chapter 4 details the experimental techniques employed in the selection and kinematic reconstruction of standard and diffractive DIS events at low x and Q^2 . Results for the structure function $F_2^{D(3)}$ in this region of phase space, as extracted via the measurement of a triple differential cross section, are discussed and presented in chapter 5. Measurements of $F_2^{D(3)}$ in this kinematic range have not been published by H1 before and the measurement presented here represents the most statistically significant measurement of $F_2^{D(3)}$ in this region of low Q^2 .

Chapter 1

The H1 Detector

1.1 Introduction

In 1992, particle physics experiments began at HERA (Hadron Electron Ring Accelerator), based at DESY (Deutsches Elektronen Synchrotron) in Hamburg. Proton and lepton beams are accelerated and stored in separate rings with circumference 6336 m. Figure 1.1 shows the experimental layout of HERA on the left with an enlarged view of the PETRA pre-accelerator ring (in the dotted box) on the right. The cross section for $e-p$ interactions is small, hence the beam currents must be high. Therefore, bunches of ~ 25 mA positrons¹ are collided every 96 ns with proton bunches of ~ 80 mA. The final energy of the protons (E_p) after acceleration is 920 GeV, and the electrons acquire an energy $E_e = 27.5$ GeV. Hence, the centre of mass energy available in the interaction (\sqrt{s}) is given by:

$$\sqrt{s} \simeq \sqrt{4E_p E_e} \sim 320 \text{ GeV}. \quad (1.1)$$

The proton and lepton beams collide at north and south interaction points on the ring, where the H1 and ZEUS experiments are respectively located. These are the multi-purpose detectors used to study the products of the interaction between the high energy positron and proton beams provided by HERA. The H1 detector, with dimensions $12 \text{ m} \times 10 \text{ m} \times 15 \text{ m}$ and a mass of 2800 tonnes, is used to identify particles originating from the $e-p$ collision and also to determine their momenta and energy. A full description of the detector is given in [9]. Fixed target experiments are situated at the east and west interaction points - the HERMES and HERA-B experiments respectively. HERMES,

¹HERA can run with either electrons or positrons. For the period under analysis in this thesis HERA ran with positrons, and the term ‘positron’ will be used to generically describe the lepton beam.

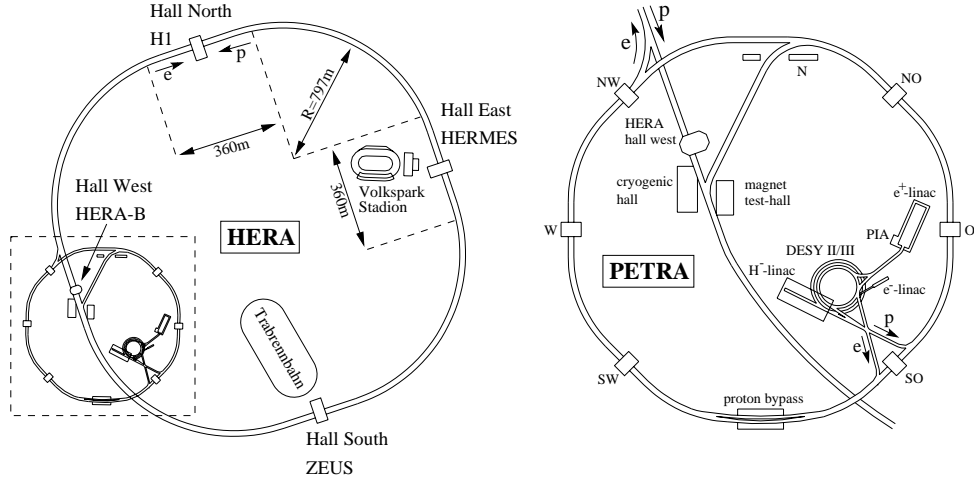


Figure 1.1: The left figure shows the HERA accelerator with the PETRA pre-accelerator in the dotted box, an enlarged view of which is given on the right.

which has been running since 1995, utilises the longitudinally polarised positron beam with polarised targets. By measuring the gluon contribution to the proton and neutron structure functions at low values of the Bjorken scaling variable, the origin of nuclear spin, about which very little is known, has been investigated. The aim of the HERA-B experiment, which became operational in 1998, was to study CP violation through the golden decay channel $B \rightarrow J/\psi K^0$. This is achieved through studying interactions between the protons and nuclei of tungsten wires which are inserted into the beam halo.

H1 is used to investigate all outcomes of $e - p$ interactions, although the principal aim is the study of deep-inelastic scattering (DIS) events, described in chapter 2. This objective imposes important experimental requirements on the detector and accelerator. The asymmetric beam conditions mean that finer granularity, deeper absorbers and extended tracking detectors are required in the forward direction, which is defined as that of the outgoing proton beam. These forward detectors perform an important role in diffractive analyses, the theory of which is described in detail in chapter 3. The resolution and efficiency for the detection and measurement of positrons must be high over a large angular range in order to reconstruct the inclusive kinematic variables from the energy and angle of the scattered positron. The calorimeters are required to be hermetic, in order to measure as well as possible the missing transverse momentum in charged current DIS, and have a high granularity for accurate positron and hadronic final state reconstruction. For particle identification and measurement of charged particle momenta and multiplicities, a large angular coverage is required by the tracking detectors. In order to study heavy flavour processes and to make searches for signatures of exotic particle production, muon detection is required over as much of the entire 4π solid angle as possible. Finally a so-

phisticated and fast multi-level triggering system is required because the detector readout time of $\sim 800 \mu\text{s}$ is much greater than the bunch crossing time (96 ns).

1.2 Overview of H1

The positron and proton beams interact at a nominal vertex position in the H1 detector after acceleration. This interaction point is made the origin of the coordinate system. The z -axis lies along the outgoing proton (forward) direction and the y -axis points vertically upward. The x -axis then completes the right-handed coordinate system. In spherical polar coordinates, the outward radial distance is denoted r , the polar angle θ is defined relative to the z -axis and ϕ is the azimuthal angle which is referenced to the y -axis. In comparison to the $z = 0$ cm nominal vertex position, the $e-p$ collision point is sometimes moved to +70 cm in the detector which is known as a “shifted vertex” configuration. Such an arrangement allows larger (smaller) values of θ (Q^2) to be accessed.

Figure 1.2 shows an isometric projection of the H1 detector. Each sub-detector is cylindrically symmetric and centred on the beam-pipe [1] which runs along the centre of the detector. The innermost layer comprises silicon micro-vertex detectors in the central and backward regions (CST and BST respectively). Further out lie the central tracking detector (CTD) [2] and the forward tracking detector (FTD) [3]. Next, the Liquid Argon Calorimeter (LAr) comprises electromagnetic [4] and hadronic [5] sections. A lead-fibre electromagnetic and hadronic calorimeter (Spacal) [12] and the Backward Drift Chamber (BDC) cover the backward direction whilst the Plug calorimeter [13] extends the measurement range for hadrons in the forward direction. Outside the LAr calorimeter is the super-conducting solenoid [6]. The muon detection system consists of the instrumented iron yoke of the solenoidal magnet [10] in the central region [9] whilst coverage in the forward region is enhanced by the Forward Muon Detector (FMD) [9] [11]. For detection of the residue of hadronic showers, the Tail Catcher (TC) also uses a subset of the instrumentation of the iron yoke. The forward tagger system (FTS) (not shown) is used in diffractive studies and comprises five scintillator arrays positioned in the forward direction at 9, 16, 24 (known as the Proton Remnant Tagger), 53 and 92 m. Also positioned at intervals along the beam-pipe in the forward direction are Roman pots, which are sealed inside the beam-pipe allowing measurements very close to the proton beam to take place. These constitute the Forward Proton Spectrometer (FPS). The Forward Neutron Calorimeter (FNC) is situated at a distance of +107 m. Lepton and photon taggers (ET and PD respectively) are positioned alongside the beam-pipe in the $-z$ direction for the

HERA Experiment H1

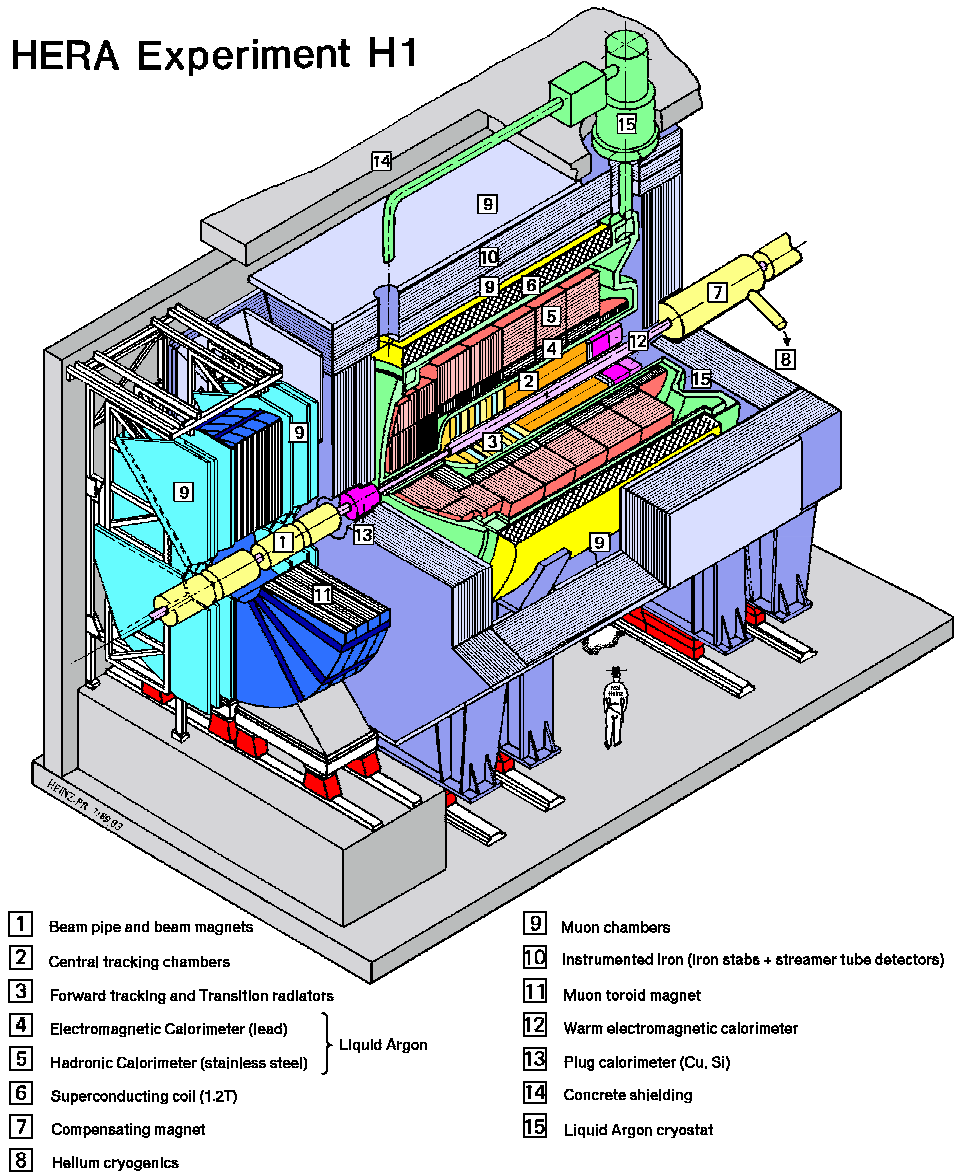


Figure 1.2: Sectional view of the H1 Detector illustrating the individual detector components.

determination of the luminosity (see section 1.7). The ET is also used to tag photoproduction ($Q^2 \sim 0$) events. The Very Low Q^2 spectrometer (VLQ) is situated immediately around the beam-pipe at $z = -2.95$ m. The entire detector is encased in concrete **14** shielding.

1.3 Tracking in the H1 Detector

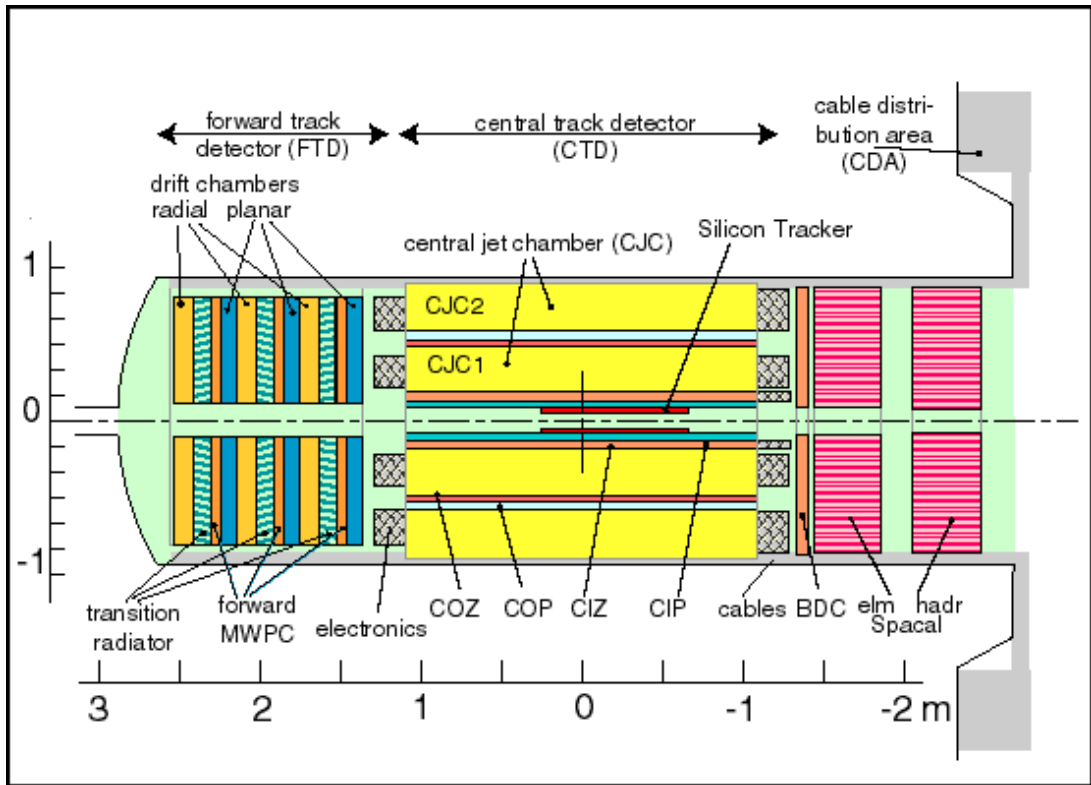


Figure 1.3: Side view of the H1 Tracking Detectors.

Figure 1.3 shows in detail the tracking detectors in H1. Their purpose is to reconstruct the tracks that charged particles produce as they pass through the detector and to assist measurement of their momenta. The CTD which covers the angular region $15^\circ < \theta < 165^\circ$ and the FTD ($7^\circ < \theta < 25^\circ$) consist of drift chambers with embedded multi-wire proportional chambers (MWPCs). The angular region of $135^\circ < \theta < 177.5^\circ$ is covered by the backward drift chambers (BDC) which are used in conjunction with the Spacal to identify positrons.

MWPCs, used for measuring particle positions, are instrumented with planes of anode wires positioned between cathode plates in a gas-filled detector. Charged particles traversing the MWPC cause the gas to ionise in the strong electric field around the anode, initiating charge multiplication. As an electron moves towards the anode, it gains energy in the electric field. Hence, collisions with the gas particles in the detector yield secondary electrons, and the process continues and so an *avalanche* of electrons is formed which also moves towards the anode. A charge proportional to the original ionisation is measured on the anode wire, hence knowledge of which wire produces the corresponding signal allows position determination. The electrostatic forces around the anode wires limit the mini-

mum anode wire spacing and hence the detector resolution, but their fast response times promote their use as triggering devices.

Drift chambers are tracking devices with a higher resolution than MWPCs. The anode (sense) wires are widely spaced and lie between two parallel rows of cathode (drift) wires enclosed by screening electrode plates. Unlike MWPCs, the electrons drift toward the anode wires in a uniform field and hence have a constant drift velocity. The charge division method is used to acquire the co-ordinate in the direction of the sense wire which is resistive. Readout of the signal at each end of the wire determines the avalanche position due to different amounts of resistance between the signal and the wire ends. Hence, together with the bunch crossing time and the time of arrival of the signal at the anode, the drift velocity can be used to determine the track position. Particle momenta can be inferred from the degree of track curvature observed in the detector, as the ionisation is detected at successive anode wires, due to the magnetic field. Identification of particles can be accomplished at low momentum via the determination of the total ionisation observed, that is the energy loss over the distance travelled ($\frac{dE}{dx}$).

1.3.1 The Central Tracking Detector (CTD)

As shown in figure 1.3 the sub-systems of the central tracker are, moving radially outwards, the Silicon Trackers, Central Inner Proportional Chamber (CIP), Central Inner Z-Chamber (CIZ), Central Jet Chamber 1 (CJC1), Central Outer Z-Chamber (COZ), Central Outer Proportional Chamber (COP) and Central Jet Chamber 2 (CJC2).

Silicon Trackers

The central and backward silicon trackers (CST [10] and BST [11] respectively), used in conjunction with the CJC information, aid the identification of primary and secondary vertices [12] as well as rejecting photoproduction background by the matching of a track with a cluster in the Spacal. The CST provides information on the vertex by accurately measuring the tracks of charged particles close to the vertex as well as detecting secondary vertices in their decays. It consists of two layers of silicon strip detectors covering the range $30^\circ < \theta < 150^\circ$. The BST comprises eight planes of single-sided silicon discs, each with a 16-fold segmentation in ϕ , with an angular range of $162^\circ < \theta < 176^\circ$ corresponding to a Q^2 range between 2 GeV² and 100 GeV². It is used in the reconstruction of tracks from backward scattered positrons and is important for precision measurements of low- x DIS events.

Central Jet Chambers

The most important central detectors are the co-axial drift chambers CJC1 and CJC2 [13]. Their sense wires lie parallel to the beam direction and, with a single hit $r - \phi$ resolution of $170 \mu\text{m}$ and z resolution of 22 mm , obtained from charge division, a reasonable overall measurement can be performed. CJC1 comprises 30 cells, each of which accommodates 24 sense wires, whereas CJC2 has 60 cells, with 32 sense wires each.

Central Z Chambers (Inner and Outer)

The CIZ [14] and COZ [15] comprise 4 layers of drift chamber in which the sense wires are oriented perpendicular to the beam-pipe, so the ionisation drifts parallel to the $+z$ axis. Hence, the CIZ and COZ improve the z -measurements with a resolution of $260 \mu\text{m}$. The CIP and COP are double layered MWPCs with wires running parallel to the $+z$ axis. Their time resolution is much smaller than the bunch crossing time interval, and they provide information on the origin of tracks. Together with the first layer of the FPC, they form the z -vertex trigger, which labels tracks from the vertex region and plays an important role in background rejection. Combining the track measurements of CJC1, CJC2, CIZ and COZ, a charged track momentum resolution of $\frac{\sigma(p)}{p} < \frac{0.01p}{\text{GeV}}$ is obtained.

1.3.2 The Forward Tracking Detector (FTD)

The highly asymmetric H1 beam conditions dictate the need for enhanced tracking equipment in the forward direction. The FTD [16], with an angular coverage of approximately 7° to 25° , comprises three identical super-modules each consisting of planar drift chambers, MWPCs, and radial drift chambers.

The planar detectors consist of three separate sets of drift chamber planes mutually offset by 60° in azimuthal angle ϕ . Each set is divided up into 32 lateral cells, each of which contains 4 sense wires spaced uniformly in the z co-ordinate. Readout is performed at one end only, hence just the drift time is measurable. The MWPCs mounted directly in front of the planar chambers constitute the Forward Proportional Counter (FPC). The radial chambers comprise 48 wedge-shaped cells, each of size 7.5° in azimuthal angle housing 12 radially strung sense wires. Readout, from pairs of wires, is achieved from both ends providing two coordinate measurements via the ionisation drift time and charge division. The single hit resolutions of the planar and radial drift chambers are $170 \mu\text{m}$ and $200 \mu\text{m}$

respectively.

1.3.3 The Backward Drift Chamber (BDC)

The purpose of the BDC [17] is to accurately measure the scattering angle of the positron for low x , low Q^2 DIS events. It comprises eight layers in z of drift chambers, divided octagonally in ϕ , housing sense wires which lie normal to the radial line through the centre of each segment. The single hit resolution of the BDC is 0.3 mm providing a resolution in θ better than 0.5 mrad. Each layer is divided into eight sectors providing a measurement of ϕ , although this is inferior to that measured in the Spacal calorimeter (described in section 1.4.2). Positron identification and measurement is achieved using the combination of BDC and Spacal information.

1.4 Calorimetry in the H1 Detector

The calorimetry system shown in figure 1.4 plays a central role in particle detection and measurement in H1. Not only can the calorimeters detect neutral particles, unlike trackers, but they can be used to distinguish between the signatures of electromagnetic and hadronic particles. The calorimeter structure comprises alternating layers of dense absorbing and sparse sampling material, the latter of which allows measurement of the energy deposition. Incident electromagnetic particles lose energy by undergoing Bremsstrahlung ($ep \rightarrow ep\gamma$) and pair production ($\gamma p \rightarrow e^+e^-p$) reactions in the Coulomb field of the absorbing layers. The resulting particles experience the same reactions, producing particle *showers* or *cascades*, until a threshold energy is reached and the cascade diminishes. The total number of particles produced is proportional to the original energy of the incident particle which is therefore measurable in the sampling layers for a fully contained shower. The interactions of electromagnetic particles, in any given material, have a characteristic *radiation length*, X_0 , defined as the distance travelled by the particle before only $1/e$ of its initial energy remains.

In analogy to the radiation length for electromagnetic particles, an *interaction length*, λ , is defined for strongly interacting particles, where λ is typically much larger than X_0 . The hadronic calorimeter detects showers caused by strong hadronic interactions with nuclei in the layers of absorber. Due to the larger range in the number of interactions and thus final state particles possible in the case of hadronic showers, large fluctuations can be observed in cluster sizes and rates of energy deposition. Other complications arise

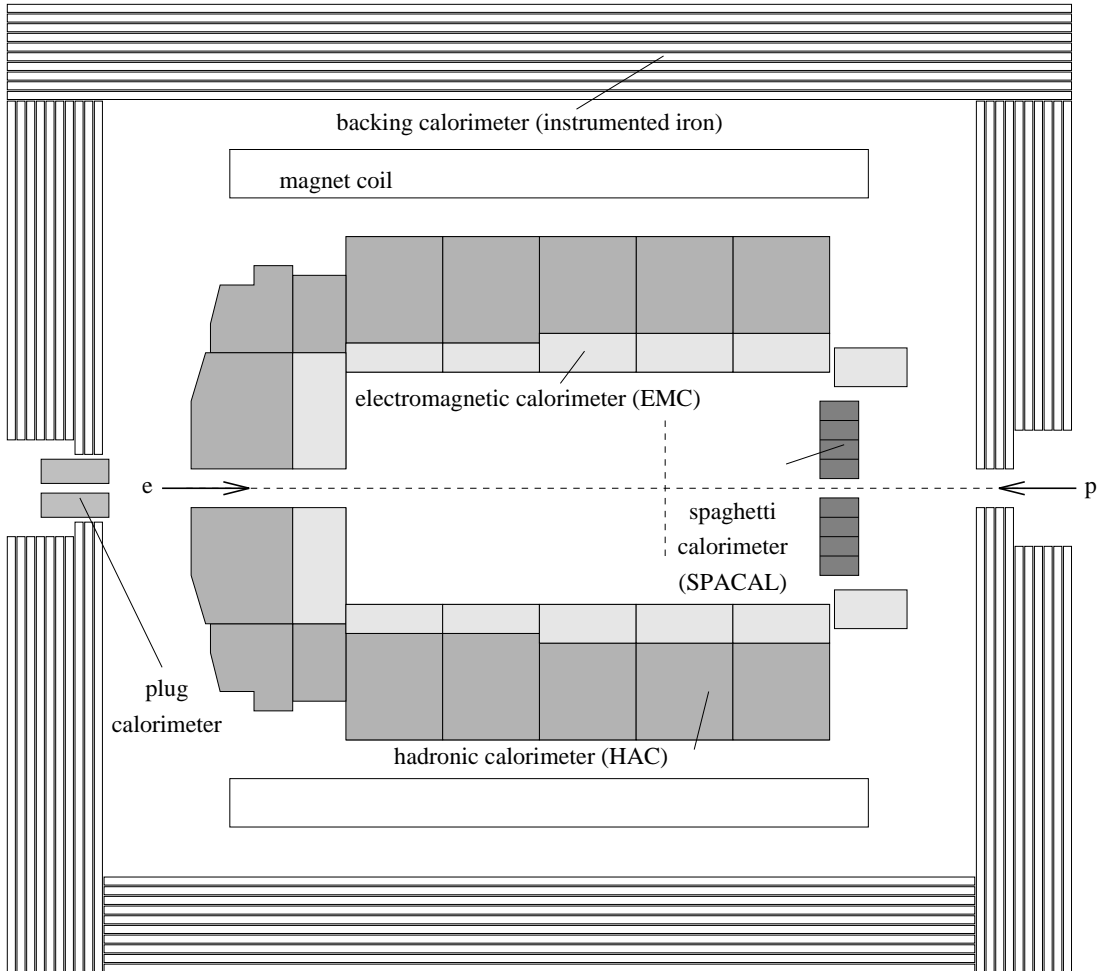


Figure 1.4: Side view of the H1 calorimetry system.

because electromagnetic particles can be produced in a shower resulting from a hadronic decay. Hadronic energy measurement is therefore less precise.

1.4.1 The Liquid Argon (LAr) Calorimeter

In order to measure high Q^2 scattered positrons and hadronic final states with minimal losses, a large calorimeter is required. The use of liquid argon provides a calorimeter with good homogeneity, fine granularity and good stability. Providing an angular acceptance between $4^\circ < \theta < 154^\circ$, the LAr calorimeter provides calorimetry in the forward and central regions of H1 [18]. Along the (z) beam direction, it comprises eight wheels, each of which is further segmented into ϕ octants. The LAr calorimeter consists of an inner electromagnetic (EMC) and an outer hadronic (HAC) calorimetry system. In the EMC plates of 2.4 mm thick lead absorber are alternated with layers of liquid Argon sampling

material of comparable thickness in which, because of its high atomic density, positrons produce high ionisation. Although positrons and photons are stopped in this section of the calorimeter, the majority of hadrons pass through and are detected in the HAC. In this section the 5 mm thick layers of sampler are alternated with layers of stainless steel plates of width 16 mm. The total thickness of the LAr calorimeter varies between 30 radiation lengths in the forward region and 20 radiation lengths in the central and backward region due to the asymmetric beam conditions. Considering the EMC and HAC together provides a variation from 4.5 to 8 interaction lengths. The energy resolutions for the EMC and HAC are $\frac{\sigma(E)}{E} \sim \frac{0.12}{\sqrt{E(\text{GeV})}} \oplus 0.01$ and $\frac{\sigma(E)}{E} \sim \frac{0.50}{\sqrt{E(\text{GeV})}} \oplus 0.02$ respectively.

1.4.2 The Spacal Calorimeter

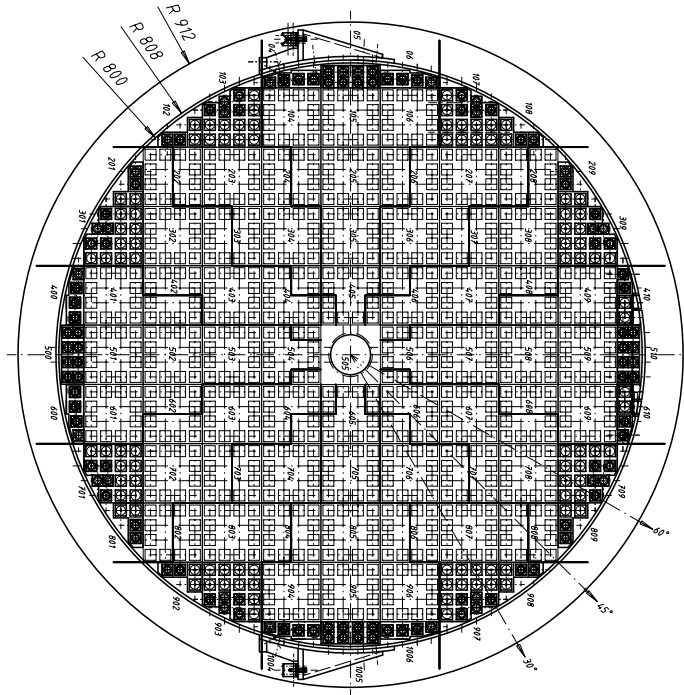


Figure 1.5: $x - y$ view of the electromagnetic section of the Spacal showing the positions of individual cells and their grouping into modules.

Providing calorimetry in the backward region of H1, the Spacal is used to measure the energy and angle of the scattered positron [19]. The angular coverage is $153^\circ < \theta < 177^\circ$ which implies a coverage in photon virtuality of $1 \text{ GeV}^2 < Q^2 < 100 \text{ GeV}^2$. The Spacal has a diameter of 1.6 m and consists of electromagnetic and hadronic sections in which scintillating fibres are embedded into lead sheets. The scintillation light is collected by photo-multiplier tubes. The electromagnetic section comprises 1192 cells each of dimensions $40.25 \text{ mm} \times 40.25 \text{ mm}$ which is larger than the average cluster size of 25.5 mm.

These cells are grouped together into larger modules, whose positions and orientations are shown in figure 1.5. The thickness of the cells is 250 mm and they have a lead-fibre ratio of 2.3:1 which amounts to approximately 28 radiation lengths (and correspondingly one interaction length for strongly interacting particles). Hence, there is negligible leakage beyond the calorimeter of the incident positrons. The hadronic part is similar but uses fibres of greater diameter, and there are 136 cells each of dimensions 119.3 mm \times 119.3 mm. The lead-fibre ratio in this part of the detector is 3.4:1 which amounts to one interaction length, doubling that from the electromagnetic section. Experiments with test beams have shown the resolutions to be $\frac{\sigma(E)}{E} \sim \frac{0.07}{\sqrt{E(\text{GeV})}} \oplus 0.04$ and $\frac{\sigma(E)}{E} \sim \frac{0.30}{\sqrt{E(\text{GeV})}} \oplus 0.20$ for positrons and hadrons respectively.

1.4.3 PLUG Calorimeter

The PLUG calorimeter [20] minimises missing transverse momentum in the forward direction from hadrons emitted near to the beam-pipe. Since it measures the forward energy flow it can also be used to discriminate between standard and diffractive DIS and photoproduction events. The angular range of the PLUG covers the region between the LAr calorimeter and the beam-pipe, hence providing acceptance over $0.6^\circ < \theta < 4^\circ$. The PLUG comprises eight layers (16 modules) of copper absorber of thickness 7.5 cm, each comprising 84 detector elements [21]. The layers of absorber are alternated with layers of silicon sampling sheets. The energy resolution of the PLUG is approximately $\frac{\sigma(E)}{E} \sim \frac{1.5}{\sqrt{E(\text{GeV})}}$.

1.4.4 The Tail Catcher (TC)

11 of the 16 layers of limited streamer chambers in the instrumented iron provide a measurement of the hadronic energy leakage from the LAr calorimeter and the Spacal [22]. This calorimeter provides acceptance for hadrons in the backward regions of H1, where there are fewer interaction lengths, and so enhances the performance of the entire calorimetry system. The energy resolution is $\frac{\sigma(E)}{E} \sim \frac{1.0}{\sqrt{E(\text{GeV})}}$ with a scale uncertainty of 35% (determined from cosmic muon data).

1.4.5 The Very Low Q^2 Spectrometer (VLQ)

The VLQ provides acceptance between 177.3° and 179.4° , which corresponds to $0.02 \text{ GeV}^2 < Q^2 < 1 \text{ GeV}^2$. It is valuable in studies of the transition region between the photoproduction and DIS regimes. It comprises two identical modules each housing a calorimeter and a tracking detector. The spatial resolution of the calorimeter is $\frac{2.1\text{mm}}{\sqrt{E/\text{GeV}}}$ whilst the tracker resolution is $18 \mu\text{m}$. These modules are situated above and below the beam-pipe at a z position of -2.95 m [23].

1.5 Muon Detection

1.5.1 The Forward Muon Detector (FMD)

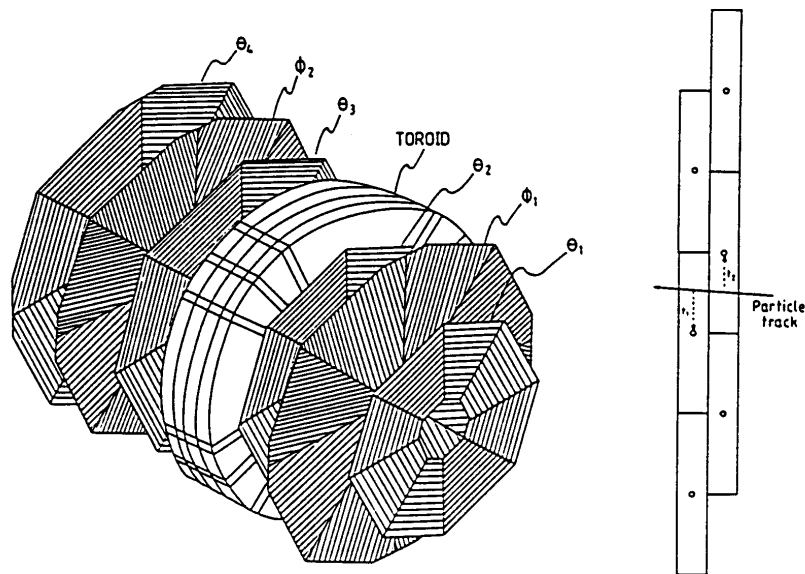


Figure 1.6: The Forward Muon Detector illustrating the pre- and post-toroid layers on the left and the double layer structure on the right.

The purpose of the FMD [24] is to identify high energy muons and measure their momenta as well as provide signals for muon triggering in the forward direction. Figure 1.6 shows the toroidal magnet and the six double layers of drift chambers which provide an angular acceptance region of $3^\circ < \theta < 17^\circ$. The toroid produces a field which varies from 1.75 T at the inner radius ($r = 0.65 \text{ m}$) to 1.5 T at the outer radius ($r = 2.90 \text{ m}$). Each layer is divided into octants comprising drift cells, where the total number of cells is 1520. In the planes that measure the azimuthal angle, ϕ , the wires are strung radially while those

in the θ layers (measuring the polar angle) are strung orthogonally. The use of double layers, with each of the single layers being staggered with respect to each other by half a cell (as shown on the right in fig 1.6), removes any ambiguities over which side of the sense wire the particle passed.

The FMD is capable of measuring muons in the momentum range $5 \text{ GeV}/c < p < 100 \text{ GeV}/c$, the lower bound of which is set by the losses experienced in the main detector due to ionisation losses, and the upper by the minimum detectable curvature in the toroidal field. In this analysis the FMD is used to aid in the selection of diffractive events as discussed in chapter 4. However only the pre-toroid layers are used because synchrotron radiation from the positron beam causes high noise levels in the post-toroid layers.

1.5.2 Central Muon Detection

The instrumented iron return yoke of the solenoidal magnet surrounding the LAr calorimeter, comprising forward and backward end-caps and a central barrel, is used for muon detection and for measuring leakage of hadronic energy from the LAr calorimeter (see above). It covers a large angular range ($4^\circ < \theta < 172^\circ$) and the instrumentation takes the form of limited streamer tubes (LSTs)². Cosmic muon studies have shown that the reconstruction efficiency for muons with a momentum greater than 2 GeV is $\sim 90\%$. However the tracks from the instrumented iron alone are often not enough to distinguish muons from the comparatively high hadronic background levels in the high activity forward direction. Therefore, the Forward Muon Detector (FMD) is also utilised. As well as the secondary hadronic activity from the $e - p$ interaction there are also non- $e - p$ backgrounds present. These arise from cosmic muons and the halo of muons that accompanies the proton beam.

1.6 Beam-line Instrumentation

There are three sets of detectors situated in the very forward region of the H1 detector, used to detect the particles close to the proton beam direction. They are very useful in diffractive studies as they can act as a veto if there is activity around the direction of the

²LSTs are tubes containing wires where the resistivity is low on three sides and higher on the fourth, the electric field being such that an *avalanche* (*streamer*) is produced across the wires when a charged particle passes through them.

outgoing proton. Although neither the FPS or FNC are used in this analysis, the FTS is important for the diffractive selection in this thesis.

1.6.1 The Forward Tagger System (FTS)

The FTS comprises five sets of scintillator surrounding the beam-pipe at $z = 9$ m, 16 m, 24 m, 53 m and 92 m in the forward direction. The particles are detected either directly or indirectly from secondary scattering arising from interactions between the proton remnant and the beam-pipe or other material in the forward region. The +24 m Proton Remnant Tagger (PRT) station detects particles produced in the range $0.06^\circ < \theta < 0.17^\circ$. It comprises seven scintillators, each of which consists of two parallel plastic scintillator sheets. The other stations, which were added at a later date, consist of four counters of the same nature. The readout is performed via photo-multipliers, and the time registered for the signal must coincide with that expected on the basis of the interaction in the main detector.

1.6.2 The Forward Proton Spectrometer (FPS)

The FPS consists of Roman pots situated 63 m, 80 m, 81 m and 90 m in front of the interaction vertex position and their purpose is the detection of intact protons at low angles ($\theta \lesssim 0.5$ mrad) which emerge down the beam-pipe unobserved in the main detector [25]. The pots contain scintillating fibre hodoscopes³ mounted inside an evacuated container. They have a concertina structure sealed inside the beam-pipe itself and are able to be brought very close to the proton beam in order to detect and measure the energy of the scattered protons at very small angles.

1.6.3 The Forward Neutron Calorimeter (FNC)

Situated 107 m forward of the nominal vertex position, the FNC covers the very forward region $\theta \lesssim 0.6$ mrad for neutral particles which are not affected by the beam optics. It is used to detect neutrons from the reaction $ep \rightarrow e'nX$, in the measurement of the pion structure function F_2^π [26] [27], where the reaction is dominated by pion exchange.

³A hodoscope is a counter which detects the scintillation light produced when a fast charged particle traverses it.

1.7 The H1 Luminosity System

The Electron Tagger (ET) and Photon Detector (PD) constitute the H1 Luminosity system [28]. Their respective acceptances are $0 - 5$ mrad and $0 - 0.45$ mrad. Coincident events in the taggers arise from the Bethe-Heitler process ($ep \rightarrow ep\gamma$). The luminosity is calculated from the rate of the Bethe-Heitler process which has a large and calculable QED cross section [29]. In addition to this however, it allows the tagging of very low $Q^2 (< 10^{-2})$ GeV² positrons for photoproduction analyses. Both taggers are Čerenkov calorimeters which contain an array of rectangular crystals. The ET has 7×7 cells and is positioned at $z = -33.4$ m whilst the PD consists of 5×5 cells situated at $z = -103.1$ m. There is also a counter in front of the PD, used to veto charged particles, placed at $z = -102.8$ m.

In 1999 a total e^+p luminosity of 27.3 pb^{-1} was delivered by HERA, out of which 20.9 pb^{-1} was saved to tape by H1. From this total, 5.81 pb^{-1} was delivered by HERA during a period of running that H1 dedicated to low Q^2 physics, a so called *minimum bias* run. During this period 4.61 pb^{-1} of data were recorded by H1, from which 3.74 pb^{-1} were selected for this analysis (see section 4.4). The total integrated luminosity produced by HERA developing over the period 1992-2000 is shown in figure 1.7 [30].

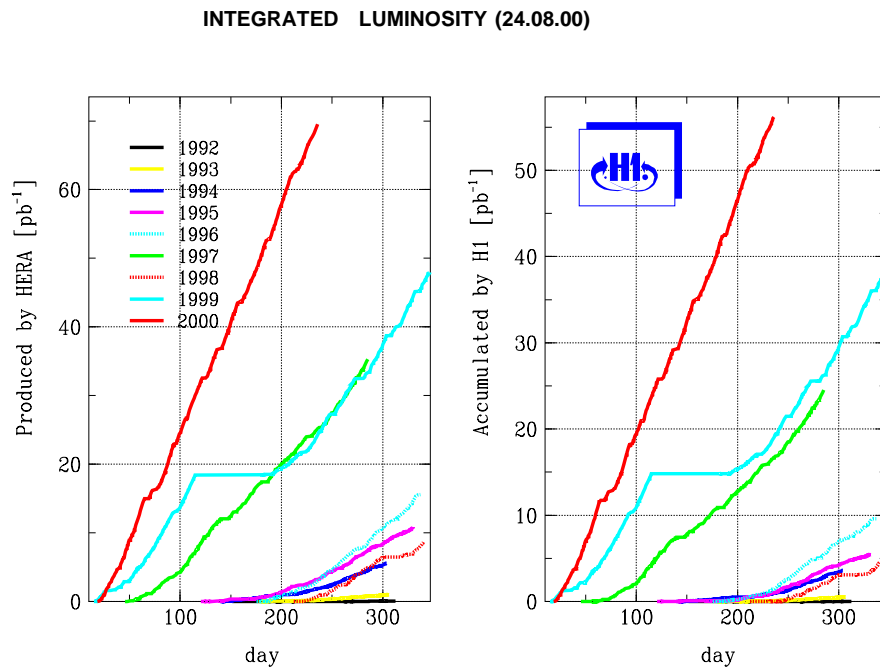


Figure 1.7: The integrated luminosity produced by HERA for the period 1992-2000.

1.8 Triggering

The triggering system is required to select interesting physics events and exclude non- $e-p$ background events. The system consists of four levels, three of which were operative in 1999: L1, L2 and L4. Most of the sub-detectors have associated trigger components and, in the first level of triggering (L1), information is passed from them to the central trigger (CTL1) [31]. In total 256 trigger elements are collected at CTL1 around $2.1 \mu\text{s}$ after the interaction. This corresponds to 22 bunch crossings after the event occurred, after which the CTL1 makes a decision taking two bunch crossings on whether the event is kept or rejected. All information from each sub-detector, from all pending bunch crossings, is stored in memory, or *pipelined*, whilst the decision is being made. This procedure eliminates *dead-time* at L1. The decision on whether to accept an event (L1KEEP) is based on 128 sub-triggers, built up from the 256 trigger elements. Providing the correct bunch crossing can be assigned the pipelines are then stopped and the dead time starts. Higher trigger levels then reject the L1KEEP signal, possibly interrupting the dead-time, or verify it. The L2 decision is performed by the Topological Trigger (L2TT) [32] and Neural Network (L2NN) [33] trigger by correlating information from different sub-triggers. If the event acquires the L2KEEP signal, full event information is then passed to level 4 (L4) where the entire event information is read into a Central Event Builder (CEB) within approximately $800 \mu\text{s}$, after which the pipelines are cleared and the dead-time ceases. Asynchronously, a limited event reconstruction is performed using several parallel processors comprising the *filter farm*. If the event passes the L4 selection, where basic cuts are applied to reject remaining background events, it is written permanently to disk. Off-line the events are then fully reconstructed and further cuts applied, although not for minimum bias runs, before being written to data storage tapes (DSTs) ready for analysis. The procedure adopted for the analysis of the 1999 minimum bias data is described in chapter 4.

1.9 HERA and H1 Upgrades

In September 2000, HERA and H1 began an upgrade procedure which produced the first luminosity of HERA II, which will run with longitudinally polarised lepton beams, in October 2001 - ten years after the first collisions at HERA. The primary purpose of the upgrade was to increase the instantaneous luminosity by a factor of five from a previous peak value of $1.5 \times 10^{31} \text{ cm}^{-2} \text{ s}^{-1}$ to $7.4 \times 10^{31} \text{ cm}^{-2} \text{ s}^{-1}$. To adapt HERA for this higher luminosity, super-conducting magnets have been installed in the H1 detector, one

in the forward and one in the backward direction [34], in order to reduce the size of the beams at the bunch crossing point. This required upgrades in the PD, ET, electronics and data acquisition (DAQ) system [35]. In order to accommodate the magnets and to improve overall performance, a large number of changes to the H1 sub-detectors was simultaneously made.

A forward silicon tracker (FST) has been built, partially from existing components of the BST and VLQ. It comprises five planes of silicon strip detectors to be used as tracking detectors in the forward region $8^\circ \leq \theta \leq 16^\circ$ and to enhance positron identification [36]. The CIZ and two planes of the CIP have been replaced with five planes of cylindrical proportional chamber [37]. Additional layers of MWPCs will aid in distinguishing $e - p$ collisions from background events and improve triggering capabilities. Additional planar chambers have been inserted into the FTD to improve track determination in a region of high primary and secondary track activity. The MWPCs and transition radiators were replaced by three planar chambers [38]. The FNC response had degraded over time and was therefore replaced with a new lead-scintillation sandwich calorimeter [39] and the PLUG calorimeter, the quality of which also degraded, has been replaced with copper absorbing plates and plastic scintillators [40]. This will improve the energy flow measurement in the forward direction.

Changes will also be made that will improve the triggering system. A new fast track trigger (FTT) will be implemented into the triggering system to allow charged particle momenta to be measured with high precision at the trigger level in the central detectors [41] and to select exclusive final states, for example $D^* \rightarrow \pi\pi$, with high efficiency. A new L1 “jet” trigger will, when used in union with the current LAr trigger, extend the capabilities of low energy deposition triggering [42]. This also aids in the rejection of backgrounds. Finally the L4 trigger and off-line reconstruction will be merged into a single system, improved to handle the increased luminosity induced data rate and reconstruct on-line the data more efficiently [43].

Chapter 2

Deep-Inelastic Scattering (DIS)

2.1 Introduction

This chapter introduces positron-proton scattering at HERA and reviews the fundamental properties of deep-inelastic scattering. The inclusive cross section is defined and the proton structure function is also presented, together with the current theories describing the data. Finally the low x , low Q^2 region of phase space is also discussed as this is relevant to the data sample under analysis in this thesis.

2.2 DIS at HERA

2.2.1 Kinematics

Figure 2.1(a) illustrates the generic deep-inelastic scattering process. *Neutral current* interactions proceed via the exchange of photons (γ) or Z^0 gauge bosons and follow the form $ep \rightarrow e'X$, where X denotes the final state system of particles. *Charged current* interactions are of the form $ep \rightarrow \nu_e X$ where a W^\pm gauge boson is exchanged.

The gauge bosons have the 4-vector momentum, q ($q^2 < 0$), and

$$Q^2 = -q^2 \tag{2.1}$$

defines the virtuality. The boson propagator contribution (T) to the amplitude is given in equation 2.2. If M_b represents the mass of the exchanged vector boson, then

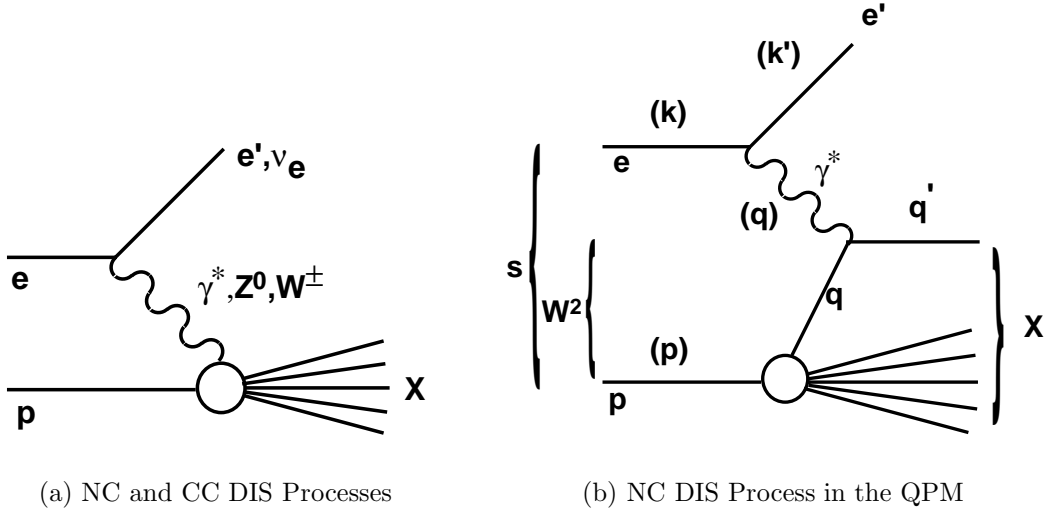


Figure 2.1: (a) NC and CC deep-inelastic scattering processes. The kinematics of NC DIS are illustrated in (b).

$$T \sim \frac{1}{Q^2 + M_b^2}. \quad (2.2)$$

Hence, photon exchange dominates the DIS cross section at low values of Q^2 . If $Q^2 \sim 0$ the photon is almost real and the interaction is called *photoproduction*, but if $Q^2 \sim M_{Z^0, W^\pm}^2$ the massive gauge bosons also contribute to the cross section. The data analysed in this thesis are in the low virtuality region $1.5 \text{ GeV}^2 < Q^2 < 45 \text{ GeV}^2$ where only virtual photon exchange is important. Hence, the exchange via massive bosons shall not be given further mention.

The value of Q^2 also determines the scale on which the proton can be probed, Δx . From the uncertainty principle,

$$Q\Delta x \sim \hbar. \quad (2.3)$$

At the HERA kinematic limit of $Q^2 = s \simeq (320 \text{ GeV})^2$ the proton is probed with a spatial resolution of $\sim 10^{-3} \text{ fm}$.

Deep-inelastic $e - p$ scattering involves $\gamma^* - p$ scattering and figure 2.1(b) highlights the relevant kinematic variables. The 4-vectors of the incoming and outgoing positrons are denoted by k and k' respectively and that of the incoming proton and final state system

by p and X respectively. Their individual components, as observed in the laboratory frame, are detailed in equations 2.4 - 2.7 below,

$$k = (E_e, 0, 0, -E_e) \quad (2.4)$$

$$k' = (E'_e, E'_e \sin \theta_e, 0, E'_e \cos \theta_e) \quad (2.5)$$

$$p = (E_p, 0, 0, E_p) \quad (2.6)$$

$$X = (E_h, p_{T,h}, 0, p_{z,h}), \quad (2.7)$$

which are valid for the case where the positron is scattered in the (x, z) plane. The 4-vector of the photon is given by,

$$q = k - k'. \quad (2.8)$$

It is convenient to express variables in terms of *Lorentz invariant* quantities and in addition to Q^2 , the following variables can be defined:

$$s = (k + p)^2 \approx 4E_e E_p \quad (2.9)$$

$$x = \frac{Q^2}{2p \cdot q} \quad (0 \leq x \leq 1) \quad (2.10)$$

$$y = \frac{p \cdot q}{p \cdot k}, \quad (0 \leq y \leq 1) \quad (2.11)$$

$$W^2 = (q + p)^2 \approx Q^2 \left(\frac{1-x}{x} \right) \quad (2.12)$$

with

$$Q^2 \approx sxy, \quad (2.13)$$

where s is the centre of mass energy (CME) squared of the $e - p$ system, x the *Bjorken scaling variable*, y the *inelasticity parameter* and W^2 the $\gamma^* - p$ CME squared. In the infinite momentum frame of the proton, x represents the fraction of the proton's longitudinal momentum transferred to the struck quark and is equal to unity for elastic collisions. In the rest frame of the proton, y is simply the fraction of the positron energy taken by the virtual photon.

2.2.2 Inclusive Proton Measurements

The probability for the inelastic process $ep \rightarrow e'X$ to occur increases relative to the elastic process as Q^2 increases. Assuming that single virtual photon exchange is dominant, the inelastic cross section in terms of Lorentz invariant variables can be written as

$$\frac{d^2\sigma(x, Q^2)}{dx dQ^2} = \frac{4\pi\alpha_{em}^2}{xQ^4} \left[\left(1 - y + \frac{y^2}{2}\right) F_2(x, Q^2) - \frac{y^2}{2} F_L(x, Q^2) \right], \quad (2.14)$$

where α_{em} is the electromagnetic coupling constant and $F_2(x, Q^2)$ and $F_L(x, Q^2)$ are *structure functions* which provide information on the quark and gluon content of the proton. For completeness terms involving the parity violating structure function F_3 due to Z^0 exchange and $\gamma - Z^0$ interference should also be included, but for $Q^2 \ll M_{Z^0}^2$ these effects are negligible and hence are not included here. The structure functions are related to cross sections (σ_T, σ_L) for transversely and longitudinally polarised photons according to

$$F_2(x, Q^2) = \frac{Q^2}{4\pi^2\alpha_{em}} \left[\sigma_T(x, Q^2) + \sigma_L(x, Q^2) \right], \quad (2.15)$$

and

$$F_L(x, Q^2) = \frac{Q^2}{4\pi^2\alpha_{em}} \sigma_L(x, Q^2). \quad (2.16)$$

The quantity $R(x, Q^2)$ can be defined as the ratio of longitudinally to transversely polarised photon cross sections and is given by,

$$R(x, Q^2) = \frac{\sigma_L(x, Q^2)}{\sigma_T(x, Q^2)} = \frac{F_2(x, Q^2)}{F_2(x, Q^2) - F_L(x, Q^2)}. \quad (2.17)$$

It can be seen from equations 2.15 and 2.16 that the condition that the transverse and longitudinal photon induced cross sections must be positive leads to

$$0 \leq F_L \leq F_2. \quad (2.18)$$

From equation 2.18 and the fact that the F_L term is proportional to y^2 in equation 2.14, it can be seen that the F_2 term is dominant in regions of low y , with the F_L term increasing

in importance as y increases. Therefore, as the F_L contribution to the total $e - p$ cross section increases as y^2 it need only be taken into account at the highest y values. The F_L contribution to the total $e - p$ cross section can safely be ignored in the following discussions as the majority of the data resides at low y ¹. Therefore, the equation for the cross section can be taken to be

$$\frac{d^2\sigma}{dx dQ^2} = \frac{4\pi\alpha_{em}^2}{xQ^4} \left(1 - y + \frac{y^2}{2}\right) F_2(x, Q^2). \quad (2.19)$$

Detailed derivations of the cross section and structure function equations can be found for example in [44], [45] and [46].

2.2.3 The Quark Parton Model (QPM) and Bjorken Scaling

The QPM [47] assumes the proton to consist of point-like charged quarks (*partons*) [48] taken to be non-interacting at large values of Q^2 . Under this assumption, Bjorken [49] predicted that in the limit $Q^2 \rightarrow \infty$,

$$F_2(x, Q^2) \rightarrow F_2(x), \quad (2.20)$$

so at a given value of x the F_2 dependence on Q^2 is flat, which is the *Bjorken Scaling Hypothesis*. The first DIS data from SLAC [2] provided experimental evidence of this property of scale invariance demonstrating the existence of point-like charged partons in the proton, identifiable as quarks.

In the Quark Parton Model (QPM) the parton momentum distribution, $f_i(x)$, defines the probability of finding a parton of species i (u, \bar{u} etc.) carrying a fraction x of the proton momentum. Therefore, it is predicted that

$$\sum_i \int x f_i(x) dx = 1, \quad (2.21)$$

where the summation is over all species of charged partons. The structure function can now be written as

¹Strictly the measured quantity is the reduced cross section, $\sigma_r = F_2(x, Q^2) - \frac{y^2}{1+(1-y)^2} F_L(x, Q^2)$. Assuming $F_L(x, Q^2)$ only contributes at large values of y , for most of the kinematic range $\sigma_r = F_2(x, Q^2)$

$$F_2(x) = \sum_i e_i^2 x f_i(x), \quad (2.22)$$

where e_i is the electric charge of parton i .

From helicity conservation arguments, it can be shown that σ_T and σ_L are dependent upon the partonic spin values. For $Q^2 \gg M_p^2$ (the mass of the proton squared), it is expected that $\sigma_T = 0$ if the partons carry spin 0, and that $\sigma_L = 0$ for spin- $\frac{1}{2}$ partons. Hence, the QPM predicts $\sigma_L(x) = F_L(x) = 0$ for spin- $\frac{1}{2}$ partons, which is one form of the Callan-Gross relation [50].

Observations at fixed target experiments [51] [52] [53], later verified by HERA [54], however showed $F_L \neq 0$, implying the existence of physics beyond the QPM. Experimental results have also provided the important observation that summing over the momenta of all the charged partons accounts for only $\sim 50\%$ of the proton's momentum (that is equation 2.21 equates to ~ 0.5 instead of 1) [55]. A review of this can be found in reference [56]. This led to the discovery that the rest of the proton momentum is carried by electrically neutral particles called gluons. The inclusion of gluons, and the corresponding gauge theory QCD, are described in the next section.

2.2.4 QCD and Gluons

The QPM in the form of equation 2.20 is successful in describing the flat structure function dependence on Q^2 as observed in [2]. However, studies soon showed that a weak logarithmic dependence on Q^2 exists and also that the structure function F_L is non-zero, signifying the breakdown of the QPM. The QPM assumes the non-interaction of quarks yet it is known that they exist bound inside the proton thus implying the existence of inter-quark forces. Hence, a more detailed theory is required to explain these discrepancies.

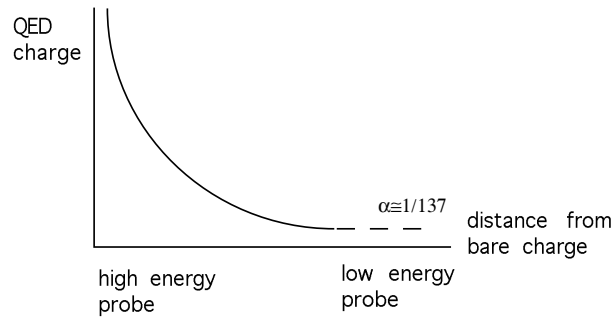
All of the above observations are explainable by the gauge field theory of *Quantum Chromodynamics* (QCD), one component of the Standard Model. This describes the strong interactions between quarks, mediated by vector *gluons*. These are the gauge bosons of the strong interaction and are massless with a spin value of 1. The strong force involves a new quantum number called the *colour charge*. Quarks carry *colour* (or anti-colour) which can either be *red*(r), *blue*(b) or *green*(g) and gluons carry combinations of colour (for example $r\bar{g}$). Both quarks and gluons are described as partons in QCD. The gluons

are not only able to couple to the quarks, but also to themselves (a portrayal of the non-Abelian nature of the theory), with a coupling α_s (analogous to the fine structure constant α_{em} in QED). Hence, the QPM can in fact be considered to be the lowest order process of QCD at high Q^2 , $\mathcal{O}(\alpha_s^0)$. QCD can thus not only explain the successes of the QPM, but also its failures.

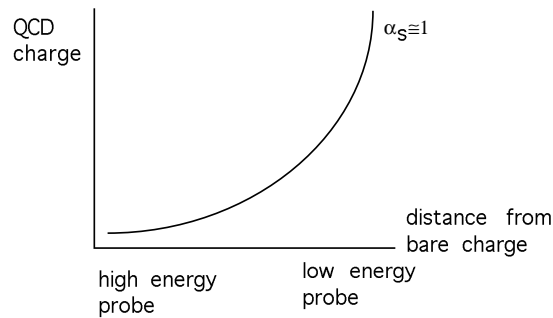
A simple comparison between QED and QCD can be made which illustrates the fundamental differences between them. Through vacuum fluctuations, an electron can emit a photon which can then produce an e^+e^- pair in QED. Therefore, the original electric charge will be surrounded by a cloud of electrons and positrons, with the positrons being attracted to the electrons and hence nearer to the electron. A high energy (short distance) probe will therefore “see” a high value for the coupling α_{em} because it penetrates the positron cloud. However, a low energy probe does not penetrate to such a distance and detects the smaller screened charge, hence the coupling is observed to be lower. This is depicted in figure 2.2(a). For the case of QCD a quark is considered, with a QCD “charge”: *colour*. In addition to the quark being able to emit a gluon which can then produce a $q\bar{q}$ pair, the gluons can also produce $g\bar{g}$ pairs, due to their ability to self-interact (unlike QED photons). Hence, the coloured quark will be surrounded by both coloured and anti-coloured charges, but the presence of colour-carrying gluons enhances the overall colour observed. Hence, a high energy test colour charge probing to small distances “observes” less charge the nearer to the coloured quark it probes, implying a low coupling. Thus, for $Q^2 \rightarrow \infty$ quarks can be considered to be free, non-interacting particles - a property known as *asymptotic freedom*. If instead a low-energy colour probe is used to examine the original quark at a large distance, more charge is observed. This is shown in figure 2.2(b). Hence, attempts to separate $q\bar{q}$ pairs by increasing the distance between them results in an increased coupling between them and they can never exist in isolation. This is known as *infrared slavery*.

2.2.5 QCD Evolution

Figures 2.3(a) and (b) show the dependence of $F_2(x, Q^2)$ on Q^2 [57] for low and high x regions respectively. Deviations from the QPM-expected behaviour of Bjorken scaling are observed for values away from $x \sim 0.13$ as shown in figure 2.3(b). These scaling violations show a Q^2 evolution which is explainable in QCD. The DGLAP [58] [59] and BFKL [60] approximations, applicable in different regions of phase space, model the evolution of $F_2(x, Q^2)$ with Q^2 and x respectively by taking appropriate terms from a full perturbative QCD expansion and they are discussed in the following sections.



(a) QED charge screening

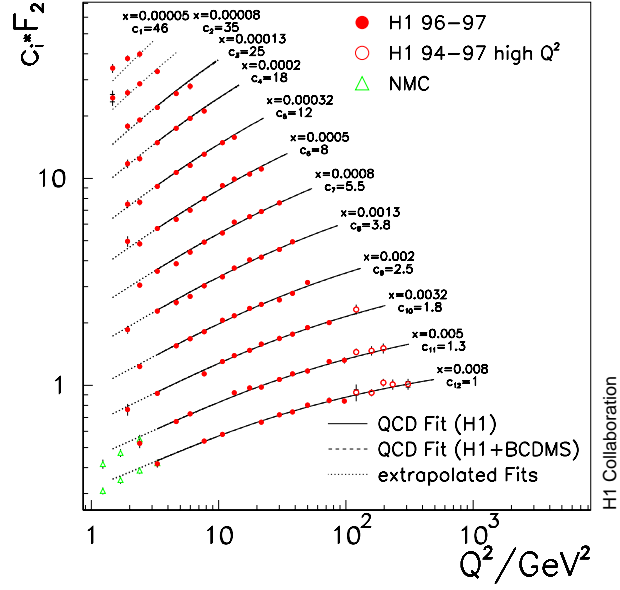


(b) QCD charge screening

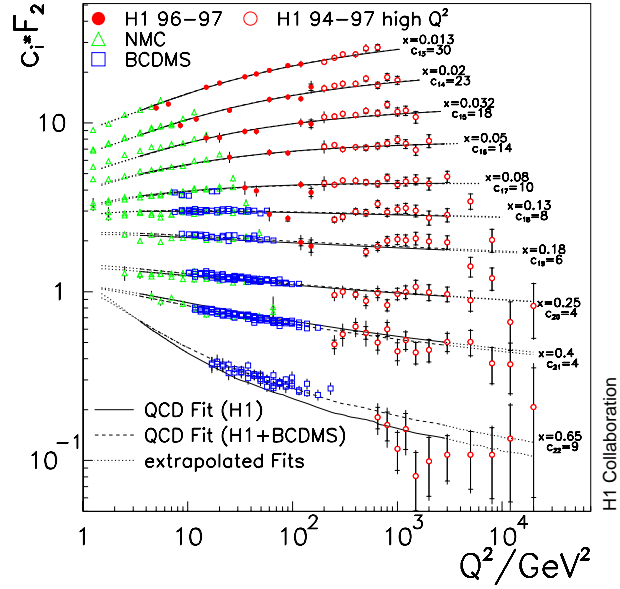
Figure 2.2: Charge screening processes in QED(a) and QCD(b).

As explained above the scaling violations of figure 2.3(b) can be physically pictured in QCD: as Q^2 increases, the virtual photon probes the proton to a smaller distance. If the proton were simply three valence quarks, without the sea of quarks, anti-quarks and gluons that is known to be present, further increases in Q^2 would not reveal any finer structure and exact scaling would be observed. However QCD predicts that higher values of Q^2 resolve more partons, with each having a lower fraction of the proton momentum x , which leads to the observed logarithmic dependence on Q^2 .

Within the *double leading log* (DLLA) approximation, all leading terms in the QCD expansion describing the inclusive structure function are taken into account. The full QCD expansion contains leading powers of the type $\alpha_s \ln(Q^2/Q_0^2)$, $\alpha_s \ln(1/x)$, and the mixed terms $\alpha_s \ln(Q^2/Q_0^2) \ln(1/x)$. The DGLAP formalism contains the $\alpha_s \ln(Q^2/Q_0^2)$ expansion terms and in the BFKL approximation terms of the type $\alpha_s \ln(1/x)$ are considered. The $F_2(x, Q^2)$ data from HERA are well described by the DGLAP equations, without the inclusion of any BFKL (low x) terms. These fundamental QCD predictions are presented in the following sections and figure 2.4 shows the kinematic plane in x and Q^2 illustrating



(a)



(b)

Figure 2.3: $F_2(x, Q^2)$ as measured by H1 (red circles), together with NMC [51] (green triangles) and BCDMS [52] (blue squares) fixed target data, as a function of Q^2 for different values of x for low x (a) and high x (b). The parameterisation shown is the result of a QCD fit.

the regions of validity for each. Also shown in this figure is the region of applicability of the GLR (Gribov, Levin, Ryskin) [61] approximation. This attempts to describe the damping of $F_2(x, Q^2)$ via the recombination process $gg \rightarrow g$ in this region of high parton densities within the DLLA framework. Not shown on figure 2.4 is the CCFM approximation, developed by Ciafaloni, Catani, Fiorani and Marchesini [62]. This attempts to combine features from both the DGLAP and BFKL approximations and it provides a satisfactory description of many aspects of the data.

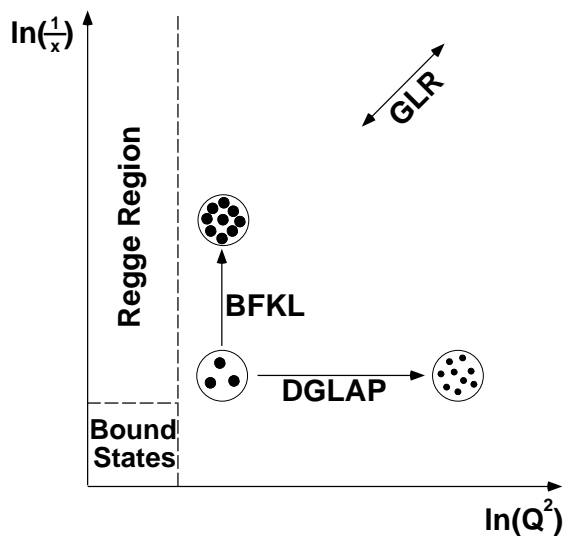


Figure 2.4: The kinematic plane in x and Q^2 showing where the DGLAP and BFKL approximations are theoretically valid.

DGLAP Evolution

In the DGLAP (Dokshitzer, Gibov, Lipatov, Altarelli and Parisi) [58] [59] approximation, only powers of $\alpha_s \ln(Q^2/Q_0^2)$ from the perturbative QCD expansion are considered in the *leading logarithm approximation* (LLA). Hence, this approach is valid where perturbative calculations are applicable, that is where Q^2 is not too small and where the x terms are unimportant. The evolution with Q^2 of the quark and gluon distributions are given respectively by equations 2.23 and 2.24,

$$\frac{dq(x, Q^2)}{d \ln Q^2} = \frac{\alpha_s(Q^2)}{2\pi} \int_x^1 \frac{dy}{y} \left[q(y, Q^2) P_{qq}\left(\frac{x}{y}\right) + g(y, Q^2) P_{qg}\left(\frac{x}{y}\right) \right], \quad (2.23)$$

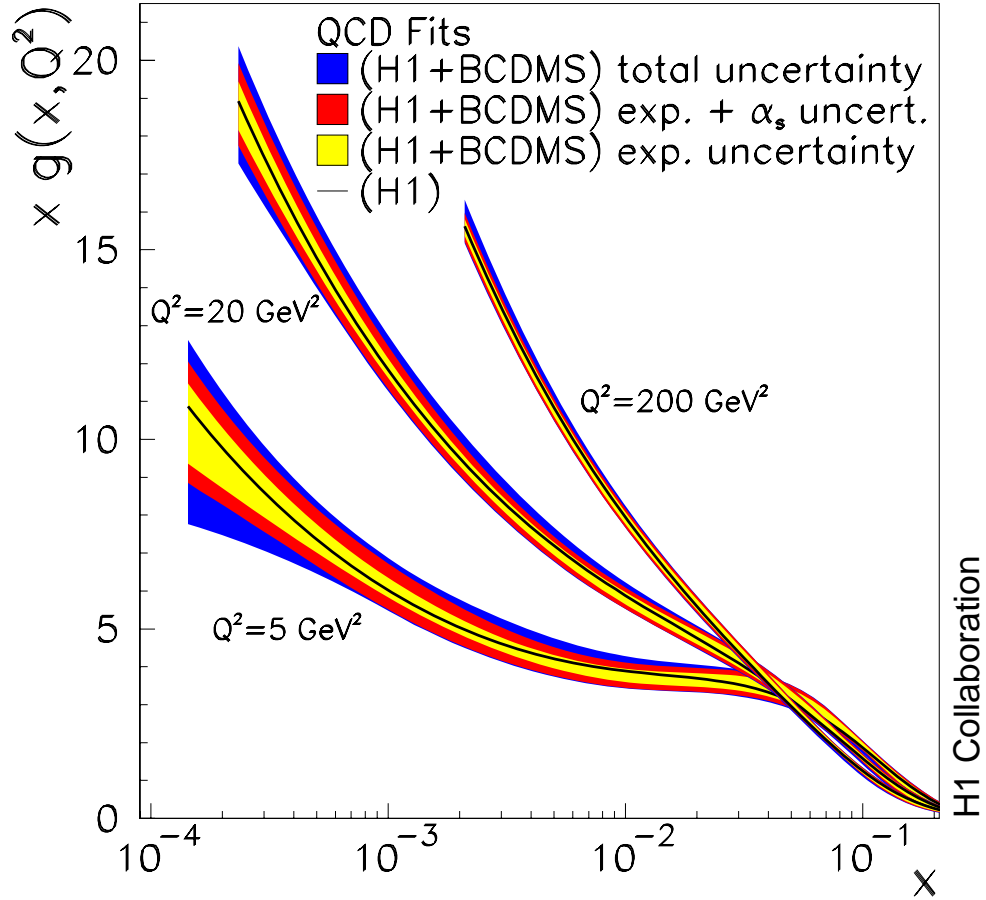


Figure 2.6: The gluon distribution from next-to-leading order (NLO) DGLAP fits with starting scale $Q_0^2 = 4.0 \text{ GeV}^2$.

$$Q^2 \gg k_{T,n}^2 \gg k_{T,n-1}^2 \gg \dots \gg k_{T,1}^2 \gg Q_0^2, \quad (2.25)$$

and also weaker ordering of longitudinal momenta,

$$x < x_n < x_{n-1} < \dots < x_1, \quad (2.26)$$

which can both be considered as time-ordering in the rest frame of the proton.

BFKL Evolution

An evolution scheme expected to be applicable in a different kinematic region is the BFKL (Balitsky, Fadin, Kuraev, Lipatov) [60] formalism. Here powers of the $\alpha_s \ln(1/x)$

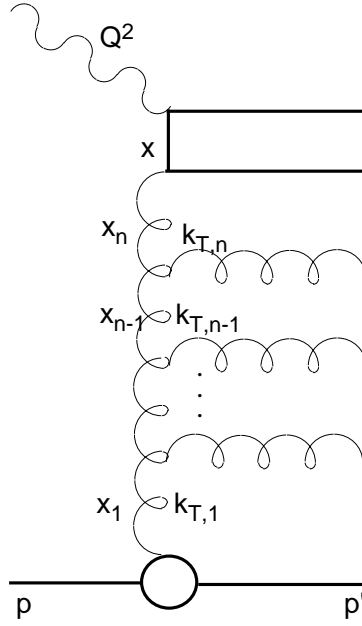


Figure 2.7: Ladder diagram illustrating the ordering in transverse and longitudinal momenta (k_T and x respectively).

terms are taken into account and the $\alpha_s \ln(Q^2/Q_0^2)$ terms are ignored in the leading logarithm approximation. Hence, this formalism is valid in the very low x kinematic region, although Q^2 must still be large enough to ensure that α_s is small and that the series is convergent. In contrast to the DGLAP approximation there is a strong ordering of longitudinal momentum fractions,

$$x \ll x_n \ll x_{n-1} \ll \dots \ll x_1, \quad (2.27)$$

which again is time-ordering in the proton rest frame, and no ordering of k_T . Hence, whereas in the DGLAP equations 2.23 and 2.24 there was an integration over the longitudinal momentum fractions, an analogous process for the transverse momentum fractions is not needed here and an *unintegrated gluon distribution* $f(x, k_T^2)$ can be defined, for gluons with an arbitrary $k_T \neq 0$,

$$xg(x, Q^2) = \int_0^{Q^2} \frac{dk_T^2}{k_T^2} f(x, k_T^2). \quad (2.28)$$

The BFKL equation is written as,

$$\frac{df(x, k_T^2)}{d\ln(1/x)} = \int dk_T'^2 K_L(k_T^2, k_T'^2) f(k_T^2, k_T'^2) = K_L \otimes f = \lambda f, \quad (2.29)$$

where \otimes symbolises the integration of K_L (the *Lipatov kernel*) and f . K_L represents the sum over powers of the $\alpha_s \ln(1/x)$ terms. The resulting integrated gluon distribution,

$$xg(x, Q^2) \sim f(Q^2)x^{-\lambda}, \quad (2.30)$$

leads to $F_2(x, Q^2) \propto x^{-\lambda}$ for a fixed value of Q^2 (for a dominant gluon contribution). The value of λ is found to be $\lambda = \frac{12\ln 2}{\pi}\alpha_s \sim 0.5$ at leading logarithm [60] and next to leading logarithm calculations yield $\lambda \sim 0.17$ [64]. Hence, the x -dependence of the structure function F_2 is predicted at low x , although the value of λ is not well constrained as can be seen from the difference between the leading and next to leading logarithm calculations. Nor does it match measurements at HERA particularly well, where λ depends strongly on Q^2 (see figure 2.9).

To date the DGLAP evolution scheme alone can describe structure function data throughout the entire HERA phase space. Hence, so far there is no unambiguous evidence for the need for BFKL contributions.

2.2.6 Photoproduction

For $Q^2 \sim 0$, the emitted photon is almost real and since the $e - p$ cross section contains a $\frac{1}{Q^4}$ term in the propagator it is dominated by these photoproduction events. Due to the fact that the majority of interactions occurring in this region are soft, where the transverse momentum p_T of the final state is low, perturbative calculations are not valid and another model must be used to describe the data. Regge [65] developed a formalism to describe scattering processes which is applicable to the kinematic region of photoproduction, and is also valid for soft low Q^2 DIS processes. This model, and its application to diffractive deep-inelastic scattering is discussed in chapter 3.

Low p_T photoproduction interactions can be described by the *Vector Dominance Model* (VDM) in which the photon fluctuates into vector mesons (comparisons with experimental data are discussed in [66]). High p_T interactions are also possible in photoproduction but are not explainable in the VDM. Generally they can be classified as either *direct* or *resolved* interactions, the difference arising from the way in which the photon interacts with the

proton. Direct processes, such as QCD-Compton scattering or boson gluon fusion (BGF), involve the entire photon interacting with the proton. In the resolved case the interaction occurs between partons in the photon and proton. Figure 2.8 illustrates the difference between the two types of reaction.

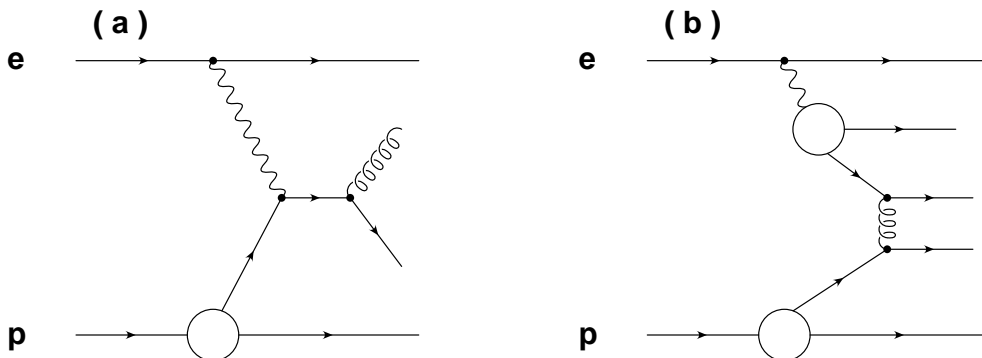


Figure 2.8: Examples of (a) direct and (b) resolved photoproduction processes.

2.2.7 Saturation in Deep-Inelastic Scattering

The first measurements of the inclusive proton structure function made by H1 [6] and ZEUS [7] revealed the existence of a rapid rise in $F_2(x, Q^2)$ at small values of x . The rate of the rise ($\partial F_2 / \partial \ln x$) is similar for all $x \lesssim 10^{-2}$. Such behaviour, as well as the observation that the rate of growth increases with increasing Q^2 , is well described above $Q^2 \sim 1 \text{ GeV}^2$ using the perturbative DGLAP evolution. The gluon density increases rapidly as $x \rightarrow 0$, implying an ever increasing number of gluons. This density cannot however continue to rise indefinitely as this would lead to a violation of unitarity, and a better understanding of high density QCD is required to explain what is theoretically expected to happen. Figure 2.9 shows the derivative of the structure function, λ , which is defined in equation 2.31,

$$-\lambda(x, Q^2) = \left(\frac{\partial \ln F_2(x, Q^2)}{\partial \ln x} \right)_{Q^2}. \quad (2.31)$$

These results, from the recent H1 publication [8], show that λ does not depend on x for $x \lesssim 0.01$, and that the behaviour of $F_2(x, Q^2)$ can be described by $F_2 \propto x^{-\lambda}$ (which is the same form as for the BFKL approximation of section 2.2.5 though the increase of λ with Q^2 is not predicted). Hence, even for the lowest values of x measured here, $x \leq 5 \times 10^{-5}$,

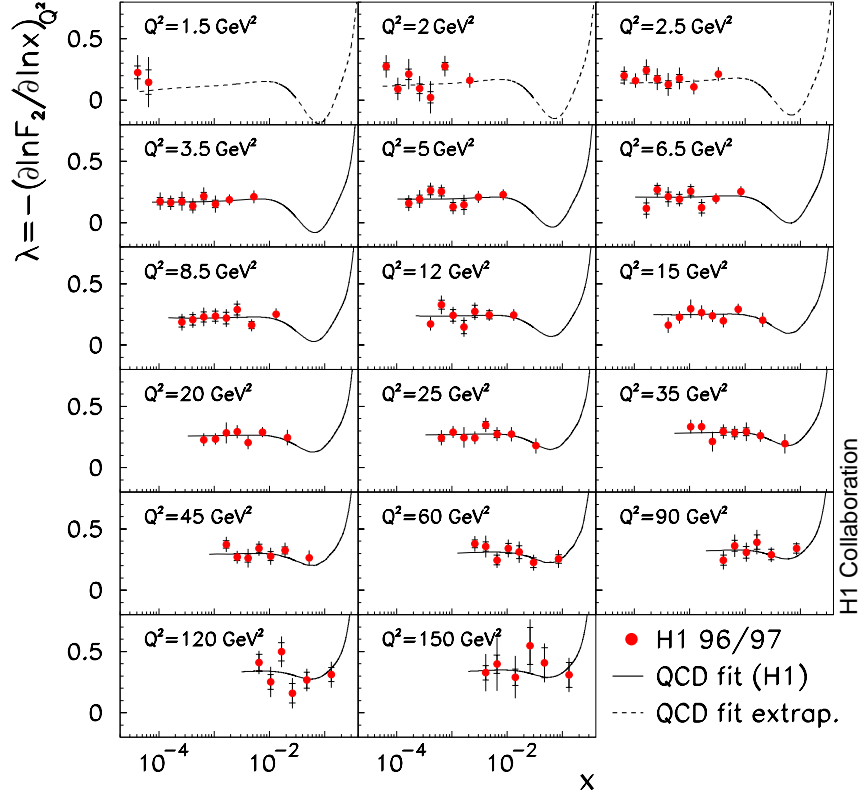


Figure 2.9: H1 measurement of the structure function derivative $\lambda(x, Q^2)$. The solid lines indicate NLO QCD fits to the data and the dotted lines represent predictions evolved from 3.5 GeV^2 to lower Q^2 .

no deviation away from this power law behaviour is observed. This implies that there is no evidence for damping of the rise of $F_2(x, Q^2)$ as $x \rightarrow 0$.

As mentioned in section 2.2.6, structure function results in the very low Q^2 , low x region can be described by Regge Theory. Figure 2.10, taken from [67], illustrates the Q^2 dependence of the structure function $F_2(x, Q^2)$ and the success of Regge and QCD fits at low and high Q^2 respectively. It can be observed that neither theory can be extrapolated into the other region of Q^2 , although it is desirable for the structure function behaviour to be described over all available phase space.

The saturation model is based upon a *colour dipole model* approach. The incident virtual photon can be described in the proton rest frame as fluctuating into a $q\bar{q}$ pair before interacting with the proton. The basis of the saturation model is that the cross section between the $q\bar{q}$ dipole and the proton “saturates” at large separation of the dipole elements. This can happen either because parton saturation occurs as $x \rightarrow 0$ (and particle recombination takes place), or, as is the case at HERA, because the proton structure function $F_2(x, Q^2)$ must tend to zero as Q^2 decreases. This model was developed to describe the physics of

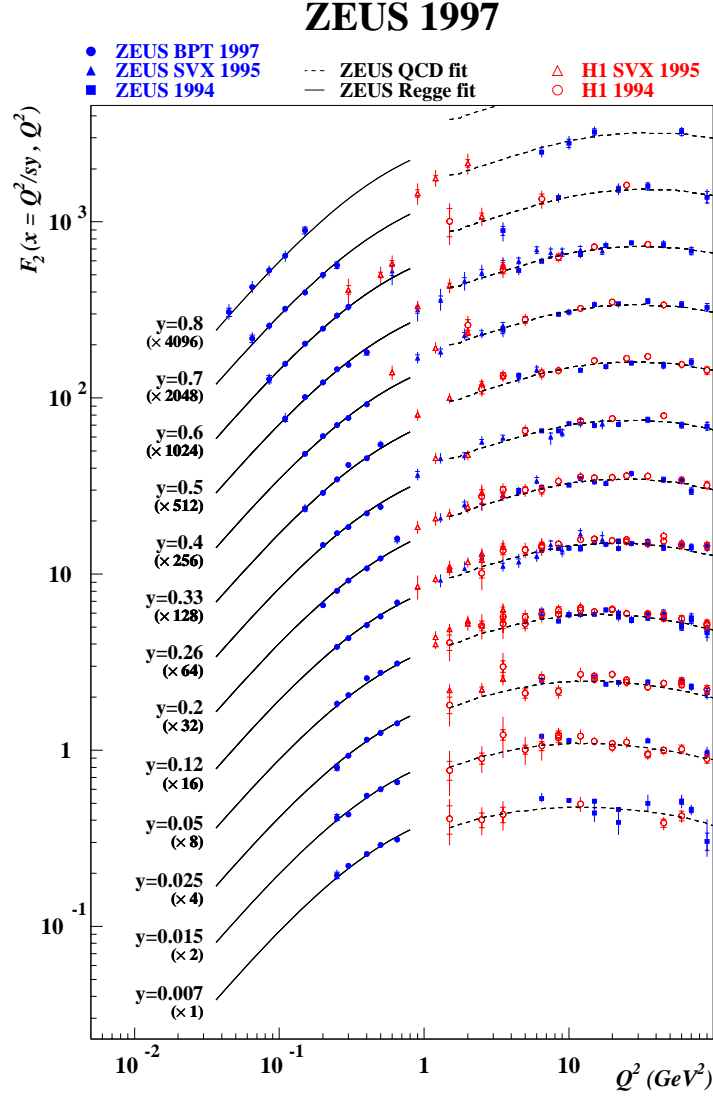


Figure 2.10: ZEUS measurement of $F_2(x, Q^2)$ as a function of Q^2 for fixed values of y .

the very low x region in particular but has been applied to all $x \lesssim 10^{-2}$ and higher values of Q^2 . The cross section for the interaction can be expressed in terms of an effective dipole wave-function ϕ and the effective dipole cross section $\hat{\sigma}$,

$$\sigma_{T,L}^{\gamma^*p} = \int dz d^2r |\phi_\gamma^{T,L}|^2 \hat{\sigma}(Q^2, r, z), \quad (2.32)$$

where $r \sim 1/Q^2$ is the transverse size of the dipole and z is the momentum fraction of the photon carried by the quark as depicted in figure 2.11.

The effective dipole cross section is expressed as,

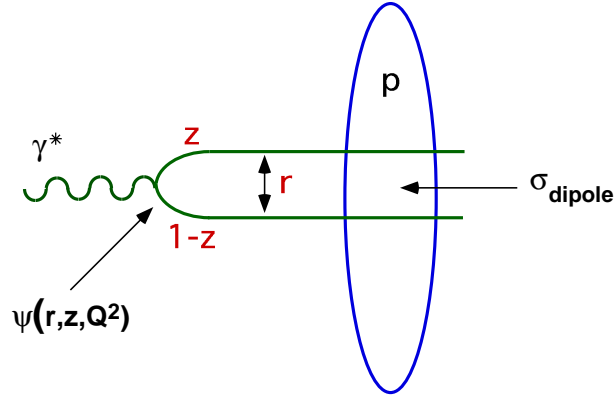


Figure 2.11: Dipole picture of $\gamma^* p$ scattering.

$$\hat{\sigma}(x, r^2) = \sigma_0 \left[1 - \exp\left(-\frac{r^2}{R_0^2(x)}\right) \right], \quad (2.33)$$

which interpreted in the framework of the saturation model gives the *saturation radius*, as given in equation 2.34 where $Q_0^2 = 1 \text{ GeV}^2$, which is dependent upon x ,

$$R_0(x) = \frac{1}{Q_0} \left(\frac{x}{x_0} \right)^{\frac{\lambda}{2}}. \quad (2.34)$$

Hence, there are just three free parameters to be determined from fits to data: x_0 , λ and σ_0 . From a recent publication [68], for $x < 0.01$ the values for these three parameters were found to be,

$$\sigma_0 = 23 \text{ mb}, \quad \lambda = 0.29, \quad x_0 = 3 \times 10^{-4}. \quad (2.35)$$

The value obtained for the cross section σ_0 has a value similar in magnitude to that of a typical soft hadronic cross section and the value for λ can be compared with that from hadron-hadron experiments where λ was observed to be much smaller (~ 0.08). An extrapolation of the results from [8] to a comparable low Q^2 value also yields a value of $\lambda \sim 0.08$.

Chapter 3

Diffractive Physics

3.1 Diffraction at HERA

Hadron-hadron scattering is mediated by the strong force and such interactions predominantly involve low momentum transfers. In this case, the coupling α_s is large and perturbative QCD approaches are inappropriate. Therefore, phenomenological models such as *Regge Theory* (discussed in section 3.4.1) must be invoked. Regge Theory is able to describe the observed rising nature of total cross sections through the introduction of a *diffractive exchange*¹ which is colourless and has the quantum numbers of the vacuum (C=P=+1).

Since the beginning of the operation of HERA, events have been observed where there is an absence of hadronic activity in the forward direction. These events contribute approximately 10% to the total inclusive cross section and can be identified as being diffractive in nature. Events of this kind are still not fully understood but measurements of the diffractive structure function (analogous to $F_2(x, Q^2)$) allow the structure of the colourless exchange to be investigated. This chapter describes diffractive deep-inelastic scattering at HERA and the theories which are used in the modelling of such processes. The diffractive structure function is also introduced, a measurement of which will be detailed in chapters 4 and 5.

¹Diffractive events are so-called because in the early experiments the observed dependence of the cross section on t resembled optical diffraction patterns at high energies.

3.2 Kinematics of Deep-Inelastic Diffraction

Diffractive events at HERA involve a virtual photon dissociating into a hadronic final state system whilst the proton remains intact or dissociates into a low mass hadronic final state that continues undetected down the beam-pipe. In inclusive DIS processes the struck parton in the proton carries colour charge. Hence, the final state particles are connected by a colour string and a continuum of particles is produced over the full range of the detector. In diffractive DIS however the absence of hadronic activity around the direction of the proton in the forward region of the detector is consistent with the exchange of a colourless object between the proton and photon. This can be identified as the same colourless exchange seen in high energy hadron-hadron processes, namely the *pomeron*, \mathbb{P} . In pomeron exchange events there is no colour string connecting the final state particles to the outgoing proton. Figure 3.1 illustrates the colour flow properties of standard (a) and diffractive (b) DIS processes.

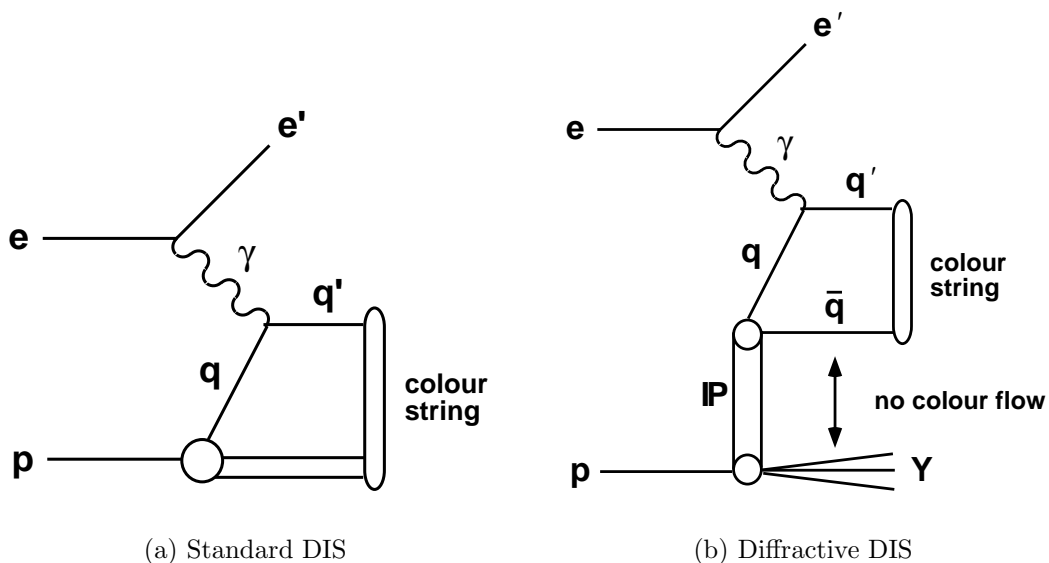


Figure 3.1: Comparison between the colour flow properties of (a) standard and (b) diffractive DIS.

Figure 3.2 shows the kinematic quantities relevant in diffractive deep-inelastic scattering $ep \rightarrow e'XY$, in addition to which the variables in equations 2.4 - 2.13 are still valid. X denotes the hadronic final state produced with an invariant mass M_X , and Y is the outgoing proton state of mass M_Y ($= M_p$ or represents a low mass excitation). The systems X and Y are typically produced in the central and very forward directions in the laboratory frame respectively. Their masses are much smaller than the γ^*p centre of mass energy, W :

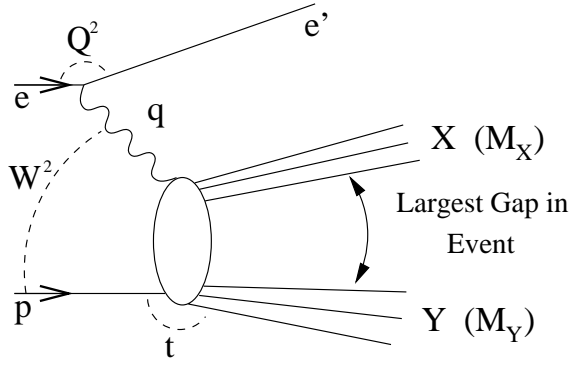


Figure 3.2: Kinematics of diffractive DIS.

$$M_X, M_Y \ll W \quad (3.1)$$

The separation of X and Y can be quantified in Lorentz invariant variables in terms of the *rapidity* of a final state particle,

$$y = \frac{1}{2} \ln \frac{E + p_z}{E - p_z}, \quad (3.2)$$

which reduces to *pseudorapidity* where the mass of the particle is unimportant:

$$\eta = -\ln \tan \frac{\theta}{2}. \quad (3.3)$$

Diffractive events are characterised by the presence of (*pseudo*)*rapidity gaps* where the forward region of the detector, in the large positive region of pseudorapidity, is empty. Rapidity gaps are not however unique to diffractive scattering as small rapidity gaps may be created via random fluctuations during fragmentation in standard DIS processes.

The 4-momentum transfer squared, t , at the pPY vertex is defined by,

$$t = (p - Y)^2, \quad (3.4)$$

where p and Y are the 4-momenta of the proton initial and final states respectively.

Two further variables can be introduced, as given in equations 3.5 and 3.6,

$$x_P = \frac{q \cdot (p - Y)}{q \cdot p}, \quad (3.5)$$

$$\beta = \frac{-q^2}{2q \cdot (p - Y)}, \quad (3.6)$$

where x_P and β are related to the scaling variable, x as in equations 2.9 - 2.12, by

$$x = x_P \beta, \quad (3.7)$$

where x_P is the fraction of the 4-momentum of the proton transferred to the pomeron and β is the fraction of the 4-momentum of the pomeron carried by the struck quark. The equations for x_P and β (analogous to x in DIS) can be written as,

$$x_P = \frac{Q^2 + M_X^2 - t}{Q^2 + W^2 - M_p^2}, \quad (3.8)$$

and,

$$\beta = \frac{Q^2}{Q^2 + M_X^2 - t}. \quad (3.9)$$

For the limits appropriate to this analysis where $M_p^2 \ll Q^2$, W^2 and $|t| \ll Q^2$, M_X^2 , equations 3.8 and 3.9 simplify to

$$x_P = \frac{M_X^2 + Q^2}{W^2 + Q^2}, \quad (3.10)$$

and

$$\beta = \frac{Q^2}{M_X^2 + Q^2}. \quad (3.11)$$

3.3 The Diffractive Structure Function

The equation relating the diffractive DIS cross section to the general diffractive structure function is given in equation 3.12 and is analogous to the inclusive cross section given in equation 2.19,

$$\frac{d^4\sigma(ep \rightarrow eXY)}{d\beta dQ^2 dx_p dt} = \frac{4\pi\alpha_{em}^2}{\beta Q^4} \left(1 - y + \frac{y^2}{2}\right) F_2^{D(4)}(\beta, Q^2, x_p, t). \quad (3.12)$$

For the data analysed in this thesis the system Y is not measured directly, hence an integration is performed over $|t| < 1 \text{ GeV}^2$ and $M_Y < 1.6 \text{ GeV}$ and a three dimensional structure function is extracted. From arguments similar to those used for the inclusive cross section, the longitudinal contribution to the diffractive structure function, F_L^D , is neglected. Figure 3.3 shows the results for the extracted diffractive structure function $F_2^{D(3)}(\beta, Q^2, x_p)$ obtained from combining the nominal vertex H1 1994 data, with a luminosity of 1.96 pb^{-1} , and shifted vertex data of luminosity 0.06 pb^{-1} [69].

The general trend observed is of $x_p F_2^{D(3)}$ decreasing or remaining constant as x_p increases at fixed β and Q^2 , except at the lowest values of β where a rise is seen at the highest values of x_p . Two bins, one taken at a low value of β , and the other at a high value of β are shown together in figure 3.4 to illustrate this contrasting behaviour. As discussed in section 3.4.2 this behaviour is due to the existence of a reggeon (meson) component, at low β values in addition to the pomeron contribution.

3.4 Models of Diffraction

3.4.1 Regge Models

At low Q^2 interactions between hadrons do not resolve the underlying quark structure, but the hadrons themselves interact in their entirety. For these soft interactions α_s is large and the equations of perturbative QCD are not valid. In this region of phase space, a good description of the cross section is provided by *Regge Theory*.

For a reaction $AB \rightarrow CD$, Mandelstam variables are defined as $s = (A + B)^2 = (C + D)^2$ and $t = (A - C)^2 = (B - D)^2$ where A , B , C and D represent the 4-vectors of the initial and final state particles. Figure 3.5 shows how the same particle may contribute to processes either as (a) a t -channel exchange or (b) an s -channel resonance in the crossed

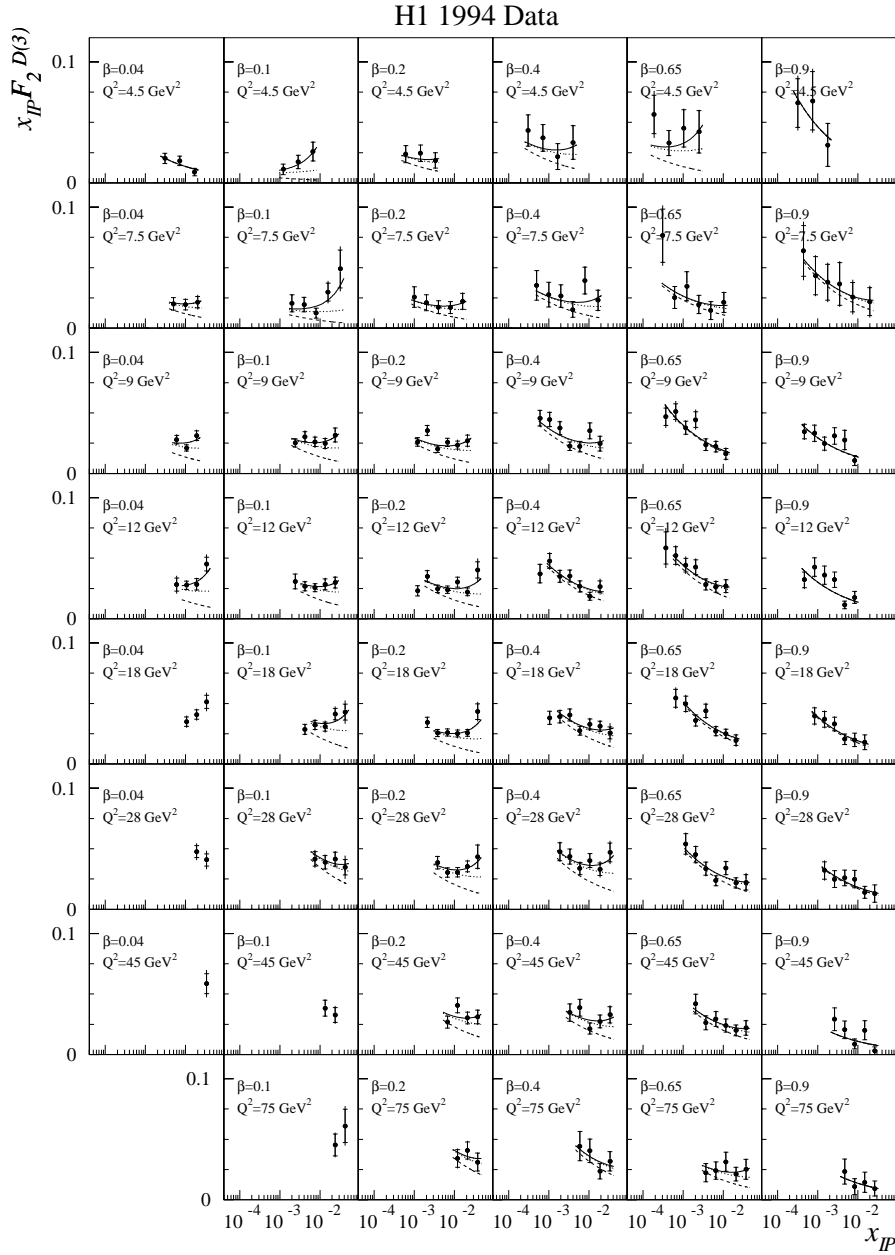


Figure 3.3: $x_{\mathbb{P}}F_2^D(\beta, Q^2, x_{\mathbb{P}})$, where $F_2^D(\beta, Q^2, x_{\mathbb{P}})$ is the diffractive structure function, shown as a function of $x_{\mathbb{P}}$ in Q^2 and β bins.

channel $A\bar{C} \rightarrow \bar{B}D$. The essence of Regge Theory is that the same amplitude describes both processes. The particles exchanged in Regge Theory are called *Regge Poles* where in the high energy limit, $s \gg |t|$, for a dominant single particle exchange the angular momentum J and mass squared M^2 of the exchanged particles are related by a linear *Regge Trajectory*. This is illustrated in the *Chew-Frautschi* plot [70] for the ρ trajectory in figure 3.6 where the angular momentum is plotted against the corresponding mass

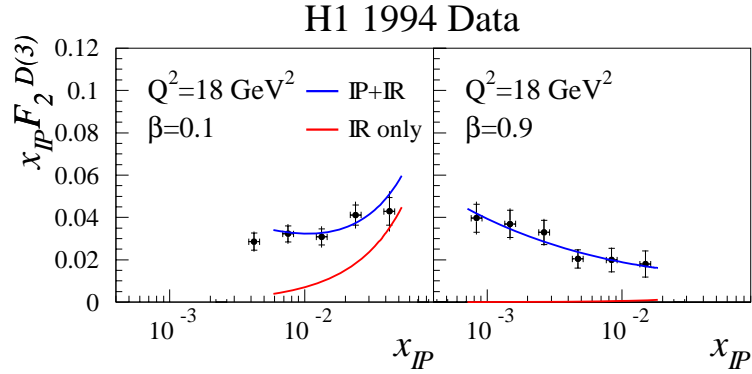


Figure 3.4: $x_{\mathbb{P}} F_2^{D(3)}(\beta, Q^2, x_{\mathbb{P}})$ shown as a function of $x_{\mathbb{P}}$ at fixed $Q^2 = 18 \text{ GeV}^2$ in bins of low and high β respectively. The red curves represent combined pomeron (\mathbb{P}) and meson (\mathbb{R}) contributions and the blue curves correspond to the meson contribution only.

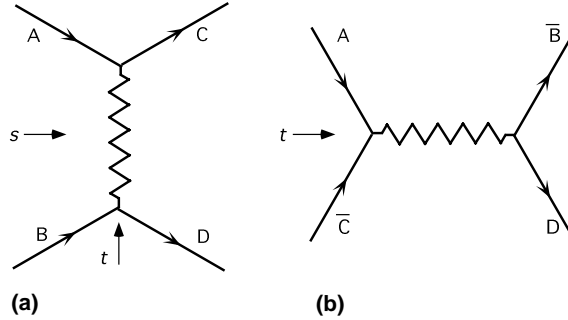


Figure 3.5: Corresponding (a) t -channel ($AB \rightarrow CD$) and (b) s -channel ($A\bar{C} \rightarrow \bar{B}D$) processes.

squared (or virtuality in the t -channel). For positive values of the particle 4-momentum squared the particle manifests itself as a resonance with integral or half integral values of angular momentum (spin). This is the s -channel resonance region. For negative 4-momentum squared the particle is an exchange lying on the same trajectory with a linear slope,

$$\alpha(t) = \alpha(0) + \alpha' t, \quad (3.13)$$

where $\alpha(t)$ is a complex variable but the s -channel resonances are observed at real integer or half-integer values of spin. $\alpha(0)$ gives the *intercept* of the trajectory and α' describes the slope, which is found to be $\sim 1 \text{ GeV}^{-2}$ for all mesons.

In the limits $s \rightarrow \infty$ and $|t| \ll s$, the Regge amplitude for an exchange $\alpha(t)$ for the reaction

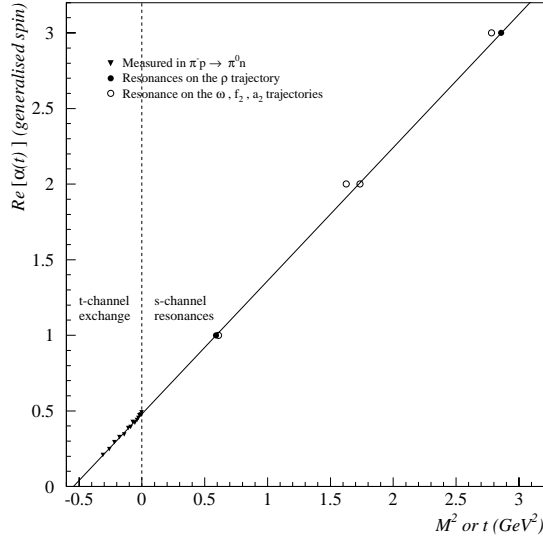


Figure 3.6: Chew-Frautschi plot for the highest intercept mesons.

$AB \rightarrow CD$ is proportional to $s^{\alpha(t)}$ and thus the elastic cross section is proportional to

$$\frac{d\sigma}{dt} \sim f(t) \left(\frac{s}{s_0} \right)^{2\alpha(t)-2}, \quad (3.14)$$

which via the optical theorem ² leads to

$$\sigma_{total} \propto s^{\alpha(0)-1}. \quad (3.15)$$

The above model based on meson exchange universally describes all hadron-hadron scattering processes in the same way (equations 3.14 and 3.15). For mesons with $\alpha(0) \leq 0.5$ it successfully describes the decrease of total and elastic cross sections as the centre of mass energy \sqrt{s} increases, for low values of \sqrt{s} . However, observations showed that as \sqrt{s} increases above a few GeV, the cross section flattens and rises gently [71]. Figure 3.6 shows that the highest intercept mesons have an intercept of $\alpha(0) \sim 0.5$ and a universal slope $\alpha' \sim 1 \text{ GeV}^{-2}$. In order to explain the gentle rising of the cross section, an exchange with a higher intercept is needed. Hence, the *pomeron*, an exchange with vacuum quantum numbers and an intercept close to unity, was postulated to mediate elastic scattering. The cross section is then described by dominant meson exchange at low \sqrt{s} which dies

²The optical theorem relates the elastic cross section ($AB \rightarrow AB$) to the total cross section ($AB \rightarrow X$)

off at high \sqrt{s} leaving the pomeron exchange. Results from Regge fits to hadron-hadron data [72] determined the value of the pomeron trajectory to be

$$\alpha_{\mathbb{P}}(t) = 1.085 + 0.25t. \quad (3.16)$$

Equation 3.14 can be rewritten, using equation 3.13, as

$$\frac{d\sigma}{dt} \sim f(t) \left(\frac{s}{s_0}\right)^{2\alpha(0)-2} \left(\frac{s}{s_0}\right)^{2\alpha't} \quad (3.17)$$

$$\sim f(t) \left(\frac{s}{s_0}\right)^{2\alpha(0)-2} e^{2\alpha' \ln(s/s_0)t} \quad (3.18)$$

$$\sim \left(\frac{d\sigma}{dt}\right)_{t=0} e^{bt}, \quad (3.19)$$

where b is the *slope parameter*,

$$b \sim b_0 + 2\alpha' \ln\left(\frac{s}{s_0}\right), \quad (3.20)$$

and the constant b_0 arises from the t -dependence of $f(t)$ which is approximately $e^{b_0 t}$. If s increases b increases logarithmically which implies that the slope of the t -distribution gets steeper. Such behaviour is known as *shrinkage*.

3.4.2 Hard Scattering Factorisation

The recently proven QCD hard scattering factorisation theorem [73] for diffraction separates diffractive hard scattering processes in DIS into a long range soft non-perturbative contribution factorised into diffractive parton densities in the same way as for the inclusive cross section, and a short range hard scattering matrix element which is fully calculable. For the diffractive cross section this factorisation can be represented by,

$$\frac{d^2\sigma(x, Q^2, x_{\mathbb{P}}, t)^{\gamma^*p \rightarrow XY}}{dx_{\mathbb{P}} dt} = \sum_i \int_0^{x_{\mathbb{P}}} d\xi \hat{\sigma}^{\gamma^*i}(x, Q^2, \xi) f_i^D(\xi, Q^2, x_{\mathbb{P}}, t), \quad (3.21)$$

where ξ is the fraction of the proton momentum carried by a diffractive parton i , $\hat{\sigma}^{\gamma^*i}$ represents the universal partonic cross sections and f_i^D the diffractive parton distributions

for a parton i . This hard scattering factorisation is valid for fixed x , $x_{\mathbb{P}}$ and t for large enough values of Q^2 . For fixed values of $x_{\mathbb{P}}$ and t the DGLAP equations are applicable in the diffractive case with evolution in β and Q^2 being equivalent to evolution in x and Q^2 for standard DIS. Hence, although not known from first principles, diffractive parton distributions can be evolved from a starting scale to higher Q^2 and lower x using the DGLAP equations.

Ingelman-Schlein Model

The diffractive proton structure function, as discussed in section 3.3, was defined by equation 3.12. A universal dependence on $x_{\mathbb{P}}$ and t as β and Q^2 change is expected if the $p\mathbb{P}Y$ vertex is factorisable, as expected in Regge Theory and represented in figure 3.7. As a further constraint in addition to QCD factorisation, Regge factorisation states that the process can be separated into a Q^2 , β dependent part and an $x_{\mathbb{P}}$, t dependent part. As employed in the Ingelman-Schlein model [74] this decomposes $F_2^{D(3)}$ into pomeron flux and structure function terms.

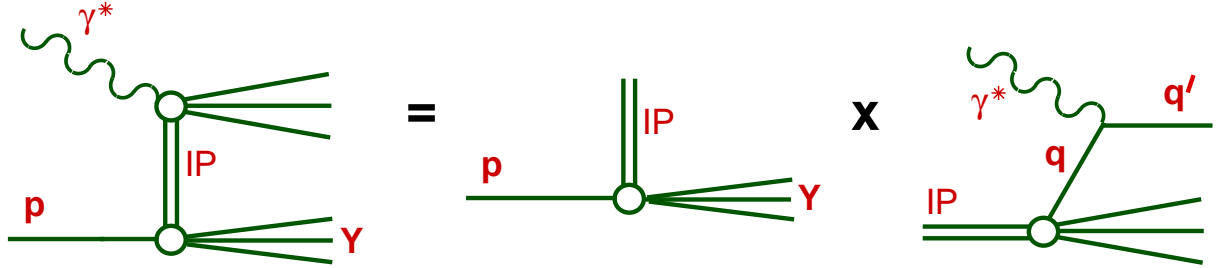


Figure 3.7: Representation of the Regge vertex factorisation hypothesis.

The $p\mathbb{P}Y$ vertex factor expressed in terms of the variables $x_{\mathbb{P}}$ and t factorises from the $\gamma^*\mathbb{P}$ vertex that is expressed in terms of β and Q^2 . The $x_{\mathbb{P}}$ dependence can be modelled in terms of Regge theory [65] [75], where the factorisation hypothesis allows the structure function to be expressed as

$$F_2^{D(3)}(\beta, Q^2, x_{\mathbb{P}}, t) = f_{\mathbb{P}/p}(x_{\mathbb{P}}, t) F_2^{\mathbb{P}}(\beta, Q^2). \quad (3.22)$$

$F_2^{\mathbb{P}}(\beta, Q^2)$ is the structure function of the pomeron and the *universal flux factor*, which describes the probability of a pomeron being present in the proton, is expressed in terms of $x_{\mathbb{P}}$ and t by,

$$f_{\mathbb{P}/\mathbb{P}}(x_P, t) \sim \frac{e^{b_{\mathbb{P}}t}}{x_P^{2\alpha(t)-1}}. \quad (3.23)$$

Regge theory with just pomeron exchange adequately describes the majority of diffractive data, including the first measurement of $F_2^{D(3)}$ at HERA [76], via the factorisable $p\mathbb{P}\mathbb{Y}$ vertex hypothesis. However, the upturn of $x_P F_2^{D(3)}$ at low β and high x_P is not described (see figure 3.4) and requires the introduction of a secondary Regge trajectory. Therefore, a reggeon component (\mathbb{R}), corresponding to the exchange-degenerate leading meson trajectory in the Chew-Frautschi plot of figure 3.6, was incorporated into the Ingelman-Schlein model to produce an H1 parameterisation so that the cross section includes terms for both the leading pomeron and sub-leading meson components,

$$F_2^D = f_{\mathbb{P}/\mathbb{P}}(x_P, t)F_2^{\mathbb{P}}(\beta, Q^2) + f_{\mathbb{R}/\mathbb{P}}(x_P, t)F_2^{\mathbb{R}}(\beta, Q^2), \quad (3.24)$$

where,

$$f_{\mathbb{P},\mathbb{R}/\mathbb{P}}(x_P, t) \sim \frac{e^{b_{\mathbb{P},\mathbb{R}}t}}{x_P^{2\alpha_{\mathbb{P},\mathbb{R}}(t)-1}}, \quad (3.25)$$

and

$$\alpha_{\mathbb{P},\mathbb{R}} = \alpha_{\mathbb{P},\mathbb{R}}(0) + \alpha'_{\mathbb{P},\mathbb{R}}t, \quad (3.26)$$

in analogy to equation 3.13. The deep-inelastic structures of the pomeron and meson exchanges are described respectively by the structure functions $F_2^{\mathbb{P}}(\beta, Q^2)$ and $F_2^{\mathbb{R}}(\beta, Q^2)$ in equation 3.24. Hence, associated parton density functions $f_i(\beta, Q^2)$, for all types of parton (i), can be defined for the pomeron and meson exchanges. This is analogous to the case of standard DIS.

The results of fits to H1 data [69] yield values of

$$\alpha_{\mathbb{P}}(0) = 1.203 \pm 0.020(\text{stat.}) \pm 0.013(\text{syst.})_{-0.035}^{+0.030}(\text{model}), \quad (3.27)$$

and

$$\alpha_{\mathbb{R}}(0) = 0.50 \pm 0.11(\text{stat.}) \pm 0.11(\text{syst.})_{-0.10}^{+0.09}(\text{model}). \quad (3.28)$$

The effective pomeron intercept determined here (equation 3.27) is not consistent with that of the soft pomeron ($\alpha(0) \sim 1.08$ [72]). The value for $\alpha_{\mathbb{P}}(0)$ can also be compared with that from predictions from the *hard pomeron model* [77] which give $\alpha_{\mathbb{P}}(0) \sim 1.4$. From section 2.2.5 it was seen that leading order and next to leading order BFKL calculations yielded predictions of $\alpha_{\mathbb{P}}(0) = 1 + \lambda \sim 1.4$ [60] and ~ 1.17 [64] respectively. The Saturation model predicted $\alpha_{\mathbb{P}}(0) = 1.29$ [68].

The value of $\alpha' = 0.25 \text{ GeV}^{-2}$ is very different to that observed for meson Regge trajectories, implying a different QCD interpretation. Whilst meson exchanges involve quarks, pomeron exchanges can most easily be pictured as being a gluon-gluon pair in an overall colour singlet state. So far the associated s -channel resonances (glueballs) have not been convincingly detected.

A summary of results from H1 and ZEUS inclusive and diffractive data on the effective pomeron intercept, as defined in equation 3.13, are shown as a function of Q^2 in figure 3.8. The Regge theory expectations are given by equations 3.29 - 3.30,

$$x_{\mathbb{P}} F_2^{D(3)} \sim A(\beta, Q^2) x^{2-2\alpha_{\mathbb{P}}(t \approx 0)}, \quad (3.29)$$

$$F_2 \sim B(Q^2) x^{-\alpha_{\mathbb{P}}(0)}. \quad (3.30)$$

There is evidence for a rise of $\alpha_{\mathbb{P}}(0)$ with Q^2 in the diffractive case which is unexpected from simple Regge pole theory. The diffractive and inclusive results are observed to be compatible at low Q^2 but inconsistent at higher values. Away from $Q^2 \lesssim 1 \text{ GeV}^2$ the physical process involves a hard scale and QCD effects may modify the simple Regge predictions. The value of $\alpha_{\mathbb{P}}$ is observed to be much larger at high Q^2 for inclusive DIS than for diffractive DIS. The ratio of diffractive to inclusive cross sections was presented in [78] and is defined as,

$$\rho^{D(3)}(\beta, Q^2, x_{\mathbb{P}}) = \frac{M_X^2 x}{Q^2} \cdot \frac{F_2^{D(3)}(\beta, Q^2, x_{\mathbb{P}})}{F_2(x, Q^2)}, \quad (3.31)$$

which is shown as a function of W at fixed values of Q^2 and β in figure 3.9. The ratio is observed to be relatively flat over the entire phase space except for large β (low M_X)

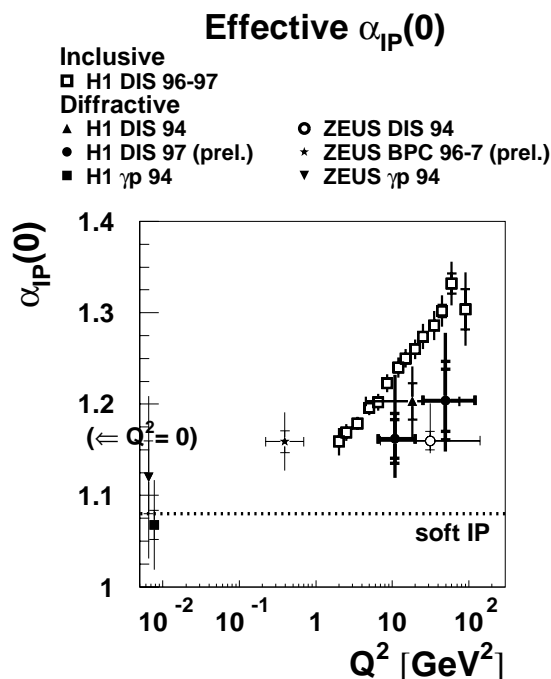


Figure 3.8: Q^2 dependence of the effective pomeron trajectory $\alpha_{\mathbb{P}}(0)$ for inclusive and diffractive ep processes. The squares correspond to $\alpha_{\mathbb{P}}(0) = 1 + \lambda$ extracted from a fit to inclusive data [63] of the form $F_2 = cx^{-\lambda(Q^2)}$ for $x < 0.01$.

where the diffractive structure function is suppressed by a factor of around 5 and low W (high $x_{\mathbb{P}}$) where the sub-leading exchanges contribute. This flatness is in contrast to the naive expectation of Regge Theory. The same dependence for diffractive and total cross sections on W was however predicted in the semi-classical model [79], which is described in section 3.4.4.

Assuming Regge factorisation the structure functions $F_2^{\mathbb{P}}(\beta, Q^2)$ and $F_2^{\mathbb{R}}(\beta, Q^2)$ describe the structure of the pomeron and meson exchanges respectively. This structure can be obtained from the data by assuming a parameterisation of the parton distributions of the pomeron and meson exchanges at a starting scale $Q_0^2 = 3 \text{ GeV}^2$, which evolve via the DGLAP [58] [59] evolution equations with increasing Q^2 .

The Q^2 dependence of $F_2^{D(3)}$ as measured from 1994-1995 low Q^2 data [80] is shown in figure 3.10(a). The low value of $x_{\mathbb{P}} (= 0.005)$ at which the measurement is performed implies that sub-leading contributions are negligible, hence the pomeron exchange dependence on Q^2 is directly visible. Figure 3.10(b) shows $x_{\mathbb{P}} F_2^{D(3)}(\beta, Q^2, x_{\mathbb{P}})$ as a function of Q^2 for the most recent H1 $F_2^{D(3)}$ measurement [78]. Rising scaling violations are visible which

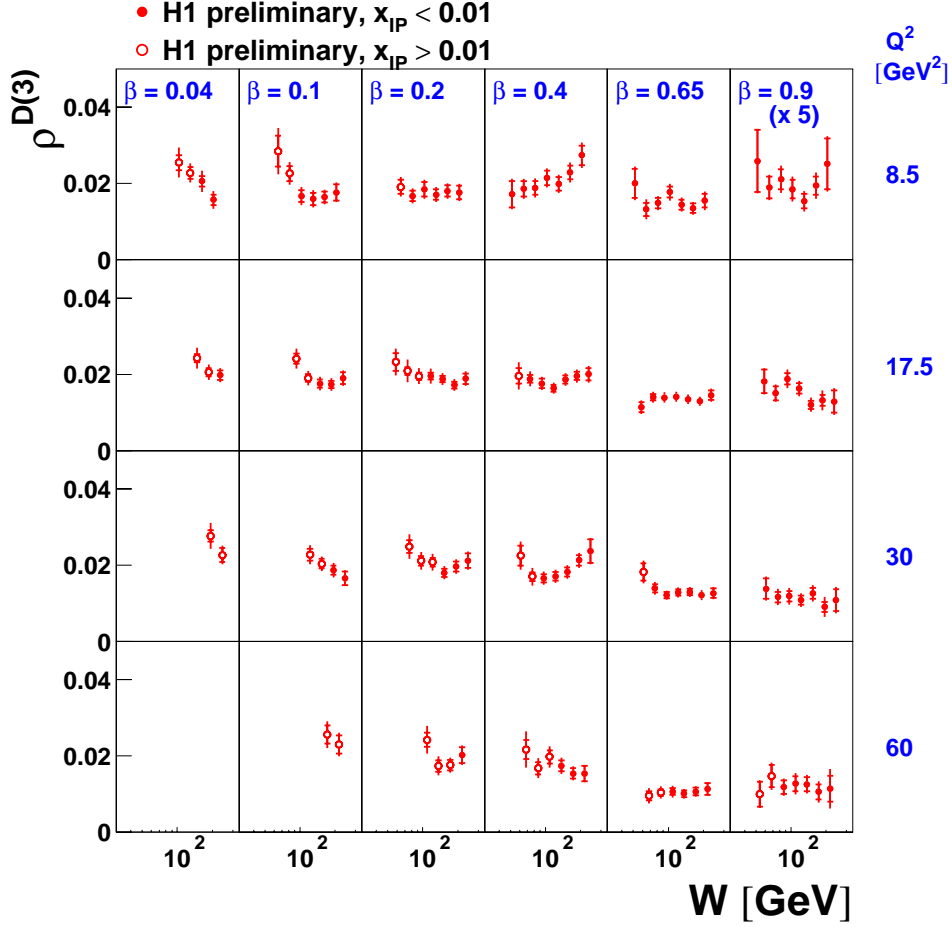


Figure 3.9: The ratio of the diffractive to the inclusive cross section, $\rho^{D(3)}$, shown as a function of W for fixed values of β and Q^2 .

persist to high β values. At fixed values of x_p the β dependence therefore evolves from high to low β as Q^2 increases which is expected for gluon radiation dominated DGLAP evolution. Hence, a large gluonic component exists even at high values of β . Figure 3.11 shows the beta dependence of $F_2^{D(3)}$ for H1 1997 data which is observed to be relatively flat with large contributions at high values of β .

Figure 3.12 shows the parton distributions which result from a QCD fit to the 1994 H1 data involving both light quarks and gluons with $Q_0^2 = 3.0 \text{ GeV}^2$, where $f(z)$ is the parton distribution function and z is the fraction of the momentum of the pomeron carried by the parton. It is observed that the momentum fraction carried by the gluon decreases with increasing Q^2 , from approximately 90% at $Q^2 = 4.5 \text{ GeV}^2$ to about 80% at $Q^2 = 75 \text{ GeV}^2$. Hence, boson-gluon fusion from the diffractive gluon density is the dominant mechanism

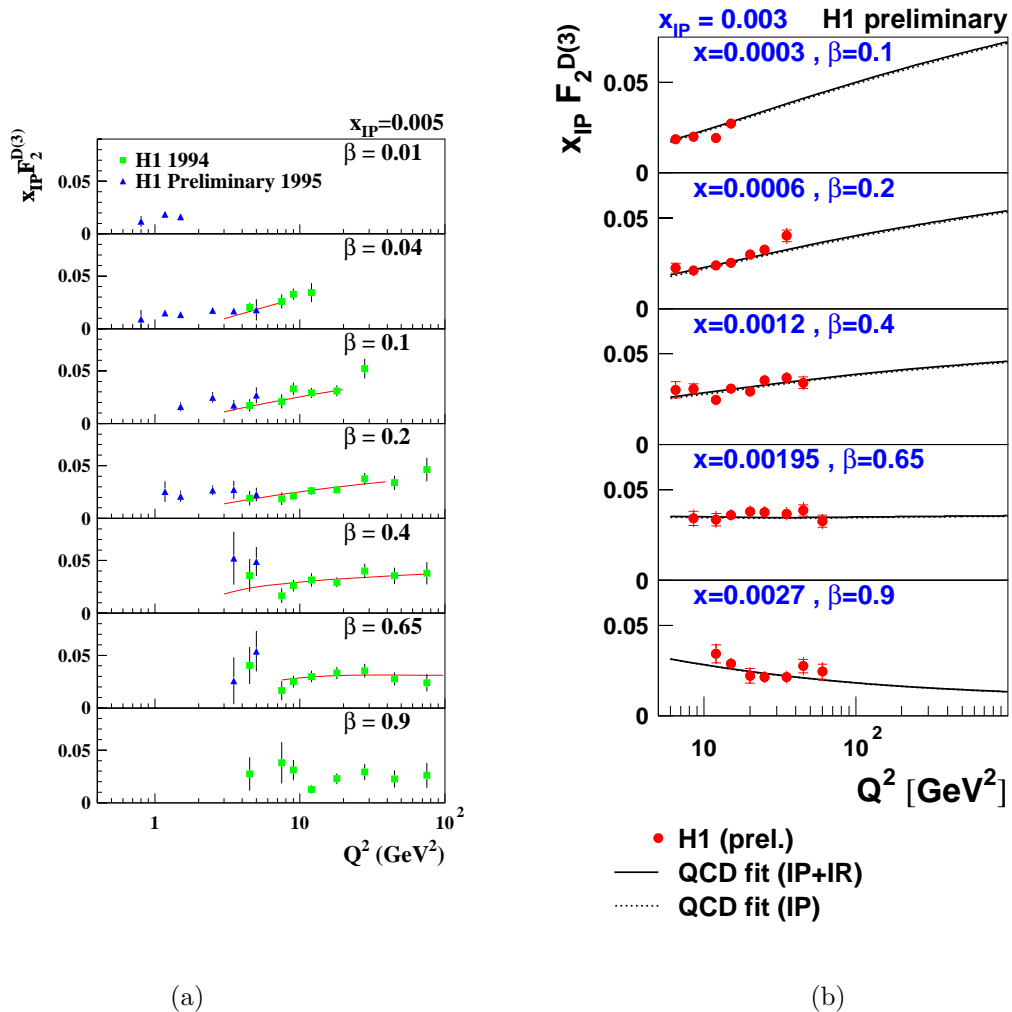


Figure 3.10: H1 measurement of $x_P F_2^{D(3)}(\beta, Q^2, x_P)$ as a function of Q^2 illustrating the presence of scaling violations for (a) H1 1994 and 1995 data and (b) H1 1997 data. The 1995 data on figure (a) were measured in a similar kinematic region to the analysis presented in this thesis. The results presented in (b) represent a measurement of superior precision in comparison.

in diffractive DIS, depicted in figure 3.13.

3.4.3 Two Gluon Exchange Models

Diffractive DIS can also be considered in terms of the elastic scattering of partonic fluctuations of the virtual photon. The simplest and dominant configurations occur when the

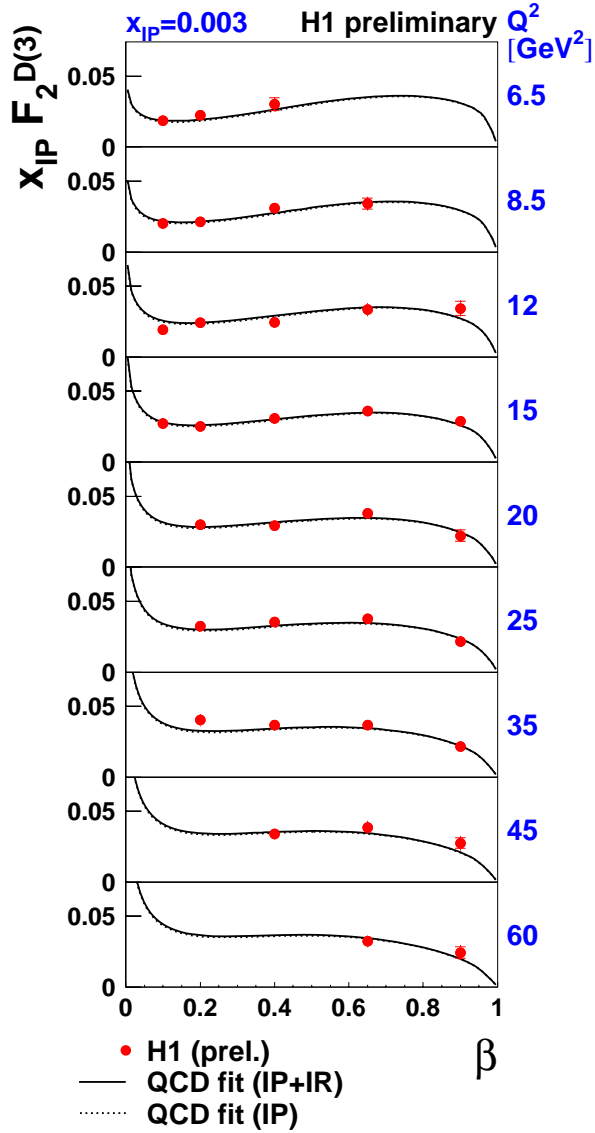


Figure 3.11: Measurement of $x_P F_2^{D(3)}(\beta, Q^2, x_P)$ at fixed $x_P = 0.003$ in bins of Q^2 as a function of β for H1 1997 data.

photon fluctuates into a $q\bar{q}$ pair, or with an additional gluon producing a $q\bar{q}g$ state. In both cases the fluctuations are usually treated as colour dipoles (triplet-antitriplet for the $q\bar{q}$ and octet-octet for the $q\bar{q}g$ case). Figures 3.14 (a) and (b) show these configurations in the proton rest frame on the left hand side compared with the infinite momentum frame depictions on the right hand side. It is possible to have other more complicated states, but these are believed to be less important and hence are neglected in the following discussion. A standard DIS event can then be considered as the interaction between the

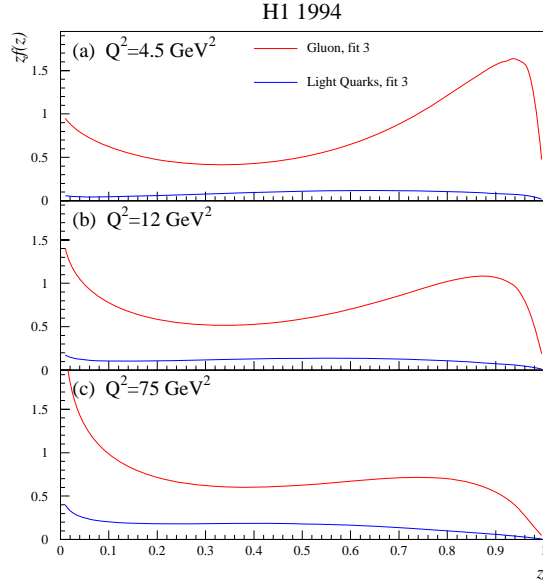


Figure 3.12: Pomeron parton distributions as a function of z in bins of Q^2 .

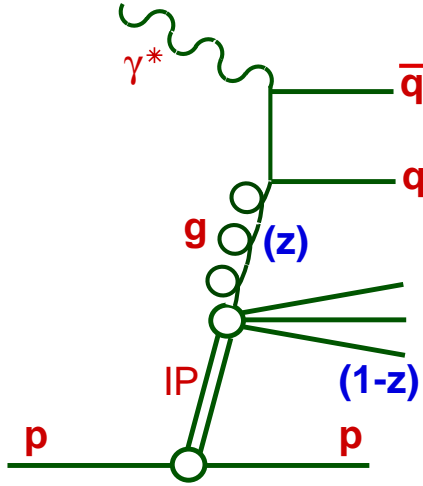


Figure 3.13: The dominant mechanism in diffractive DIS, Boson-Gluon Fusion.

proton and the $q\bar{q}$ dipole (or higher multiplicity). A diffractive process occurs when the dipole scatters elastically.

Viewed in the proton rest frame, the photon fluctuates into the partonic system a long time before the interaction with the proton occurs. The diffractive cross section for longitudinally (L) and transversely (T) polarised photons can be written as,

$$\sigma_{T,L}^{\gamma^*p} = \int dz d^2r |\phi_{\gamma}^{T,L}|^2 \hat{\sigma}^2(Q^2, r, z), \quad (3.32)$$

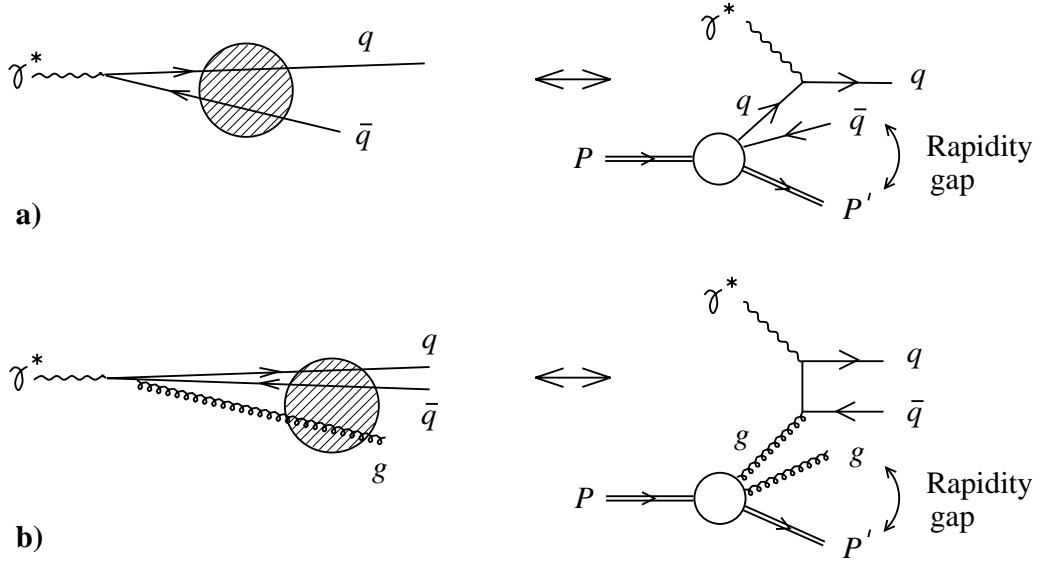


Figure 3.14: (a)The virtual photon fluctuates into a $q\bar{q}$ pair or (b) a $q\bar{q}g$ state. The left hand diagrams illustrate the processes in the proton rest frame, whilst the infinite momentum frame interpretation is shown on the right.

which is analogous to the inclusive photon cross section in equation 2.32. Equation 3.32 contains a $\hat{\sigma}^2$ term whereas the inclusive equation 2.32 contained a $\hat{\sigma}$ term. Hence, given that the dipole cross section $\hat{\sigma}$ is largest at large dipole sizes, this bigger contribution from large (soft) dipole sizes in diffraction may explain the different effective $\alpha_{\mathbb{P}}(0)$ observed compared with inclusive DIS (see figure 3.8). Colour dipole model approaches also offer an opportunity to study the longitudinal contribution to the diffractive structure function.

It can be seen in equation 2.32 that there is a factorisation into terms containing the effective dipole wave-function and the dipole cross section. In the model for $F_2^{D(3)}$ prescribed by Bartels, Ellis, Kowalski and Wüsthoff [81] longitudinally polarised photon contributions to $F_2^{D(3)}$ are dominated by fluctuations into $q\bar{q}$ pairs, whereas a transversely polarised photon can fluctuate into either a $q\bar{q}$ pair or a $q\bar{q}g$ state. The dependence of the various polarisation cross sections on β are summarised in equations 3.33 - 3.35 below,

$$\sigma_{T,q\bar{q}} \sim \beta(1 - \beta) \quad (3.33)$$

$$\sigma_{T,q\bar{q}g} \sim (1 - \beta)^\gamma \quad (3.34)$$

$$\sigma_{L,q\bar{q}} \sim \beta^3(1 - 2\beta)^2, \quad (3.35)$$

where γ is a free parameter and the longitudinal contribution represents a higher twist contribution and is suppressed by $1/Q^2$. The $q\bar{q}_L$ term dominates at high β , $q\bar{q}_T$ at medium

β and $q\bar{q}g_T$ at low β . The diffractive structure function $F_2^{D(3)}(\beta, Q^2, x_P)$ is shown as a function of β for fixed $x_P = 0.001$ in figure 3.15 with the separate distributions of the longitudinal and transverse components indicated.

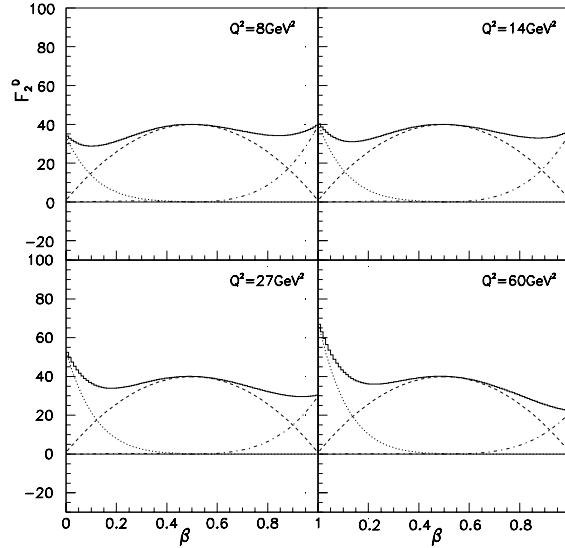


Figure 3.15: The diffractive structure function $F_2^{D(3)}$, parameterised by H1 using the BEKW model [81], as a function of β at fixed $x_P = 0.001$. The dotted line gives the $q\bar{q}g$ contribution, the dashed and dotted-dashed lines show the $q\bar{q}$ transverse and longitudinal components respectively, and the sum total is represented by the solid line.

Saturation in Diffractive DIS

The saturation model, introduced in section 2.2.7, was originally devised for inclusive proton measurements but can be extended to apply to diffractive physics [82]. In this case the dipole interacts with two gluons from the proton, which can be identified with the pomeron. The same dipole cross section parameterisation can be used to predict the diffractive cross section for $t = 0$, or an additional parameter, b , to describe the t -dependence (e^{bt}) can be introduced to describe the diffractive structure function data. Figure 3.16 shows the Q^2 dependence of $F_2^{D(3)}(\beta, Q^2, x_P)$ at low Q^2 [83]. The qualitative features of the data are described, although there are normalisation problems at the lowest values of Q^2 , and a clear transition is observed at $Q^2 \approx 1 \text{ GeV}^2$. Figures 3.17(a) and (b) show the β and Q^2 dependences at fixed $x_P = 0.003$ of $x_P F_2^{D(3)}(\beta, Q^2, x_P)$ (as in figures 3.11 and 3.10(b)) compared with predictions from the saturation model of Golec-Biernat and Wüsthoff [68] [78]. A good description of the data is observed, except for small values of β and Q^2 .

ZEUS 1995-1997 PRELIMINARY

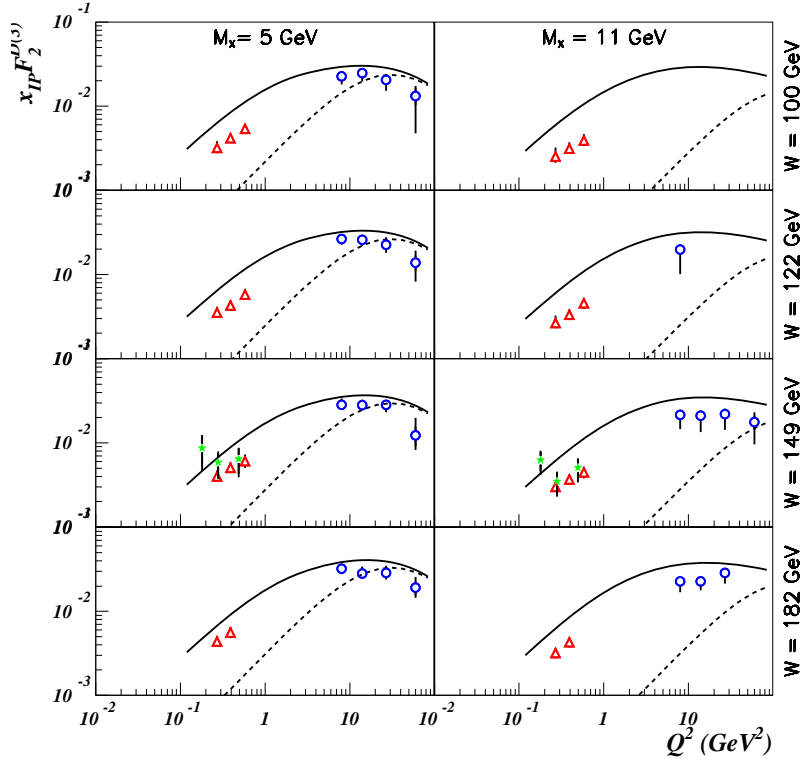


Figure 3.16: Q^2 dependence of $F_2^{D(3)}$ showing the transition at low Q^2 . The triangles are from a ZEUS analysis [83], the stars are Leading Proton Spectrometer data from the same publication and the circles are from a higher Q^2 analysis [84]. The dashed and solid curves show the saturation model predictions with $q\bar{q}$ and combined $q\bar{q}$ and $q\bar{q}g$ terms respectively.

3.4.4 Soft Colour Models

Edin, Ingelman and Rathsman formulated an alternative model for diffraction [86] which describes the diffractive process in terms of *Soft Colour Interactions (SCIs)*. The initial assumption is that diffractive and non-diffractive reactions are identical in the hard subprocess, and it is the rearrangement of colour in the fragmentation process that gives rise to either inclusive or diffractive DIS events. Figure 3.18 depicts the deep-inelastic scattering process. Soft interactions occur between pairs of outgoing partons with colour exchange, but no momentum exchange. Figure 3.18(a) illustrates a standard Boson-Gluon Fusion (BGF) DIS interaction in which all the final state particles are connected by colour strings, and figures (b) and (c) show possible situations where there is a large rapidity gap in the final state, which is diffractive in nature.

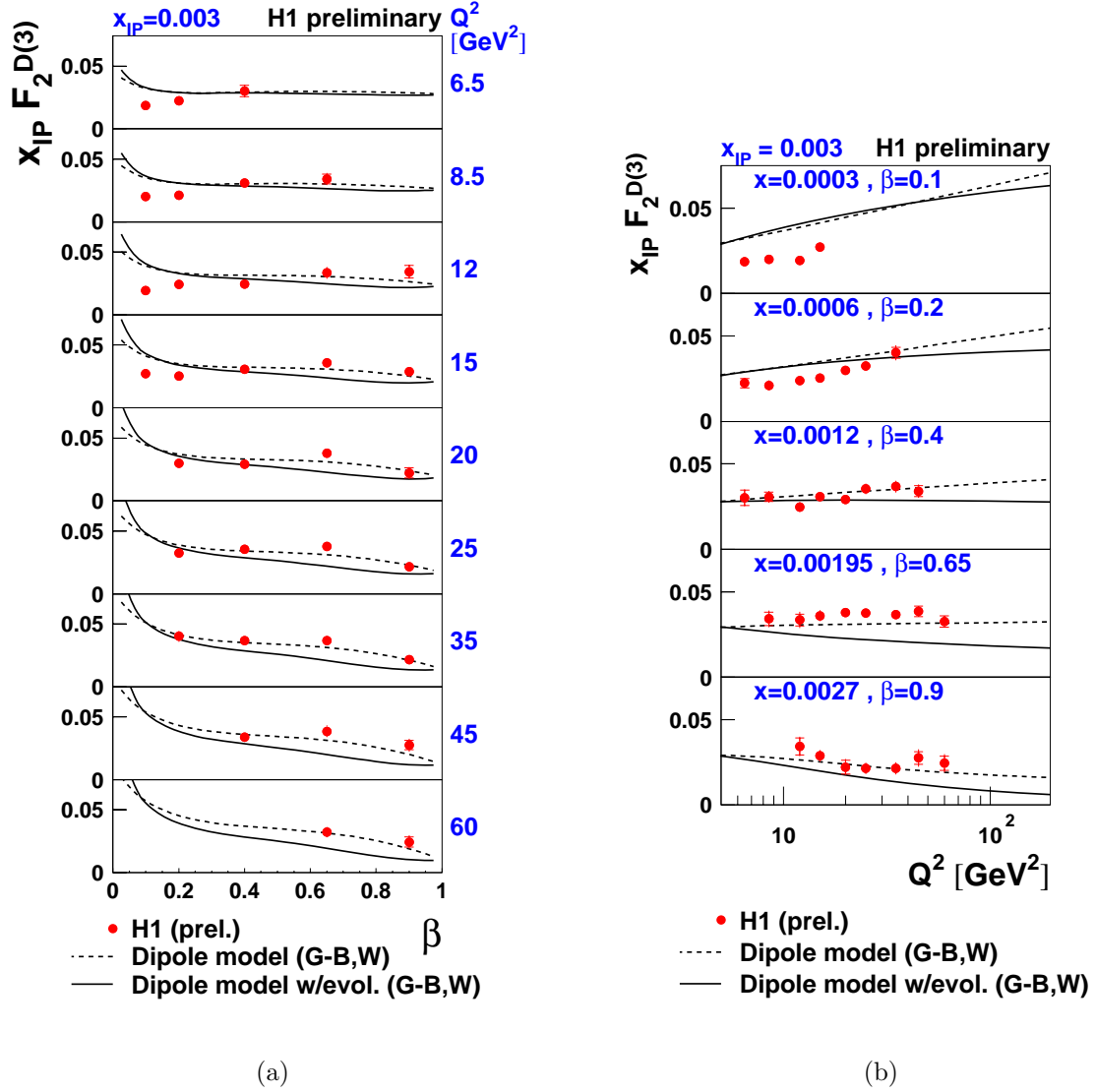


Figure 3.17: Measurement of $x_p F_2^{D(3)}(\beta, Q^2, x_p)$ as a function of (a) β and (b) Q^2 for H1 1997 data (red points) [78]. The curves represent two versions of the colour dipole model of [68] [82] (dashed) and an alternative model with QCD evolution taken from [85] (solid).

Semi-Classical Model

Similar to the SCI model, Buchmüller, Gehrman and Hebecker [87] postulated the *semi-classical model*. Viewed in the proton rest frame, the virtual photon fluctuates into either $q\bar{q}$ or $q\bar{q}g$ states which then scatter off the *soft colour fields* of the proton. This is an example of another colour dipole model, but the dipole cross section is modelled non-

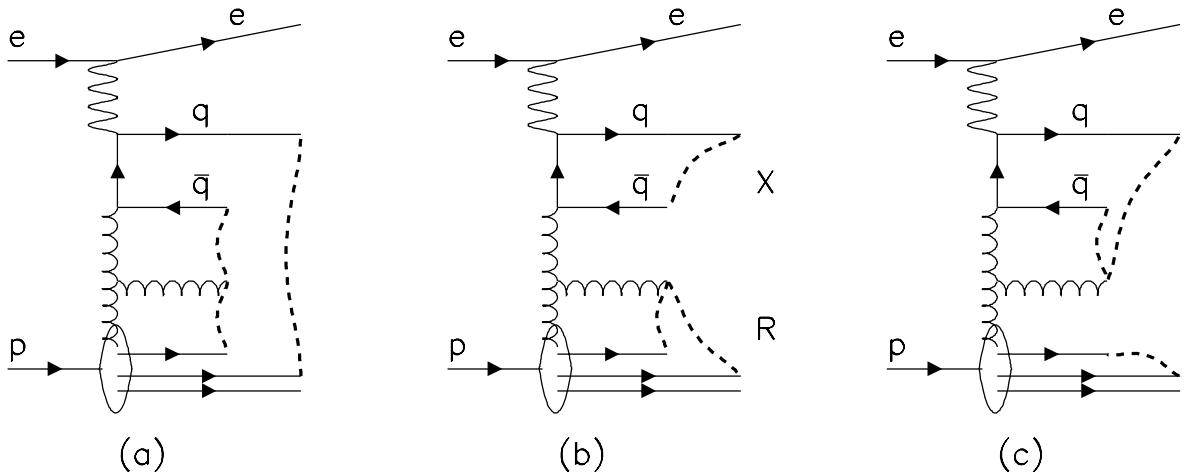


Figure 3.18: Soft colour interactions in diffractive scattering. (a) shows the colour strings (dashed lines) which exist between the final state particles, (b) and (c) illustrate how the rapidity gaps characteristic of diffractive interactions can be formed in the final state.

perturbatively in this case. The $q\bar{q}$ and $q\bar{q}g$ states undergo colour rotations as they pass through the soft colour field of the proton with a finite chance that the particle will emerge as a colour singlet state (that is be diffractive in nature). Figures 3.19(a) and (b) show $x_p F_2^{D(3)}(\beta, Q^2, x_p)$ for the H1 1997 data [78] as a function of β and Q^2 respectively for fixed $x_p = 0.003$. The general features of the data are reproduced by the model although not at small β and Q^2 .

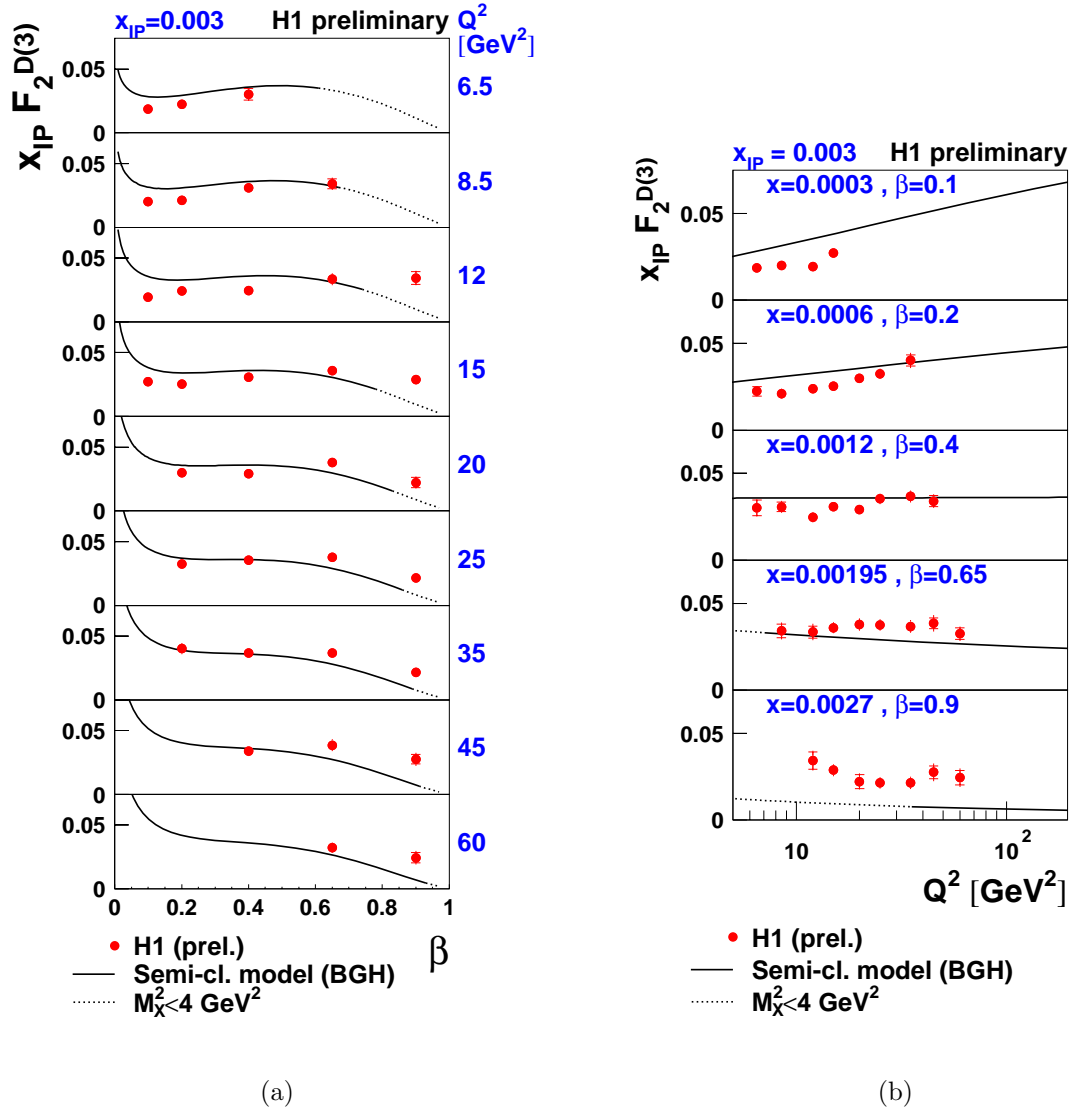


Figure 3.19: Measurement of $x_p F_2^{D(3)}(\beta, Q^2, x_p)$ as a function of (a) β and (b) Q^2 for H1 1997 data (red points) [78]. The data are compared with semi-classical model predictions [87] (solid curves). An extension to the model for $M_X^2 < 4 \text{ GeV}^2$, where the model is not expected to be valid, is represented by the dotted curves.

Chapter 4

Event Selection

4.1 Introduction

This chapter details the methods used in the selection of diffractive deep-inelastic scattering events which are used in the measurement of the structure function $F_2^{D(3)}(\beta, Q^2, x_p)$ presented in chapter 5. Firstly an introduction to the Monte Carlo models used in the structure function extraction are outlined in section 4.2. Then the event selection procedure is presented in sections 4.3 and 4.4, along with the reconstruction methods used in section 4.5. After this the specific requirements relating to the selection of standard and diffractive deep-inelastic scattering events are discussed in sections 4.6 and 4.7 respectively. The final diffractive DIS selection is summarised in section 4.8.

4.2 Monte Carlo Models

The extraction of the diffractive structure function can only proceed once the necessary tools are in place to correct the data for experimental bias. Monte Carlo generators are used to model the physics process being studied and to predict the kinematic dependence of events according to theoretical expectations. The detector simulation stage, and reconstruction using the same tools as for the data, provides the modelling of experimental resolutions, efficiencies and acceptances. In order to describe all aspects of the data, a combination of several different Monte Carlo models may be needed to match the actual physical processes including backgrounds. The inclusive and diffractive components of deep inelastic scattering are modelled separately by the DJANGO [88] and RAPGAP [89] Monte Carlo generators respectively. DJANGO describes the inclusive positron-proton

DIS interaction $ep \rightarrow eX$. An interface to HERACLES [90] provides the $\mathcal{O}(\alpha_{\text{em}})$ QED radiative corrections, whilst those for QCD are simulated, through the parton shower approach [91], using LEPTO [92]. The fragmentation and hadronisation of quarks is simulated in JETSET [93] using the Lund String Model. RAPGAP, which also provides a full $ep \rightarrow eXY$ description, models diffraction according to the Saturation Model prescription described in sections 2.2.7 and 3.4.3. Hence, inclusive DIS events, described using DJANGO for $x_{\mathcal{P}} > 0.1$ or $M_Y > 5$ GeV, and diffractive events, modelled using RAPGAP for $x_{\mathcal{P}} < 0.1$, are combined to provide a complete Monte Carlo description over the full range of phase space.

Although RAPGAP and DJANGO alone are able to provide a reasonable description of the data there are also background effects which must be considered. The background at low Q^2 , arising from hadrons produced in photoproduction being misidentified as electrons, is described by PHOJET [94]: a Monte Carlo able to describe both elastic and inelastic processes to fully model high energy photon-proton interactions. Although no single *exclusive* particles are explicitly selected from the hadronic final state in this analysis, the presence of vector mesons is still observable in the data. Hence, the DIFFVM [95] Monte Carlo generator is used to model these channels, where the vector mesons ($\rho, \omega, \phi, J/\psi$) are simulated in the framework of Regge phenomenology and the Vector Meson Dominance Model [96]. As described in section 4.7.5 a separate sample of this Monte Carlo is also used for $M_Y < 5$ GeV. This is needed for the correction applied to account for background arising from diffractive dissociation of the proton, due to the fact that RAPGAP does not model such events well. For this study the J/ψ is chosen for the simulation, it is assumed that the proton and photon vertices can be factorised, and the hadronisation is again modelled in JETSET.

Events of the type $ep \rightarrow e\gamma X$ can also enter the selected data sample and hence must also be modelled by Monte Carlo. The important contributions are *QED-Compton scattering* and *Initial State Radiation (ISR)*. In the QED-Compton scattering reactions, both the positron and photon are observed in the detector but the final state system X escapes undetected down the beam-pipe. The COMPTON [97] Monte Carlo generator is used to model events of this kind. In ISR events, the photon is not detected in the main detector but the positron and X -system are detected. Corrections calculated from RAPGAP interfaced to HERACLES for ISR, *Final State Radiation (FSR)* and QED virtual e^+e^- loop events are applied to the measurement of $F_2^{D(3)}$ so that it is quoted at the QED-Born level. The application of these corrections is described in the next chapter in section 5.2.4.

After the generation stage, Monte Carlo events are subjected to a full simulation of the

detector response in order that they can be compared with the data. The response of the generated particles to the H1 detector is modelled including the geometrical acceptance of the detectors and allowing for dead or inefficient detector regions. This is done using the H1SIM [98] program package which is based on the software of GEANT [99].

4.3 Event Selection

When events are selected for a physics analysis the aim is to reject as much background contamination as possible whilst retaining the channel of interest with high efficiency. At low Q^2 the cross section for DIS is very high. Hence, these relatively soft processes are usually down-scaled at level four of the triggering process so that the data-taking rate is not too high. This down-scaling is not applied during minimum bias running periods and therefore a detailed study of the low Q^2 region can be performed on data taken at such times.

The level one trigger elements (see section 1.8) used in this analysis are the *inclusive electron trigger* (IET) of the Spacal, the *z-vertex trigger* and the *forward ray trigger*. These were combined with further L2 and L4 conditions to form three sub-triggers which were used together to select events from the minimum bias running period at the end of 1999. The requirements at each trigger level are presented below.

4.3.1 Level 1 Trigger Conditions

The IET Spacal trigger is used in the triggering of low Q^2 DIS events. It makes a decision based purely on the presence of an electromagnetic cluster in the Spacal. Combinations of 4×4 cells are taken together in order to contain as much of the shower as possible, and overlapping groups are considered to avoid inefficiencies. These are compared with three preset thresholds which yield three trigger elements. The trigger elements are further divided into inner and outer Spacal regions with the inner region corresponding to the region $-16 < x < 8$ cm and $-8 < y < 16$ cm. Table 4.1 summarises the energy thresholds for each trigger element as they were programmed for the 1999 minimum bias period.

The *z-vertex trigger*, as mentioned in section 1.3.1, comprises the CIZ, COZ and the first layer of the FPC. 16 segments in ϕ are defined for the trigger and if coincident hits in the $r - z$ plane are observed in the detectors then a *ray* is defined. A *z-vertex histogram* is constructed, with 16 bins of width 5.4 cm each, which contains all possible

Trigger Element (Inner Region)	Trigger Element (Outer Region)	Energy Threshold
SPCLe_IET_cen1	SPCLe_IET>0	2 GeV
SPCLe_IET_cen2	SPCLe_IET>1	5 GeV
SPCLe_IET_cen3	SPCLe_IET>2	10 GeV

Table 4.1: Spacal IET trigger element definitions for the 1999 minimum bias running period.

rays extrapolated to $r = 0$. The bin with the most entries above the background from random coincidences is identifiable as that of the interaction vertex. The `zVtx_T0` trigger element is used in this analysis and it demands that at least one ray is present. This trigger level requirement of a reconstructed vertex is successful in rejecting most of the non- $e - p$ induced background. The `zVtx_mul<7` requirement, which demands less than 200 entries in the z -vertex histogram, is also used to veto background events which have many tracks in the detector. The CIP and FPC form the forward ray trigger and are used to detect rays in the forward direction originating from the nominal vertex position. Hits are required to be observed in all but one of the detector chambers. Again there are 16 ϕ sectors and the `Fwd_Ray_T0` condition accepts tracks of any multiplicity in any ϕ sector.

4.3.2 Sub-triggers for the 1999 Minimum Bias Run

Table 4.2 summarises the L1 trigger element combinations for the three sub-triggers used in this analysis: s0, s3 and s9. s0 is the principal trigger for low Q^2 DIS events. The L2 topological trigger requirements on the radial distance of the centre of the positron cluster in the Spacal from the beam-pipe (R_{SPACAL}) are also shown in table 4.2. The absence of a restriction on R_{SPACAL} for s3 allows very low Q^2 events to be detected. In s9 the lower energy threshold imposed in the `SPCLe_IET_cen1(IET>0)` condition allows high y events to be accessed. The L4 requirements are also shown for each sub-trigger, where r_{CLUS} represents the transverse size of the electromagnetic cluster observed in the Spacal and E'_e is the energy of the scattered positron measured in the Spacal.

The sub-triggers s0, s3 and s9 also include other trigger elements which are used for timing and background rejection purposes. These are assumed to be 100% efficient and are not included here for clarity. A combination of s0, s3 and s9 was used in the selection of data and Monte Carlo events. The efficiencies of s0, s3 and s9 are shown for data in figure 4.1 as a function of scattered positron energy E'_e . The data sample was selected for $E'_e > 5$ GeV hence the lowest energy threshold of table 4.1 for s9 is not visible. Due to prescaling (discussed in section 4.3.3), s9 triggered the most infrequently leading to the

Sub-trigger	L1	L2	L4
s0	SPCLe_IET>1 or SPCLe_IET_cen2	$R_{SPACAL} > 10$ cm	$r_{CLUS} < 4$ cm $Q^2 > 0.5$ GeV ² $E'_e > 4$ GeV
s3	SPCLe_IET>2 or SPCLe_IET_cen3	No requirement	$r_{CLUS} < 4$ cm $Q^2 > 0.5$ GeV ² $E'_e > 4$ GeV
s9	SPCLe_IET>0 or SPCLe_IET_cen1 and zVtx_mul<7 and (zVtx_T0 or FwdRay_T0)	$R_{SPACAL} > 16$ cm	$r_{CLUS} < 5$ cm $R_{SPACAL} > 15$ cm $E'_e > 2$ GeV

Table 4.2: L1, L2 and L4 conditions for the s0, s3 and s9 sub-triggers during the minimum bias 1999 running period.

greater statistical fluctuations seen in figure 4.1. The combination of the three trigger elements is consistent with being 100% efficient above the final measurement cut of $E'_e = 6$ GeV.

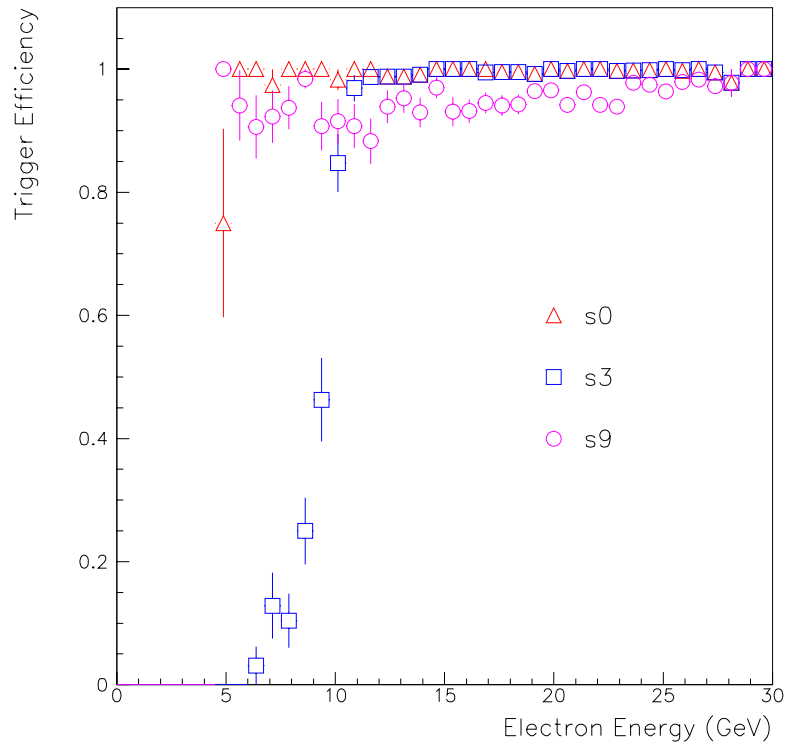


Figure 4.1: Efficiencies for the three sub-triggers used in the 1999 minimum bias analysis: s0 (red triangles), s3 (blue squares) and s9 (purple circles), shown as a function of scattered positron energy E'_e .

4.3.3 Trigger Phases and Prescale Factors

There are four phases of triggering corresponding to the different stages of a luminosity fill. Phase 1 is initiated when luminosity is declared and typically only the calorimeters are switched on at this stage, with phase 2 not being attained until all of the tracking detectors can be made operational. There are prescale factors associated with each phase of triggering which typically decrease with increasing phase. Revised appropriate prescale factors are calculated regularly and their values determine when phases 3 and 4 begin. Due to the fact that some detectors are not operational, and high prescale factors are applied, data recorded during phase 1 are not used in this analysis. Events from all higher phases are accepted. During data runs there are sometimes periods when an important detector is not available, for example due to trips in tracking detectors or readout crashes. Hence, runs are classified according to which major and minor systems are operational. Good and medium quality runs are selected for analysis and poor runs are rejected in which both CJC1, CJC2 and the CST are not functional, or if the LAr or Spacal calorimeters or the luminosity system are out of operation.

4.4 Preliminary Data Selection

After the data has been collected according to the criteria described previously, cuts are applied to specific variables to provide a data sample which is then recorded in files for personal analysis. For present purposes an inclusive deep-inelastic scattering selection is first performed, followed by a diffractive selection. The inclusive selection demands three Spacal conditions: the positron energy E'_e must be in the range 5 to 32 GeV, the electromagnetic cluster radius r_{CLUS} must be ≤ 5 cm and the polar angle of the scattered positron θ_e must be $> 150^\circ$. The diffractive condition states that if the most forward energy deposit in the LAr calorimeter has a pseudorapidity $\eta_{MAX} \leq 3.3$, and the number of reconstructed pairs of hits in the two layers of the FMD nearest to the interaction region ($N_{FMD(1,2)}$) is < 2 and the number of pairs in the third layer $N_{FMD(3)}$ is < 3 , then all events are saved. Otherwise a down-scaling factor of 10 is applied, a correction for which is applied in the measurement extraction. Together these conditions select a sample of low Q^2 DIS events with a down-scaling of non-diffractive events to reduce the sample size. The luminosity of the final data sample selected for the measurement of $F_2^{D(3)}(\beta, Q^2, x_P)$ for the 1999 minimum bias running period is 3.74 pb^{-1} . This corresponds to a total of 382 runs, taken from 31 HERA luminosity fills.

4.5 Reconstruction methods

The H1 detector was designed for the detection and measurement of both the positron and the hadronic final state. Therefore, there are several methods via which the reconstruction of the kinematic variables x , y and Q^2 (the relationship between which was given in equation 2.13) can be performed. Hence, the kinematic variables are *over-constrained*. The reconstruction methods relevant to the analysis presented in this thesis are described in sections 4.5.1 - 4.5.4.

4.5.1 Electron Method

As its name suggests the Electron Method uses only variables from the incident and scattered leptons and is the simplest reconstruction method. However, it is highly sensitive to the case where the incident positron emits initial state QED radiation, as described at the end of section 4.2. At high y , the Electron Method gives very good resolution, but this degrades as y decreases. The kinematic variables as given by the Electron Method are summarised in equations 4.1 - 4.3:

$$y_e = 1 - \frac{E'_e}{E_e} \sin^2 \frac{\theta_e}{2}, \quad (4.1)$$

$$Q_e^2 = 4E_e E'_e \cos^2 \frac{\theta_e}{2}, \quad (4.2)$$

$$x_e = \frac{Q_e^2}{s y_e}. \quad (4.3)$$

4.5.2 Hadron Method

In contrast to the Electron Method, the Hadron Method uses only variables from the hadronic final state in the reconstruction of the kinematic variables. This method is therefore completely independent of the Electron Method and demonstrates the fact that the reconstruction at H1 is over-constrained. Equations 4.4 - 4.6 detail the reconstruction of y , Q^2 and x in this case:

$$y_h = \frac{E_h - p_{z,h}}{2E_e}, \quad (4.4)$$

$$Q_h^2 = \frac{\sqrt{(p_{x,h}^2 + p_{y,h}^2)}}{1 - y_h}, \quad (4.5)$$

$$x_h = \frac{Q_h^2}{s y_h}, \quad (4.6)$$

where E_h , $p_{T,h} = \sqrt{p_{x,h}^2 + p_{y,h}^2}$ and $p_{z,h}$ are the 4-vector components of the reconstructed hadrons, as defined in equation 2.7 in section 2.2.1.

4.5.3 Double Angle Method

As the formulae in equations 4.7 - 4.10 indicate, the Double Angle Method does not rely on any energy measurements - just those of the positron and hadronic angles. The resolution at low values of y is therefore good. This is a useful reconstruction method for detectors with poor calorimetry systems. The angle of the final state hadrons γ can be defined as,

$$\cos \gamma = \frac{p_{x,h}^2 + p_{y,h}^2 - (E_h - p_{z,h})^2}{p_{x,h}^2 + p_{y,h}^2 + (E_h - p_{z,h})^2}, \quad (4.7)$$

from which the following kinematic variables can be obtained:

$$y_{DA} = \frac{\sin \gamma (1 + \cos \theta_e)}{\sin \gamma + \sin \theta_e + \sin(\theta_e + \gamma)}, \quad (4.8)$$

$$Q_{DA}^2 = \frac{4E_e^2}{\tan(\frac{\theta_e}{2})(\tan(\frac{\theta_e}{2}) + \tan(\frac{\gamma}{2}))}, \quad (4.9)$$

$$x_{DA} = \frac{Q_{DA}^2}{s y_{DA}}. \quad (4.10)$$

4.5.4 Electron-Double Angle Method

In [69] the Electron and Double Angle Reconstruction Methods were combined to obtain the benefit of their superior resolutions at high and low y respectively. This is the main reconstruction method adopted in this analysis, and equations 4.11 - 4.13, which represent an empirical reconstruction method optimised for the H1 detector kinematic coverage, provide the details:

$$y_{eDA} = y_e^2 + y_{DA}(1 - y_{DA}), \quad (4.11)$$

$$Q_{eDA}^2 = \frac{4E_e^2(1 - y_{eDA})}{\tan(\frac{\theta_e}{2})^2}, \quad (4.12)$$

$$x_{eDA} = \frac{Q_{eDA}^2}{s y_{eDA}}. \quad (4.13)$$

4.5.5 Resolutions in x and Q^2

For the measurement of both $F_2(x, Q^2)$ and $F_2^{D(3)}(\beta, Q^2, x_F)$, the size chosen for each x and Q^2 bin must be larger than the detector resolution in order for sensible results to be extracted. The quality of the reconstruction can be determined using Monte Carlo samples from the function δ of any variable v which is defined as,

$$\delta(v) = \frac{v(g) - v(r)}{v(g)}, \quad (4.14)$$

where g and r represent the generator and reconstructed level variables respectively. Figures 4.2(a) and (b) show $\delta(x)$ and $\delta(Q^2)$ respectively together with the values of the resolution (the root-mean squared of the Gaussian fit to the data) and bias (mean position). Both distributions are observed to have small resolutions and biases for the chosen reconstruction method, the Electron-Double Angle method defined in section 4.5.4, with the Q^2 distribution having a smaller resolution and bias than the x distribution.

4.6 DIS Event Selection

After the preliminary event selection described in section 4.4 was performed, further selections were then applied to ensure a pure sample was available for analysis. Hence, tighter cuts were applied at this stage to improve the selection as outlined below:

Spacal Cuts:

- $E'_e > 6$ GeV:

The scattered positron energy cut is chosen to select electromagnetic clusters in a region of the Spacal with high trigger efficiency. A lower cut would lead to an

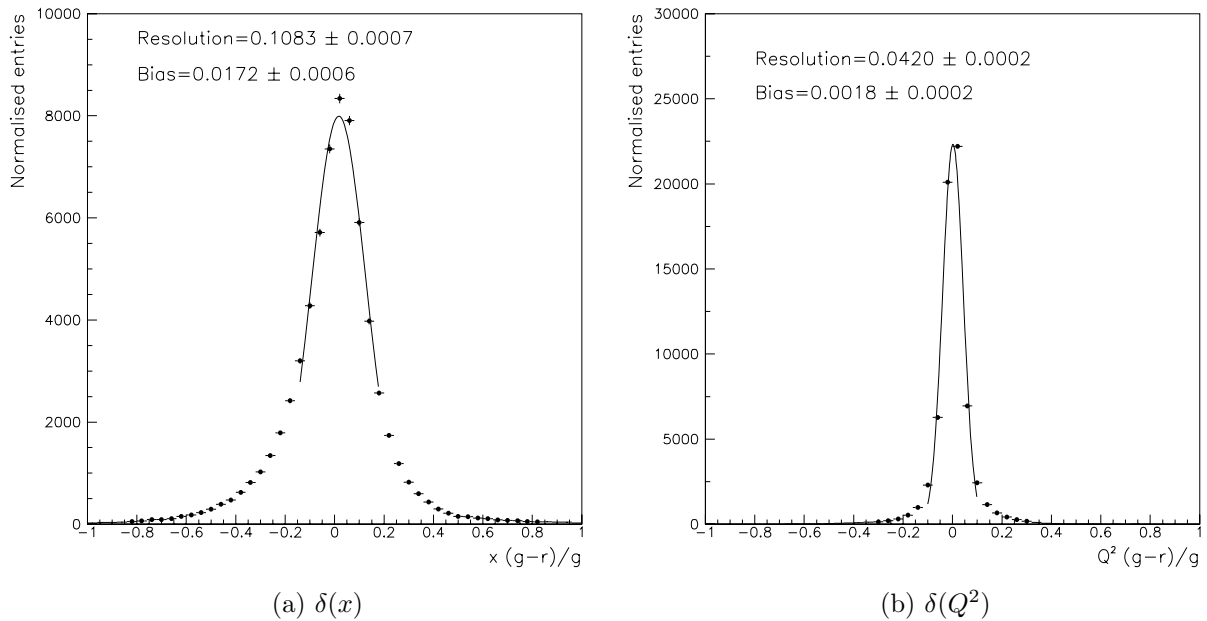


Figure 4.2: The quality of the kinematic reconstruction illustrated by the function δ defined in equation 4.14, for x (a) and Q^2 (b), using the Electron-Double Angle reconstruction method.

increased photoproduction background arising from misidentified hadrons in the Spacal.

- $r_{CLUS} < 4$ cm:

Requiring the cluster size observed in the Spacal to be small reduces the chance of contamination from hadronic showers. Typically, hadronic candidates have a much larger transverse size than those arising from electromagnetic showers.

- $153^\circ < \theta_e < 176.5^\circ$:

The polar angle of the scattered positron is required to be within the angular acceptance of the Spacal and BDC for all interaction vertices. θ_e is reconstructed from the BDC instead of the Spacal because of the superior resolution in polar angle measurement, as described in section 1.3.3.

- $E_{VETO} < 1$ GeV:

The veto layer of the Spacal is positioned adjacent to the beam-pipe. It is therefore sensitive to leakage from the Spacal which is required to be small in order to achieve precise energy measurement. Hence, the total energy observed in the veto detector is required to be low.

- $E_{HADR} < 0.5$ GeV:

The electromagnetic Spacal should fully contain the incident positron showers since it is many radiation lengths deep (see section 1.4.2). Therefore, energy deposits observed in the hadronic part of the Spacal, behind an observed electromagnetic cluster, indicate the possibility of a hadron faking a positron signal. The variable E_{HADR} represents the total energy that is detected within a cone behind the electromagnetic cluster. This cone is defined with respect to the direction of the positron candidate and has an opening angle of 4° .

- $11 \text{ cm} < R_{SPACAL} < 67 \text{ cm}$:

R_{SPACAL} is the radial distance of the cluster from the beam-pipe, calculated as $\sqrt{x_{SPACAL}^2 + y_{SPACAL}^2}$. The low R_{SPACAL} region corresponds to low Q^2 events. Hence, the inner cut is required to be as low as possible in order not to reject large numbers of events. This innermost region however corresponds to a region of very high background rates. The higher limit corresponds to the outer limit of the BDC detector.

- $0 \text{ cm} < \text{BDC-SPACAL} < 3 \text{ cm}$:

This cut acts on the distance between the centres of a cluster observed in the Spacal and the extrapolation of the BDC track into the Spacal $r - z$ plane. It therefore reduces contamination from neutral particle background events where photons, produced from pion decays ($\pi^0 \rightarrow \gamma\gamma$), deposit energy in the Spacal but leave no charged track signature in the BDC.

- Fiducial cuts:

The Spacal cell efficiencies determined from the data vary due to dead or inefficient cells, inefficient trigger channels and varying high voltage conditions. Therefore, inefficient regions are rejected in order that the sample is based on a high quality positron selection with high efficiency. The regions of the Spacal from which events were rejected from the sample are [100]:

- $-12.5 \text{ cm} < x < 8.5 \text{ cm}$ and $-4.5 \text{ cm} < y < 4.5 \text{ cm}$
- $-12.5 \text{ cm} < x < -8.4 \text{ cm}$ and $-8.5 \text{ cm} < y < -4.0 \text{ cm}$
- $-53.0 \text{ cm} < x < -40.0 \text{ cm}$ and $-24.5 \text{ cm} < y < -20.0 \text{ cm}$
- $-57.0 \text{ cm} < x < -44.0 \text{ cm}$ and $-29.0 \text{ cm} < y < -24.0 \text{ cm}$
- $-8.5 \text{ cm} < x < -4.0 \text{ cm}$ and $-12.5 \text{ cm} < y < -8.0 \text{ cm}$
- $8.0 \text{ cm} < x < 12.5 \text{ cm}$ and $-4.5 \text{ cm} < y < 4.5 \text{ cm}$
- $-8.5 \text{ cm} < x < -4.0 \text{ cm}$ and $-8.5 \text{ cm} < y < 4.0 \text{ cm}$

- $0.0 \text{ cm} < x < 4.5 \text{ cm}$ and $4.0 \text{ cm} < y < 12.0 \text{ cm}$

In addition to the above cuts, the region $-8.5 \text{ cm} < x < 8.5 \text{ cm}$ and $-8.5 \text{ cm} < y < 8.5 \text{ cm}$ was also rejected for $E'_e > 10 \text{ GeV}$ because this is a region of low efficiency for the SPCLe_IET>2 trigger element. As described in section 4.6.2, additional cells were also excluded as part of the Spacal calibration procedure.

Overall Final State Cuts:

- $E - p_z > 35 \text{ GeV}$:

For a perfectly measured event the total $E - p_z$ of the positron and hadronic final state is expected to be $2E_e \approx 55 \text{ GeV}$ from energy and momentum conservation arguments¹. Due to detector efficiency effects the actual values observed are distributed around this value. In photoproduction a fake positron signal can be observed in the Spacal from a final state hadron. The $E - p_z$ in this case will be much lower due to the undetected positron. Hence, such a cut dramatically reduces this background. This cut also reduces initial state QED radiation (ISR) corrections which originate when the positron emits a photon, which escapes down the beam-pipe in the backward direction, before the interaction with the proton.

Vertex and Track Cuts:

- $-30 \text{ cm} < z_{VTX} < 30 \text{ cm}$:

The vertex position is nominally at $z = 0 \text{ cm}$ and has an approximately Gaussian distribution of width $\sim 10 \text{ cm}$. Such a cut reduces the background arising from interactions of one of the beams with residual gas in the beam-pipe or off-momentum beam particles interacting with the beam-pipe walls. These are respectively called *beam-gas* and *beam-wall* interactions.

- Vertex Type:

Vertices calculated from tracks in both the central and the forward tracking detectors were selected. Vertex efficiency studies (presented in section 4.6.1) in this analysis showed that requiring forward vertices in addition to central vertices led to an improved efficiency at low y .

¹Note: $E + p_z$ is expected to show a peak at $2E_p \approx 1840 \text{ GeV}$. However, the outgoing proton or its remnants carry large $E + p_z$ and are not detected. By contrast these losses have negligible effect on $E - p_z$.

- $N_{TRACKS} + N_{LAR} + N_{SPACAL} > 1$:

At least two hadronic objects are required to be observed in the detector. This cut helps reduce the QED Compton background present in the sample.

Kinematic Cuts:

- $y_{eDA} > 0.05$:

The low y region of phase space has to be excluded because of the low vertex and trigger efficiencies observed in that region, which are poorly described in the simulation.

- $Q_{eDA}^2 > 1.25 \text{ GeV}^2$:

The limiting value of Q^2 is chosen to be as low as possible whilst remaining in a region of high acceptance in the Spacal for most values of y .

4.6.1 Vertex Efficiency

The vertex efficiency is defined as the probability of detecting an event that passes the standard DIS selection described above, except for the cuts on z_{vtx} and vertex type, with a vertex in either the central or forward tracking detectors. Figure 4.3 shows the vertex efficiency for data which is represented by the red points and Monte Carlo (DJANGO and PHOJET), the blue points, as a function of y_{eDA} ². Agreement within a few percent between data and Monte Carlo is observed and a high efficiency is observed at high values of y . The efficiency at low y is improved when both central and forward vertices are included, as shown here, compared with just using central vertices. The efficiency is observed to steadily decrease as y decreases. No correction was made for this in the analysis but the y_{eDA} cut presented in section 4.6 above was chosen to ensure that events with very low vertex efficiencies were excluded from the data and Monte Carlo samples.

4.6.2 Spacal Calibration

In order to make precise measurements of the DIS cross section, and hence of $F_2(x, Q^2)$ and $F_2^{D(3)}(\beta, Q^2, x_P)$, the scattered positron must be precisely measured. Hence, the response of the Spacal calorimeter needs to be well understood. A calibration of the positron energy

²No cut was applied to y_{eDA} for this investigation in order that the vertex efficiency over the entire y range may be studied.

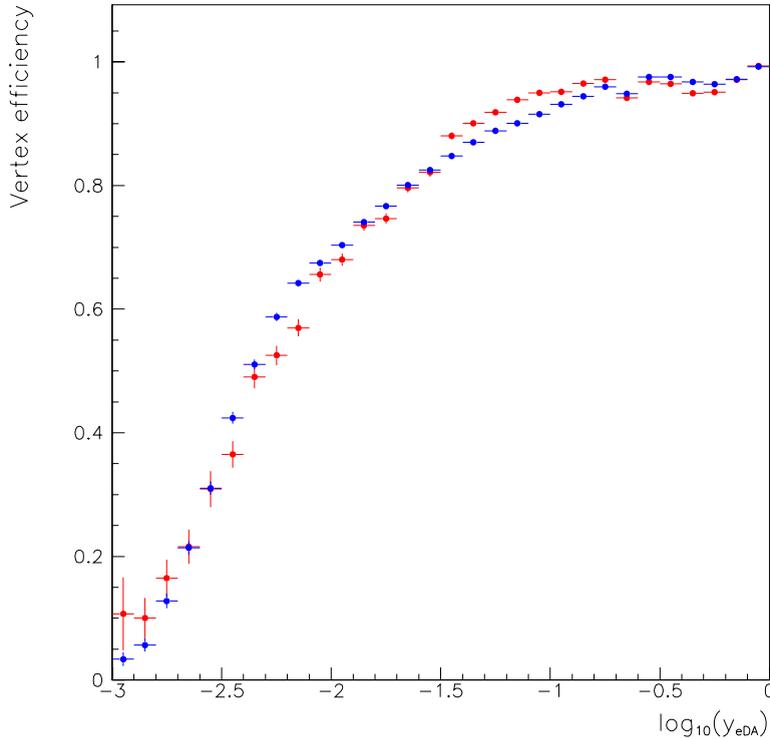


Figure 4.3: Vertex efficiency shown as a function of y_{eDA} for data (red points) and combined DJANGO and PHOJET Monte Carlo (blue points).

measured in the Spacal was performed using the *Kinematic Peak method* [101], [102], [103] and this is described in detail below.

The positron energy distribution as observed at HERA has a characteristic shape at low and moderate Q^2 , with a kinematic peak at the positron beam energy and asymmetric tails. Imposing the selection $0.005 < y_h < 0.05$, in addition to the standard DIS selection presented in section 4.6 and without applying the y_{eDA} cut, primarily selects positrons in a small, background free range around the kinematic peak position. In tracing the origin of the kinematic peak, the inclusive cross section, given in equation 2.19 can be rewritten as,

$$\frac{d^2\sigma}{dydQ^2} = \frac{4\pi\alpha_{em}^2}{yQ^4} \left(1 - y + \frac{y^2}{2}\right) F_2(y, Q^2). \quad (4.15)$$

For fixed Q^2 the differential cross section is then proportional to $\frac{1-y+y^2/2}{y}$ because the structure function is relatively flat over all phase space. The kinematic peak calibration is

performed in a region of very low y hence, using equation 4.1, the cross section increases approximately as,

$$\frac{1}{y} = \frac{E_e}{E_e - E'_e \sin^2(\frac{\theta_e}{2})}. \quad (4.16)$$

Therefore, the cross section is largest where $E_e \sim E'_e \sin^2(\theta_e/2)$ so this is where a peak is observed in the distribution corresponding to $E_e \sim E'_e$ for $\theta_e \sim \pi$. The lower limit on the y_h selection cut is imposed to avoid uncertainties in describing the inclusive structure function in the Monte Carlo as $y \rightarrow 0$. The upper y_h limit at 0.05 corresponds to the cut applied in the selection of inclusive DIS events. Therefore, the sample chosen for the calibration studies is independent to that used in the measurement of the inclusive and diffractive structure functions.

Since the peak position is determined mainly by kinematic factors, the positron energy distribution generated in the Monte Carlo represents the true distribution that should be observed. Hence, the reconstructed Monte Carlo and the data were corrected to this generator level distribution in order that the Spacal is well modelled. The Spacal comprises many cells and the high voltages in each can vary as can the gains of the photomultiplier tubes. In addition some cells are inoperative or inefficient implying the energy resolution is not constant. Therefore, the calibration was carried out on an individual cell by cell basis where possible.

The structure of the Spacal was discussed in section 1.4.2. The electromagnetic part comprises 1192 cells of size 40.25 mm \times 40.25 mm. For the calibration corrections calculated in this analysis, a cell by cell kinematic peak calibration was performed for the “inner” region of the Spacal ($-32 \text{ cm} < x < 32 \text{ cm}$ and $-32 \text{ cm} < y < 32 \text{ cm}$) but outside of this region the sample was more statistically limited. Hence, groups of four cells (*outer sections*) in each direction were treated together. The inner region calibration was performed over $16 \times 16 = 256$ cells and the outer region calibration was used for the “sections” outside of this region. The calibration procedure is outlined below. The calibration was performed using all low Q^2 events to make use of the superior statistics available for the inclusive compared with the diffractive sample. The nature of the final state system is irrelevant so the calibration performed here is equally applicable to diffractive events as it is to inclusive events. Small corrections were first applied to the nominal x (-0.095 cm) and y (-0.42 cm) positions in the Spacal to correct a misalignment between the Spacal and the rest of the H1 detector. At each stage cells where the positron energy distributions could not be fitted, or where the disagreement between data and Monte Carlo was very

significant, were cut out and not used in the analysis. The three phases of the calibration are:

1. Correct the reconstructed Monte Carlo energy (E_{REC}) to that observed at the generator level (E_{GEN}). The distribution of E_{GEN}/E_{REC} was plotted for each cell or section and the reconstructed energy corrected accordingly. Figure 4.4 shows this distribution, with a Gaussian fit, for the inner cell $-16 \text{ cm} \lesssim x_{SPACAL} \lesssim -12 \text{ cm}$ and $-16 \text{ cm} \lesssim y_{SPACAL} \lesssim -12 \text{ cm}$. This distribution, like that for all other cells and sections, was corrected from the mean fit value (1.016 in this case) to be centred at unity.

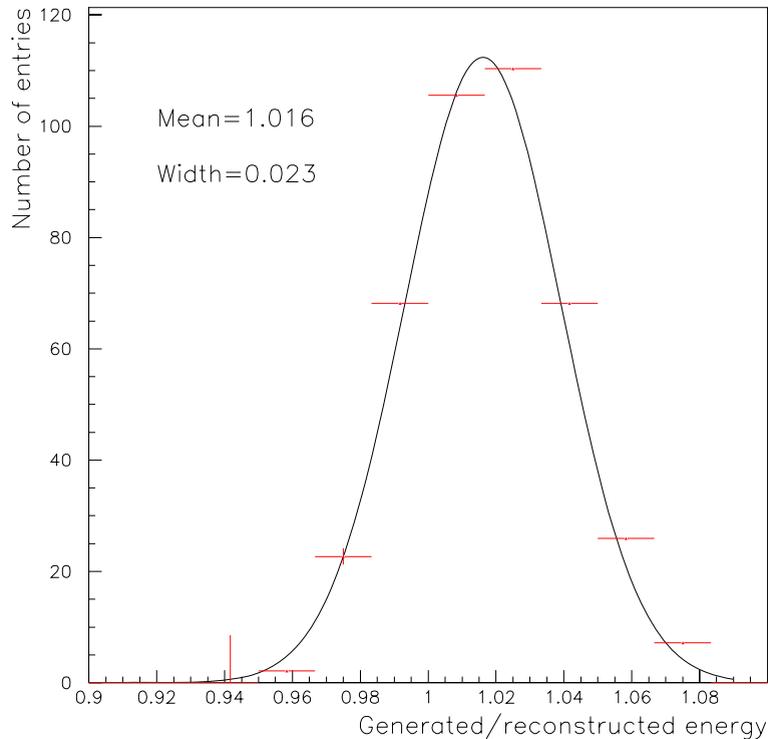


Figure 4.4: Distribution of generated divided by reconstructed positron energy for DJANGO in the cell $-16 \text{ cm} \lesssim x_{SPACAL} \lesssim -12 \text{ cm}$ and $-16 \text{ cm} \lesssim y_{SPACAL} \lesssim -12 \text{ cm}$. The mean of the distribution is 1.016 ± 0.005 and the width 0.023 ± 0.010 .

2. Correct the positron energy distribution in the data to the corrected reconstructed Monte Carlo energy. Figure 4.5 shows the distributions for data (blue points) and Monte Carlo (red points) for the outer section $-48 \text{ cm} \lesssim x_{SPACAL} \lesssim -32 \text{ cm}$ and $0 \text{ cm} \lesssim y_{SPACAL} \lesssim 16 \text{ cm}$. Both distributions were fitted to Gaussians. The mean positions were $26.1 \pm 0.1 \text{ GeV}$ and $26.7 \pm 0.1 \text{ GeV}$ for data and Monte Carlo

respectively. The data position was corrected to that of the Monte Carlo. This was repeated for all cells and sections.

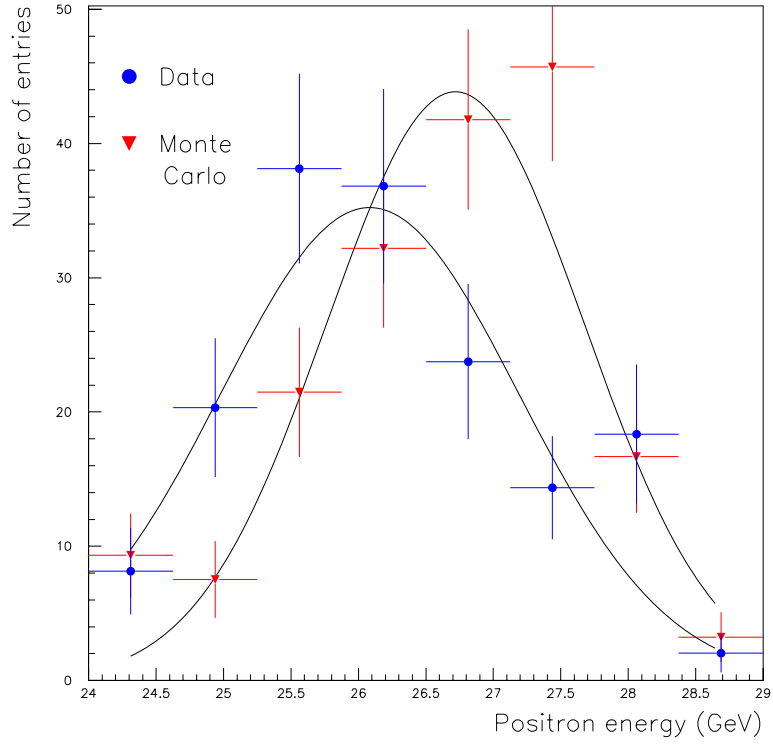


Figure 4.5: Reconstructed positron energy distribution for data (blue points) and DJANGO (red points) in the Spacal section $-48 \text{ cm} \lesssim x_{SPACAL} \lesssim -32 \text{ cm}$ and $0 \text{ cm} \lesssim y_{SPACAL} \lesssim 16 \text{ cm}$.

- Smear the Monte Carlo distributions because these are too sharp in comparison with the data, that is the detector smearing is not well simulated. Figure 4.5 shows a Spacal section where the width of the data distribution was 1.1 ± 0.1 and that of the Monte Carlo was 1.0 ± 0.1 . The smeared energy is defined as,

$$E'_e(\text{SMEARED}) = E'_e(\text{CORRECTED}) + \text{RND} \times \sigma(\text{SMEAR}), \quad (4.17)$$

where RND represents a Gaussianly distributed random number for each Monte Carlo event and $\sigma(\text{SMEAR})$ relates the Gaussian widths of the data and Monte Carlo distributions by:

$$\sigma(\text{SMEAR}) = \sqrt{\sigma(\text{DATA})^2 - \sigma(\text{MC})^2}. \quad (4.18)$$

4.6.3 Hadronic Calibration

Variables derived from LAr calorimeter measurements also do not show perfect agreement between data and Monte Carlo. Hence, a calibration must be applied here as well. For the purpose of this analysis, standard H1 calibration constants applicable for the low Q^2 region were applied. These constants were calculated for each octant of each wheel of the LAr calorimeter. The ratio $p_{T,h}/p_{T,e}$ for data events is weighted accordingly until it matches that of the simulation and then the transverse momentum balance is corrected to unity in both data and Monte Carlo [103] [104].

Figures 4.6 and 4.7 show a selection of variables before the positron and hadron calibrations were applied to the data. Figure 4.6(a) shows the positron energy observed in the Spacal. The ratio of the double angle method prediction, $E_{DA} = \frac{E_e(1-y_{DA})}{\sin^2(\theta_e/2)}$ (where y_{DA} was defined in section 4.5.3) to the measured positron energy is shown in figure 4.6(b). It can be seen that neither the mean positions of the distributions, nor the shapes, are consistent for data and Monte Carlo. Figures 4.7(a), (b) and (c) show the total $E - p_z$ of the positron and hadronic final state, transverse momentum balance and y balance, before the Spacal and LAr calibrations, which are all calculated from both the positron and hadron variables. Again the Monte Carlo and data show quite different distributions.

Figures 4.8 and 4.9 show the same distributions after the cell by cell Spacal calibration (described in section 4.6.2) and the LAr calorimeter calibration have been applied. The Spacal calibration was performed in a separate region of phase space to that in which the measurement is performed and figures 4.8(a) and (b) demonstrate the success of the calibration in this higher y region. Figures 4.9(a)-(c), which depend on both calibrations, demonstrate the success of the hadronic calibration.

4.6.4 Inclusive Control Distributions

The reason for making control distributions is to ensure that there is a good agreement between the data and the Monte Carlo simulations, with all the cuts, selections and corrections applied, to validate the reliability of the final measurement of the cross section or structure function.

Figure 4.10 shows various inclusive kinematic distributions plotted for data (the black points shown with statistical errors), DJANGO, which models inclusive deep inelastic scattering (the green histogram), and PHOJET (the purple histogram) to describe the photoproduction background. An overall normalisation correction of 0.8 is applied to the

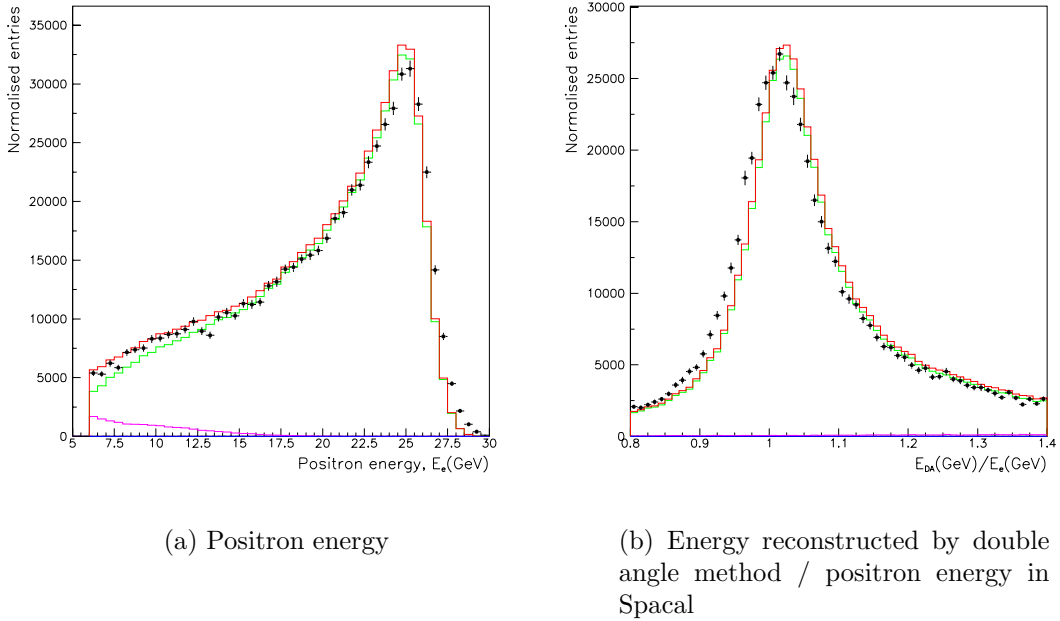
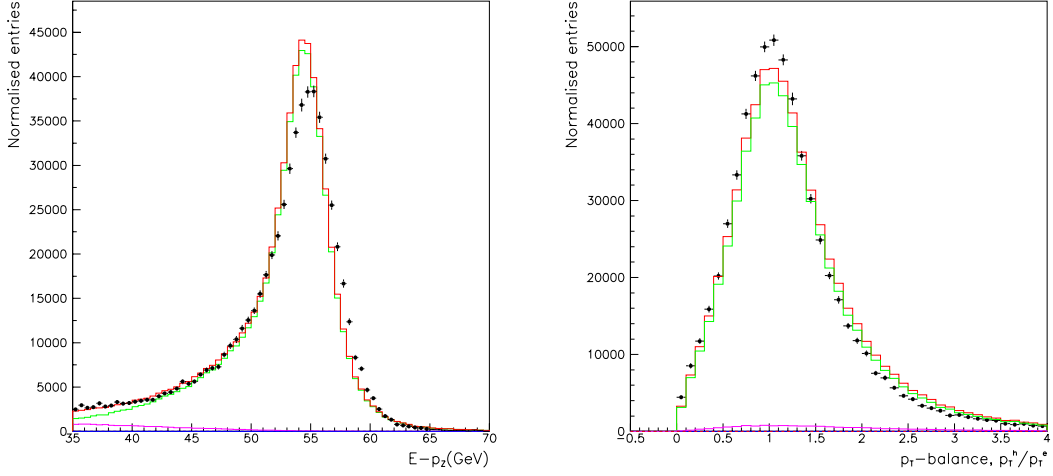


Figure 4.6: Control distributions before the application of Spacal and LAr calorimeter calibrations for the positron energy (a), and ratio of double angle method to measured energy (b). The data points are shown, with statistical errors, by the black points, the DJANGO and PHOJET Monte Carlo contributions are denoted by the green and purple histograms respectively and the total Monte Carlo is shown in red.

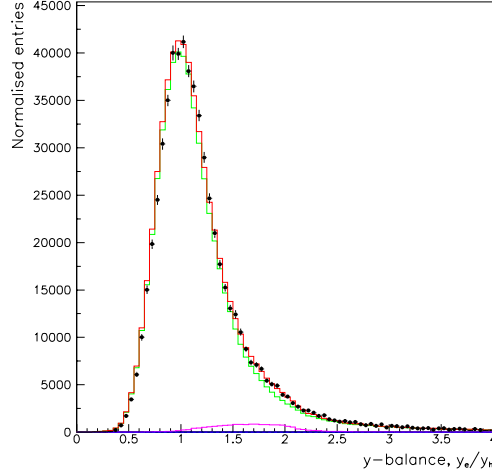
PHOJET events in both the inclusive and diffractive cases. For clarity the statistical errors on the Monte Carlo are not shown here.

Figures 4.10(a)-(i) demonstrate the good agreement between data and Monte Carlo for inclusive variables in addition to those presented in section 4.6.3. The plots in figures 4.10(a)-(c) show the positron and hadronic angles, where the dramatic variations in the positron azimuthal angle plot (c) originate from parts of the Spacal being rejected by the fiducial cuts. The z -vertex and R_{SPACAL} distributions are shown in figures (d) and (e) respectively. The sum of the component Monte Carlos describes the data well. The kinematic variables used in the binning of $F_2(x, Q^2)$, presented in the next chapter, are shown in figures 4.10(f)-(i). Here the Q^2 distribution, both at the lowest end and over the whole range, and distributions for the scaling variables x and y are presented. Q^2 , x and y here are derived from the electron-double angle reconstruction method as described in section 4.5.4. The well described control distributions, together with the small resolutions observed for x and Q^2 presented in section 4.5.5, illustrate the benefit of using the electron-double angle method for reconstruction.



(a) Total $E - p_z$ of the positron and hadronic final states

(b) Transverse momentum balance



(c) y balance

Figure 4.7: Control distributions before the application of Spacal and LAr calorimeter calibrations for the total $E - p_z$ (a), transverse momentum balance (b) and y balance (c). The data points are shown, with statistical errors, by the black points, the DJANGO and PHOJET Monte Carlo contributions are denoted by the green and purple histograms respectively and the total Monte Carlo is shown in red.

4.7 Diffractive DIS Event Selection

The selection of diffractive events is based on identifying events with a large rapidity gap in the forward region of the H1 detector between the hadronic final state (X) and the outgoing proton system (Y). This section describes the diffractive forward detector

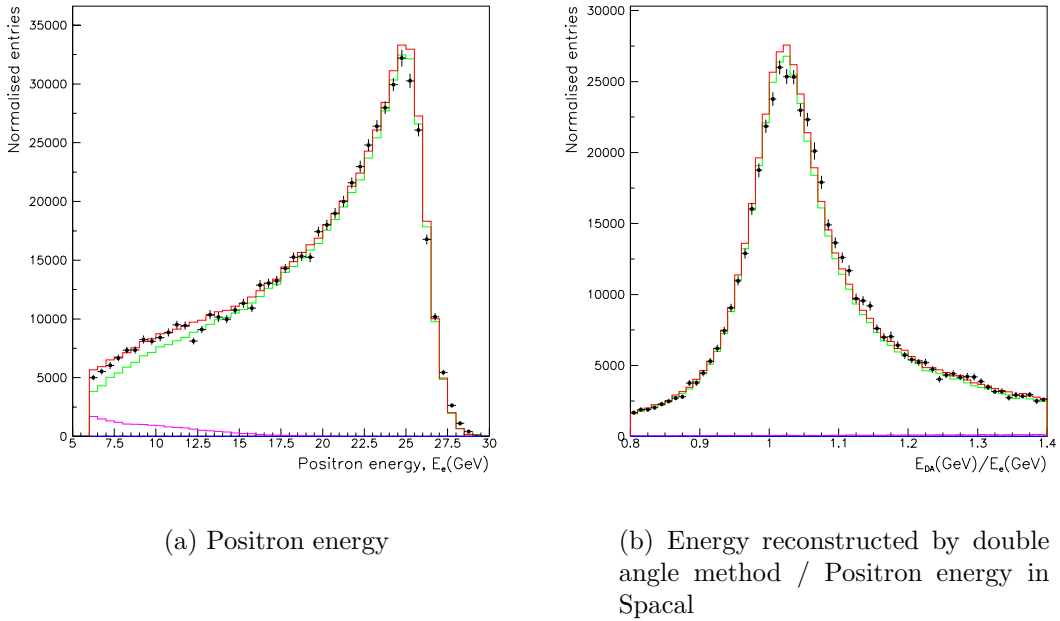
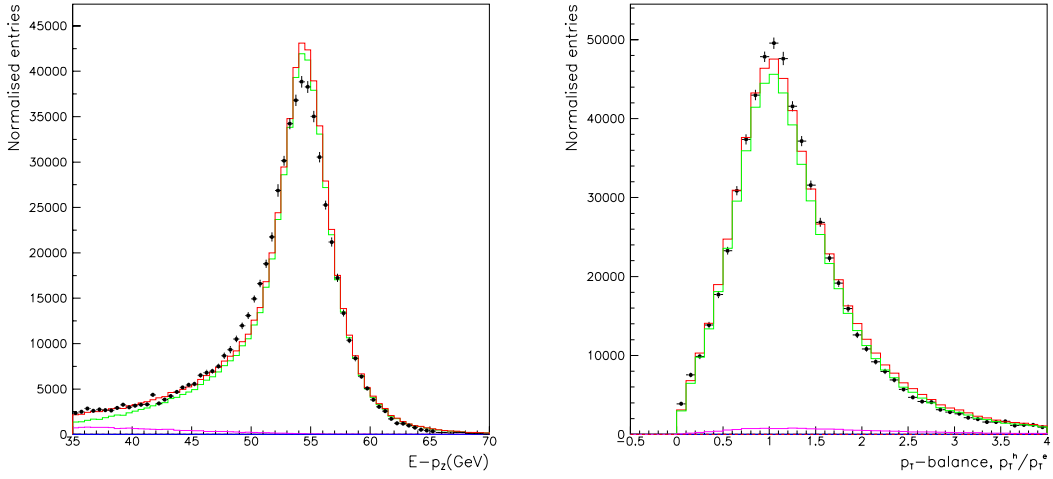


Figure 4.8: Control distributions after the application of Spacal and LAr calorimeter calibrations for the positron energy (a), and the ratio of double angle method to measured energy (b). The data points are shown, with statistical errors, by the black points, the DJANGO and PHOJET Monte Carlo contributions are denoted by the green and purple histograms respectively and the total Monte Carlo is shown in red.

selection in detail.

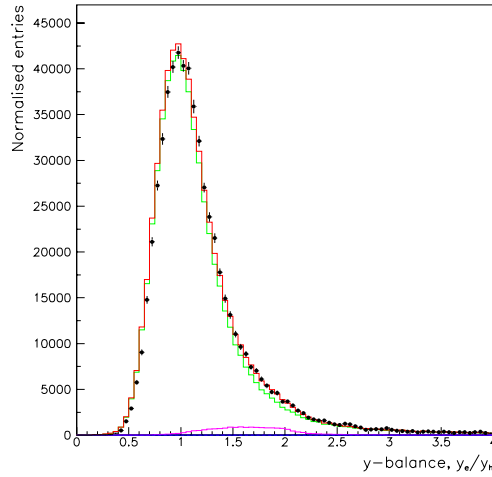
4.7.1 Forward Detector Selection

The full diffractive structure function is dependent on five variables: Q^2 , x_P , β , M_Y and t . Since the outgoing proton state is not detected, measurements of M_Y and t are not generally possible. Hence, the $F_2^{D(3)}$ measured is the distribution summed over the region $|t| < 1.0 \text{ GeV}^2$ and $M_Y < 1.6 \text{ GeV}$ in order to principally select events with an elastic proton whilst minimising systematic errors associated with unknown M_Y and t dependencies. Cuts are imposed using the forward detectors, as will be described in this section, to limit the activity observed in the forward region. The variable x_P , which is used in the binning of events for the diffractive structure function, must be reconstructed with a reasonable acceptance and purity (defined in equations 5.3 and 5.4 in chapter 5) and this means events with $x_P > 0.05$ are excluded.



(a) Total $E - p_z$ of the positron and hadronic final states

(b) Transverse momentum balance

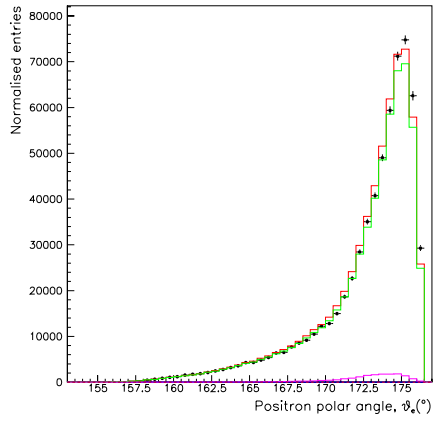


(c) y balance

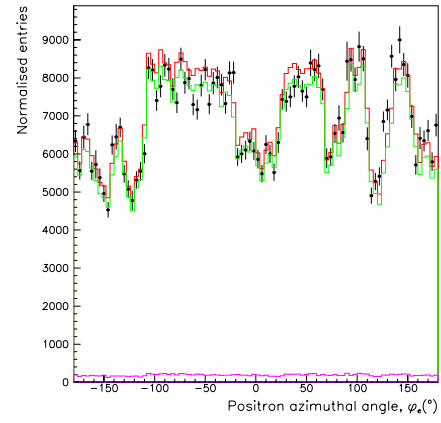
Figure 4.9: Control distributions after the application of Spacal and LAr calorimeter calibrations for total $E - p_z$ (a), transverse momentum balance (b) and y balance (c). The data points are shown, with statistical errors, by the black points, the DJANGO and PHOJET Monte Carlo contributions are denoted by the green and purple histograms respectively and the total Monte Carlo is shown in red.

The LAr selection

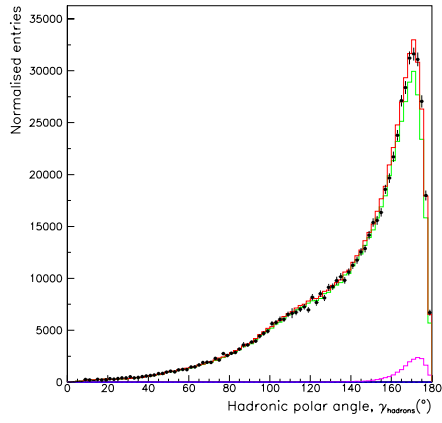
Demanding no activity, above the noise level of 300 MeV, in the forward region of the Liquid Argon Detector can reduce the contamination from high x_p and large M_Y proton dissociation backgrounds. However, because there is random noise present in the calorime-



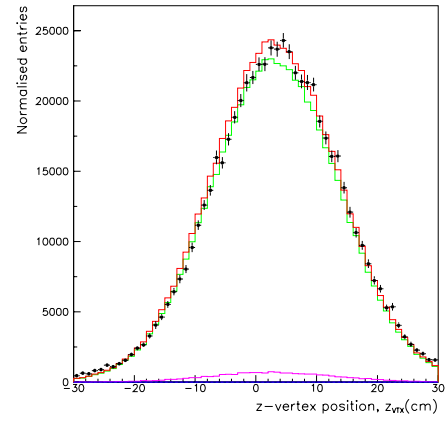
(a) Positron polar angle



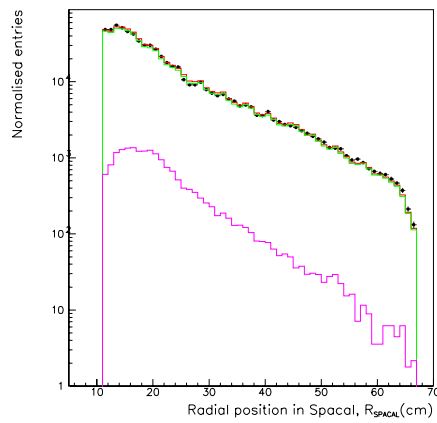
(b) Positron azimuthal angle



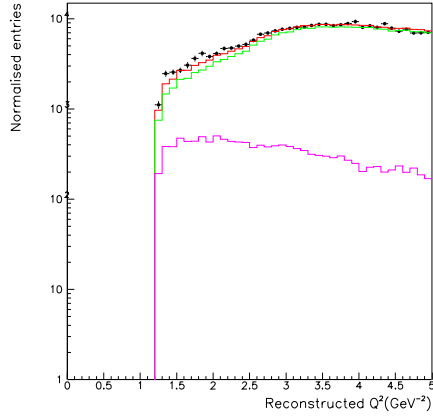
(c) Hadronic polar angle



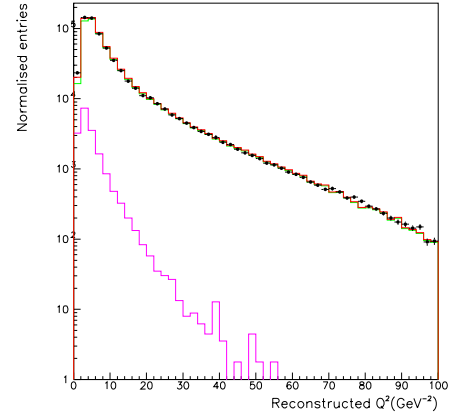
(d) z -vertex distribution



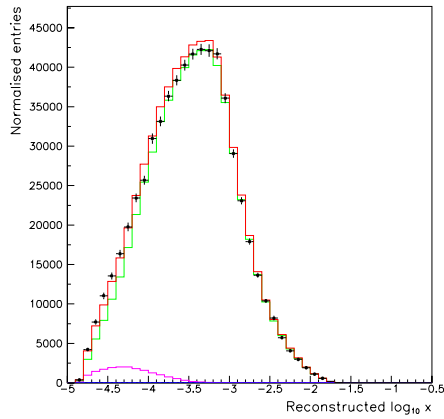
(e) R_{SPACAL}



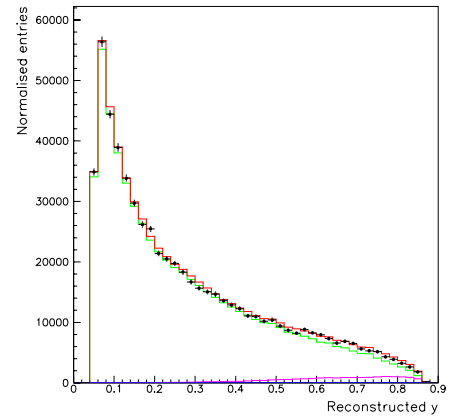
(f) Low photon virtuality, Q^2



(g) Photon virtuality, Q^2



(h) Bjorken scaling variable, x



(i) Inelasticity, y

Figure 4.10: Control distributions for the positron polar angle (a), positron azimuthal angle (b), hadronic polar angle (c), z -vertex distribution (d), and R_{SPACAL} (e). The kinematic distributions of Q^2 , x and y are shown in figures (f)-(i). The data points are shown, with statistical errors, by the black points, the DJANGO and PHOJET Monte Carlo contributions are denoted by the green and purple histograms respectively and the total Monte Carlo is shown in red.

ter, approximately 2.5% of diffractive events are lost after this cut. The LAr calorimeter covers a region of pseudorapidity extending to 3.4 and the distribution of η_{MAX} , which was defined in equation 3.3, can be decomposed into diffractive and non-diffractive regions. Non-diffractive events show a peak at the highest values of η_{MAX} , falling off rapidly to zero by about $\eta_{MAX} = 2$ whilst the diffractive data show a lower plateau spanning the region of moderate rapidity (see figure 4.15(m) or 4.16 as examples). The different behaviours are due to the fact that in DIS the struck partons and proton remnant are connected by a colour string but the diffractive final state shows disconnected colour strings. Hence, the cut on η_{MAX} is chosen to maximise the diffractive event selection whilst rejecting non-diffractive events. The selection for diffractive events in this analysis is,

$$\eta_{MAX} < 3.3. \tag{4.19}$$

The Forward Muon Detector Selection

The Forward Muon Detector, which was described in section 1.5.1, is situated at the front end of the main detector and was originally designed for the detection of high energy muons. It is also invaluable in diffractive analyses as it can be used by requiring that little or no activity is observed in it. This rejects non-diffractive events, since such events give track segments in the FMD either due to particles directly produced in the $e - p$ interaction or via secondary scattering with the beam-pipe or surrounding material. The selection on the number of hit pairs in the FMD,

$$N_{FMD(1,2)} \leq 1, \tag{4.20}$$

$$N_{FMD(3)} \leq 2, \tag{4.21}$$

is imposed where the numbers in brackets refer to the layers of the detector with 1 being the innermost. The three post-toroid layers are not used in the selection procedure as the synchrotron radiation from the incident positron beam produces high background levels in them. The two separate cuts 4.20 - 4.21 are chosen, rather than one on all three layers, to minimise the correction to the data required because of residual noise in the detector whilst retaining as tight a selection as possible. The third layer suffers from much higher noise levels than the first and second.

The noise correction for the FMD is calculated from *randomly triggered* data events

which comprise approximately 1% of the total data recorded. These events are written to tape irrespective of whether a physics event is indicated from the sub-triggers. Hence, the sample represents the pedestal on which the FMD information sits. If a randomly triggered event has noise in the FMD but not in the LAr calorimeter (the Monte Carlo simulation already simulates noise in the LAr calorimeter) this is classed as a noise event. For each HERA luminosity fill the percentage of noise observed in the FMD is determined and the data corrected accordingly. Figure 4.11 shows the fill by fill noise levels recorded for the 1999 minimum bias running period. The fraction of diffractive events lost due to noise in the FMD alone is $\sim 1.6\%$ on average. The noise correction presented here is calculated not only for the FMD but also the PRT, FTS and Plug calorimeter as well, but these contributions are less important.

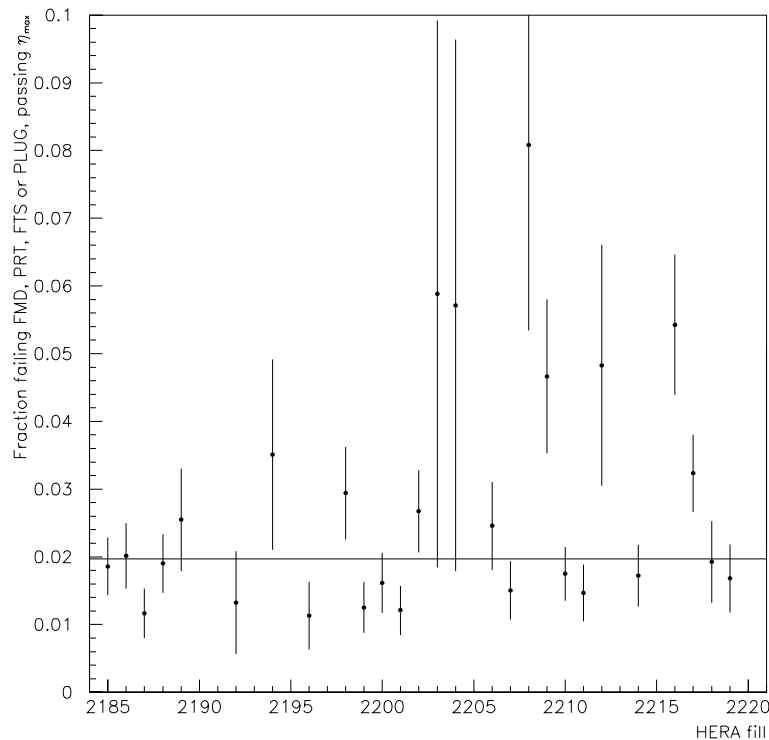


Figure 4.11: Percentage of randomly triggered events with noise in the forward detectors shown for each HERA luminosity fill. The solid line represents the average noise level of $\sim 2\%$ over all fills.

The Forward Tagging System Selection

As described in section 1.6.1 the Forward Tagging System comprises five scintillating fibre detector stations, positioned at $z = 9, 16, 24, 53, 92$ m in the forward direction. These will be referred to as FTS1, FTS2, PRT, FTS3 and FTS4 respectively. The residual noise present in these detectors is negligible, except for the sixth layer of the PRT (which was not used in this analysis), hence the selection requirement for diffractive events is that there should be no activity present in these detectors. The outer FTS stations (FTS3 and FTS4) were not used because in comparisons between data and Monte Carlo large discrepancies were observed. Hence, the FTS selection can be summarised as:

$$N_{PRT(1,2,3,4,5,7)} = 0, \quad (4.22)$$

$$N_{FTS(1,2)} = 0. \quad (4.23)$$

Since the FTS and PRT are important in the diffractive event selection, it is also important that there is a good agreement between data and Monte Carlo on the level of activity in these detectors for non-diffractive events. For various combinations of “anti-diffractive” cuts, the detection efficiency, as defined in equation 4.24, of the PRT and FTS stations was compared for data and Monte Carlo. The results, summarised in columns 1-2 in table 4.3 show that the efficiency of the Monte Carlo simulation is too high and therefore must be downgraded. This behaviour has been observed in previous analyses for the PRT and is attributable to known deficiencies in the PRT simulation. The correction method presented here is based on work presented in [105] though the procedure has been performed separately for the 1999 minimum bias data sample. The efficiency is calculated as in equation 4.24 and the Monte Carlo used was DJANGO:

$$\text{Efficiency} = \frac{\text{Events passing anti - diffractive cuts}}{\text{Total number of events}} \quad (4.24)$$

The recalibration factors by which the FTS and PRT efficiencies must be downgraded in the simulation were calculated by imposing the anti-diffractive selections $\eta_{MAX} > 3.3$, $N_{FMD}(1,2) > 1$ and $N_{FMD}(3) > 2$ and the recalibration factor, F , defined in equation 4.25, was calculated using DJANGO and data:

$$F = \frac{\text{Data Events with Hits in FTS(PRT)} / \text{All Data}}{\text{MC Events with Hits in FTS(PRT)} / \text{All MC}}. \quad (4.25)$$

Condition	Efficiency (%)		
	Data	MC	MC FTS
$\eta_{MAX} > 3.3$	72.7342 ± 0.0557	85.0879 ± 0.0017	–
$N_{FMD} > 1$	68.9660 ± 0.0586	81.6931 ± 0.0016	–
$N_{FTS} > 0$	12.9526 ± 0.0425	33.2536 ± 0.0006	13.6459 ± 0.0002
$E_{PLUG} > 5 \text{ GeV}$	47.8104 ± 0.0632	66.2944 ± 0.0013	–
$\eta_{MAX} > 3.3 \&$ $N_{FTS} > 0$	10.5920 ± 0.0309	30.1727 ± 0.0005	12.4960 ± 0.0002
$\eta_{MAX} > 3.3 \&$ $N_{FMD} > 0$	63.6391 ± 0.0609	77.4224 ± 0.0015	–
$N_{FMD} > 1 \&$ $N_{FTS} > 0$	11.0224 ± 0.0396	29.8749 ± 0.0005	12.3174 ± 0.0002
$\eta_{MAX} > 3.3 \&$ $N_{FMD} > 1 \&$ $N_{FTS} > 0$	9.2172 ± 0.0366	27.2864 ± 0.0005	11.1381 ± 0.0002

Table 4.3: Efficiency of detecting activity with various combinations of the forward detectors for data and inclusive DIS Monte Carlo (MC). The “MC FTS” column represents the Monte Carlo efficiency after the application of the FTS recalibrations and conditions which are unaffected are indicated by “–”.

Separate recalibration factors were calculated for FTS1, FTS2 and the PRT. The results are summarised in table 4.4.

Detector	Recalibration Factor
PRT	0.703 ± 0.007
FTS1	0.550 ± 0.005
FTS2	0.664 ± 0.006

Table 4.4: Recalibration corrections signifying the probability with which activity is ignored in the Monte Carlo simulation for the PRT and FTS stations.

Application of the recalibration factors to the Monte Carlo yields a much improved agreement with the data, as shown by comparing the second and fourth columns of table 4.3. Discrepancies remain in the fraction of events with $\eta_{MAX} > 3.3$, $N_{FMD} > 1$ and $E_{PLUG} > 5 \text{ GeV}$ after the anti-diffractive cuts. These are partly due to the poor simulation of proton dissociation events in DJANGO, which typically give hits in the PRT and FTS but not in the FMD and have $\eta_{MAX} < 3.3$. The extent to which inadequacies of the dead material and beam-pipe simulation play a role is not yet fully understood. However, the effect on the measurement of these discrepancies is small, and covered by the systematic errors, since several forward detectors are used in combination and only one is required to reject a non-diffractive event. The overall rejection efficiency is in excess

of 99%.

The Plug Calorimeter Selection

The PLUG calorimeter was also found to aid in the selection of diffractive events. It is particularly useful in rejecting high x_P background contributions. There is random noise present in the Plug calorimeter which is not included in the Monte Carlo simulation. The total noise correction due to the FMD, PRT, FTS and Plug was $\sim 2\%$ for the 1999 minimum bias data (see figure 4.11). The diffractive cut applied in the analysis was,

$$E_{PLUG} < 5 \text{ GeV}. \quad (4.26)$$

4.7.2 Reconstruction and Resolution of Diffractive Variables

Following the selections described above (section 4.7.1) to restrict the data sample to diffractive events, the diffractive structure function $F_2^{D(3)}$ was extracted by binning the data in Q^2 , x and β . The resolutions for Q^2 and x were presented in section 4.5.5 and the resolution in β is discussed here. β is derived from equation 3.11 which depends on M_X , the mass of the hadronic final state system. This is reconstructed by combining Spacal and LAr calorimeter cluster information with CJC track information with measures taken to avoid double counting. This mass can then be reconstructed from the energy and momentum of the final state. It was found in [69] that a superior reconstruction was obtained if the value of M_X was corrected by a ratio of y measurements³. Therefore, M_X is reconstructed benefitting from the optimal y_{eDA} reconstruction method, giving the mass of the final state as,

$$M_X^2 = (E^2 - p_x^2 - p_y^2 - p_z^2)_h \cdot \frac{y_{eDA}}{y_h}, \quad (4.27)$$

where y_{eDA} was defined in section 4.5.4 and y_h is the inelasticity as calculated by the hadron reconstruction method (see section 4.5.2). The measured value of M_X was also scaled by a factor of 1.07 to account for residual losses beyond the detector acceptance in the backward direction. This latter factor was calculated from the observed bias in the resolution plot defined by,

³The final state mass squared can be rewritten as $M_X^2 = (E - p_z)(E + p_z) - p_T^2$ hence the inclusion of $y_h \sim E - p_z$ in the denominator cancels with the hadron $E - p_z$ in the numerator.

$$\delta(M_X) = \frac{M_X(\text{g}) - M_X(\text{r})}{M_X(\text{g})}, \quad (4.28)$$

where the letters in brackets denote generated (g) and reconstructed (r) level Monte Carlo. Figure 4.12 shows the quality of the reconstruction of M_X , which can be compared with those for the inclusive variables x and Q^2 in figure 4.2. It can be noted that the resolution for M_X determines that of β , which is calculated from equation 3.11 in chapter 3. The resolution and bias for M_X are both observed to be larger in magnitude than for x and Q^2 (see section 4.5.5).

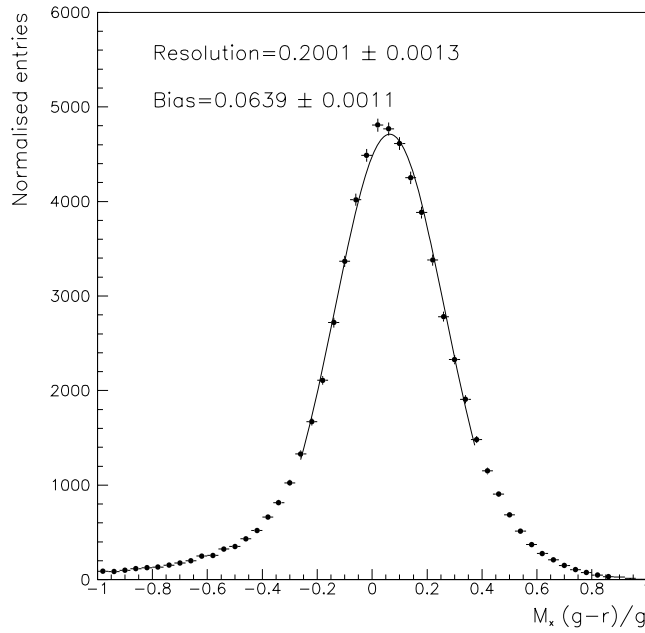
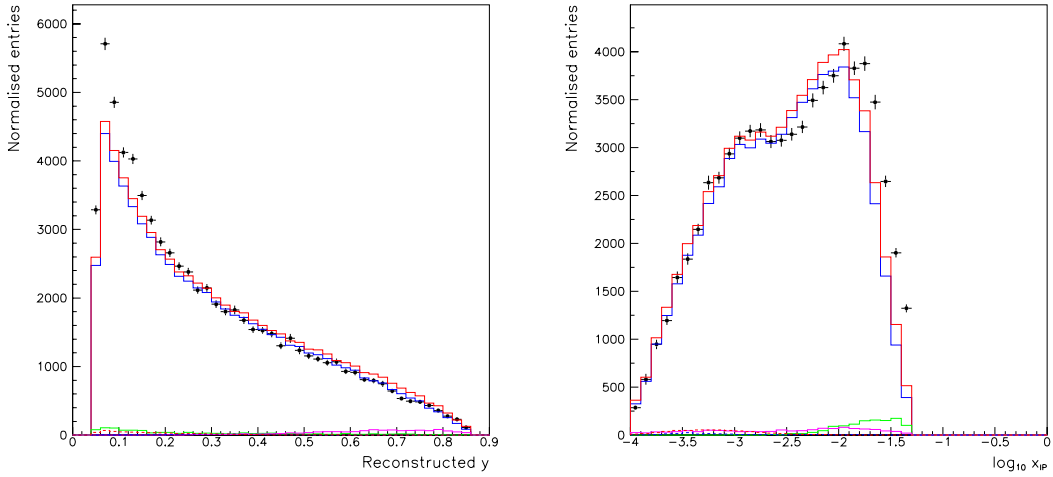


Figure 4.12: The quality of the reconstruction illustrated by the function δ defined in equation 4.28, for the diffractive variable M_X .

4.7.3 RAPGAP Reweight

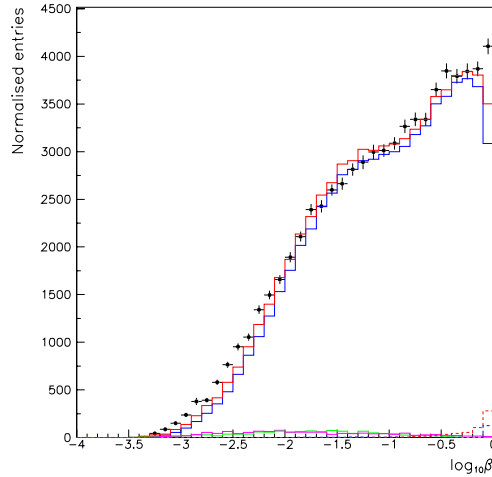
As will be presented in section 4.7.4, the RAPGAP Monte Carlo fails to give a good description of the data when control distributions are made for the diffractive selection. In particular the low positron energy (high y) region was poorly described, and also the shapes of the distributions of the diffractive variables x_P and β . This is shown in figure 4.13. Since the DJANGO and PHOJET Monte Carlos provided a good description of the inclusive data, the differences in the diffractive case are attributable to a failure to describe the low Q^2 diffractive cross section by the saturation model used in RAPGAP. Hence, to correct for this effect the Monte Carlo was reweighted at the generator level to give an improved description of the data. The procedure adopted was to plot the ratio of

data to RAPGAP Monte Carlo for the y , x_P and β distributions after first subtracting the photoproduction contribution, in order to determine the reweighting functions needed to improve the agreement between data and Monte Carlo. It was found that fourth order polynomial reweights for the y and x_P variables, and a seventh order polynomial function for β resulted in a good description.



(a) Inelasticity, y

(b) x_P



(c) β

Figure 4.13: Diffractive control distributions before the application of the reweighting functions to RAPGAP for the inelasticity (a), x_P (b) and β (c). The data points are shown, with statistical errors, by the black points, the DJANGO and PHOJET Monte Carlo contributions are denoted by the green and purple histograms respectively, as before, and the RAPGAP, DIFFVM and COMPTON distributions are represented by the blue, dotted red and dotted blue histograms respectively. The total Monte Carlo is indicated by the solid red line.

Ideally the reweight would have been performed with respect to a previous measurement or another Monte Carlo prediction which is known to describe diffractive data at low Q^2 but this was not possible⁴. This measurement represents the first statistically significant $F_2^{D(3)}$ extracted in this kinematic region and hence no previous measurement exists for this low Q^2 range. A good description of the inclusive data was obtained using the DJANGO Monte Carlo generator, without need for reweighting, and also for RAPGAP in a closely related measurement at higher Q^2 [78]. Hence, the problem is with the Monte Carlo generator rather than the simulation of the detector.

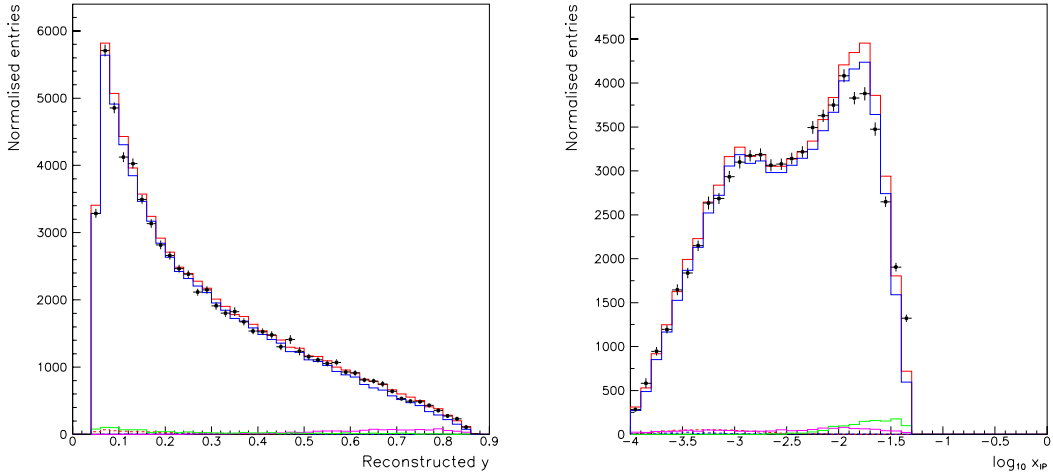
Figure 4.14 shows the same distributions as in figure 4.13 after the RAPGAP Monte Carlo has been reweighted according to the above prescription. The data are observed to agree well with the reweighted Monte Carlo, indicating that the reweighting procedure was successful. The reweight has the greatest effect at high x_p , high β and low y .

4.7.4 Diffractive Control Distributions

Control plots were made for the diffractive data and Monte Carlo for the same distributions as in the inclusive case. Due to the presence of a rapidity gap in the diffractive final state there are now extra quantities which can be also plotted to check that true diffractive events have been selected.

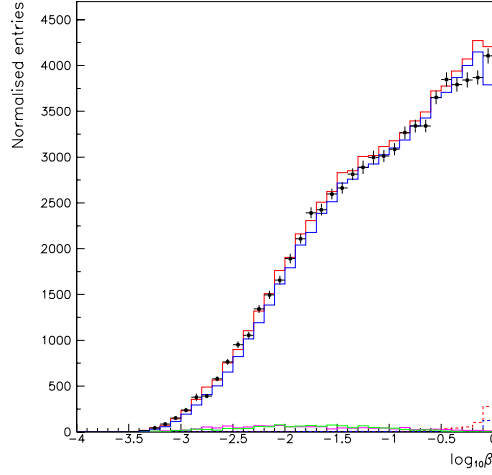
Figure 4.15 shows some of the diffractive control distributions plotted for data and all the Monte Carlo contributions. In comparison to figures 4.8, 4.9 and 4.10, plots (a)-(l) demonstrate that a good agreement between data and Monte Carlo for inclusive variables is also obtained when diffractive DIS events are selected, after the reweight on RAPGAP (described in section 4.7.3) has been applied. Plots (m) and (n) show variables relevant to the diffractive analysis. The pseudorapidity distribution is shown in figure 4.15(m) and the non-diffractive peak can clearly be seen contributing at the highest values of η_{MAX} whereas the diffractive Monte Carlo RAPGAP describes the fairly flat plateau observed in the middle region of the plot. The mass of the hadronic final state is shown in figure 4.15(n) where it can be observed that most of the events have a low mass. With the reweight applied at the Monte Carlo generator level, a good agreement at the reconstructed level is observed for all variables, including those presented in figure 4.14. The residual differences at high x_p in the x_p plot of figure 4.14(c) are not fully understood and are covered in the systematic errors in this analysis.

⁴An improvement which could be made is to perform a QCD fit to the data, as was carried out in [69], and then use the resolved pomeron model (as described in section 3.4.2) to generate the events again.



(a) Inelasticity, y

(b) x_p

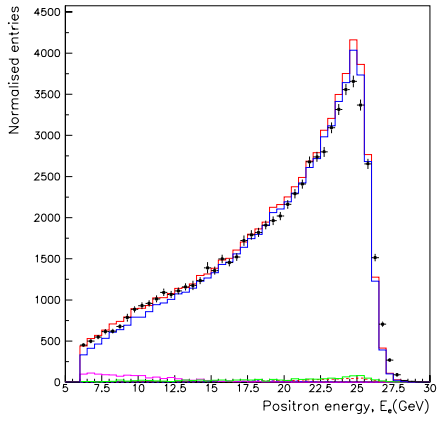


(c) β

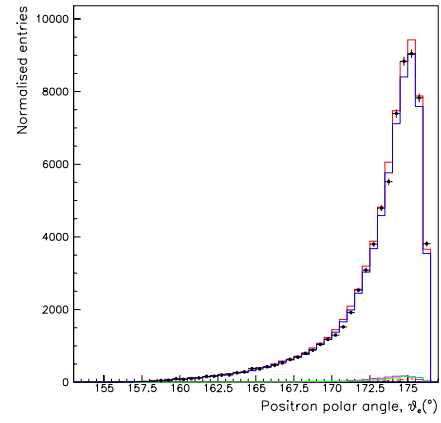
Figure 4.14: Difractive control distributions after the application of the reweighting functions to RAPGAP for the inelasticity (a), x_p (b) and β (c). The data points are shown, with statistical errors, by the black points, the DJANGO and PHOJET Monte Carlo contributions are denoted by the green and purple histograms respectively, as before, and the RAPGAP, DIFFVM and COMPTON distributions are represented by the blue, dotted red and dotted blue histograms respectively. The total Monte Carlo is indicated by the solid red line.

4.7.5 M_Y Migration Correction

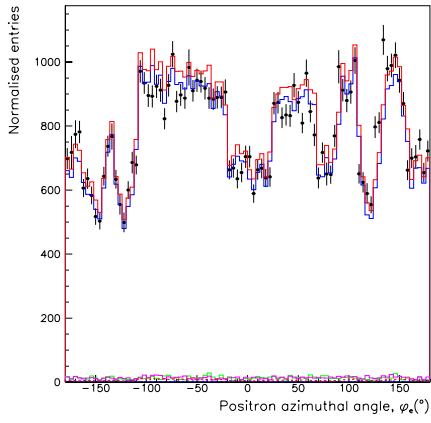
The measurement of the diffractive structure function $F_2^{D(3)}$ is made within the kinematic boundary $M_Y < 1.6$ GeV and $|t| < 1$ GeV². There will however be some migration or



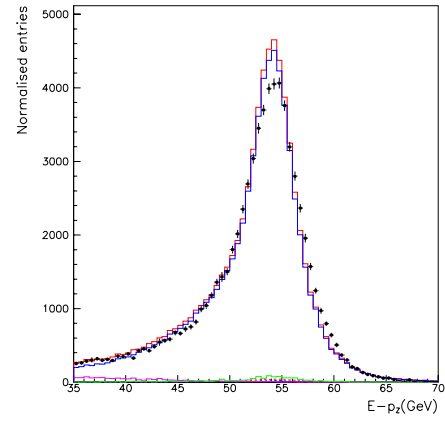
(a) Positron energy



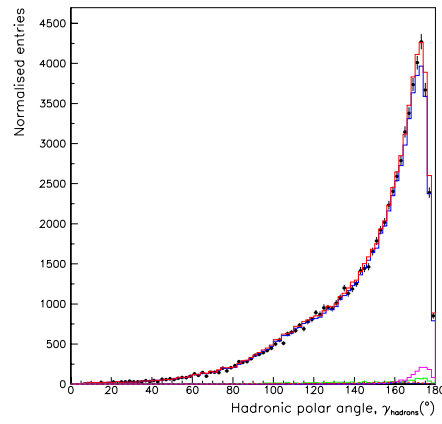
(b) Positron polar angle



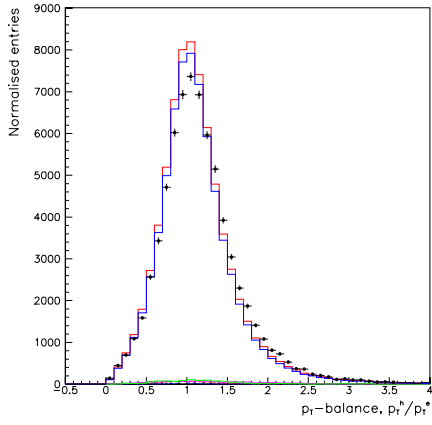
(c) Positron azimuthal angle



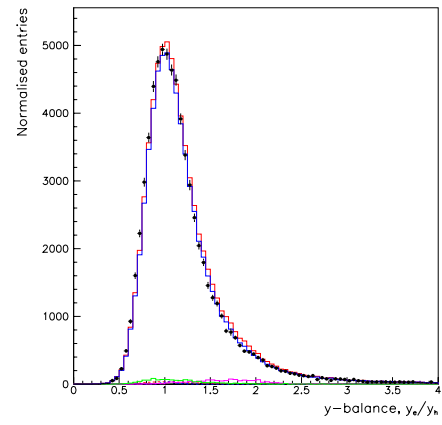
(d) Total $E - p_z$



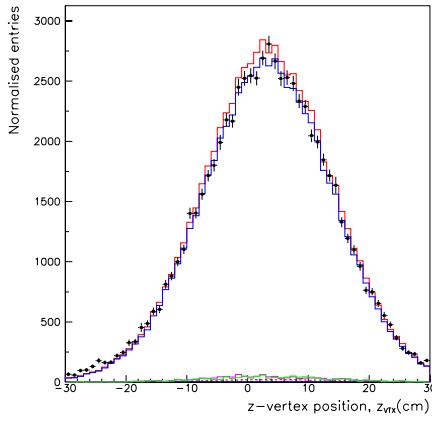
(e) Hadronic angle



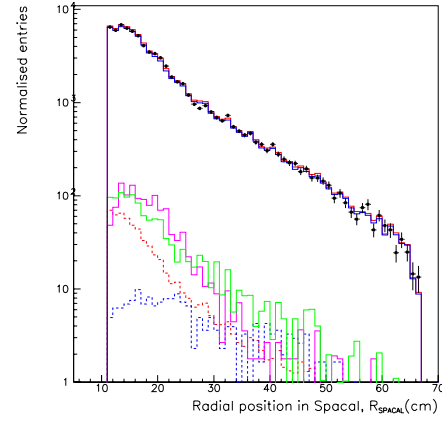
(f) p_T balance



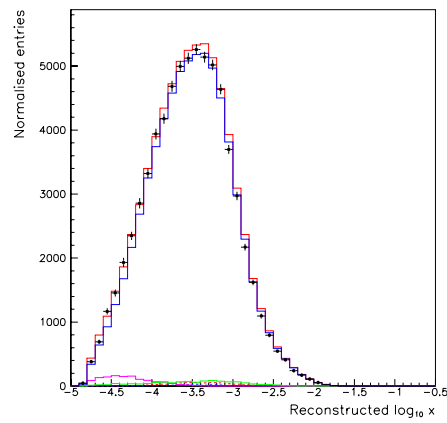
(g) y balance



(h) z -vertex distribution



(i) R_{SPACAL}



(j) Bjorken scaling variable, x

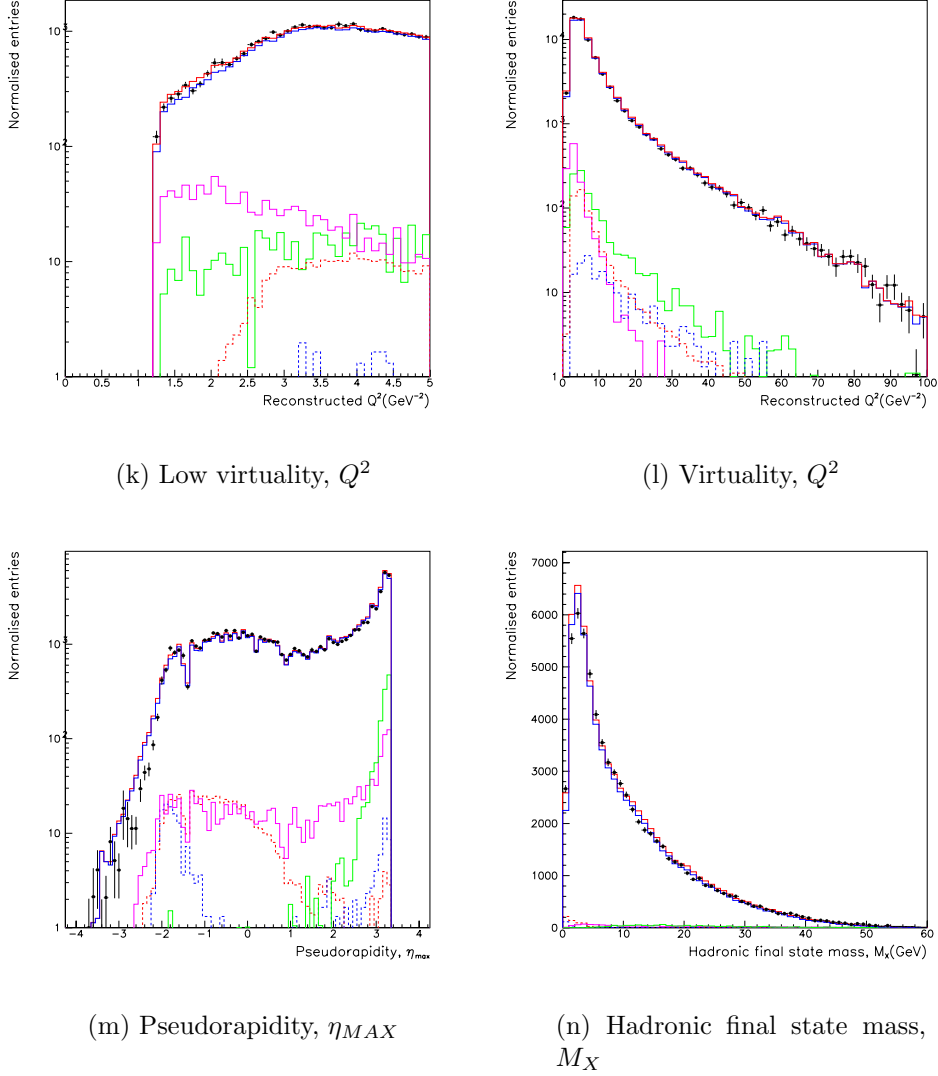


Figure 4.15: Control distributions after the application of the diffractive selection. The positron energy and angles are shown in figures (a)-(c), and the total $E - p_z$ of the positron and hadronic final state is shown in (d). The hadronic polar angle is given in (e) with p_t and y balance plots in (f) and (g). Figures (h)-(l) show the z -vertex, R_{SPACAL} and kinematic distributions, whilst the diffractive variables η_{MAX} and M_X , are shown in plots (m)-(n). The data points are shown, with statistical errors, by the black points, the DJANGO and PHOJET Monte Carlo contributions are denoted by the green and purple histograms respectively, as before, and the RAPGAP, DIFFVM and COMPTON distributions are represented by the blue, dotted red and dotted blue histograms respectively. The total Monte Carlo is indicated by the solid red line.

smearing of events across this boundary which needs to be corrected for in the calculation of the diffractive cross section. This is not accounted for in RAPGAP which only simulates elastically scattered protons. Figure 4.16 below shows the η_{MAX} distribution for data compared with the RAPGAP and DJANGO mixture before diffractive cuts. It can be seen that the data and Monte Carlo agree at each edge of the distribution, but the central region is now poorly described, with the discrepancy of the order of a factor of two approximately. This difference is due to the fact that proton dissociation is not modelled in either RAPGAP or DJANGO.

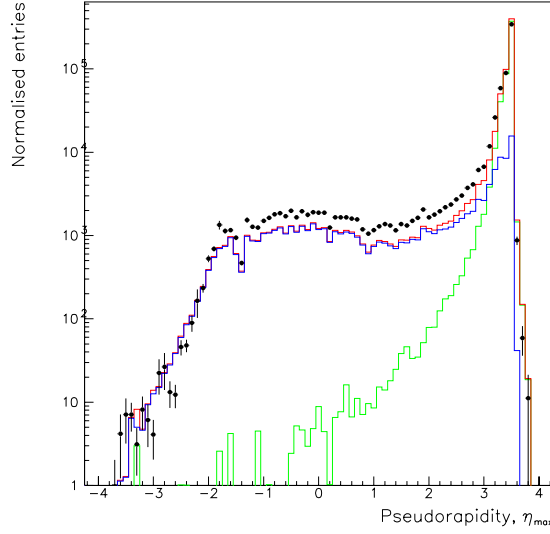


Figure 4.16: The η_{MAX} distribution for data (black points) and RAPGAP (blue histogram) and DJANGO (green histogram) Monte Carlos before diffractive cuts are applied. The total Monte Carlo is indicated by the red histogram.

Following the method presented in [105] this boundary correction factor, P , is calculated from the elastic and proton dissociative DIFFVM Monte Carlo as,

$$1 - P = \frac{\text{Net Number of Events Migrating from } M_Y < 1.6 \text{ to } M_Y > 1.6 \text{ GeV}}{\text{Total Number of Generated Events}} \quad (4.29)$$

$$= \frac{\text{Net Migrations out of } M_Y < 1.6 \text{ GeV}, |t| < 1 \text{ GeV}^2}{\text{Events Generated in } M_Y < 1.6 \text{ GeV}, |t| < 1 \text{ GeV}^2}. \quad (4.30)$$

The correction factor can be expressed as,

$$1 - P = \frac{N_{gen}^{PD}(M_Y < 1.6 \text{ GeV}, |t| < 1 \text{ GeV}^2) - N_{rec}^{PD}}{N_{gen}^{PD}(M_Y < 1.6 \text{ GeV}, |t| < 1 \text{ GeV}^2) + R_{PD}^{EL} \cdot N_{gen}^{EL}(|t| < 1 \text{ GeV}^2)}, \quad (4.31)$$

where N_{gen}^{PD} represents the number of generated proton dissociation events, N_{rec}^{PD} is the number of reconstructed proton dissociation events after the diffractive selection, N_{gen}^{EL} gives the number of elastic generated events for the same luminosity as the proton dissociation Monte Carlo and R_{PD}^{EL} denotes the ratio of proton elastic to dissociative cross sections. The value of the correction is given in equation 4.32 below. There is an associated systematic error on this value, which is in fact the dominant systematic error on the measurement of $F_2^{D(3)}$. The four contributions to this error are:

- R_{PD}^{EL} was assumed to equal unity in equation 4.31. This ratio between the elastic and dissociative cross sections is varied between 1:2 and 2:1. This gave rise to a systematic error of $\pm 1.48\%$.
- The simulated efficiencies of the forward detectors used in the selection were varied in accordance with the method described in [105]. The recalibration factors of the PRT and FTS (given in table 4.4) are varied making them 100% efficient, and less efficient by the same amount, and the detection efficiency of the FMD was varied by $\pm 4\%$. The FMD contribution to the total systematic error was $\pm 0.53\%$. The contribution from varying the PRT and FTS factors yielded systematic errors of $\pm 7.51\%$ and $\pm 2.01\%$ respectively.
- The generated M_Y^2 distribution in the proton dissociation Monte Carlo simulation was varied by $(\frac{1}{M_Y^2})^{\pm 0.3}$, which contributes $\pm 2.48\%$ to the total systematic error.
- The slope parameter, b , in proton dissociation was varied by $\pm 1 \text{ GeV}^2$ according to the generated t -distribution e^{bt} . This contributed an additional $\pm 1.64\%$ to the systematic error.

The total systematic error on the net smearing, P , was found to be ± 0.085 , hence the final result for the smearing into the region $M_Y < 1.6 \text{ GeV}$ was:

$$P = 1.026 \pm 0.004 \text{ (stat.)} \pm 0.085 \text{ (syst.)}. \quad (4.32)$$

The significance of the correction being larger than unity is that more events are smearing into the region $M_Y < 1.6 \text{ GeV}$ than are smearing out of it.

The assumption that the ratio of proton elastic to dissociation events equals unity and does not vary with β , Q^2 or x_p is standard procedure for H1 $F_2^{D(3)}(\beta, Q^2, x_p)$ measurements but was tested here. Elastic diffractive scattering events involve dissociation at the $\gamma^* \mathbb{P}$

vertex (see figure 3.2 in chapter 3) whilst the intact proton escapes down the beam-pipe. Events of this kind (single dissociation events) are selected by demanding all diffractive cuts to be satisfied. Events where the proton also dissociates (double dissociation) into a low mass state are selected by requiring that at least one of the forward detector cuts is failed, but that either $\eta_{MAX} < 3.3$ or that there is a rapidity gap somewhere in the main detector spanning at least two units in pseudorapidity. Figure 4.17 shows the ratio of single (elastic) to double dissociation selections as a function of pseudorapidity η_{MAX} for uncorrected data events. It can be observed that this uncorrected ratio is consistent with a flat distribution (indicated by the straight line fit). Figure 4.18(a) shows the same ratio for two regions of Q^2 , with events in the range $1.25 \text{ GeV}^2 < Q^2 \leq 3.5 \text{ GeV}^2$ represented by the black data points and events in the region $3.5 \text{ GeV}^2 < Q^2 \leq 60 \text{ GeV}^2$ denoted by the red points. The black points in figure 4.18(b) represent the ratio for $0.00001 < x \leq 0.0002$ whilst the red points are for $0.0002 < x \leq 0.01$. There is no evidence for any variation with either Q^2 or x within the statistical errors shown. This is in accordance with the Regge factorisation hypothesis given in section 3.4.2. The ratio of the two selections is approximately 0.7 throughout the measured phase space. Crudely correcting for the efficiencies of the selections gives a single to double dissociation ratio of order unity, as assumed in equation 4.31.

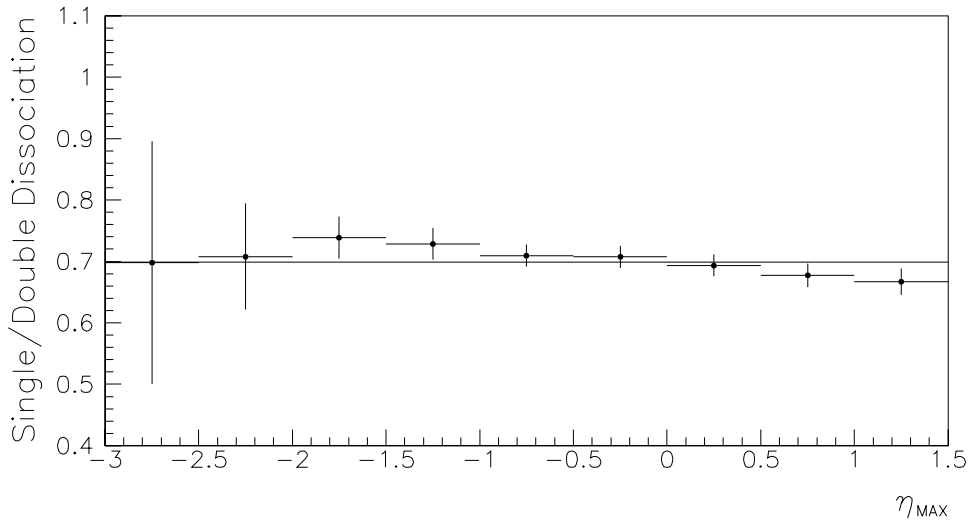
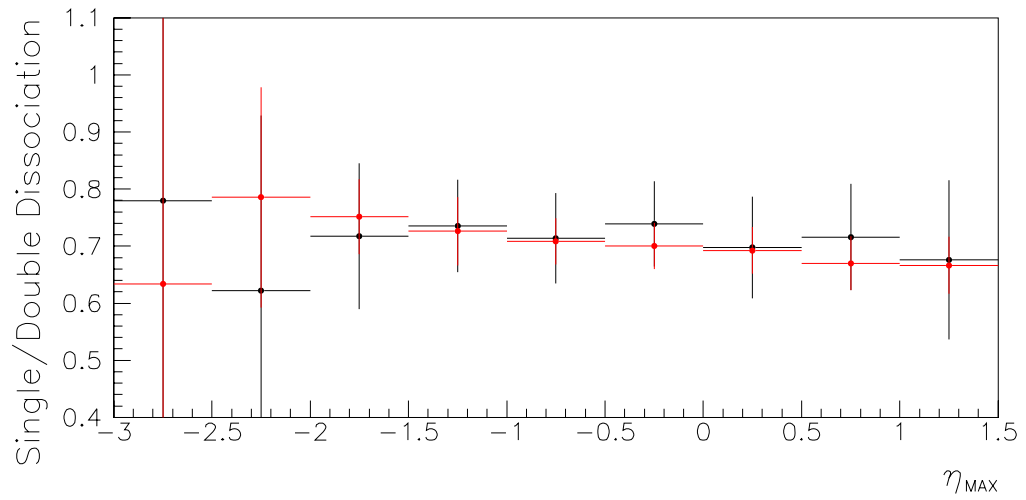
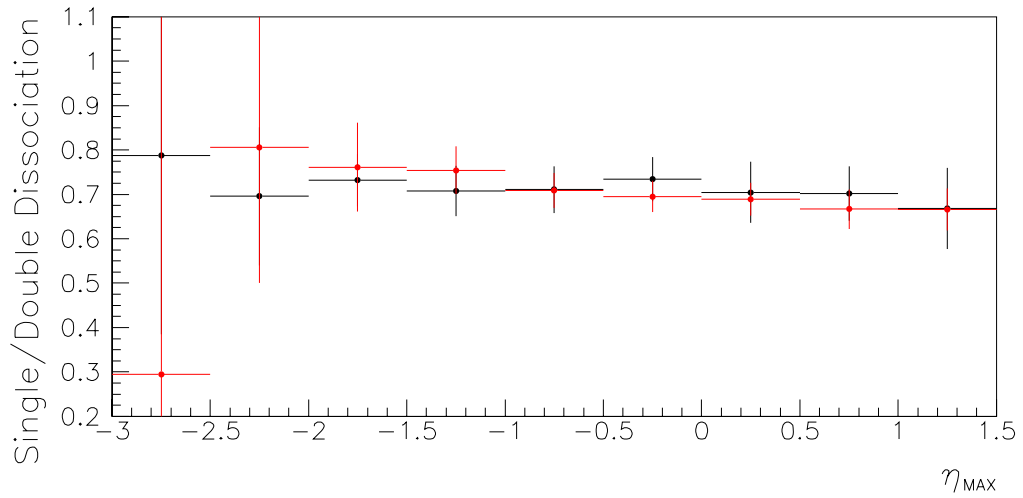


Figure 4.17: Uncorrected ratio of elastic to proton dissociation data events as a function of pseudorapidity η_{MAX} .



(a)



(b)

Figure 4.18: Uncorrected ratio of elastic to proton dissociation data events as a function of pseudorapidity η_{MAX} . Figure(a) represents the ratio in bins of low and high Q^2 represented by the black and red points respectively. The black and red points in figure (b) represent the ratio for low and high regions of x respectively.

4.8 Summary of Diffractive Selection

The diffractive structure function is measured in the region,

$$M_Y < 1.6 \text{ GeV}, \quad (4.33)$$

$$|t| < 1 \text{ GeV}^2, \quad (4.34)$$

$$x_{\mathcal{P}} < 0.05, \quad (4.35)$$

where, after the selection of an inclusive deep inelastic scattering sample, diffractive events are selected by the following demands on activity in the forward detector region of H1:

$$\eta_{MAX} < 3.3, \quad (4.36)$$

$$N_{PRT}(1, 2, 3, 4, 5, 7) = 0, \quad (4.37)$$

$$N_{FTS}(1, 2) = 0, \quad (4.38)$$

$$N_{FMD(1,2)} \leq 1 \text{ hit pair}, \quad (4.39)$$

$$N_{FMD(3)} \leq 2 \text{ hit pairs}, \quad (4.40)$$

$$E_{PLUG} < 5 \text{ GeV}. \quad (4.41)$$

Chapter 5 describes the extraction of the inclusive and diffractive structure functions and presents the results obtained from the 1999 minimum bias data.

Chapter 5

Measurement of the Diffractive Proton Structure Function

5.1 Inclusive DIS Studies

The inclusive control distributions of figures 4.8 - 4.10 demonstrated the good agreement achieved between data and Monte Carlo. The scattered positron and hadronic final state are well measured and understood after the application of Spacal and LAr calorimeter calibration factors. The inclusive structure function $F_2(x, Q^2)$ can therefore be extracted and compared with previous H1 measurements as a means of checking the procedure used to obtain cross sections and structure functions before the measurement is extended to diffraction. The 1999 minimum bias data studies for $F_2(x, Q^2)$ are presented in this section, and the diffractive measurement can be found in section 5.2.

5.1.1 Extraction of $F_2(x, Q^2)$

The relationship between the inclusive cross section and structure function was given in equation 2.19 in section 2.2.2. Neglecting the longitudinal contribution (and Z^0 exchange) to the inclusive cross section this can be rewritten in terms of the variables used in the measurement of $F_2(x, Q^2)$ as,

$$F_2(x, Q^2) = \frac{(N_{DATA} - N_{BG}) \cdot BCC \cdot RADC}{ACC \cdot BV \cdot LUM \cdot FAC} \frac{x_c Q_c^4}{4\pi\alpha^2 \left(1 - y_c + \frac{y_c^2}{2}\right)}, \quad (5.1)$$

where N_{DATA} is the number of data events in a given analysis bin and N_{BG} is the back-

ground contribution from photoproduction events (modelled by PHOJET). BCC is the bin centre correction and BV is the volume of the bin $\int dx dQ^2$, $RADC$ is the radiative correction (not explicitly calculated for this measurement) and ACC is the “smeared acceptance” (defined in section 5.1.5), calculated from DJANGO. x_c , Q_c^2 and y_c are the values at which the data point is quoted. The determination of these quantities is discussed in the following sub-sections. LUM is the luminosity of the data in units of pb^{-1} and FAC is a factor equal to $(\hbar c)^2 = 389379660 \text{ GeV}^2 \text{ pb}$ which is required to maintain a consistent treatment of units. The scheme used for the binning of the data is also presented in 5.1.3.

5.1.2 Background Contributions

The inclusive control plots of figures 4.8 - 4.10 showed the background contamination due to photoproduction events in the data sample at low E'_e (high y) and low Q^2 . The estimation of the number of photoproduction events obtained from PHOJET (N_{BG}) is subtracted from the number of data events (N_{DATA}), which have passed the standard DIS selection detailed in 4.6. The contribution is found to be small everywhere with the largest corrections, for the lowest values of Q^2 and highest y , being approximately 2%.

5.1.3 Binning Scheme

The binning scheme adopted for the measurement of $F_2(x, Q^2)$ is taken from a recent H1 publication [63] which presented $F_2(x, Q^2)$ measured from combined 1996 and 1997 data in the range $2 \text{ GeV}^2 < Q^2 < 150 \text{ GeV}^2$. The Q^2 and x values used are presented in tables 5.1 and 5.2 respectively. The data were divided into 13 Q^2 bins and 12 x bins.

5.1.4 Bin Centre Corrections

$F_2(x, Q^2)$ is calculated at the centres of the Q^2 and x bins defined in tables 5.1 and 5.2. However a small correction is required since the area under the F_2 function in each bin will not be symmetric about the bin centre due to the variation of $F_2(x, Q^2)$ across the bin. Also selections on y for example cut into the bin implying that only part of a bin is actually usable. Hence, the data are shifted up or down to correct for this effect. The bin centre correction (BCC) is defined as:

Q^2 bin	Lower limit (GeV ²)	Central Value (GeV ²)	Upper limit (GeV ²)
1	1.25	1.5	1.75
2	1.75	2.0	2.25
3	2.25	2.5	3.0
4	3.0	3.5	4.25
5	4.25	5.0	5.75
6	5.75	6.5	7.5
7	7.5	8.5	10.25
8	10.25	12.0	13.5
9	13.5	15.0	17.5
10	17.5	20.0	22.5
11	22.5	25.0	30.0
12	30.0	35.0	40.0
13	40.0	45.0	52.5

Table 5.1: Q^2 binning as used in the 1999 minimum bias data measurement of the inclusive structure function $F_2(x, Q^2)$.

x bin	Lower limit	Central Value	Upper limit
1	0.000026	0.000032	0.000041
2	0.000041	0.00005	0.000065
3	0.000065	0.00008	0.000105
4	0.000105	0.00013	0.000165
5	0.000165	0.0002	0.00026
6	0.00026	0.00032	0.00041
7	0.00041	0.0005	0.00065
8	0.00065	0.0008	0.00105
9	0.00105	0.0013	0.00165
10	0.00165	0.002	0.0026
11	0.0026	0.0032	0.0041
12	0.0041	0.005	0.0065

Table 5.2: x binning as used in the 1999 minimum bias data measurement of the inclusive structure function $F_2(x, Q^2)$.

$$BCC = \frac{F_2 \text{ at bin centre}}{\langle F_2 \rangle \text{ over bin}} = \frac{F_2(Q_c^2, x_c)}{\left[\frac{\int dQ^2 dx F_2(x, Q^2)}{\int dx dQ^2} \right]} = \frac{F_2(Q_c^2, x_c)}{\int F_2(x, Q^2) dQ^2 dx} \cdot BV, \quad (5.2)$$

where all integrals are over the x , Q^2 range of the analysis bin, BV is the bin volume, $\int dx dQ^2$, and $F_2(x, Q^2)$ represents a parameterisation of the H1 measurement taken from [63]. In order for this correction to be applicable to the data, the regions cut out

by y cuts etc. in the data must be rejected. Hence, the following cuts are imposed at the generator level of the Monte Carlo for the acceptance determination (section 5.1.5) and the integrals in equation 5.2,

- $E'_e(\text{gen}) > 6 \text{ GeV}$
- $153^\circ < \theta_e(\text{gen}) < 176.5^\circ$
- $E - p_z(\text{gen}) > 35 \text{ GeV}$
- $Q^2(\text{gen}) > 1.25 \text{ GeV}^2$
- $y(\text{gen}) > 0.05$

which exactly match the analysis cuts in section 4.6.

Figure 5.1 shows the bin centre corrections as a function of x for fixed Q^2 . The *BCCs* are observed to be reasonably constant with a value approximately equal to unity, with deviations only observed at the extremes of the ranges of x and Q^2 where the θ_e , y and E'_e cuts are important.

5.1.5 Acceptance and Purity Correction

The measurement of $F_2(x, Q^2)$ relies on binning the data and Monte Carlo according to the scheme in section 5.1.3. Corrections must be made for the loss of events due to the imperfect acceptance and efficiency of the detector using the Monte Carlo simulation. It is also possible for an event to be reconstructed in the wrong bin due to the finite resolution. A correction must therefore be performed for the smeared acceptance, defined as the ratio of reconstructed Monte Carlo events to generated Monte Carlo events. In order to calculate an error on this, the reconstructed and generated numbers of events must be divided into components with uncorrelated errors. Hence, the acceptance (*ACC* in equation 5.1) can be written as,

$$\text{Acceptance} = \frac{N(\text{rec})}{N(\text{gen})} = \frac{N_{\text{stay}} + N_{\text{come}}}{N_{\text{stay}} + N_{\text{go}} + N_{\text{lose}}}, \quad (5.3)$$

where, for events passing the reconstructed level cuts, N_{stay} defines the number of events generated in a bin and reconstructed in the same bin, N_{go} gives the number of events

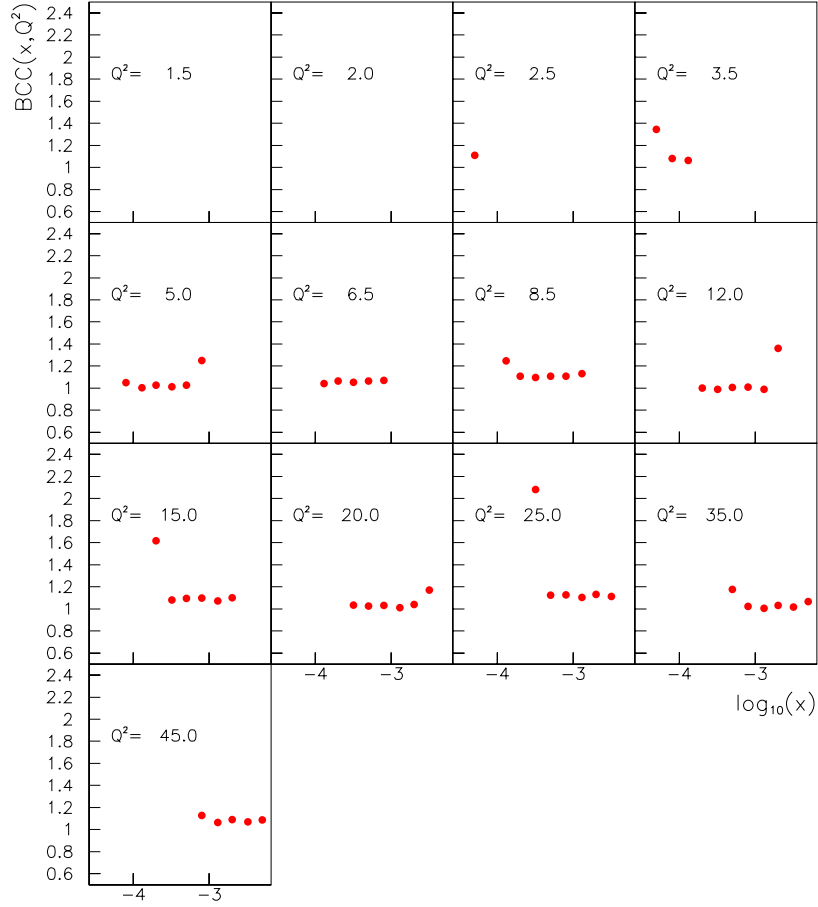


Figure 5.1: Bin centre corrections for the inclusive proton structure function $F_2(x, Q^2)$ as a function of x in bins of Q^2 .

generated in a bin but reconstructed elsewhere and N_{come} describes events reconstructed in a bin that were generated elsewhere. For events failing the reconstructed level cuts, N_{lose} gives the number of events generated in a bin. In terms of the same component variables, purity, stability and smearing terms can also be defined:

$$\text{Purity} = \frac{N(\text{gen and rec})}{N(\text{rec})} = \frac{N_{\text{stay}}}{N_{\text{stay}} + N_{\text{come}}}, \quad (5.4)$$

$$\text{Stability} = \frac{N(\text{gen and rec})}{N(\text{gen})} = \frac{N_{\text{stay}}}{N_{\text{stay}} + N_{\text{go}} + N_{\text{lose}}}, \quad (5.5)$$

$$\text{Smearing} = \frac{N(\text{gen}) - N(\text{rec})}{N(\text{gen})} = \frac{N_{\text{go}} + N_{\text{lose}} - N_{\text{come}}}{N_{\text{stay}} + N_{\text{go}} + N_{\text{lose}}}, \quad (5.6)$$

For a perfect acceptance, purity and stability, a value of 1 is expected, and a smearing value of 0. For this measurement both the acceptance and purity in each bin were required to be greater than 30%.

5.1.6 Systematic Errors

There are, as with every cross section measurement, several systematic uncertainties arising from imperfect understanding of detector components and of the models used in generating the Monte Carlo events. A full systematic error analysis was not performed for the $F_2(x, Q^2)$ measurement. Instead for those systematic effects which are common to both measurements the average fractional systematic errors as calculated for $F_2^{D(3)}(\beta, Q^2, x_{\mathcal{P}})$ (for which a full description is given in section 5.2.7) were applied to the $F_2(x, Q^2)$ measurement. The total systematic error shown on the data points takes into account uncertainties in the positron energy and polar angle, hadronic Spacal and LAr calorimeter energy scales, vertex and trigger efficiencies, and bin centre corrections. An uncertainty is also included to compensate for the absence of radiative corrections on the data points. This corresponds to a total error of $\pm 8.7\%$. A normalisation error, arising from uncertainties in the luminosity determination and BDC efficiency, is not shown but contributes an additional 2.2% error.

5.1.7 Results for $F_2(x, Q^2)$

The results obtained for $F_2(x, Q^2)$ are shown at fixed values of x as a function of Q^2 in figure 5.2 and at fixed values of Q^2 as a function of x in figure 5.3. The red points are $F_2(x, Q^2)$ measured in this analysis and the blue points are from a recent H1 publication on 1996-1997 data [63]. Both measurements are shown with inner statistical and outer total (statistical and systematic added in quadrature) errors.

The 1999 minimum bias data sample comprises much less luminosity than the 1996-1997 published data and were selected for a diffractive physics measurement, hence the non-diffractive events were down-scaled as described in section 4.4. This means the sample has about a factor 10 less statistics than the published H1 measurement shown in figures 5.2 and 5.3. In addition no detailed work on systematic errors or radiative corrections has been done for this $F_2(x, Q^2)$ extraction. The published data extend to lower Q^2 and lower y than the present measurement due to the additional use of the BST for vertex finding. That detector has not been used in the present analysis. Some low Q^2 , low x

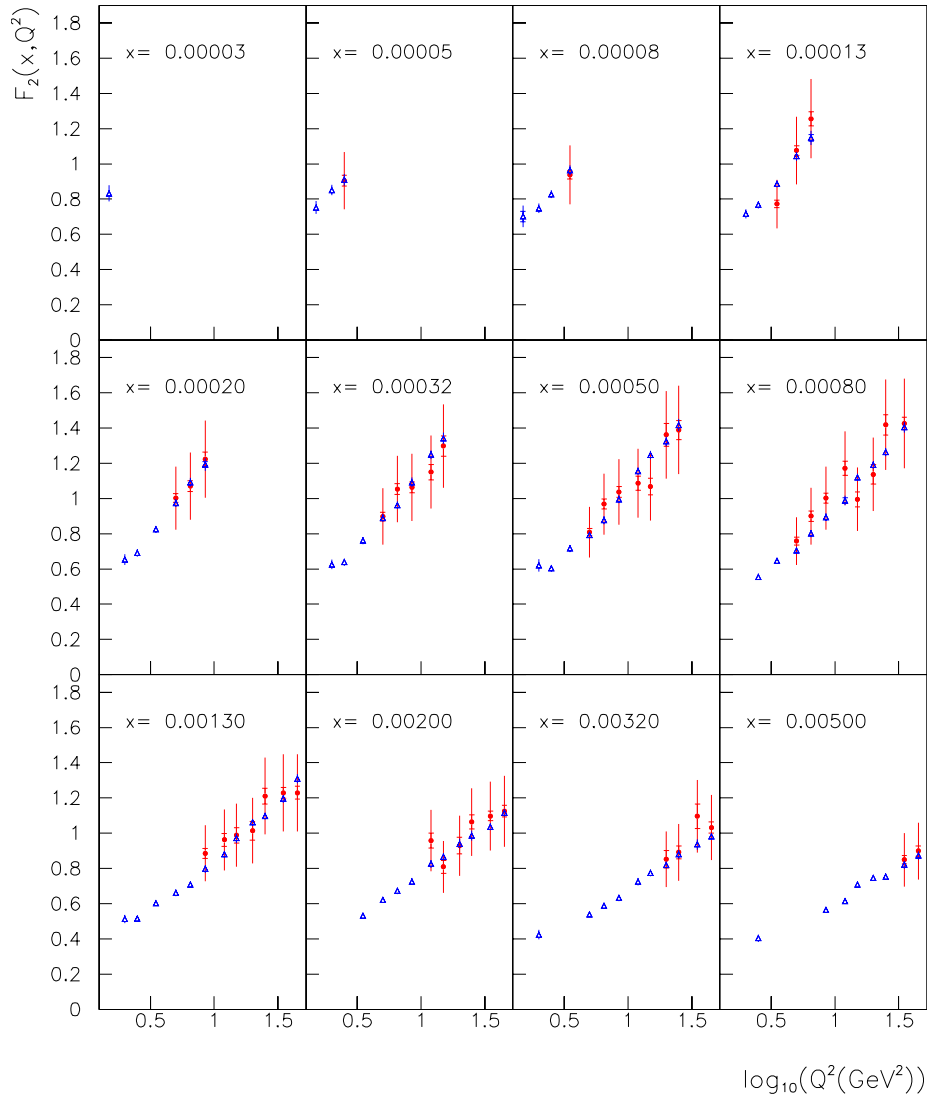


Figure 5.2: The inclusive proton structure function $F_2(x, Q^2)$ extracted from this measurement (red points) compared with a previous H1 publication [63] (blue points). The measurements are shown as a function of Q^2 in bins of x .

points are also lost due to low acceptance originating from applying the Spacal fiducial cuts. However, a good agreement is observed between the two measurements within errors, with the implication that the data are well understood and properly modelled by the inclusive Monte Carlo. Therefore, with the positron detection in the Spacal under control, the extension to diffraction is well founded.

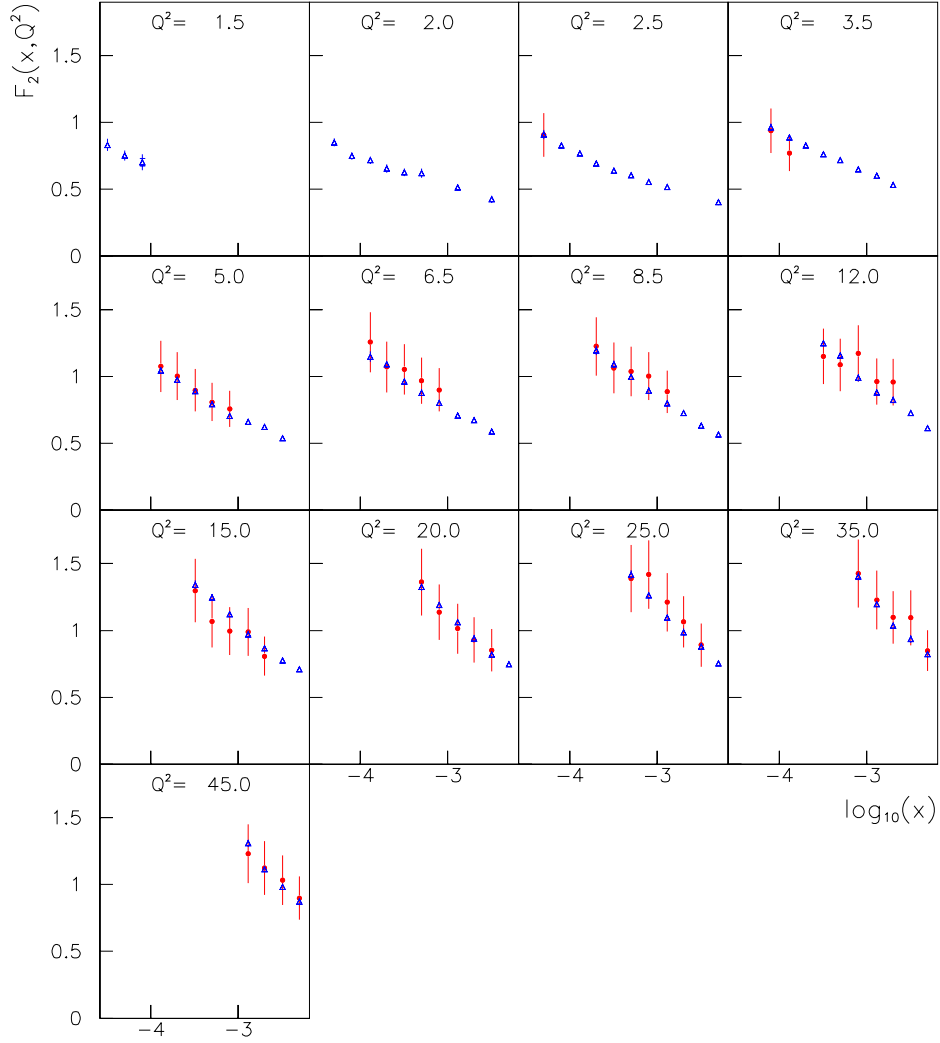


Figure 5.3: The inclusive proton structure function $F_2(x, Q^2)$ extracted from this measurement (red points) compared with a previous H1 publication [63] (blue points). The measurements are shown as a function of x in bins of Q^2 .

5.2 Diffractive Measurements

The following sections describe the extraction of the structure function $F_2^{D(3)}(\beta, Q^2, x_p)$. The control plots in chapter 4 showed that a reasonable description of the diffractive data was obtained after the RAPGAP Monte Carlo was reweighted in accordance with the method detailed in section 4.7.3. Hence, the diffractive proton structure function can be measured following the same method used for $F_2(x, Q^2)$. The final results are presented in section 5.2.8.

5.2.1 Measurement of $F_2^{D(3)}(\beta, Q^2, x_P)$

Neglecting the small $F_L(x, Q^2)$ contributions, the diffractive structure function as given in equation 3.12, can be rewritten in terms of the “measurement variables” as,

$$F_2^{D(3)}(\beta, Q^2, x_P) = \frac{(N_{DATA} - N_{BG}) \cdot BCC \cdot RADC}{ACC \cdot BV \cdot P \cdot LUM \cdot FAC} \frac{\beta_c Q_c^4}{4\pi\alpha^2 \left(1 - y_c + \frac{y_c^2}{2}\right)}, \quad (5.7)$$

where $RADC$ is the radiative correction defined in equation 5.8, which is required because the cross section is defined at the QED Born Level, P is the correction due to smearing across the $M_Y < 1.6$ GeV, $|t| < 1$ GeV² boundary (as described in section 4.7.5) and the other variables are as described in section 5.1.1. The number of background events N_{BG} now also takes QED-Compton scattering events into account (section 5.2.2) and the acceptance correction, ACC , is calculated using RAPGAP, DJANGO and DIFFVM for the diffractive case. Note that since the binning is performed in x but $F_2^{D(3)}$ is defined as a function of $x_P = x/\beta$, the x_c term on the right hand side of equation 5.1 has changed to β_c .

5.2.2 Background Contributions

There are two sources of background (N_{BG}) to the diffractive DIS sample for which the cross section has to be corrected. The background arising from photoproduction events, estimated using the PHOJET Monte Carlo, contributes mainly at low Q^2 and high y typically at a level of 1 – 2%. A background due to QED-Compton scattering processes, modelled by COMPTON, is also present with the largest contributions at high β . The correction to the data is typically less than 1% at low-medium β .

5.2.3 Binning scheme

The x and Q^2 binning is inherited from the inclusive measurement. Hence, the values in tables 5.1 and 5.2 are still valid, but now the data are also binned in β as in [69] and [78] but extending the β range slightly lower (due to the lower Q^2 values accessible). Table 5.3 below details the binning scheme in β .

The final value for the structure function is given in terms of Q^2 , x_P and β . x_P here is simply evaluated from the bin centre values and $x_P = \frac{x}{\beta}$, as defined in equation 3.7 in

β bin	Lower limit	Central Value	Upper limit
1	0.0005	0.001	0.005
2	0.005	0.01	0.023
3	0.023	0.04	0.07
4	0.07	0.1	0.14
5	0.14	0.2	0.3
6	0.3	0.4	0.5
7	0.5	0.65	0.8
8	0.8	0.9	1.0

Table 5.3: β binning used in the 1999 minimum bias data measurement of the diffractive structure function $F_2^{D(3)}(\beta, Q^2, x_P)$.

section 3.2.

5.2.4 Radiative Corrections

A correction is applied to the data in order to correct $F_2^{D(3)}(\beta, Q^2, x_P)$ to the QED Born level after removing smearing due to initial and final state photon radiation and correcting for virtual loops. The correction factor is given by,

$$RADC = \frac{F_2^{D(3)}(\text{NON - RADIATIVE})}{F_2^{D(3)}(\text{RADIATIVE})}, \quad (5.8)$$

which is calculated from separate samples of Monte Carlo (RAPGAP) generated with and without QED radiative effects, with the requirement $E - p_z > 35$ GeV applied at the generator level. The luminosity of each sample was approximately 95 pb^{-1} . The correction factor ($RADC$) obtained, shown in figure 5.4, was observed to be reasonably constant over the entire phase space with a value typically equal to 0.95 which varied only by 20% at most for the highest x_P values.

5.2.5 Bin Centre Corrections

As described in section 5.1.4, the inclusive data were bin-centre-corrected before the structure function was evaluated. The same arguments apply here and the process must be repeated, this time including the β binning and using a parameterisation of $F_2^{D(3)}(\beta, Q^2, x_P)$

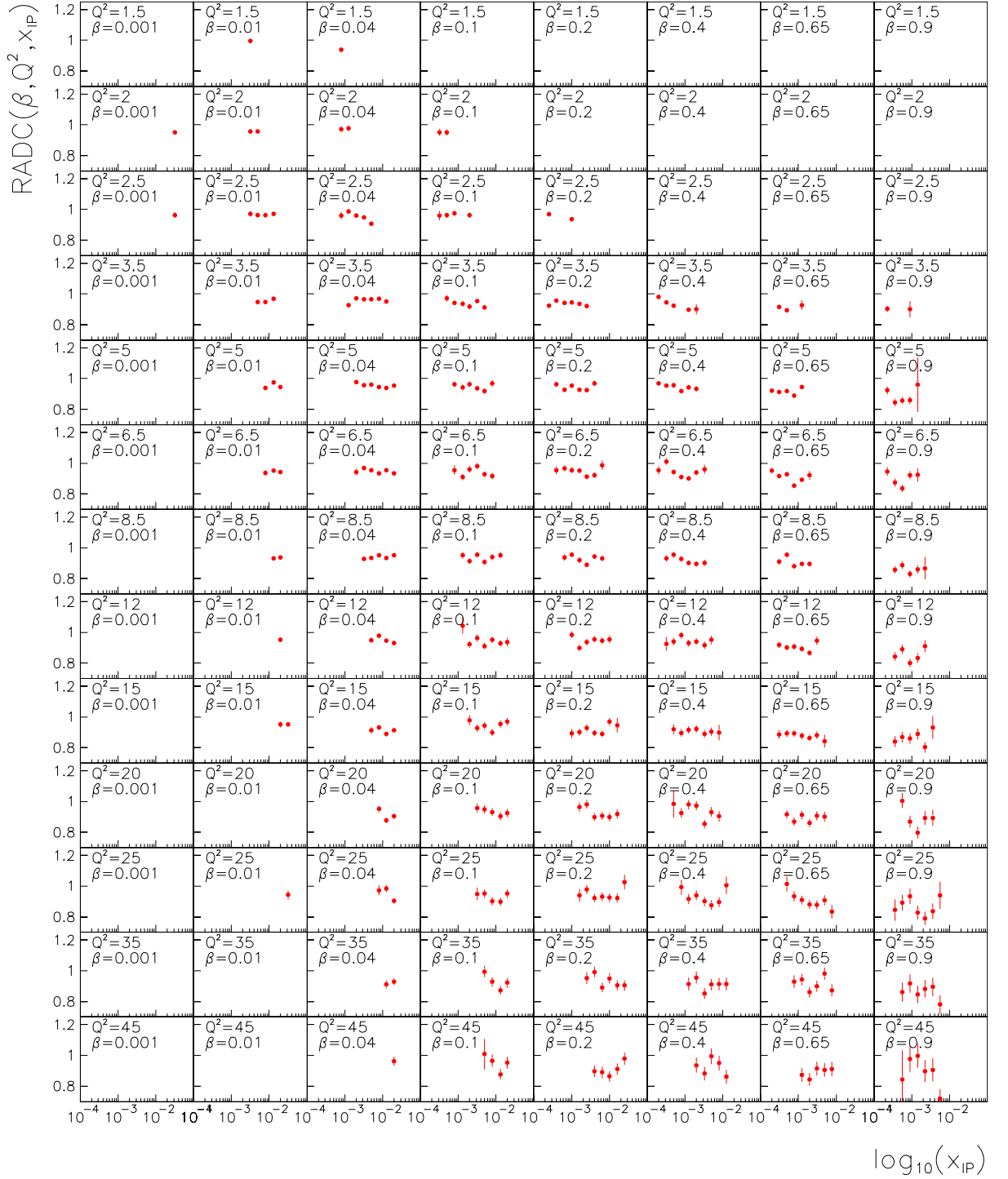


Figure 5.4: Radiative corrections for the diffractive structure function, $F_2^{D(3)}(\beta, Q^2, x_P)$ shown as a function of x_P for fixed values of β and Q^2 , with β increasing from left to right and Q^2 increasing from top to bottom.

taken from [69]. Hence, the bin centre correction for the diffractive structure function is given by,

$$BCC = \frac{F_2^{D(3)}(\beta_c, Q_c^2, x_c)}{\int F_2^{D(3)} d\beta dQ^2 dx} \cdot BV. \quad (5.9)$$

The additional diffractive generator level cuts applied, for the same reasons as in the inclusive case, were:

- $M_Y(\text{gen}) < 1.6 \text{ GeV}$
- $|t(\text{gen})| < 1 \text{ GeV}^2$

Figure 5.5 shows the bin centre corrections for $F_2^{D(3)}(\beta, Q^2, x_P)$. As for the $F_2(x, Q^2)$ measurement the corrections are observed to be approximately equal to one for the most part, with occasional deviations occurring at the kinematic limits of the measurement.

5.2.6 Acceptance and Purity Calculations

Equations 5.3 - 5.6 are still valid for the diffractive measurement. Again cuts on acceptance and purity are imposed but in this case the acceptance is factorised into an inclusive part where standard DIS cuts are applied and a diffractive DIS part where the diffractive selection is applied in addition. Respective acceptance cuts of 20% and 50% are applied. A cut at 20% on purity is applied which is lower here than that in the inclusive case due to the three-dimensional binning. Figures 5.6 and 5.7 respectively show the factorised diffractive acceptance and purity in all bins of Q^2 and β , including those that are rejected for the $F_2^{D(3)}(\beta, Q^2, x_P)$ measurement, as a function of x_P . The diffractive acceptance is observed to be reasonably constant except for the low β , high x_P (high η_{MAX}) and low Q^2 , high x (high θ_e) regions. The purity is approximately flat except at the limits of the measurement.

5.2.7 Systematic Errors

A full systematic error analysis was performed for the measurement of $F_2^{D(3)}(\beta, Q^2, x_P)$. The systematic uncertainties arise from imperfect understanding of detector components

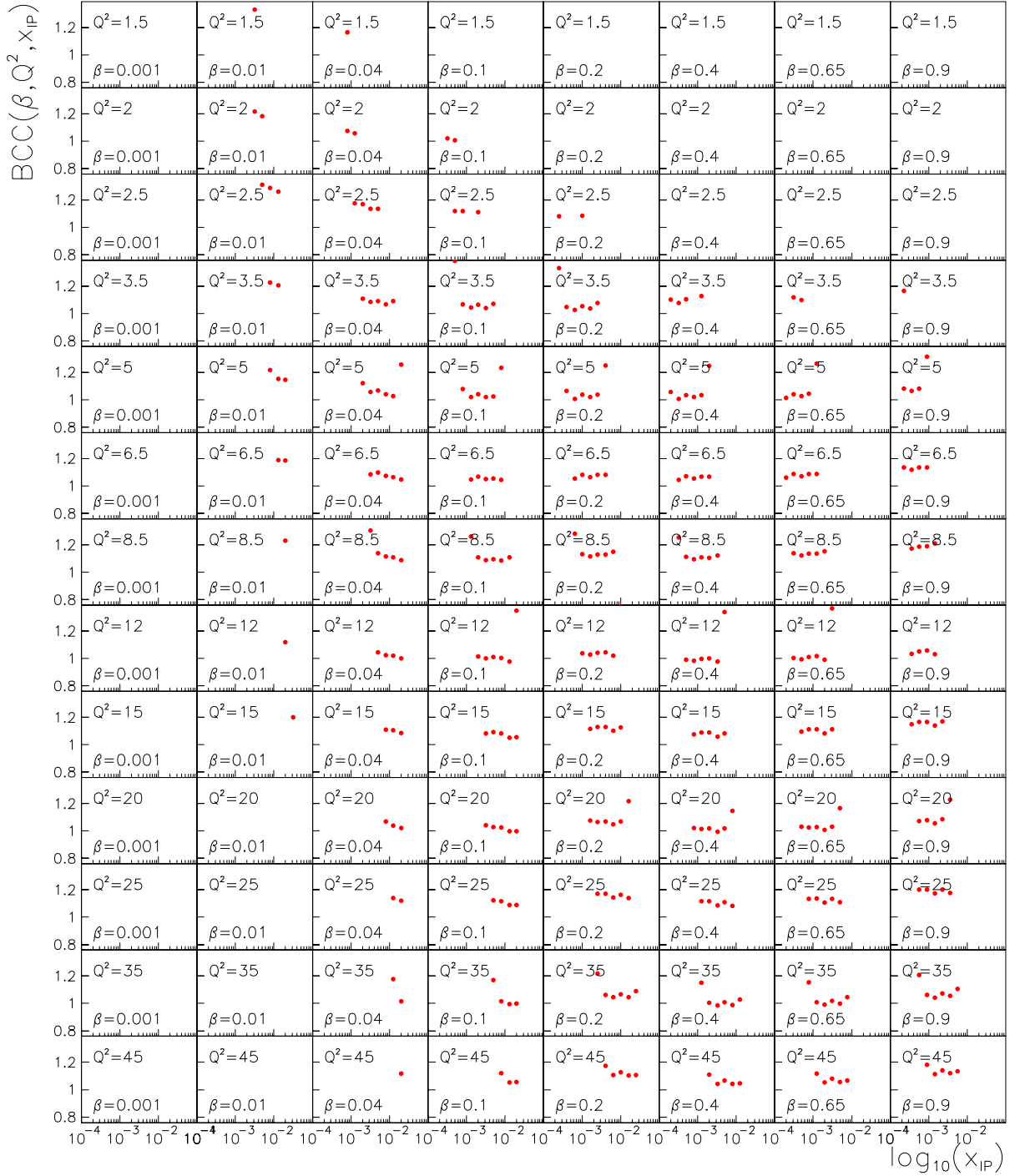


Figure 5.5: Bin centre corrections for the diffractive structure function, $F_2^{D(3)}(\beta, Q^2, x_P)$ shown as a function of x_P for fixed values of β and Q^2 , with β increasing from left to right and Q^2 increasing from top to bottom.

and uncertainties in the models used in generating the Monte Carlo events. The systematic uncertainties taken into account for this measurement and evaluated separately for each

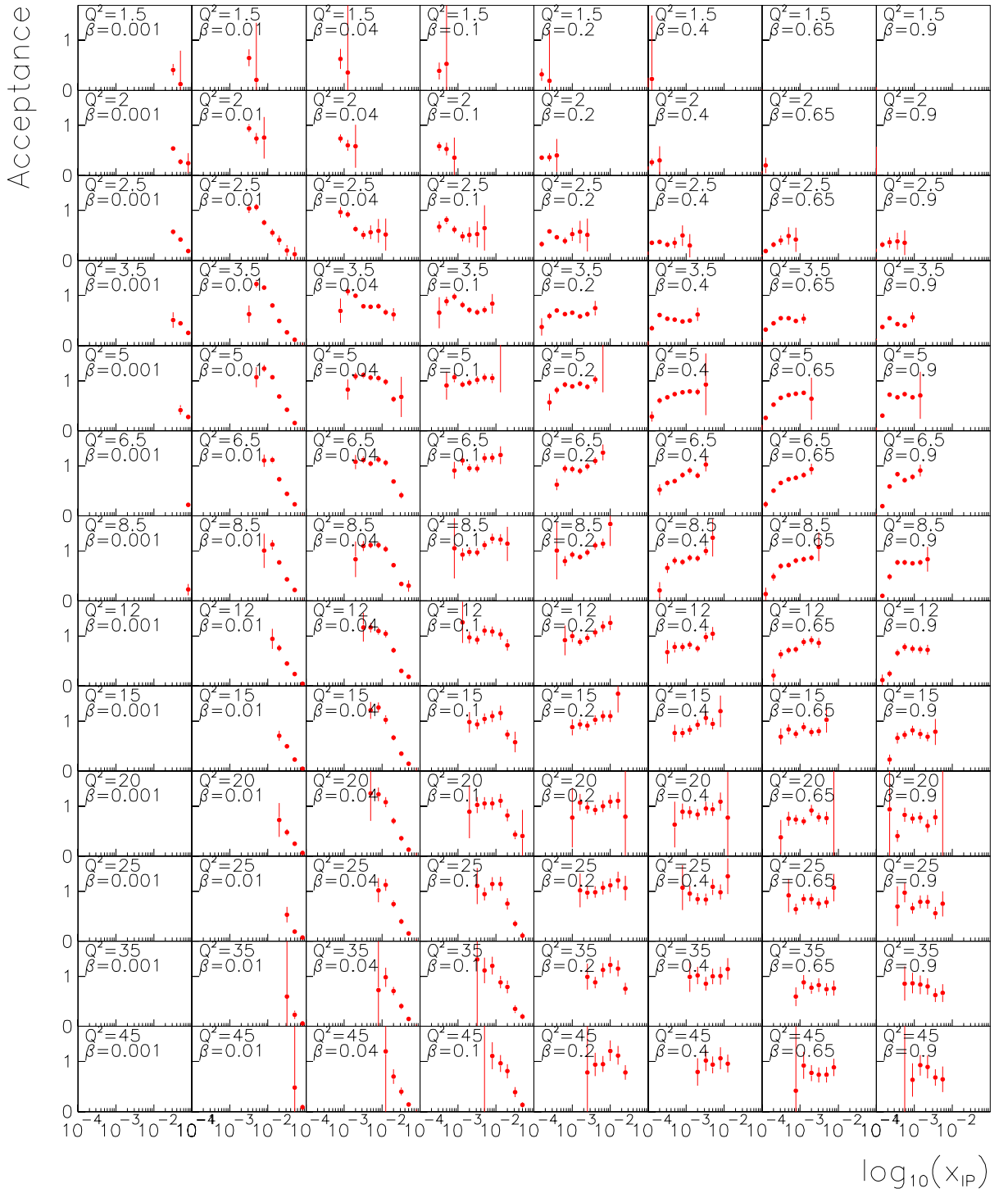


Figure 5.6: Diffractive acceptance for the extraction of the diffractive structure function, $F_2^{D(3)}(\beta, Q^2, x_P)$ shown as a function of x_P for fixed values of β and Q^2 , with β increasing from left to right and Q^2 increasing from top to bottom.



Figure 5.7: Purity for the extraction of the diffractive structure function, $F_2^{D(3)}(\beta, Q^2, x_P)$ shown as a function of x_P for fixed values of β and Q^2 , with β increasing from left to right and Q^2 increasing from top to bottom.

bin of the measurement are summarised below:

Detector Calibration and Efficiency Uncertainties:

- *The LAr energy scale:*

The uncertainty in performing the hadronic calibration of the liquid argon detector leads to an uncertainty in the absolute LAr calorimeter energy scale of $\pm 4\%$ which corresponds to an uncertainty in the final measurement of $\sim \pm 1.5\%$.

- *The Spacal hadronic energy scale:*

The equivalent error for the absolute Spacal hadronic energy scale is 7% which leads to an uncertainty of $\sim \pm 1.4\%$.

- *Energy carried by tracks:*

The fraction of energy in the hadronic final state algorithm described in section 4.7.2 carried by tracks is varied by $\pm 3\%$. This propagates $\sim \pm 1\%$ error into the final $F_2^{D(3)}(\beta, Q^2, x_P)$.

- *The Spacal positron energy scale:*

The uncertainty in the energy scale in the electromagnetic part of the Spacal is $\pm 1\%$ yielding an error on the final measurement of $\sim \pm 2.9\%$.

- *Determination of θ_e :*

The uncertainty in measuring the polar angle of the positron is $\pm 1.5 \text{ mrad}$ ¹ giving the second largest individual error of $\sim \pm 4.5\%$.

- *Forward detectors:*

The forward detectors are not fully efficient hence the frequency with which activity is ignored for the PRT and FTS is varied by 25% . The efficiency of the forward muon detector is varied by $\pm 5\%$ as a measure of the systematic uncertainty. The uncertainty in the Plug calorimeter energy scale is $\pm 30\%$. Together these errors contribute $\sim \pm 0.9\%$ to the final $F_2^{D(3)}(\beta, Q^2, x_P)$ measurement in addition to the errors they induce on the M_Y smearing correction (see section 4.7.5).

¹This number is larger than is usually quoted ($\pm 0.5 \text{ mrad}$) since no detailed Spacal-BDC alignment information was available.

Monte Carlo Uncertainties:

- *Simulated x_P distribution:*

The uncertainty in the x_P distribution modelled in RAPGAP is estimated by reweighting the distribution by $(1/x_P)^{\pm 0.2}$. This choice is larger than the range of possibilities allowed by the measured data points, which is also the case for the other Monte Carlo uncertainty systematic errors below. The variation leads to an error on the final measurement of $\sim \pm 1.4\%$.

- *Simulated β distribution:*

The β distribution is reweighted by factors $\beta^{\pm 0.1}$ and $(1 - \beta)^{\pm 0.1}$ to provide systematic uncertainties of $\sim \pm 0.8\%$ and $\sim \pm 0.6\%$ in the measured $F_2^{D(3)}(\beta, Q^2, x_P)$ respectively.

- *t slope:*

Similarly the t distribution is reweighted by $\pm e^{\pm 2t}$, which propagates to an uncertainty of $\sim \pm 0.2\%$ on $F_2^{D(3)}(\beta, Q^2, x_P)$.

- *Q^2 distribution:*

The uncertainty in the Q^2 distribution in the Monte Carlo is evaluated by reweighting the distribution by factors $\log_{10}(Q^2)^{\pm 0.2}$. This leads to an error of $\sim \pm 0.4\%$ in the structure function measurement.

- *High x_P background:*

It is possible for events generated in the region $x_P > 0.1$ and $M_Y > 5$ GeV simulated using DJANGO to enter the sample. Hence, the number of DJANGO events is varied by $\pm 100\%$ resulting in a $\sim \pm 2.3\%$ effect on the measurement.

- *Vector meson simulation:*

The normalisation of the DIFFVM simulation was varied by $\pm 50\%$ to provide the systematic uncertainty. This was found to be $\sim \pm 1.1\%$.

- *Photoproduction background:*

The uncertainty in the number of events entering the sample due to photoproduction background is estimated by varying the PHOJET normalisation by $\pm 100\%$. This provides an uncertainty in the measurement of $F_2^{D(3)}$ of $\sim \pm 4\%$.

- *QED Compton background:*

The uncertainty on background from QED Compton events is evaluated by varying the number of contributing events by $\pm 50\%$. An uncertainty in the measurement of $\sim \pm 2.5\%$ is obtained.

Uncorrelated Errors:

The following uncertainties are applied in the form of a percentage error which is the same in all bins. They are treated as uncorrelated between bins in the fits that follow in section 5.3 due to a lack of knowledge about the correlations between them.

- *Trigger efficiency:*

The triggers used in this analysis were assumed to be 100% efficient, which was demonstrated in section 4.3.2. The uncertainty in this is estimated to be $\sim \pm 1\%$ [78].

- *Ratio of elastic to proton dissociation processes:*

The contributing uncertainties to the correction for smearing about the M_Y limit of the measurement were described in section 4.7.5. The variation of the ratio of elastic to proton dissociation events leads to an uncorrelated error of $\sim \pm 1.5\%$.

- *Bin-centre and radiative corrections:*

Evaluation of the bin-centre and radiative corrections, described in sections 5.2.4 and 5.2.5 respectively, have a related systematic uncertainty of $\pm 3\%$.

Normalisation Uncertainties:

The uncertainty in determining the luminosity leads to an overall normalisation error on all data points of $\pm 2\%$. The uncertainty in the efficiency of the BDC is taken to be $\pm 1\%$ and the error in determining the noise corrections required for the forward detectors is $\pm 0.6\%$. The remaining contributions to the correction for migrations across the M_Y and t measurement boundary (section 4.7.5) are also taken to contribute to the normalisation uncertainty. This combined smearing error of $\pm 8.2\%$ is the dominant systematic error in the measurement of the diffractive structure function. The total normalisation error, which is not shown on the final data points is $\pm 8.5\%$.

5.2.8 Results for $F_2^{D(3)}(\beta, Q^2, x_P)$

The measured $F_2^{D(3)}(\beta, Q^2, x_P)$ is shown in figure 5.8 as a function of x_P in bins of Q^2 (which increase down the page) and β (which increase across the page). The data points are shown with inner statistical and outer total (statistical and systematic added in quadrature) errors. The normalisation uncertainty of $\pm 8.5\%$ is not shown. The vertical scale in the first three Q^2 bins has been altered with respect to the others in order that the behaviour of the distribution may be more easily examined in this new low Q^2 region.

The data are observed to stay constant or rise slowly with decreasing x_p at fixed β and Q^2 . This behaviour is consistent with previous measurements and therefore typical of the pomeron exchange observed in DIS. The points at the smallest x_p are observed to lie lower than expected, which will have an effect on the phenomenological fits presented in section 5.3. The reason for this is unknown and requires further investigation in the future.

The data were compared with two previous H1 measurements. Figure 5.9 shows the measured $F_2^{D(3)}(\beta, Q^2, x_p)$ compared with a low Q^2 measurement on shifted vertex data collected in 1995 [80] which had a luminosity of 0.12 pb^{-1} (compared with 3.74 pb^{-1} for this measurement). It can be seen that the superior statistics of the 1999 minimum bias data allow the evaluation of the structure function at more x_p bins with much smaller errors. Phenomenological fits to the data are therefore more easily performed and these will be discussed in section 5.3. The plot shows $F_2^{D(3)}$ in the region of overlap between the 1999 minimum bias measurement and that performed on the shifted vertex 1995 data, which is $1.5 \text{ GeV}^2 < Q^2 < 5 \text{ GeV}^2$. Hence, although the minimum bias running does not access the lowest values of Q^2 reached in a shifted vertex set-up (the 1995 measurement spans $0.4 \text{ GeV}^2 < Q^2 < 5 \text{ GeV}^2$) a more statistically significant measurement has been performed in the region of overlap and no H1 $F_2^{D(3)}$ data have been published below $Q^2 = 4.5 \text{ GeV}^2$. An extra bin in the Q^2 interval for 2.0 GeV^2 is also possible due to the higher statistics. The level of agreement is acceptable, except at $Q^2 = 1.5 \text{ GeV}^2$ where the reason for the disagreement is not yet known.

The 1999 minimum bias $F_2^{D(3)}(\beta, Q^2, x_p)$ values were also compared with the latest $F_2^{D(3)}(\beta, Q^2, x_p)$ measurement on 1997 data to be released as preliminary by H1. Figure 5.10 shows the 1999 minimum bias data points compared with the 1997 data [78] and figure 5.11 makes this comparison for fixed β values at $Q^2 = 6.5 \text{ GeV}^2$. Figure 5.12 compares the two measurements for the entire region of overlap where $(F_2^{D(3)}(1999) - F_2^{D(3)}(1997))/F_2^{D(3)}(1999)$ is plotted as a function of x_p . The discrepancies between the 1997 and the 1999 data at the lowest x_p (highest y) values are clearly visible. Elsewhere however an excellent agreement is observed between the 1999 measurement, extracted using the saturation model in RAPGAP, and the 1997 measurement for $6.5 \text{ GeV}^2 < Q^2 < 120 \text{ GeV}^2$ which used the resolved pomeron model in RAPGAP. The forward detector selections and other systematics are also rather different between the two measurements. The 1999 measurement is the most statistically significant measurement of $F_2^{D(3)}(\beta, Q^2, x_p)$ yet at low Q^2 extending to $\sim 12 \text{ GeV}^2$ after which the 1997 measurement is statistically better. The good agreement with this higher Q^2 data gives confidence in the lower Q^2 $F_2^{D(3)}(\beta, Q^2, x_p)$ measurement down to the lowest Q^2 values (1.5 GeV^2).

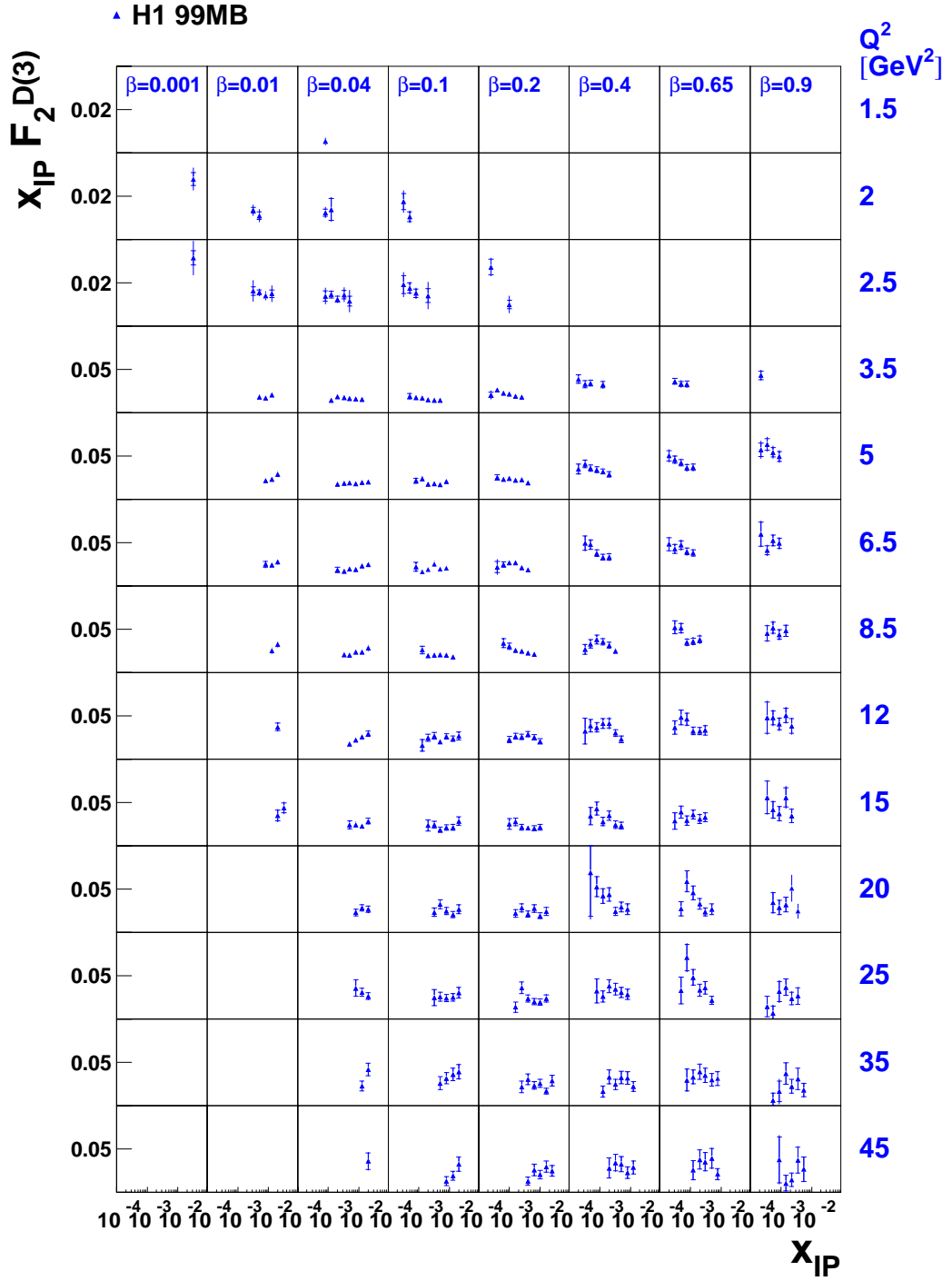


Figure 5.8: The diffractive proton structure function extracted from the 1999 minimum bias data. $x_{IP} F_2^{D(3)}(\beta, Q^2, x_{IP})$ is shown as a function of x_{IP} for fixed values of β and Q^2 , with β increasing from left to right and Q^2 increasing from top to bottom. The data points are shown with inner statistical and outer total (statistical and systematic in quadrature) errors. A normalisation error of $\pm 8.5\%$ is not shown.

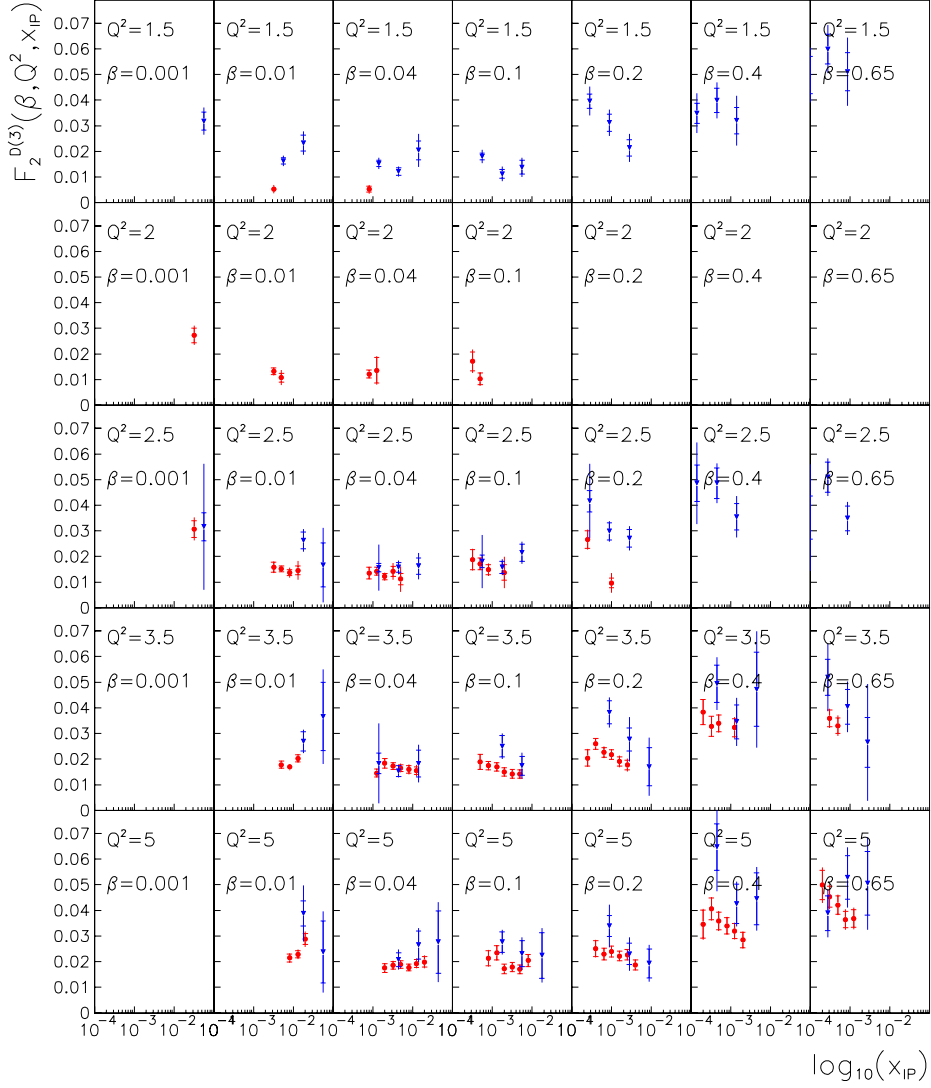


Figure 5.9: The diffractive proton structure function from this measurement (red points) compared with a previous unpublished H1 measurement [80] (blue points). $x_P F_2^{D(3)}(\beta, Q^2, x_P)$ is shown as a function of x_P for fixed values of β and Q^2 . Both measurements are shown with total (statistical and systematic) errors. The statistical errors for the 1999 measurement are represented by the inner error bars.

Hence, this measurement extends the kinematic region from which H1 has extracted the diffractive structure function by a substantial amount.

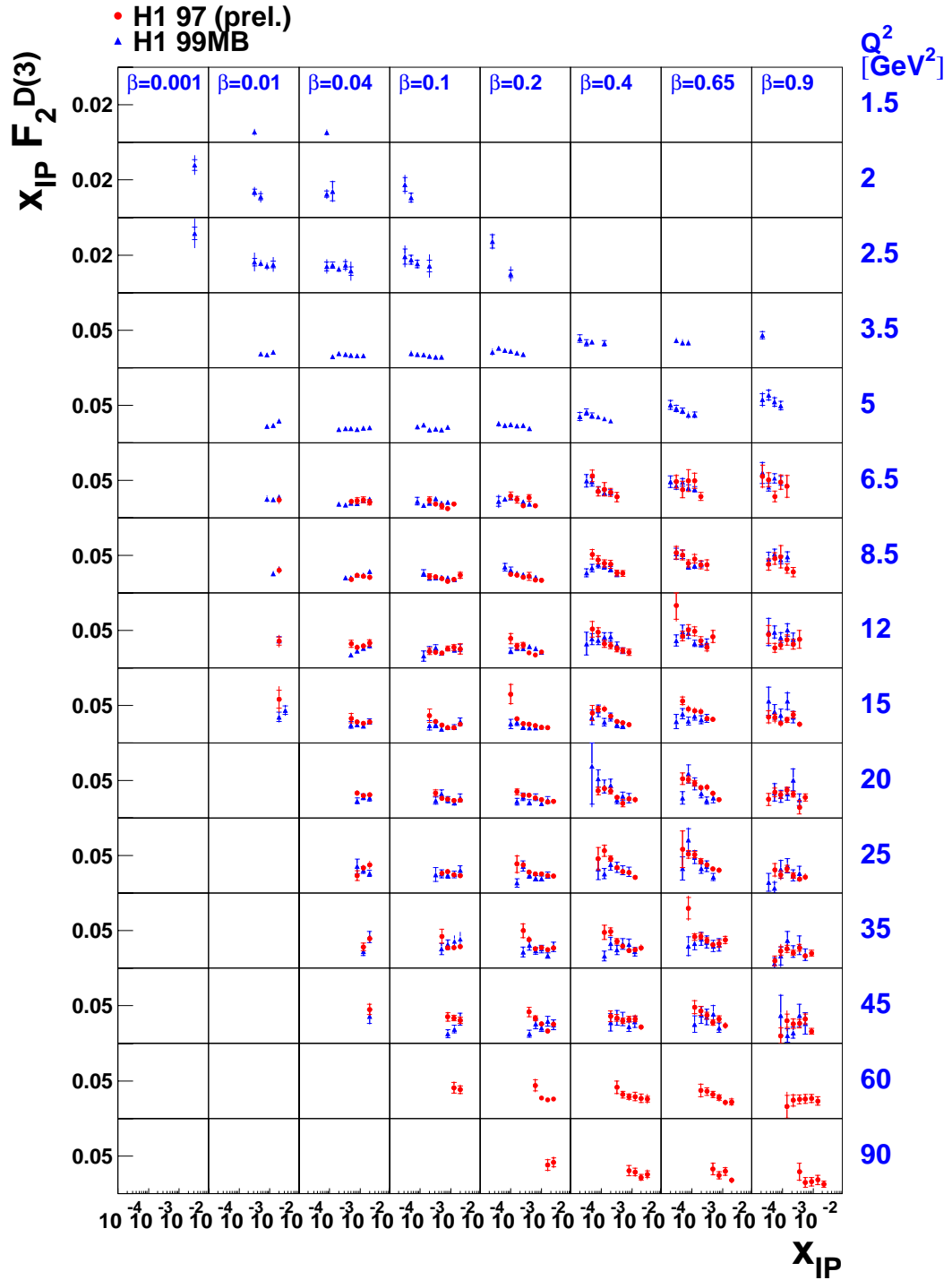


Figure 5.10: The diffractive structure function from this measurement (red points) compared with a recent H1 measurement [78] (blue points). $x_{\mathcal{P}} F_2^{D(3)}(\beta, Q^2, x_{\mathcal{P}})$ is shown as a function of $x_{\mathcal{P}}$ for fixed values of β and Q^2 , with β increasing from left to right and Q^2 increasing from top to bottom. Both measurements are shown with inner statistical and outer total (statistical and systematic added in quadrature) errors. The vertical scale in the first three Q^2 bins has been altered with respect to the others.

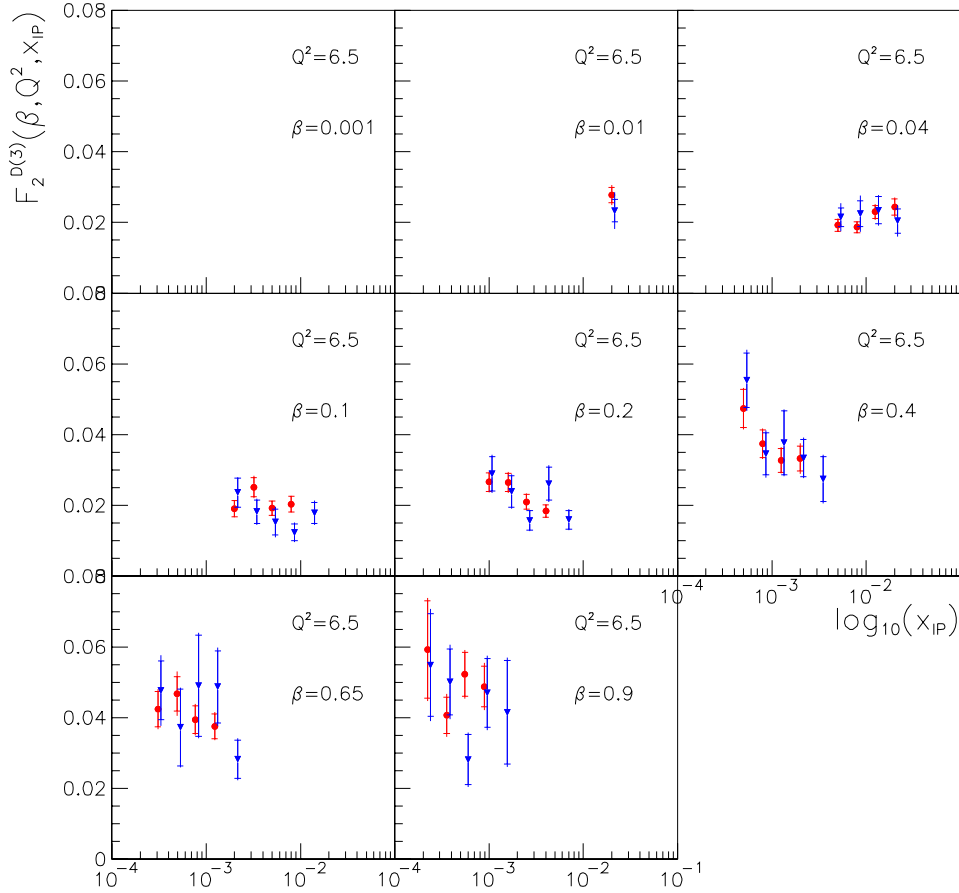


Figure 5.11: The diffractive structure function from this measurement (red points) compared with a recent H1 measurement [78] (blue points). $x_{\mathbb{P}} F_2^{D(3)}(\beta, Q^2, x_{\mathbb{P}})$ is shown as a function of $x_{\mathbb{P}}$ at $Q^2 = 6.5 \text{ GeV}^2$ for fixed values of β . Both measurements are shown with inner statistical and outer total (statistical and systematic) errors. The 1997 data points are offset slightly from the central $x_{\mathbb{P}}$ values for clarity.

5.3 Interpretation of Results

5.3.1 Regge Parameterisation

A phenomenological fit, following the method in [69] and [78], to the $x_{\mathbb{P}}$ dependence of $F_2^{D(3)}(\beta, Q^2, x_{\mathbb{P}})$ of figure 5.8 was performed for fixed β and Q^2 . The data were parameterised according to a Regge-motivated fit of the form of equation 3.25 in section 3.4.2 with,

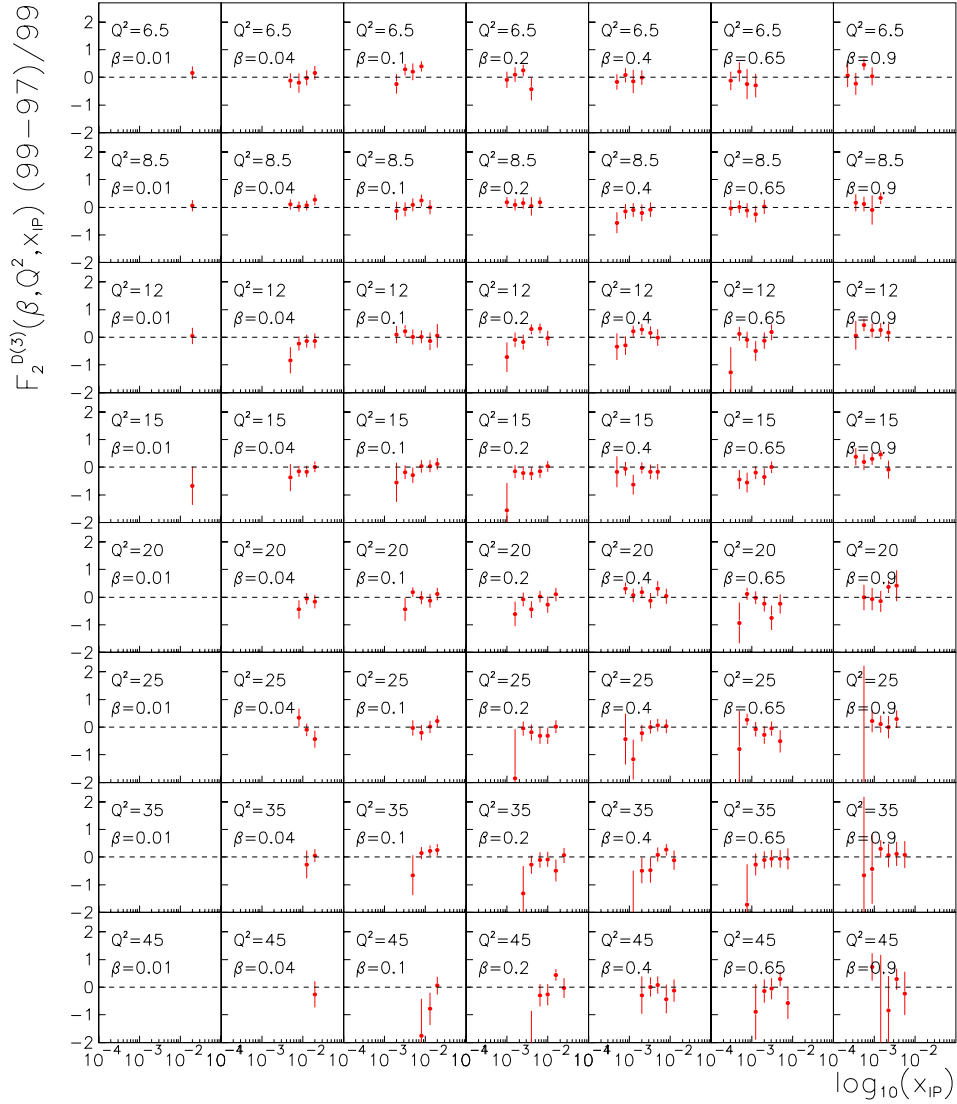


Figure 5.12: Comparison of the 1999 and 1997 $F_2^{D(3)}(\beta, Q^2, x_{\mathbb{P}})$ measurements evaluated as $(F_2^{D(3)}(1999) - F_2^{D(3)}(1997))/F_2^{D(3)}(1999)$ and presented as a function of $x_{\mathbb{P}}$ in bins of β increasing across the page and Q^2 increasing down the page. The error takes into account total errors on both measurements.

$$f_{\mathbb{P},\mathbb{R}}(x_{\mathbb{P}}) = \int_{-1}^{t_{min}} \frac{e^{B_{\mathbb{P},\mathbb{R}}t}}{x_{\mathbb{P}}^{2\alpha_{\mathbb{P},\mathbb{R}}(t)-1}} dt, \quad (5.10)$$

where $|t_{min}|$ is the minimum value of $|t|$ allowed kinematically and the pomeron and meson trajectories are linear as defined in equation 3.13. The parameter values, given in equations 5.11- 5.15 with statistical errors only, were taken from previous measurements,

$$\alpha_{\mathbb{R}}(0) = 0.50 \pm 0.16, \quad (5.11)$$

$$\alpha'_{\mathbb{P}} = 0.26 \pm 0.26 \text{ GeV}^{-2}, \quad (5.12)$$

$$\alpha'_{\mathbb{R}} = 0.90 \pm 0.10 \text{ GeV}^{-2}, \quad (5.13)$$

$$B_{\mathbb{P}} = 4.6 \pm_{2.6}^{3.4}, \quad (5.14)$$

$$B_{\mathbb{R}} = 2.0 \pm 2.0. \quad (5.15)$$

Two fits were performed in (β, Q^2) bins with a cut of $y < 0.45$ applied to minimise the longitudinal contribution to the diffractive structure function, which is hereafter taken to be negligible. The value of $\alpha_{\mathbb{P}}$ is assumed to be constant for all β and Q^2 values fitted. Fit A uses data with $Q^2 > 6.5 \text{ GeV}^2$, which was the lower limit for the 1997 phenomenological fit [78] and fit B takes data from the entire $1.5 \text{ GeV}^2 < Q^2 < 45 \text{ GeV}^2$ range into account. The results of fits A and B are shown respectively in figures 5.13 and 5.14. Data included in the fits are indicated by a solid circle whilst those excluded are depicted by a hollow circle. The solid curves represent the sum of pomeron and meson contributions whilst the dotted lines correspond to pomeron exchange only. The need for the meson trajectory in addition to the pomeron trajectory is noticeable in both figures in the low β bins where the data points can lie above the pomeron exchange predictions by more than a factor of two for the highest $x_{\mathbb{P}}$ values. Conversely at the highest values of β a decrease with increasing $x_{\mathbb{P}}$ is generally observed. This behaviour is consistent with figure 3.4.

The values of $\alpha_{\mathbb{P}}(0)$ resulting from the two fits are summarised in table 5.4. The statistical errors only are shown. The systematic and model dependence errors have not yet been evaluated but the errors are expected to be similar to those for the 1997 data in [78] where the systematic error was evaluated to be 0.017. The model dependence error was $\pm_{0.035}^{0.063}$, the dominant contribution to which originated from the lack of knowledge about the longitudinal structure function $F_L^{D(3)}$.

Fit	$\alpha_{\mathbb{P}}(0)$	χ^2 / degree of freedom
A	1.104 ± 0.036	0.78
B	1.107 ± 0.026	0.68

Table 5.4: Values for the effective pomeron intercept $\alpha_{\mathbb{P}}(0)$ extracted for $Q^2 > 6.5 \text{ GeV}^2$ (fit A) and for all values of Q^2 (fit B). The latter is taken to be the actual value.

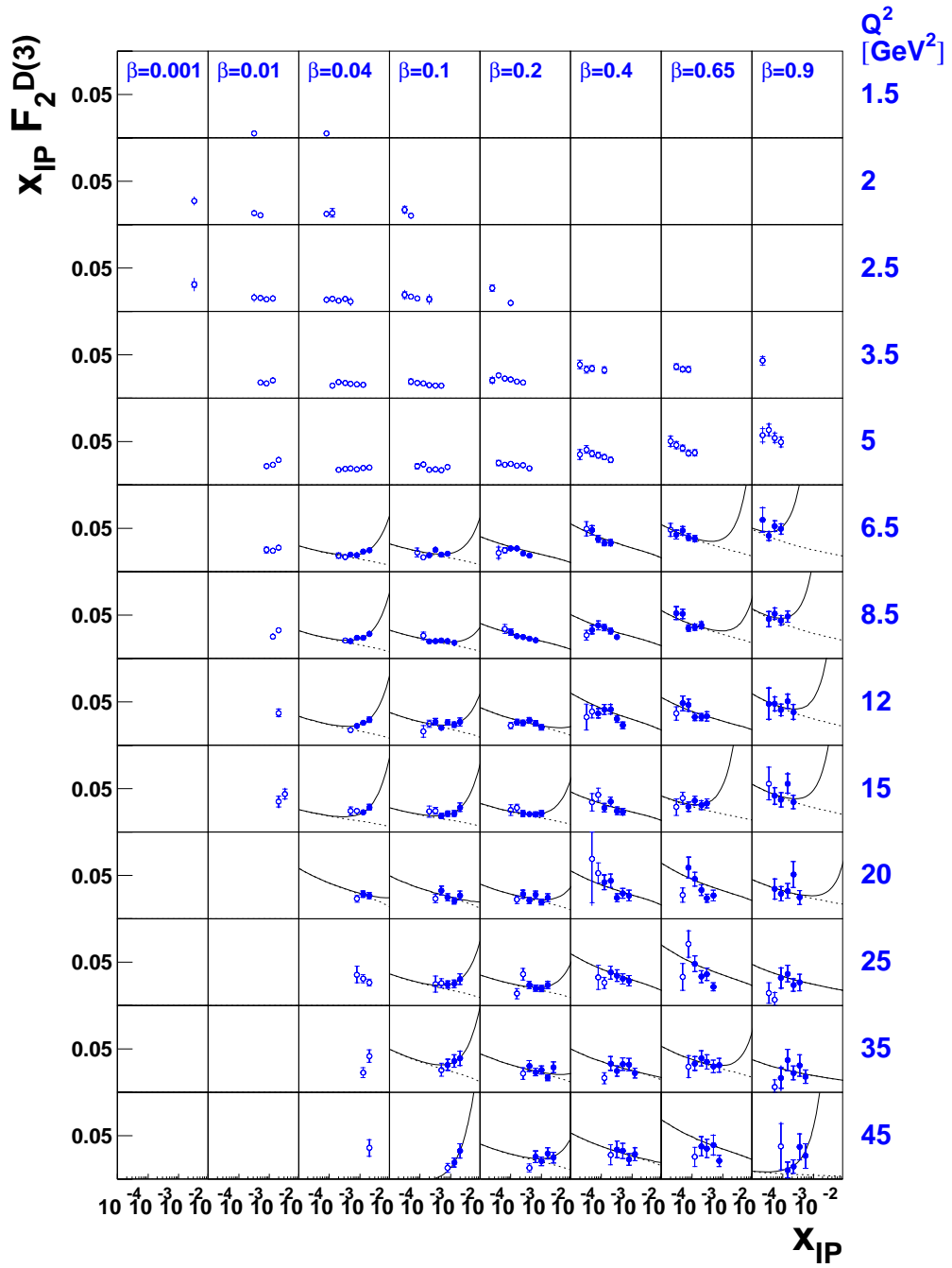


Figure 5.13: $x_{\mathcal{P}} F_2^{D(3)}(\beta, Q^2, x_{\mathcal{P}})$ from 1999 minimum bias data is shown as a function of $x_{\mathcal{P}}$ for fixed values of β and Q^2 , with β increasing from left to right and Q^2 increasing from top to bottom. The result of a phenomenological Regge fit to the data for $Q^2 > 6.5 \text{ GeV}^2$ is also shown for combined pomeron and meson exchange contributions (solid curve) and pomeron exchange only (dotted curve). The open circles indicate data points which were excluded from the fit.

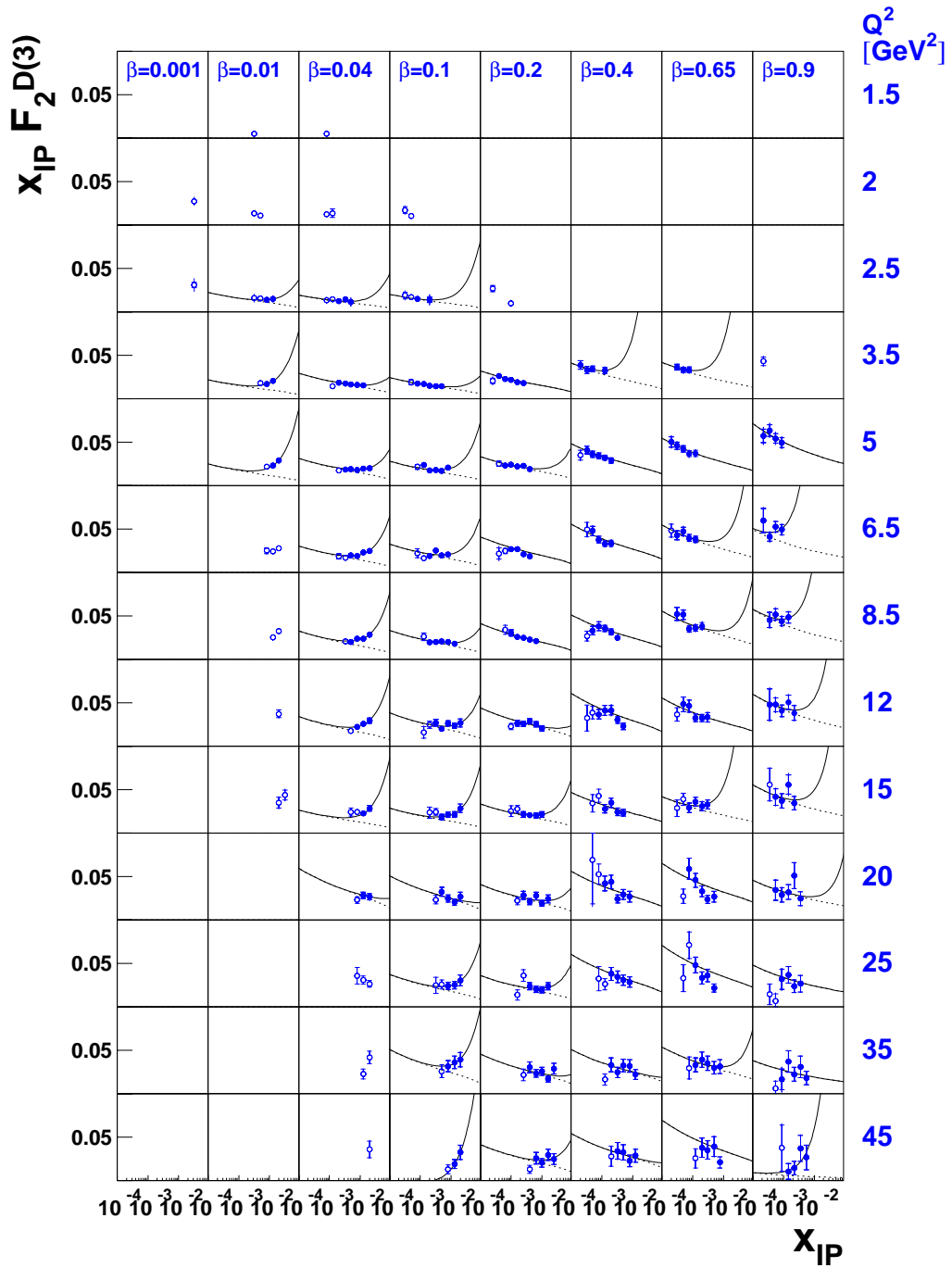


Figure 5.14: $x_{\mathbb{P}} F_2^{D(3)}(\beta, Q^2, x_{\mathbb{P}})$ from 1999 minimum bias data is shown as a function of $x_{\mathbb{P}}$ for fixed values of β and Q^2 , with β increasing from left to right and Q^2 increasing from top to bottom. The result of a phenomenological Regge fit to the data for all Q^2 is also shown for combined pomeron and meson exchange contributions (solid curve) and pomeron exchange only (dotted curve). The open circles indicate data points which were excluded from the fit.

The extracted values of $\alpha_{\mathbb{P}}(0)$ are therefore consistent with the soft pomeron intercept $\alpha_{\mathbb{P}}(0) \sim 1.08$ which describes soft hadron-hadron interactions. Within statistical errors the values are inconsistent with previous H1 measurements [69], [80] and [78] where $\alpha_{\mathbb{P}}(0) \sim 1.2$. Assuming that the systematic and model dependence errors would be of similar magnitude to previous measurements, the pomeron intercept extracted here would be consistent with previous measurements within the total errors.

5.3.2 Comparison with QCD Fits

As discussed in section 3.4.2 the structure functions $F_2^{\mathbb{P}}(\beta, Q^2)$ and $F_2^{\mathbb{R}}(\beta, Q^2)$ describe the partonic structure of the pomeron and meson exchanges respectively. In addition to the phenomenological model (section 5.3.1) describing the pomeron and meson $x_{\mathbb{P}}$ dependence, the β and Q^2 evolution of the structure function can be described by the DGLAP equations (section 2.2.5). QCD fits have not been performed for the 1999 minimum bias data itself, although comparisons have been made with those from the H1 1994 [69] QCD fits. Here the pomeron and meson exchanges were parameterised in terms of non-perturbative parton input distributions for light quarks (u, d, s) and gluons at a low starting scale $Q_0^2 = 3 \text{ GeV}^2$. This is known as “H1 QCD fit 2”. The evolution is performed separately in β and Q^2 . Again the region of phase space $y > 0.45$ was excluded because of the uncertainty in the knowledge about the longitudinal structure function contribution. Because of vector meson and possible higher twist contributions, points with $M_X < 2 \text{ GeV}$ were also excluded.

Figure 5.15 shows the 1999 minimum bias data from this analysis (blue points) compared with the QCD fit 2 to the H1 1994 data [69] which was performed on data with $Q^2 > 4.5 \text{ GeV}^2$. It can be observed that a reasonable agreement exists in the low Q^2 , low β region. At higher Q^2 however the data are consistently below the 1994 fit. The data exhibit a flatter dependence on $x_{\mathbb{P}}$, for large β and small $x_{\mathbb{P}}$, than the QCD fit to the 1994 data. This behaviour is consistent with that observed for the 1997 data [78], which can be seen from the data comparison in figure 5.10.

5.3.3 $F_2^{D(3)}$ Model Comparisons

The measured $F_2^{D(3)}(\beta, Q^2, x_{\mathbb{P}})$ was compared with predictions from the the Soft Colour Interaction model of Edin, Ingelman and Rathsman (section 3.4.4) and the semi-classical model of Buchmüller, Gehrmann and Hebecker (section 3.4.4). In addition, comparisons

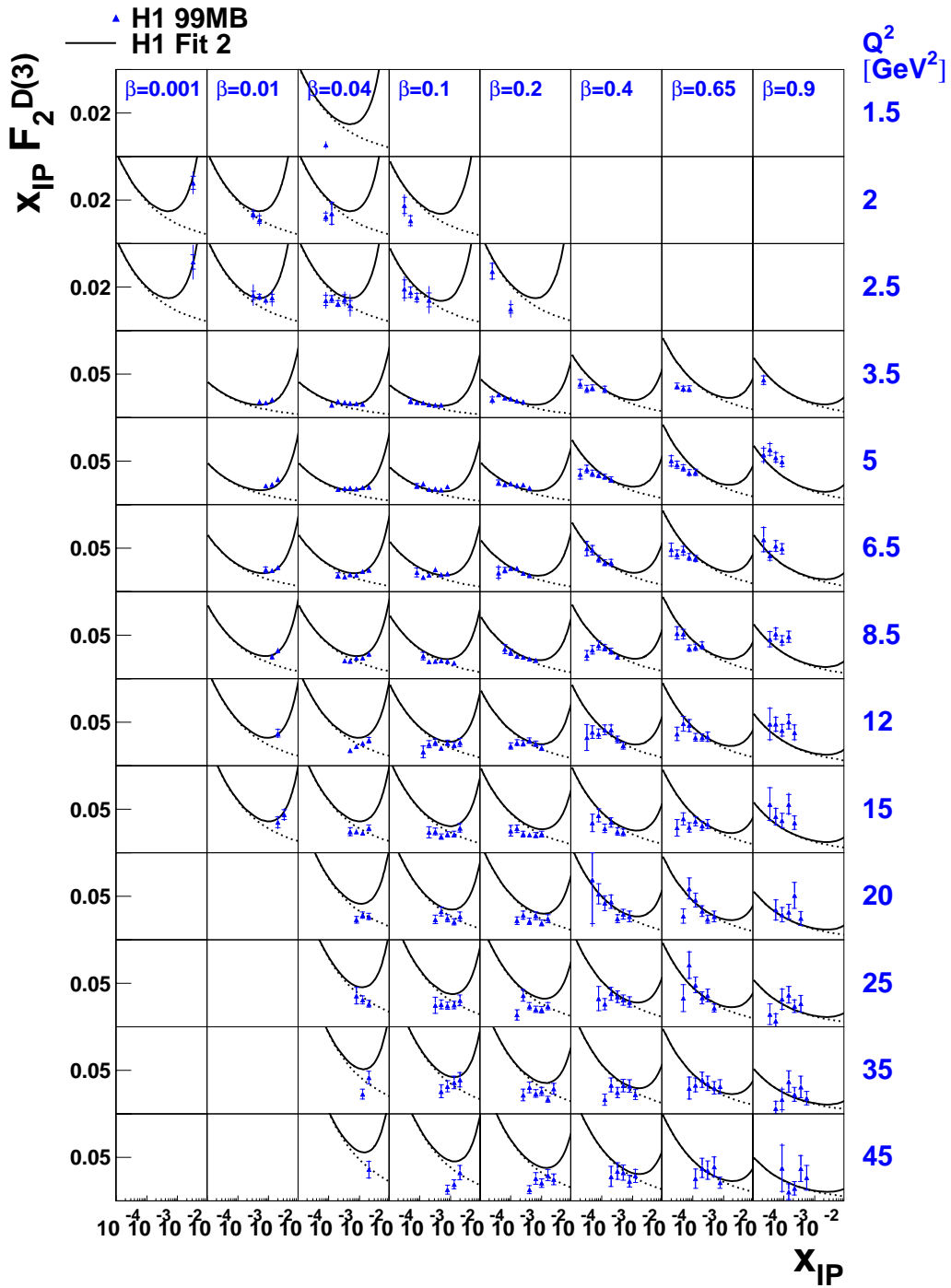


Figure 5.15: $x_P F_2^{D(3)}(\beta, Q^2, x_P)$ from 1999 minimum bias data is shown as a function of x_P for fixed values of β and Q^2 , with β increasing from left to right and Q^2 increasing from top to bottom. The result of the QCD fit to the 1994 H1 data for both pomeron and meson exchange contributions is indicated by the solid curve and for pomeron exchange only by the dotted curve. The vertical scale in the first three Q^2 bins has been altered with respect to the others.

with the saturation dipole model of Golec-Biernat and Wüsthoff (sections 2.2.7 and 3.4.3) are made in section 5.3.4.

Figure 5.16 shows $F_2^{D(3)}(\beta, Q^2, x_p)$ extracted from the 1999 minimum bias data compared with two versions of the prediction from the Soft Colour Interactions model, obtained from the LEPTO [92] Monte Carlo generator. In the SCI model the diffractive hard scattering interaction is modelled in the same way as that for inclusive deep-inelastic scattering. It is the soft colour rearrangements in the final state that determine whether or not a rapidity gap, and therefore a diffractive final state, is produced. In the first version of the fit diffractive final states are produced with a single free parameter, the universal colour rearrangement probability P_0 , fixed by a fit to previous $F_2^{D(3)}$ [86] data (dotted curves). The second version modifies P_0 based on a generalised area law [106] (solid curves) which takes into account the areas of the string configurations before and after the interaction. It can be seen that a more reasonable description of the data is achieved for the second version than for the original SCI prediction except for the high β , low Q^2 (very low M_X) region. In the low $M_X < 2$ GeV region the model is not expected to be valid, due to the exclusion of higher twist terms, although the predictions in this region are still included in the figure. Discrepancies with both predictions are also observed in the lowest β bins. The phase space extension obtained from the present data demonstrate the large differences between the original model and the revised area law model, with the latter giving a better description in this low Q^2 region.

The comparison of the 1999 minimum bias data points and the prediction from the semi-classical model [87] is shown in figure 5.17. This is another colour dipole approach where partonic fluctuations of the photon, which scatter off the colour fields of the proton, are modelled in a non-perturbative way. The model depends on just four free parameters, which were obtained from a fit to combined inclusive and diffractive structure function data. Generally the data are observed to have a flatter x_p dependence and lie below the model prediction (solid curves). At high β (low M_X^2) the model is not expected to be valid because possible higher twist contributions are not included in the model predictions. This region is indicated by dotted curves and here the data are generally observed to lie above the predictions. No obvious difference in the data-model agreement is observed for the new low Q^2 region compared with the rest of the kinematic region. The rising behaviour observed in the low β bins, attributable to the meson exchange contribution in section 5.3.1, is clearly not reproduced by this model.

5.3.4 β and Q^2 dependence of $F_2^{D(3)}$

The β and Q^2 dependences of $F_2^{D(3)}(\beta, Q^2, x_P)$ at fixed values of x_P have been examined in previous measurements [69] [78]. A good description of the data was obtained by modelling the x_P dependence with a fit inspired by Regge theory, and using the DGLAP equations to describe the evolution in β and Q^2 . The diffractive parton distributions indicated the presence of a high gluonic content in the proton, characterised by the β dependence evolving from high to low β with increasing Q^2 (see section 3.4.2). Rising scaling violations were observed for low and medium values of β , falling only for the highest values of β .

Figure 5.18(a) shows the Q^2 dependence of $F_2^{D(3)}(\beta, Q^2, x_P)$ at a fixed value of $x_P = 0.003$ in bins of x and β . To produce this plot, the nearest data points to $x_P = 0.003$ at each β and Q^2 value were “swum” to $x_P = 0.003$ using the results of the Regge fits. The maximum distance by which points were “swum” was 0.33 in $\log(x_P)$. Also shown are the H1 1997 data points [78] directly extracted at $x_P = 0.003$ using an alternative binning scheme, and the QCD fit 2 from the H1 1994 data [69] (described in section 5.3.2). The 1999 minimum bias data clearly exhibit rising scaling violations for β values up to 0.4, with the behaviour at 0.65 being flatter. Consistent with previous measurements, falling scaling violations are observed for the highest β bin ($\beta = 0.9$). A good agreement is observed with both the 1997 data and the 1994 QCD fit at medium and high β , although the behaviour of $F_2^{D(3)}$ at low β is not as steep as either previous measurement. The β dependence of $F_2^{D(3)}(\beta, Q^2, x_P)$ for $x_P = 0.003$ at fixed values of Q^2 is presented in figure 5.18(b), again compared with the 1997 data and the 1994 QCD fit. The data exhibit a reasonably flat dependence on β . This behaviour persists to high values of Q^2 , where both the 1997 data and the 1994 QCD fit lie significantly above the data. In this region the 1999 data sample is statistically limited and due to the “swimming” scheme, the lowest x_P data points, which tend to be lower than the previous measurements, are usually used. In the low Q^2 region however a good agreement is observed with the previous measurements. Therefore, although QCD fits have not been performed on the 1999 data they are broadly consistent with the conclusions from the earlier measurements that the pomeron is gluon-dominated with boson-gluon fusion being the dominant mechanism occurring in diffractive interactions at HERA.

Comparisons of the data with colour dipole models were presented in section 5.3.3. The β and Q^2 dependences of the data compared with these models were also examined and are presented here. In each case the distributions are shown only for one fixed value of $x_P = 0.003$, as chosen for figure 5.18. Figure 5.19 shows the Q^2 and β dependence of

the $F_2^{D(3)}$ data compared with the predictions of the semi-classical model as described in section 5.3.3. In general although some of the features of the data are described, the model does not agree well with the data, with the data lying below the prediction at low Q^2 and low β and above the model for high Q^2 and high β . A similar level of agreement between data and the model was observed for the H1 1997 data [78].

Finally the Q^2 and β dependence of the data compared with the saturation model [68] [82] is shown in figure 5.20. This model is based on a colour dipole approach and fits to data for the inclusive structure function $F_2(x, Q^2)$ are used to describe the $q\bar{q}$ and $q\bar{q}g$ dipole cross sections. Assuming two-gluon exchange, these cross sections are used to predict the diffractive structure function $F_2^{D(3)}(\beta, Q^2, x_P)$ with the addition of just one additional free parameter for the t dependence e^{Bt} , where $B = 6 \text{ GeV}^{-2}$. The saturation model contains higher twist terms and therefore is valid over the entire kinematic range measured. The predictions shown here are revised with respect to the original model of [68] [82] after an incorrect treatment of the extra colour factor applied for $q\bar{q}g$ dipoles was used originally. Throughout the whole range of the measurement the data are in excellent agreement with the saturation model predictions. In contrast to previous data sets, the low x_P , high Q^2 , low β region appears to be reproduced well here.

5.4 Summary

A sample of diffractive deep-inelastic scattering events with a luminosity of 3.74 pb^{-1} was selected from H1 data collected with minimally biased triggers in 1999. The diffractive proton structure function $F_2^{D(3)}(\beta, Q^2, x_P)$ was measured in the kinematic region covering $1.5 \text{ GeV}^2 < Q^2 < 45 \text{ GeV}^2$, $0.001 < \beta < 0.9$ and $10^{-4} \lesssim x_P < 0.05$. Previously published H1 results for $F_2^{D(3)}(\beta, Q^2, x_P)$ only exist for $Q^2 \geq 4.5 \text{ GeV}^2$ and $\beta \geq 0.01$ hence this analysis accessed lower Q^2 and β values than has previously been possible. The new data points were observed to agree with previous H1 results based on H1 1994 [69], 1995 [80] (unpublished) and 1997 [78] data throughout most of the phase space covered in this analysis. The new 1999 minimum bias data points represent the most statistically significant H1 $F_2^{D(3)}(\beta, Q^2, x_P)$ results for $Q^2 < 12 \text{ GeV}^2$ to date. Evaluation of the structure function has also been performed at more β , x_P and Q^2 values. Hence, future opportunities to improve the modelling and understanding of low Q^2 diffraction now exist. Comparisons with predictions from the semi-classical and Soft Colour Interactions models were made, which generally only described the data in certain kinematic regions. The updated saturation model predictions provided an excellent description of the β and

Q^2 dependences of the $F_2^{D(3)}(\beta, Q^2, x_{\mathcal{P}})$ data at a fixed value of $x_{\mathcal{P}}$. A new value for the effective pomeron intercept was calculated by performing a Regge fit to the data. This was found to be consistent with that of the soft pomeron, unlike other recent measurements at H1 [69], [78], [80]. In summary, the lowest Q^2 bins of the $F_2^{D(3)}$ measurement dramatically increase the H1 kinematic coverage at high precision although there are several areas in which work still needs to be done in order to complete the analysis, which unfortunately are beyond the time-scale of this thesis.

5.5 Future Prospects

The forward detector selection ideally requires further investigation. The sixth layer of the PRT was not used due to high noise levels present in the detector, but this leads to a large contribution to the systematic error for the correction due to smearing across the measurement boundary $M_Y < 1.6$ GeV and $|t| < 1$ GeV². This is the largest systematic error on the measurement. Hence, work is required to try to reduce it. The second largest systematic error originates from the uncertainty in measuring the polar angle of the positron in the Spacal. Further study is therefore needed to understand the details of the alignment between the Spacal and BDC detectors. Work for this is currently ongoing implying this systematic error can be significantly reduced in the near future.

The efficiency for finding an event vertex was presented in section 4.6.1, which illustrated that this efficiency decreases with decreasing y . This has the effect that events with low values of y are not well detected or modelled by Monte Carlo. A correction could be applied in order to regain lost events at low y . Previous studies, for example [103], have shown the BST to be useful in improving the vertex efficiency at low y as well as reducing the amount of photoproduction background present in the data sample. The BST has been used in inclusive analyses on the 1999 minimum bias data [107] and hence effort should be made in the future to do this for diffraction as well. The region of discrepancy between the 1999 minimum bias and 1997 data at low $x_{\mathcal{P}}$ (high y) also requires further investigation.

Finally, an alternative binning scheme in x , Q^2 and $x_{\mathcal{P}}$ (rather than x , Q^2 and β) for $F_2^{D(3)}(\beta, Q^2, x_{\mathcal{P}})$ is being developed whereby the β and Q^2 dependence of $F_2^{D(3)}(\beta, Q^2, x_{\mathcal{P}})$ can be evaluated for fixed values of $x_{\mathcal{P}}$. This method has the benefit of allowing more $\beta = x/x_{\mathcal{P}}$ bins to be obtained allowing precise measurements of the scaling violations. The calculation of the effective intercept $\alpha_{\mathcal{P}}(0)$ could be affected by the low $x_{\mathcal{P}}$ region so a final value is not possible until the low $x_{\mathcal{P}}$ region is better understood.

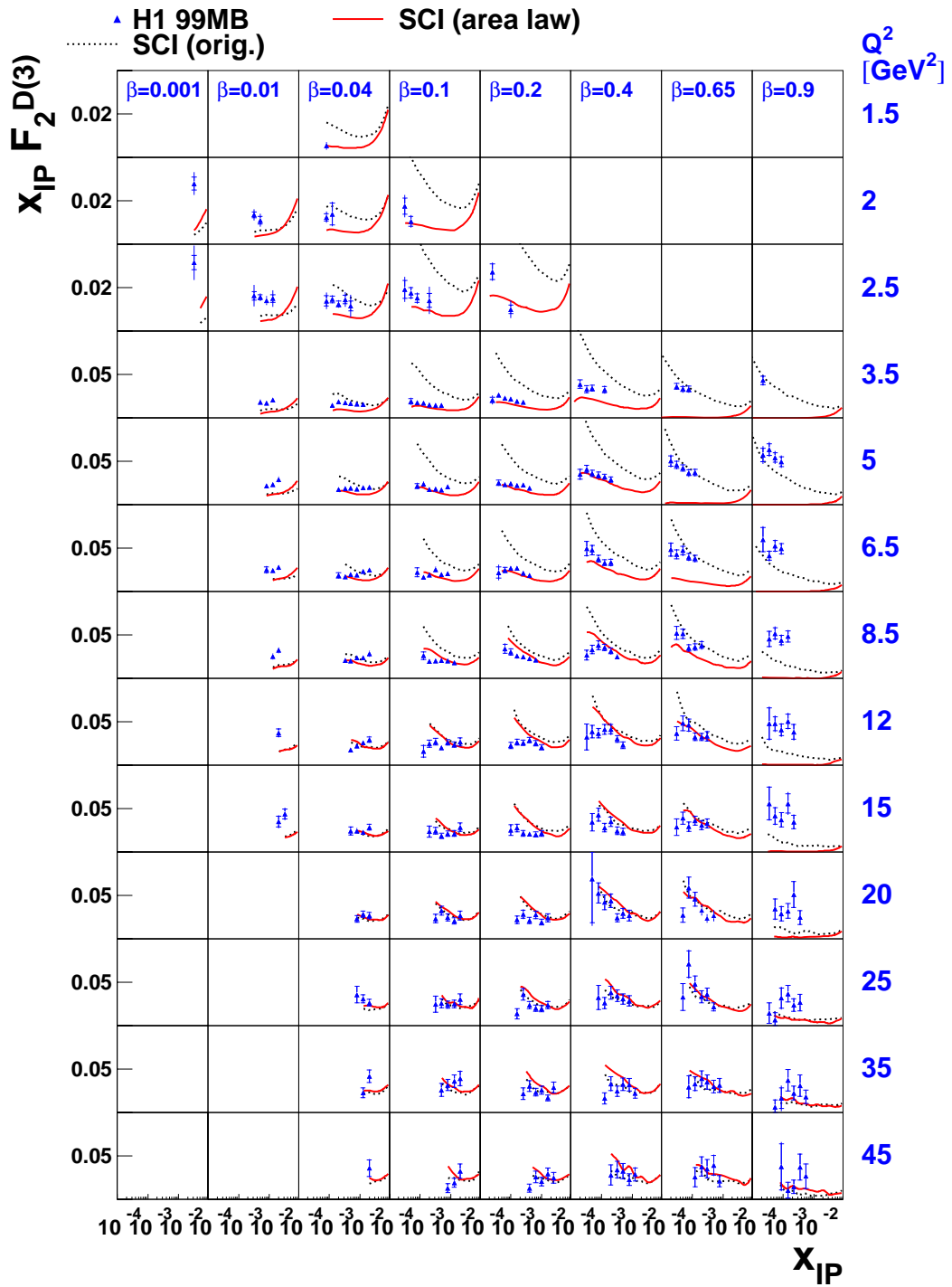


Figure 5.16: $x_P F_2^{D(3)}(\beta, Q^2, x_P)$ from 1999 minimum bias data (blue points) is shown as a function of x_P for fixed values of β and Q^2 , with β increasing from left to right and Q^2 increasing from top to bottom. The data are compared with predictions of the Soft Colour Interactions model [86] (dotted curves) and a refined version based on a generalised area law [106] (solid curves). The vertical scale in the first three Q^2 bins has been altered with respect to the others.

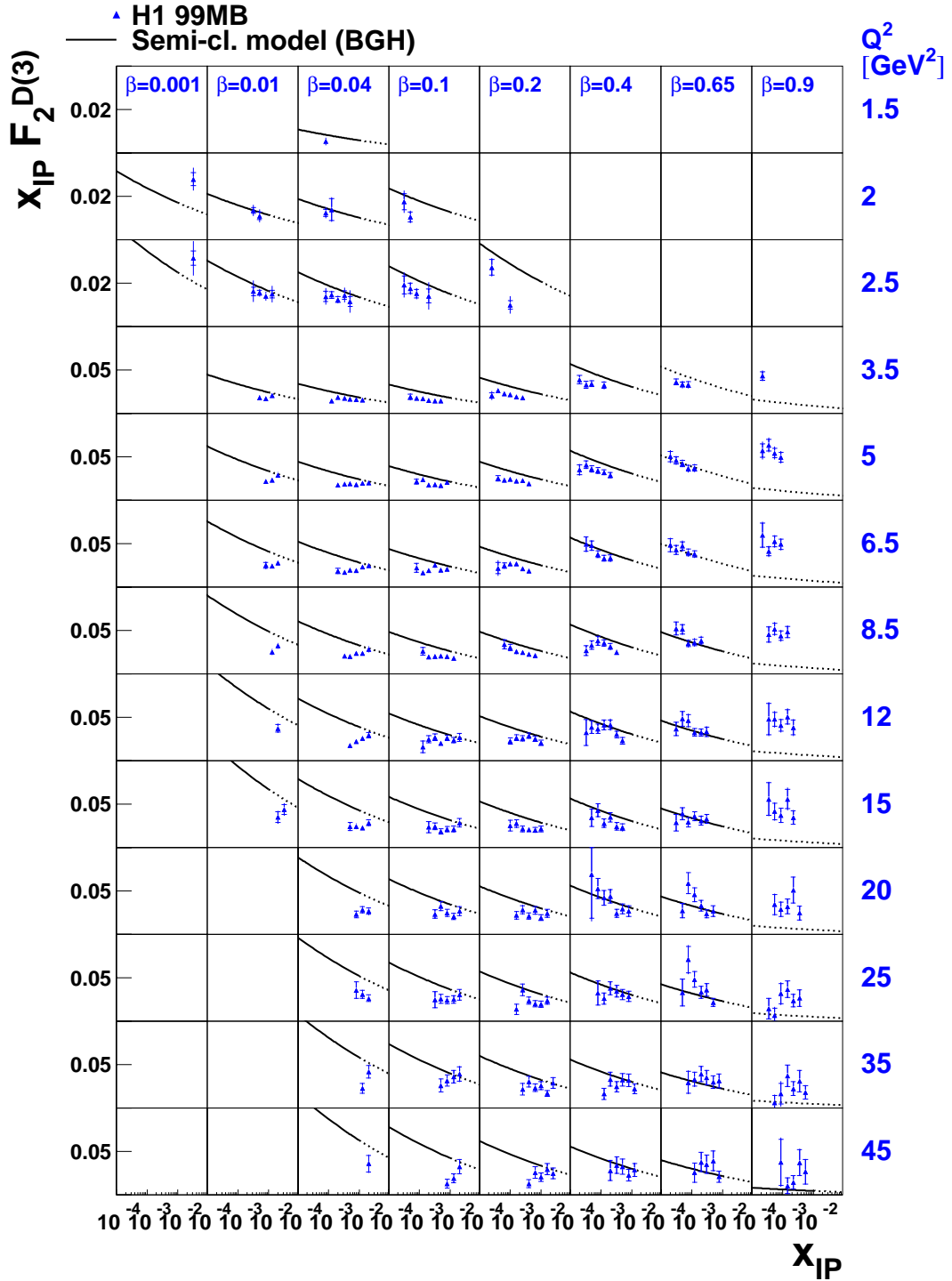
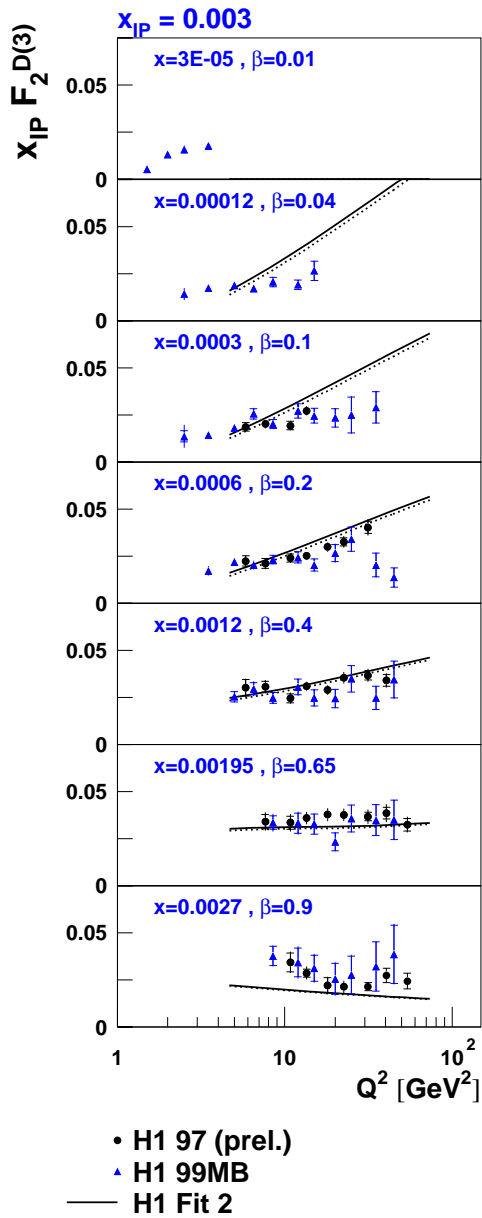
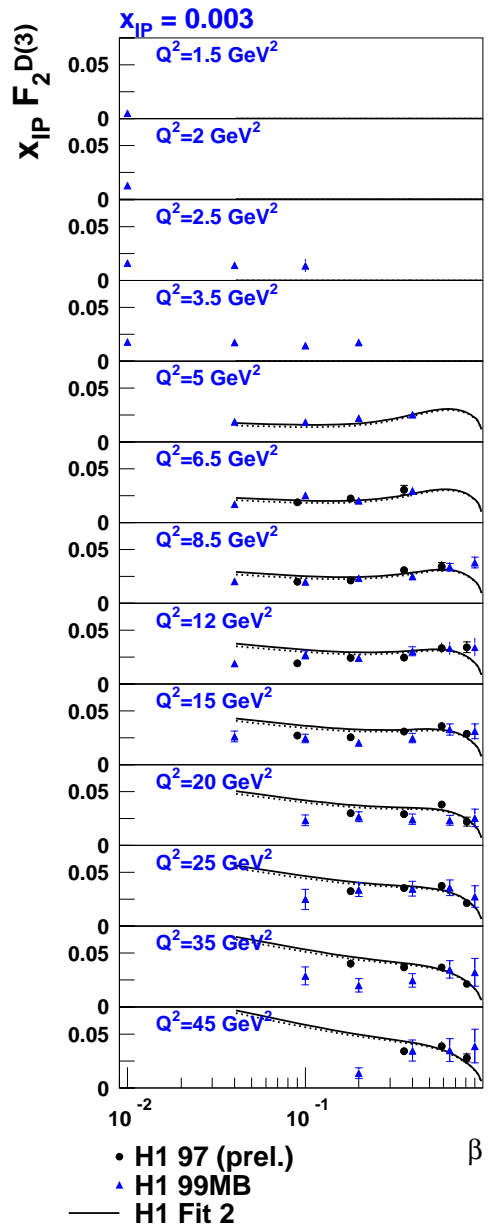


Figure 5.17: $x_p F_2^{D(3)}(\beta, Q^2, x_p)$ from 1999 minimum bias data (blue points) is shown as a function of x_p for fixed values of β and Q^2 , with β increasing from left to right and Q^2 increasing from top to bottom. The data are compared with the prediction of the semi-classical model [87] (solid curves). The dotted curves represent an extension of the model to $M_X^2 < 4 \text{ GeV}^2$, where the model is not expected to be valid. The vertical scale in the first three Q^2 bins has been altered with respect to the others.

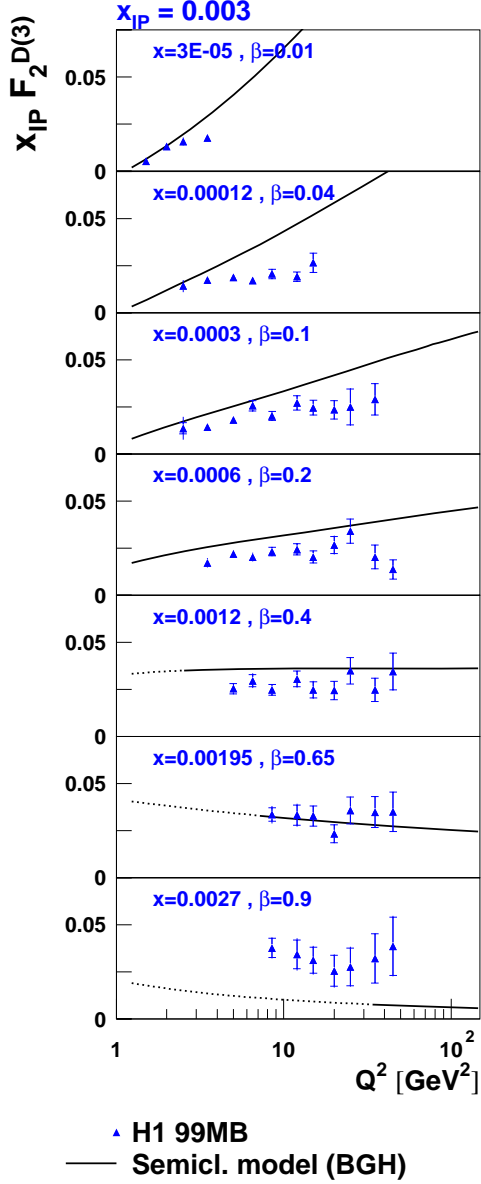


(a)

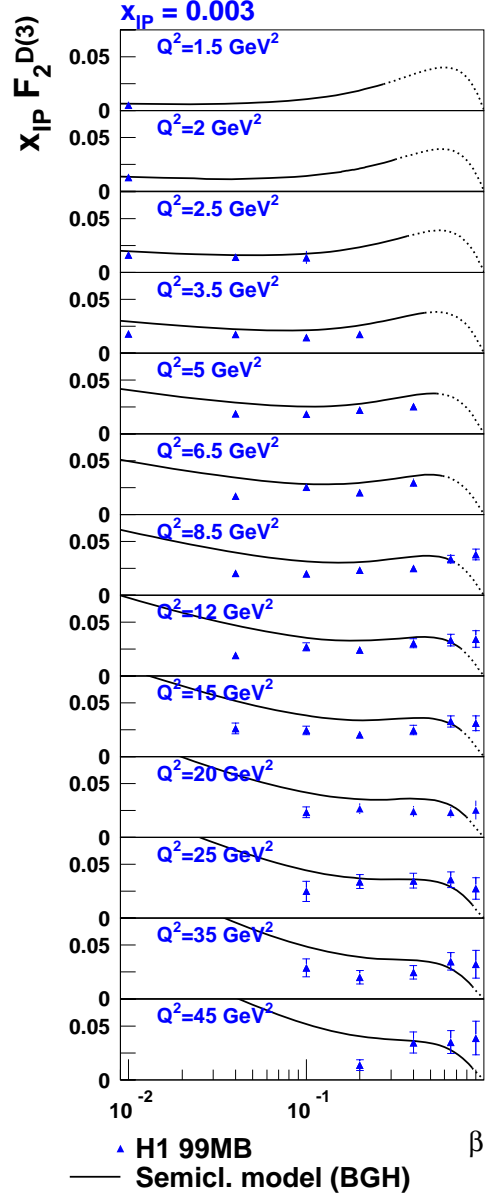


(b)

Figure 5.18: $x_p F_2^{D(3)}(\beta, Q^2, x_p)$ at fixed x_p shown as a function of Q^2 (a) and β (b). The blue points represent the new 1999 data, the black points are H1 1997 data [78] and the curves are the result of a QCD fit to H1 1994 data [69] including both pomeron and meson contributions (solid curve) and pomeron only (dotted curves).



(a)



(b)

Figure 5.19: $x_p F_2^{D(3)}(\beta, Q^2, x_p)$ at fixed x_p shown as a function of Q^2 (a) and β (b). The data (blue points) are compared with the prediction of the semi-classical model [87] (solid curves). The dotted curves represent an extension of the model to $M_X^2 < 4 \text{ GeV}^2$, where the model is not expected to be valid.

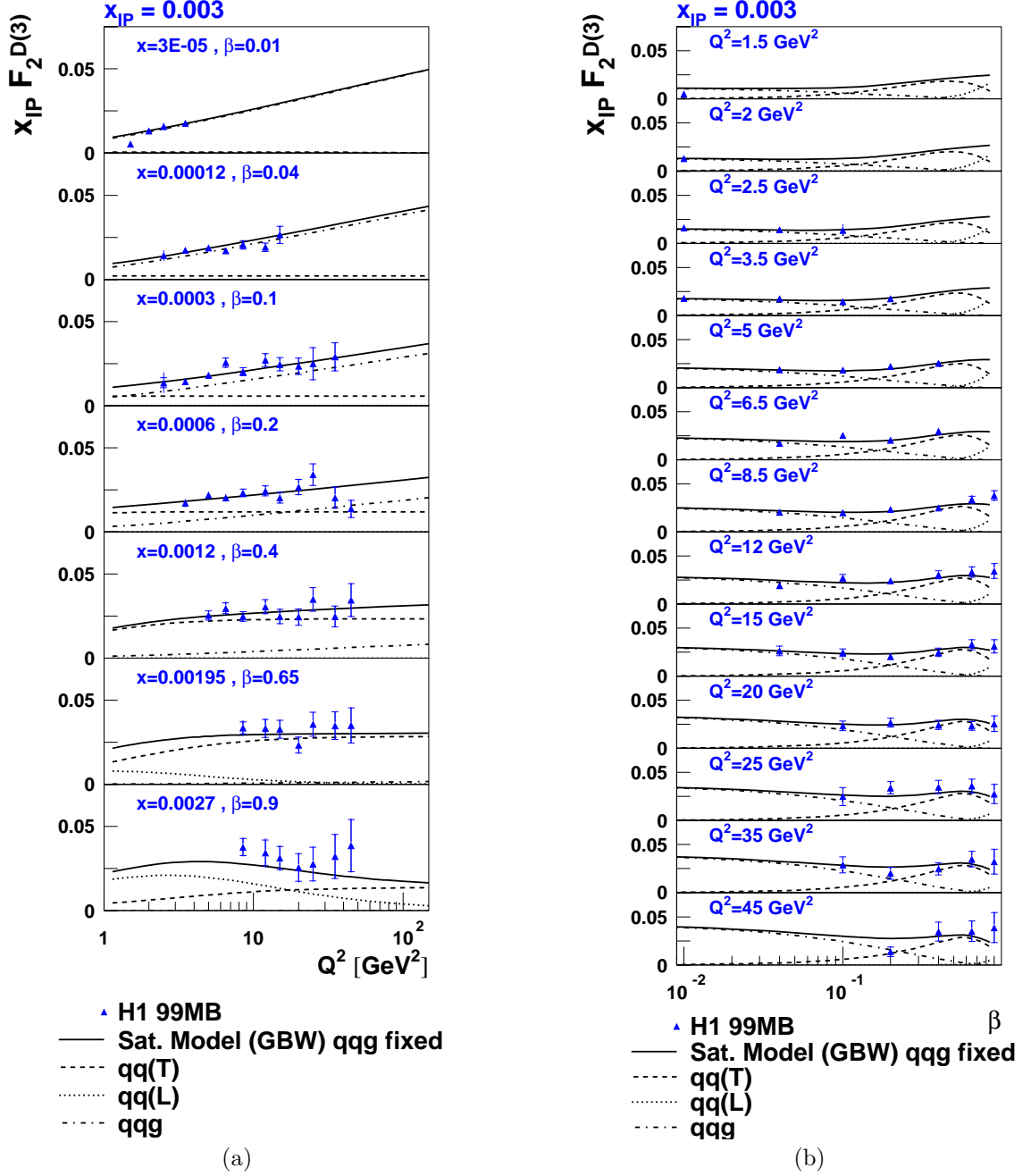


Figure 5.20: $x_{\text{IP}} F_2^{D(3)}(\beta, Q^2, x_{\text{IP}})$ at fixed x_{IP} shown as a function of Q^2 (a) and β (b). The data (blue points) are compared with the prediction of the saturation model [68] (solid curves). The $q\bar{q}$ transverse component is represented by the dashed curve, the longitudinal contribution by the dotted curve and the qqg term by the dotted-dashed curve.

Bibliography

- [1] S. Glashow, Nucl. Phys. B8(1961), 579
S. Weinberg, Phys. Rev. Lett. 19(1967) 1264
- [2] M. Breidenbach et al., Physics Review Letters 23(1969), 935
- [3] J. D. Bjorken, Phys. Rev. 179(1969), 1547
M. Gell-Mann, Phys. Lett. 8(1964) 214
- [4] D. J. Gross. F. Wilczek, Phys. Rev. Lett. 30(1973), 1343
H. D. Politzer. Phys. Rev. Lett. 30(1973), 1346
H. Fritzsche, M. Gell-Mann, Proc. XVI International Conference on High Energy Physics, Fermilab (1972), Volume 2, 135
H. Fritzsche, M. Gell-Mann, H. Leutwyler, Phys. Lett. 47B(1973), 365
- [5] T. Muta, *Foundations of Quantum Chromodynamics*, Lecture Notes in Physics Volume 57, Second Edition (2000), World Scientific, Singapore
- [6] H1 Collaboration, Nucl. Phys. B407(1993), 515
- [7] ZEUS Collaboration, Phys. Lett. B316(1993) 412
- [8] H1 Collaboration, Phys. Lett. B520(2001), 183
- [9] H1 Collaboration, Nucl. Instr. Meth. A386(1997), 348
- [10] D. Pitzl et al., Nucl. Instr. Meth. A454(2000),334
- [11] W. Eich et al., Nucl. Instr. Meth A386(1987), 81
- [12] H. Behrend et al., H1 Internal Note 92-226(1992)
- [13] J. Bürger et al., Nucl. Instr. Meth. A279(1989), 217
- [14] S. Egli et al., Nucl. Instr. Meth. A312(1992), 457

- [15] H. Ehrlichmann et al., H1 Internal Note 94-350(1994)
- [16] S. Burke et al., Nucl. Instr. Meth. A373(1996), 227
- [17] H1 Collaboration, *Technical Proposal to Upgrade the Backward Scattering Region of the H1 Detector*(1993)
- [18] H1 Collaboration, Nucl. Instr. Meth. A336(1993), 460
- [19] H1 Collaboration, Nucl. Instr. Meth. A180(1981), 429
H1 Collaboration, Nucl. Instr. Meth. A374(1996), 149
H1 Collaboration, Nucl. Instr. Meth. A382(1996), 398
H1 Collaboration, Nucl. Instr. Meth. A386(1997), 397
- [20] W. Hildesheim, V. Reich, M. Seidel, H1 Internal Note 94-372(1994)
- [21] W. Hildesheim, M. Seidel DESY 95-139 (hep-ex/9507013), (1995)
- [22] J. E. Wuppertal, H1 Internal Note 95-448(1995)
- [23] H1 Collaboration *Technical Proposal to Build a Special Spectrometer Covering Very Small Momentum Transfers*, TP-VLQ(1996)
- [24] H. Croström et al., Nucl. Instr. Meth. A340(1994) 304
- [25] H1 Collaboration, *The Forward Proton Spectrometer of H1*, published in the proceedings of the 28th International Conference on High Energy Physics, ICHEP96, Warsaw, Poland, Z. Ajduk, K. Wroblewski (eds.), World Scientific, Singapore(1997)
- [26] H1 Collaboration, *Proposal for a Forward Neutron Calorimeter for the H1 Experiment at DESY*(1995)
- [27] H1 Collaboration, Eur. Phys. J. C6 (1999), 587
- [28] H1 Collaboration, *Luminosity Measurement in the H1 Experiment at HERA*, published in the proceedings of the 28th International Conference on High Energy Physics, ICHEP96, Warsaw, Poland, Z. Ajduk, K. Wroblewski (eds.), World Scientific, Singapore(1997)
- [29] H. Bethe, W. Heitler, Proc. Roy. Soc. A146(1934), 83
- [30] H1 Luminosity System Webpage, <http://www.desy.de/h1/www/general/home/intra-home.html>

- [31] E. Elsen, H1 Internal Note 93-262(1993)
F. Sefkow et al., H1 Internal Note 94-407(1994)
- [32] J. C. Bizot et al., H1 Internal Note 92-212 (1992)
L. Goerlich et al., H1 Internal Note 97-508(1997)
- [33] J. Keohne et al., H1 Internal Note 97-509(1997)
- [34] H1 Collaboration, H1 Internal Note 97-531(1997)
- [35] H1 Collaboration, *Proposal for an Upgrade of the H1 Luminosity System and its Associated Electronics for HERA 2000*, DESY PRC 98/05(1998)
- [36] H1 Collaboration, *A Forward Silicon Tracker for H1*, DESY PRC 99-01(1999)
- [37] M. Cuje et al., *H1 High Luminosity Upgrade 2000*, DESY PRC 98-02(1998)
- [38] H1 Collaboration, *Proposal to Upgrade the H1 Forward Track Detector*, DESY PRC 98-06(1998)
- [39] W. Brückner et al., *Upgrade of the H1 Forward Neutron Calorimeter*, Draft of proposal(1999)
- [40] Joint Institute for Nuclear Research, Dubna, *Upgrade of the H1 Hadron PLUG Calorimeter*, First draft of proposal(1998)
- [41] H1 Collaboration *A Fast Track Trigger with High Resolution for H1*, DESY PRC 99-06(1999)
- [42] H1 Collaboration *Proposal to Upgrade the LAr Calorimeter Trigger: The Jet Trigger*, DESY PRC 99-02(1999)
- [43] A. Campbell et al., *Proposal to Merge Level-4 and Level-5 Systems of the H1 Experiment*, DESY PRC 99-03(1999)
- [44] R. G. Roberts, *The structure of the proton: deep-inelastic scattering*, C.U.P.(1990)
- [45] W. E. Burcham, M Jobes, *Nuclear and Particle physics*, Longman(1995)
- [46] F Halzen, A. D. Martin, *Quarks and Leptons: An Introductory Guide to Modern Particle Physics*, John Wiley & Sons Inc.(1984)
- [47] R. Feynman, Phys. Rev. Lett. 23(1969), 1415
- [48] M. Gell-Mann, Phys. Lett. 8(1964), 214

- [49] J. Bjorken, Phys. Rev. 163(1967), 1767
- [50] C. Callan, D. Gross, Phys. Rev. Lett. 21(1968), 311
- [51] NMC Collaboration, Nucl. Phys. B483(1997), 3
- [52] BCDMS Collaboration, Phys. Lett. B223(1989), 485
- [53] L. W. Whitlow et al., Phys. Lett. B250(1990), 193
L. W. Whitlow et al., Phys. Lett. B282(1992), 475
- [54] H1 Collaboration, Phys. Lett. B393(1997), 452
- [55] J. G. H. de Groot et al., Z. Phys. C1(1979), 143
- [56] D. H. Perkins, *Introduction to High Energy Physics*, Addison Wesley Publishing Company Inc.(1987)
- [57] H1 Collaboration, Nucl. Phys. B470(1996),
- [58] V. Gribov et al., Sov. J. Nucl. Phys. 15(1972), 438
- [59] G. Altarelli, G. Parisi, Nucl. Phys. B126(1977) 298
- [60] E.Kuraev, L. Lipatov, V. Fadin, Sov. Phys. JETP. 44(1976), 443
Y. Balitsky, L. Lipatov, Sov. J. Nucl. Phys. 28(1978), 822
- [61] L. Gribov, E. Levin, M. Ryskin Phys. Rep. 100(1983) 1
- [62] M. Ciafaloni, Nucl. Phys. B296(1998), 49
S. Catani, F. Fiorani, G. Marchesini, Phys. Lett. B234(1990), 339
S. Catani, F. Fiorani, G. Marchesini, Nucl. Phys. B336(1990), 18
- [63] H1 Collaboration, Eur. Phys. J. C21 (2001) 33-61
- [64] V. Fadin. L. Lipatov, Phys. Lett. B249(1998), 127
G. Camici. M. Ciafaloni, Phys. Lett. B430(1998), 349
S. Brodsky. G. Lepage, P. Mackenzie, Phys. Rev. D28(1983), 228
- [65] T. Regge, Nuovo Cimento 14(1959), 951
T. Regge, Nuovo Cimento 18(1960), 947
- [66] T. Bauer et al., Rev. Mod. Phys. 11(1989) 1

- [67] ZEUS Collaboration, Phys. Lett. B487(2000), 1-2, 53-73
- [68] K. Golec-Biernat, M. Wüsthoff, Phys. Rev. D60(1999), 114023
E. Levin, *Physics and Experimentation at a Linear Electron-Positron Collider*, Volume 4: *The THERA Book. Electron-Proton Scattering at $\sqrt{s} \sim 1$ TeV*, Ed. U. Katz, M. Klein, A. Levy, S. Schlenstedt(2001)
- [69] H1 Collaboration, Z. Phys. C76(1997), 613
- [70] G. Chew, S. Frautschi, S. Mandelstam, Phys. Rev. 126(1962), 1202
- [71] A. Donnachie, P. Landshoff, Phys. Lett. B296(1992) 227
- [72] A. Donnachie, P. Landshoff, Nucl. Phys. B231(1983), 189
- [73] J. C. Collins, Phys. Rev. D57(1998), 3051
erratum Phys. Rev. D61(1998), 2000
- [74] G. Ingelman, P. Schlein, Phys. Lett. B152(1985) 256
- [75] P. D. B. Collins, *An Introduction to Regge Theory and High Energy Physics*, CUP(1977)
- [76] H1 Collaboration, Phys. Lett. B348 (1995) 681
- [77] A. Donnachie, P. Landshoff, Phys. Lett. B437(1998), 408
- [78] H1 Collaboration, *Measurement of the Diffractive Structure Function $F_2^{D(3)}(\beta, Q^2, x_p)$ at HERA*, submitted to EPS2001, Budapest, Hungary, July 2001, and LP2001, Rome, Italy, July 2001
- [79] W. Buchmüller, Phys. Lett. 353(1995), 335
W. Buchmüller, A. Hebecker, Nucl. Phys. B476(1996), 203
- [80] H1 Collaboration, *Measurements of the diffractive structure function $F_2^{D(3)}$ at low and high Q^2 at HERA*, published in the proceedings of the 29th International Conference on High Energy Physics, ICHEP98, Vancouver, Canada, A. Astbury, D. Axen. J. Robinson (eds.), World Scientific, Singapore(1999)
T. Nicholls, C. Royon, L. Schoeffel, A. Van Haecke, H1 Internal Note 99-567(1999)
- [81] J. Bartels, J. Ellis, H. Kowalski, M. Wüsthoff, Eur. Phys. J. C7(1999) 443
- [82] K. Golec-Biernat, M. Wüsthoff, Phys. Rev. D59(1999), 014017

- [83] ZEUS Collaboration, “Measurement of the diffractive cross section at $Q^2 < 1 \text{ GeV}^2$ at HERA”, published in the proceedings of the 30th International Conference on High Energy Physics, ICHEP2000, Osaka, Japan, C. S. Lim, T. Yamanaka (eds.), World Scientific, Singapore(2001)
- [84] ZEUS Collaboration, Eur. Phys. J. C6(1999) 43
- [85] K. Golec-Biernat, M. Wüsthoff, Eur. Phys. J. C20(2001), 313
- [86] A. Edin, G. Ingelman, J. Rathsman, Phys. Lett. B366(1996) 371
A. Edin, G. Ingelman, J. Rathsman, Z. Phys., C75(1997) 57
- [87] W. Buchmüller, T. Gehrmann, A. Hebecker, Nucl. Phys. B537(1999) 477
- [88] K. Charchula et al., Software Manual: *Combined QED and QCD Radiative Effects in Deep Inelastic Lepton Proton Scattering: The Monte Carlo Generator DJANGO06*
- [89] H. Jung, Software Manual: *The RAPGAP Monte Carlo for Deep Inelastic Scattering, Version 2.08/00*(1999)
- [90] A. Kwiatkowski, H. Speisberger, H. Möhring, Comp. Phys. Comm. 69(1992), 155
- [91] M. Bengtsson, T. Sjöstrand, Z. Phys. C37(1988), 465
- [92] A. Edin, G. Ingelman, J. Rathsman, Comp. Phys. Comm. 101(1997), 108
- [93] T. Sjöstrand, Comp. Phys. Comm. 39(1986), 347
- [94] R. Engel, *PHOJET Manual*, University of Siegen preprint 95-05(1995, revised 1997)
- [95] B. List, A. Mastroberardino, *DIFFVM: A Monte Carlo Generator for diffractive processes in ep scattering*, in A. Doyle, G. Grindhammer, G. Ingelman, H. Jung (eds.): *Monte Carlo Generators for HERA Physics*, DESY-PROC-1999-02 (1999), 396
- [96] J. J. Sakurai, Ann. Phys. 11(1960), 1
J. J. Sakurai, D. Schildknecht, Phys. Lett. B40(1972), 121
M. Greko, Nucl. Phys. B63(1973), 398
- [97] A. Courou, P. Kessler, Phys. Rev. D46(1992), 117
- [98] H1 Collaboration, *Guide to the simulation program H1SIM*, H1 Software Note 3 (1989)

- [99] R. Brun, F. Carminati, *GEANT Detector description and Simulation Tool, CERN Program Library W5013(1993)*
- [100] H1 Collaboration, ELAN Working Group, Tomas Lastovicka, internal communication(2000)
- [101] A. Meyer, Measurement of the Structure Function $F_2(x, Q^2)$ of the Proton at Low Q^2 with the H1 Detector at HERA Using the New Detector Components Spacal and BDC, Ph.D. Thesis, University of Hamburg (1997)
- [102] A. Glazov, Measurement of the Proton Structure Function $F_2(x, Q^2)$ and $F_L(x, Q^2)$ with the H1 Detector at HERA, Ph.D. Thesis, Humboldt University Berlin (1998)
- [103] V. Arkadov, Measurement of the Deep-Inelastic ep Scattering CrossSection Using the Backward Silicon Tracker at the H1 Detector at HERA, Ph.D. Thesis, Humboldt University Berlin(2000)
- [104] Cigdem Issever, *The Calibration of the H1 Liquid Argon Calorimeter*, IX International Conference on Calorimetry in Particle Physics, Annecy, October 9-14(2000)
- [105] P. Thompson, *Open Charm Production in Inclusive and Diffractive Deep-Inelastic Scattering at HERA*, Ph.D. Thesis, University of Birmingham (1999)
- [106] J. Rathsman, Phys. Lett. B452(1999), 364
- [107] D. Eckstein, *Messung der Longitudinalen Strukturfunktion $F_L(x, Q^2)$ mit dem HERA-Experiment H1*, Ph,D, Thesis, Humboldt University Berlin (2002)
H1 Collaboration, *A New Measurement of the Deep Inelastic Cross Setion and of F_L at low Q^2 and Bjorken- x at HERA*, submitted to EPS2001, Budapest, Hungary, July 2001, and LP2001, Rome, Italy, July 2001